Pattern recognition-based real-time myoelectric control for anthropomorphic robotic systems

A thesis presented in partial fulfilment of the requirements for the degree of

Doctor of Philosophy

In

Mechatronics

at Massey University, Manawatū,

New Zealand.

Jingpeng Wang

2019

Abstract

Advanced human-computer interaction (HCI) or human-machine interaction (HMI) aims to help humans interact with computers smartly. Biosignal-based technology is one of the most promising approaches in developing intelligent HCI systems. As a means of convenient and non-invasive biosignal-based intelligent control, myoelectric control identifies human movement intentions from electromyogram (EMG) signals recorded on muscles to realise intelligent control of robotic systems.

Although the history of myoelectric control research has been more than half a century, commercial myoelectric-controlled devices are still mostly based on those early threshold-based methods. The emerging pattern recognition-based myoelectric control has remained an active research topic in laboratories because of insufficient reliability and robustness. This research focuses on pattern recognition-based myoelectric control. Up to now, most of effort in pattern recognition-based myoelectric control research has been invested in improving EMG pattern classification accuracy. However, high classification accuracy cannot directly lead to high controllability and usability for EMG-driven systems. This suggests that a complete system that is composed of relevant modules, including EMG acquisition, pattern recognition-based gesture discrimination, output equipment and its controller, is desirable and helpful as a developing and validating platform that is able to closely emulate real-world situations to promote research in myoelectric control.

This research aims at investigating feasible and effective EMG signal processing and pattern recognition methods to extract useful information contained in EMG signals to establish an intelligent, compact and economical biosignal-based robotic control system. The research work includes in-depth study on existing pattern recognition-based methodologies, investigation on effective EMG signal capturing and data processing, EMG-based control system development, and anthropomorphic robotic hand design. The contributions of this research are mainly in following three aspects:

- Developed precision electronic surface EMG (sEMG) acquisition methods that are able to collect high quality sEMG signals. The first method was designed in a single-ended signalling manner by using monolithic instrumentation amplifiers to determine and evaluate the analog sEMG signal processing chain architecture and circuit parameters. This method was then evolved into a fully differential analog sEMG detection and collection method that uses common commercial electronic components to implement all analog sEMG amplification and filtering stages in a fully differential way. The proposed fully differential sEMG detection and

collection method is capable of offering a higher signal-to-noise ratio in noisy environments than the single-ended method by making full use of inherent common-mode noise rejection capability of balanced signalling. To the best of my knowledge, the literature study has not found similar methods that implement the entire analog sEMG amplification and filtering chain in a fully differential way by using common commercial electronic components.

- Investigated and developed a reliable EMG pattern recognition-based real-time gesture discrimination approach. Necessary functional modules for real-time gesture discrimination were identified and implemented using appropriate algorithms. Special attention was paid to the investigation and comparison of representative features and classifiers for improving accuracy and robustness. A novel EMG feature set was proposed to improve the performance of EMG pattern recognition.
- Designed an anthropomorphic robotic hand construction methodology for myoelectric control validation on a physical platform similar to in real-world situations. The natural anatomical structure of the human hand was imitated to kinematically model the robotic hand. The proposed robotic hand is a highly underactuated mechanism, featuring 14 degrees of freedom and three degrees of actuation.

This research carried out an in-depth investigation into EMG data acquisition and EMG signal pattern recognition. A series of experiments were conducted in EMG signal processing and system development. The final myoelectric-controlled robotic hand system and the system testing confirmed the effectiveness of the proposed methods for surface EMG acquisition and human hand gesture discrimination. To verify and demonstrate the proposed myoelectric control system, real-time tests were conducted onto the anthropomorphic prototype robotic hand. Currently, the system is able to identify five patterns in real time, including hand open, hand close, wrist flexion, wrist extension and the rest state. With more motion patterns added in, this system has the potential to identify more hand movements. The research has generated a few journal and international conference publications.

Acknowledgements

First and foremost, I would like to thank my supervisor Dr. Liqiong Tang and co-supervisor Prof. John Bronlund for the inspiration, guidance, support, encouragement, patience and opportunities presented to me.

I would also like to thank Dr. Bob Colborne for offering the job position with the School of Veterinary Science of Massey University in my PhD studying period.

I wish to acknowledge the assistance and support from the staff of the School of Engineering and Advanced Technology during my research.

Finally, I would like to thank my wife and other family members who have given me their unwavering love and support throughout the journey of study.

Table of Contents

List of Figures

List of Tables

Chapter 1
Introduction

Scientific and technological advancements have significantly improved the quality of human daily life. Specifically, the methods used for humans to interact with a machine have been largely extended by using techniques to enhance human volitional conveyance. Research in this area has grown to a separate attractive discipline—the human-computer interaction/interface (HCI) or human-machine interface (HMI) [1].

Humans can interact with computers in many ways. A crucial point associated with this interaction is the interface between humans and computers. The keyboard, mouse and joystick are some of the most common HMI devices. However, more efficient and smarter ways to communicate between humans and machines are always in pursuit of researchers. Alternative methods that can easily, comfortably and independently interact with machines and devices are desired in the future for human daily life. With the rapid development in computer science and artificial intelligence, newly emerging HCI technologies, such as biosignal-based control, computer vision, and voice recognition, have presented an excellent prospect.

A biosignal is usually referred to as a bioelectric signal that is originated due to the physiological processes in living beings and can be measured and monitored continuously. Electroencephalogram (EEG), electromyogram (EMG), electrocardiogram (ECG), electrooculogram (EOG) are some examples of biosignals originated due to physiological activities in the human body. The research of biosignal-based control in recent years has been active. It focuses on studying the characteristics of human body physiological electric signals and utilising them to build human-machine interfaces or smart control systems.

This chapter briefs the background of HCI/HMI, especially outlining the control scheme driven by a human physiological signal from muscular activity—the surface EMG signal. In addition to providing a foundation for further knowledge, the concise prologue sets out the aim and objectives of this research. The thesis organisation is also drawn in this chapter to offer readers an overall concept for appreciation.

1.1 Background and challenges

HCI or HMI allows for the control of external supportive or assistive devices by using information collected from the human body. Either a "direct" medium—human perceptual modalities such as speech, touch, vision and gesture, or an "indirect" physiological signal of brain or muscular activity can serve as the data source for deciphering human intentions and generating corresponding external device control commands. The use of a HCI system that employs physiological signals is usually to extend functionalities of human beings by translating their intents into commands towards external peripherals, or to help amputees or disabled people to communicate with the external environment. In recent years, smart biosignal-based intelligent systems, which can understand human intentions for autonomous control of health assistive devices, have attracted huge attention. Figure 1-1 represents a generic model of such systems, which mainly includes two phases, i.e. the physiological signal acquisition and processing carried out by the transducer functional block to give a series of logical symbols, and the translation of the logical symbol sequences to corresponding commands by the control interface block towards an output device [2].

Figure 1-1. A generic model of the HCI system [3].

The electroencephalogram (EEG) and electromyogram (EMG) signals are two of the most commonly used biosignals in HCI research. Electroencephalography is a means of measuring brain activity and it plays a key role in an advanced HCI—the brain-computer interface (BCI) [4], whereas electromyogram represents muscular activity. The electrical physiological signal obtained by using electromyography is usually referred to as the EMG signal, which is a term that stems more from the historical perspective rather than the contemporary. Some researchers use the term ‘‘myoelectric signal (MES)" instead of the historical one—"EMG". The term of "myoelectric control" is thus widely utilised for such control systems that involve the interpretation of human intentions from the EMG signal.

The discovery and use of EMG signals have a long history. Modern research and investigation of EMG started in the 1940s. The early 1960s saw a revolutionary advance in this field—myoelectric control of externally powered prostheses [5, 6]. It is generally believed that the EMG signal from muscle contractions reflects the voluntary intention of the human central nervous system and in turn, the user's

volition. Therefore, the EMG signal can be used for identification of the user's intentions to control various assistive devices, prostheses, and exoskeletons, or be applied to even more applications such as teleoperation of robots and virtual reality. Prosthetics and rehabilitation are currently common application areas of myoelectric control.

The primary types of EMG include surface EMG and intramuscular EMG [7]. Compared to the intramuscular EMG, the surface EMG is a convenient and non-invasive method, hence the common option in research and clinical usage. Surface EMG signals contain rich information from which the user's intents of muscular contraction can be deciphered. With residual muscles, or muscles to which nerves are rewired using targeted muscle reinnervation (TMR) surgery [8], amputees or patients with neuromuscular diseases or disability are able to generate repeatable, although gradually varying, EMG signal patterns during different levels of either static or dynamic muscle contractions. These patterns can then be used to develop smart EMG-based systems for different healthcare applications or automatic control systems that mimic human activities.

Accurate human movement intention discrimination is an important research topic that attracts an enormous of attention and effort from many researchers. Most of the publications in myoelectric control focus on improving the accuracy of human movement intention discrimination algorithms. However, the usability of the myoelectric-controlled devices is not just dependent on the accuracy of software algorithms [9]. From the engineering point of view, the development of an EMG-driven system primarily integrates EMG acquisition, human movement intention discrimination, and output device creation and control [10]. The success of the EMG-driven system is associated to all influential factors in these aspects. These will be briefly introduced in sequence from the next section. On the basis of investigating the status quo and the challenges in these aspects, the research gaps will be identified to propose the research topics of this thesis.

1.2 EMG noises and signal detection

Although myoelectric control has been a hot research field for several decades, up until now there is no standard EMG database used for evaluating and comparing different myoelectric control methods [11]. Therefore, researchers have to acquire EMG signals by themselves. In addition, real-time myoelectric control experiments or applications also request collecting EMG data at the same time the targeted muscular contractions are performing. All these cause the demand of EMG acquisition systems.

The EMG signal is formed by superposed action electrical potentials resulting from depolarisation and repolarisation of physiological variation of muscle fibre membranes. Different methods have been developed to detect the EMG signal—the electrical currents created in contracting muscles. Up until

now, the biggest problem with EMG signal acquisition is how to remove most of various noises. The main sources involved in contaminating the EMG signal include [12]:

- Inherent noise in electronics equipment
- Ambient noise
- Motion artefacts
- Inherent instability of signal
- Electrocardiographic (ECG) artefacts
- Cross talk

Given the complex noise environment and the difficulty to remove these noises, the design of an appropriate EMG signal detection and pre-processing circuit is still by no means trivial despite the advances seen in modern electronics. The market provides a wide variety of commercially available professional multi-channel EMG systems that are able to record high-quality EMG signals [13]. However, they are often very expensive, such as the Delsys® Trigno™ wireless EMG system that is priced at about 20,000 US$ [14]. Although some affordable consumer-grade EMG devices are now available on the market, their performance is usually limited. A typical example is the Myo armband (priced at US$199) [14]. It has a low sampling rate of 200 Hz, which is reported unsuitable to existing myoelectric control methods [15].

Apart from commercial EMG acquisition equipment, an alternative is to develop a specific EMG acquisition system using common commercial electronic components. Contrary to the usual expectation, only little attention has been devoted to the EMG signal detection and pre-processing in the literature of myoelectric control research, compared with the focus on the accuracy of movement intention discrimination. Additionally, the existing publications in EMG acquisition available to the public are mainly concerned with general principles such as the shape, size, interspace and placement of the electrodes [16], or the overall specifications of EMG signal amplification and filtering [12, 17-21]. It is hard to find a complete design with details that can be directly referenced or used by others to integrate it into different application systems. This might be a consequence of the fact that the utilitarian and detailed EMG acquisition system design is a high value asset for potential profits to commercial organisations. This also leads to an implication for researchers that it is difficult to theoretically compare these proprietary products due to technical confidentiality.

An economic, yet precision EMG acquisition system for EMG-based control is desired, and it could provide a study platform to support research interest in this field, especially for the development of EMG-driven smart systems in healthcare applications and robotics. This leads to the necessity of research on economic EMG acquisition system design for EMG-based control in this thesis.

1.3 Movement intention discrimination

Except for the effort dedicated to provide more informative EMG signals, another major issue to increase the success of myoelectric control is to accurately extract more information contained in EMG signals [7]. This is why movement intention discrimination is a central research topic in this area.

Since the 1960s, a few generations of myoelectric control schemes from the earliest on/off control to newly developed regression algorithms, have been proposed, including [6, 9, 22, 23]:

- On/off control
- Proportional control
- Direct control
- Finite state machine control
- Pattern recognition-based control
- Posture control
- Regression control

The early developed non-pattern recognition-based control schemes are primarily established on the basis of pre-defined thresholds or finite states, using EMG signals from either one or two muscle groups to determine an 'on' or 'off' state, or mapping individual EMG signals to individual functions of a myoelectric control device to realise the control purpose. As a result, the number of movements that the device can generate is limited by the number of independently controllable EMG channels. This limitation prevents implementation of multifunction in such devices.

On the other hand, regression control is newly developed to overcome the lack of simultaneous multifunction and proportional control, which is presented in previous non-pattern recognition-based and pattern recognition-based myoelectric control schemes, without giving rise to an increase of device complexity or a decrease of control robustness. The regression control algorithms use a mapping function that translates the information extracted from the EMG signal into continuous kinematics that can be used as control signals. Although the regression method offers great promise, it is nevertheless in its early stage.

In contrast to those early on/off state based methods, pattern recognition-based methods offer a means of multifunctional control by classifying different muscle activation patterns. The pattern recognition-based myoelectric control methods provide more degrees of freedom while using the same number of EMG channels as the on/off state based methods. This increases the variety of control functions and improves system robustness. The wide use of microprocessors in embedded systems facilitates the development of pattern recognition-based myoelectric control schemes. However, pattern recognition is only able to classify muscular movements in sequence, resulting in the lack of simultaneous control

capability. Although the advances in pattern recognition-based myoelectric control are encouraging, it is still largely research-based and confined to the laboratory environment. The reasons why there have not been widespread clinical applications are due to several factors:

- The difference between real-life situations and static laboratory conditions for training and testing,
- The uncertainty in the relationship between device controllability and classification accuracy, which is often reported in research studies, and
- Changes in robustness and reliability over time [9, 24].

The function of motion pattern discrimination of a typical pattern recognition-based myoelectric control system can be divided into several main steps: data segmentation, feature extraction, dimensionality reduction, and classification. Data segmentation is used to window the EMG signals to improve classification accuracy and reduce response time. The selection of a longer window length is able to improve the stability of the features by reducing the variance to increase classification performance, but will incur a longer delay in classification decision. Feature extraction attempts to extract usable information from the EMG signals by increasing the information density of the EMG signals. The selected or extracted EMG features, instead of raw EMG signals, are fed into a classifier to improve classification efficiency. Studies have shown that choosing a feature set that is representative of the data is more critical than the choice of the classifier for high classification accuracy. If the resultant feature set forms a high-dimensional space, it may be necessary to apply the dimensionality reduction strategy before classification. The classifier recognises signal patterns and makes decisions within a pre-defined category set which corresponds to device controller commands.

Notwithstanding the decades of research on pattern recognition-based myoelectric control, there is still not a widely accepted and standard method suitable to different kinds of pattern recognition-based myoelectric control applications. One difficulty of motion pattern discrimination is that it is subject to multiple factors. For instance, specific methods or parameters used for each functional step, intertwine to produce influences on the acceptability of pattern recognition-based myoelectric control, by affecting accuracy and robustness. More research is necessary to search out better methods or methodologies to improve the performance of the pattern recognition-based myoelectric control.

Another challenge that limits pattern recognition-based myoelectric control in laboratory research is validation. Many publications on myoelectric control research use offline classification accuracy as the performance criterion. However, high offline performance may not be able to automatically result in good controllability in complex tasks [25]. Performance metrics, such as completion rate, throughput, completion time, path efficiency, speed and overshoots, are not possible to be assessed and analysed through offline testing [26, 27]. On the other hand, online performance provides more thorough

assessment on the controllability than the offline counterpart. Virtual prosthesis control and computer games are typical online assessment methods. However, these online virtual testing methods still have limitations, e.g. not considering the prosthesis weight that is an important realistic influence factor [28]. This implies that a physical validation system is needed to facilitate the transition from the laboratory to real-life applications. The use of prosthetic hands is a typical example for this purpose. However, commercially available prosthetic hands are very expensive, which are often beyond the reach of many researchers. Specifically for this research, an economic physical validation platform is a feasible solution to evaluate and justify the proposed pattern recognition-based myoelectric control algorithms and methodologies.

This research aims to propose pattern recognition-based intelligent EMG control methods that can be applied to different applications, such as teleoperation of robots, prosthetics, assistance and rehabilitation. The human hand is a dexterous part of the human body and it is also a typical and good source to get inspiration for bionic design. In addition, the surface EMG signal obtained from the human upper limb is an intuitive control signal for a robotic hand. Therefore, it was expected that the proposed EMG-based control method by this research could be demonstrated and validated on a robotic hand platform in real time. To get round of the high cost barrier, developing an economic anthropomorphic robotic hand system became a feasible option for this research.

1.4 Research aim and objectives

The aim of this research is to investigate feasible and effective EMG signal processing and pattern recognition methods that are able to be implemented on an economic platform for general robotic system control. This intention is obviously facing the challenge of finding effective methods for biosignal capturing, noise removal and bio-data pattern recognition. As the EMG signal is a human biosignal and contains human motion intention information, it is selected as the first biosignal this research will focus on. The research work includes the investigation on reliable methods and methodologies to improve EMG signal capturing precision, and EMG pattern recognition accuracy and robustness. To validate and demonstrate the effectiveness of the proposed methods and approaches, an economic anthropomorphic robotic hand system will be developed as a physical testing platform, since the human hand is a complicated bio-structure that is driven by biosignals and it is a typical and ideal imitation target for development and evaluation of biosignal-based intelligent control. To reach the expected goals, the following research objectives must be fulfilled:

- Search for effective surface EMG signal capturing methods with high noise and interference rejection,
- Investigate and develop feasible and robust EMG pattern recognition methods,

- Design a feasible real-time robotic control system that uses EMG as the input signals to control an economic anthropomorphic robotic hand for the evaluation of the methods, methodologies and systems developed by this research.

1.5 Research methodology

Experiments and testing will first be conducted on the proposed methods and systems for EMG acquisition and gesture discrimination. EMG acquisition precision will be analysed in both time and frequency domains. The influences of using different classifiers and EMG feature sets will also be compared for optimising the movement intention discrimination algorithms.

Real-time myoelectric control experiments will be carried out on the developed physical robotic prototype testing system to validate the methods and methodologies developed by this research, and to evaluate the overall performance of the myoelectric-controlled robotic system.

1.6 Thesis organisation

This thesis consists of 7 chapters. Besides the abstract and the introduction chapter, a brief of the remaining chapters is presented below.

- Chapter 2 is a literature review. It reviews related work and methods, mainly focusing on the areas of EMG signal acquisition, pattern recognition-based myoelectric control, and anthropomorphic robotic hand construction and control.
- Chapter 3 presents the research work conducted by this research in EMG acquisition. The first contribution of this research proposes a high performance EMG detection, amplification and filtering approach with single-ended signalling and a fully differential configuration of EMG signal acquisition.
- Chapter 4 covers the development of a pattern recognition-based real-time human hand motion discrimination method, which is the second contribution of this research.
- Chapter 5 describes the development and integration of an EMG-driven anthropomorphic multi-fingered robotic hand and its execution strategy for myoelectric control.
- Chapter 6 states the experiments. It includes both offline and real-time experiment settings, testing, outcomes, and the verification of the proposed methods.
- Chapter 7 concludes and summarises this research and states the recommendations for further research.

Chapter 2
Background and Literature Review

This chapter covers an introduction in the three aspects that relate to the design and construction of an EMG-driven robotic system, i.e. surface EMG signal detection and data acquisition, human hand gesture discrimination, and anthropomorphic robotic system construction and control. In addition, this chapter will review the achievements and advancements of techniques or approaches in precision EMG collection, reliable and robust hand gesture identification, and dexterous anthropomorphic robotic hand development. The problems of existing approaches will also be highlighted for the purpose of improvement.

2.1 Surface EMG signal detection and data acquisition

2.1.1 Data sources for myoelectric control research

Researchers of myoelectric control use the EMG datasets provided by others such as the EMG data set of the University of Paderborn [29] or obtained by themselves from carefully designed experiments for testing their methods. Most of publications in the myoelectric control research area employ specific and professional EMG acquisition systems from commercial suppliers, such as Delsys Incorporated [30], Motion Lab Systems Inc. [31], or BTS Bioengineering [32], to collect required EMG data sets. The commercial professional EMG system method features a very high cost. Therefore, to develop an affordable precision EMG acquisition system is often a feasible and realistic option for EMG-based intelligent control research. Solutions using specifically designed analog application-specific integrated circuit (ASIC) for EMG acquisition are reported in literature [33-36]. However, the ASIC method needs a great deal of effort and knowledge for ASIC design, and is not suitable for the majority of myoelectric control researchers. Therefore, an economic but high quality EMG system composed of commercial electronic components is desirable for the development of an affordable EMG-based robotic control system. A few reference designs for different functional parts of EMG acquisition can be found from literature [13, 37-40]. They often use an instrumentation amplifier (INA or IA) to implement a biosignal analog front end amplifier. However, it is hard to find a complete and detailed solution that can be directly applied to such a low-cost EMG-based robotic control system.

2.1.2 The biomedical fundamentals of the EMG signal

The EMG signal is the electrical manifestation of neuromuscular activation during muscular contraction, representing the current produced by the ionic flow across muscle fibre membranes and transmitted through intervening tissues to the detection site. Despite the fact that EMG signals are measured from muscles, it is generally considered that the EMG signal contains similar information to the recordings directly attained from the neural cells. The central nervous system and nerve fibre innervation establish a sophisticated mechanism bestowed by nature. Figure 2-1 shows a simplified schematic diagram of the central motor system and the concept of two motor units [41].

Figure 2-1. The schematic representation of motor units (a) the basic motor control mechanism of a motor unit; (b) two motor units [41].

Skeletal muscles are made up of many motor units (MUs), each of which consists of a motor neuron, its axon, and muscle fibres innervated by the axonal branches [41, 42]. A motor unit is the most elementary functional unit that can be activated by volitional effort, which is able to generate a motor unit action potential (MUAP) when stimulated by a neural signal. Repeated continuous activation to a motor unit from the central nervous system generates a motor unit action potential train (MUAPT). Multiple motor unit action potential trains from concurrently active motor units are superimposed to form the EMG signal [5]. The MUAP of the nerve-innervated muscle fibres is one-by-one associated with the action potential travelling along the axon of each motor neuron. The EMG signal is thus strictly associated to the neural signal sent from the spinal cord to the muscles [43].

2.1.3 The characteristics of the EMG signal

The amplitude of the EMG signal is stochastic and its distribution can be represented by a Gaussian function. The amplitude of EMG signals typically ranges from hundreds of μV to several mV (0–10

mV_{pp} or 0–1.5 mV_{rms}) and the useful energy is mainly distributed in the 0–500 Hz frequency range with the dominant components limited within 50–150 Hz. An example of the EMG signal and its frequency spectrum are presented in Figure 2-2 (a) [19].

(a) (b)

Figure 2-2. The characteristics of the EMG signal: (a) The spectrum of a typical EMG signal [19]; (b) the spectrum of the mix of a surface EMG signal and a white noise [16].

The amplitude, time and frequency properties of the detected EMG signals are influenced by the anatomical and physiological characteristics of muscles, the control mechanism of the nervous system and the instrumentation of detection. More specifically, they depend on multiple factors such as the timing and intensity of muscle contraction, the distance from the electrode to the target muscle, the amount of adipose tissue between the skin and the muscle, the properties of the electrode and the amplifier, and the quality of contact between the skin and the electrode [17].

The detection of the EMG signal is inevitably affected by miscellaneous noise sources. Several major types of noise sources are involved in the process of EMG signal acquisition, including [19, 20, 44]:

- The inherent noise of the electronic parts inside the detection and recording instrumentation (thermal noise);
- The ambient noises from electromagnetic radiation sources in the environment (the dominant concern is the power line noise);
- Two kinds of motion artefacts with electrical signals mainly in the frequency 0-20 Hz range from the relative displacement of the electrode-skin contact surface (movement artefact noise) and from the motion of the cable which is connecting the electrodes to the amplifier (cable motion artefact);

- The inherent instability of the EMG signal leading to unstable components in 0-20 Hz due to the quasi-random nature of the firing rate of the muscular motor units;
- The noise at the skin-electrode interface (electrochemical noise).

These noises can cause significant changes to the mixed signal spectrum, e.g. the substantially increased median frequency of the underlying signal when a band-limited white noise is added to a surface EMG spectrum, shown in Figure 2-2 (b) [16].

As for the stability, the EMG signal waveforms exhibit both transient and steady states. The transient state occurs in the transition from rest to a constant muscle contraction level, and the steady state is kept in the constant muscle contraction period. Although some publications report that the transient state can also be used in myoelectric control, most of the literature work considers the use of steady state EMG data because of the benefit of reducing the classification error rates compared with using transient data [45].

2.1.4 Electrodes for EMG signal detection

The electrode unit is the closest part to the target biosignal source in the signal processing chain and its design acts as the most crucial aspect of the biosignal-based application system because it is very difficult to improve the quality of the signal beyond this point. Two types of electrodes, the non-invasive (surface) electrode and the invasive electrode (inserted wire or needle), are mainly used to detect the EMG signal [5, 17]. Most commercially available myoelectric control systems employ the surface electrode to detect the EMG signal and this is also the case in circumstances where a surgical technique targeted muscle reinnervation (TMR) is used for high-level upper-limb amputees [8, 46, 47]. The surface electrode, however, has a limited capacity to detect signals from deeper or smaller muscles. In addition, it is influenced by motion artefacts and a significant amount of crosstalk between muscles. To overcome the drawback of the surface electrode, the implantable EMG electrode was tried, using the intramuscular EMG signal or the combination of the surface and the intramuscular EMG signal instead of the surface EMG signal only [7, 48, 49]. The classification performance of using both surface and intramuscular EMG signals was compared and the experimental results showed there was no significant difference between these two measurement techniques [7].

The surface electrode can be further identified into two categories, the passive and the active. The passive electrode has only a conductive (commonly metal) detection surface touching with the skin, while the active electrode contains a differential electronics amplifier in the same housing place as the detection surface instead of transmitting the very weak signal to an analog front amplifier on the main device through long lead wires. The active electrode arrangement can reduce the effects of capacitance coupling between the amplifier input wires and the power line, together with providing very low output

impedance [50]. The advantage of the active electrode is that the reduced capacitance coupling and the very low output impedance will not introduce significant noises from the power line and the cable movement artefact, but such commercially available active electrodes are very expensive [19].

The properties of electrodes have a significant impact on the EMG electronics apparatus design. Impedance, noise and DC voltage are three important factors of electrodes. Different materials, such as noble metals, carbon and silver chloride, and different technologies, including dry and non-dry or wet contact (with a layer of conductive gel), have been used for manufacturing surface EMG electrodes [51]. The wet Ag–AgCl electrode is currently preferred for surface EMG applications. Figure 2-3 shows the basic modelling concepts of skin electrode interface [52]. In general, the contact electrode-skin impedance may range from a few kΩ to a few MΩ, depending on electrode size and skin condition, with the characteristics of larger electrodes having lower impedance and noise, but accompanied by increased smoothing effects (low-pass filtering) [21, 53]. It is generally considered that the noise level of 1–2 μV_{rms} may be contributed by the electronics and 1–4 μV_{rms} by the electrode-skin interface. Two kinds of possible sources cause DC voltages generated between a pair of electrodes. One is due to the metal-electrolyte interface "battery" effect which can generate DC voltages. The other is attributed to a number of physiological reasons that lead to DC or slowly changing voltages presenting between two electrodes on the skin. The DC voltage between two electrodes may reach as high as a few hundred mV [21].

Figure 2-3. Basic concepts of skin electrode interface: (a) Ideal situation; (b) a model of the real situation; (c) a model of electrode with finite area [52].

The simplest electrode arrangement for surface EMG acquisitions is to use an electrode to detect electrical potential with respect to a reference electrode located in an electrically unrelated area. This configuration is called monopolar (Figure 2-4 a). This configuration has the disadvantage of detecting all signals (including unwanted noises) in the vicinity of the detection point. On the contrary, bipolar or differential configuration, along with a differential amplifier, can be used to record only the potential

difference between a pair of electrodes at a fixed distance (Figure 2-4 b). In such an arrangement, either DC noise or AC noise from a more distant place, such as the power line interference and cross talk from distant muscles, relative to the localised electrochemical events occurring in the contracting muscle fibres, will be regarded as "common-mode" signals and eliminated by the differential amplifier [5]. Other more complicated configurations, such as the double differential configuration and the high-density surface EMG [21, 54-56], can also be utilised for more spatial selectivity or for getting more information.

(a) (b)

Figure 2-4. Electrode configuration: (a) monopolar configuration, (b) bipolar configuration [5].

2.1.5 EMG conditioning

The characteristics of the surface EMG signal and the properties of surface EMG electrodes necessitate the EMG amplifier with appropriate specifications, which typically include high common-mode rejection ratio, high input impedance, low noise, low input bias current, and flat passband with sharp roll-off in transition band. Different amplification chains have been proposed and can be used to develop EMG amplifiers and filters with expected performance. Figure 2-5 demonstrates two general amplification chains for EMG acquisition, wherein the chain of panel (a) is suitable during either voluntary or electrically-elicited contraction whereas the panel (b) is only for voluntary contraction [21].

Figure 2-5. Amplification chain block diagrams for a single channel [21].

2.1.5.1 Front end amplifier

The input stage is the most crucial part of an EMG amplification chain. Three critical parameters, input impedance, common-mode rejection ratio (CMRR) and input noise, are mainly dependent on this stage.

Traditionally, an instrumentation amplifier (INA or IA) can be used as the front end amplifier, which is also known as the pre-amplifier, for each EMG signal processing channel [37, 39, 57-59]. Since the impedance of the EMG amplifier must be at least 100 times greater than the largest expected electrode-skin impedance which can reach 1MΩ in the case of small dry electrodes, INAs with input impedance lower than 100 MΩ are not recommended. The CMRR of INAs indicates the ability of rejecting a common-mode signal with respect to a differential signal. Ideally, the CMRR should be infinite but it is not the case in reality. The common-mode voltage presenting between the electrode pair can reach to the order of few volts; therefore, a CMRR greater than 100 dB is necessary to limit the power line interference to a level which can be considered negligible with respect to the useful surface EMG signal. In addition to the finite CMRR, the unbalance of the electrode-skin impedances and the finite INA input impedances can convert part of the common-mode signal to a differential signal at the INA inputs, which is usually considered the main source of power line interference. Low and balanced electrode-skin impedances and high INA input impedances are required to reduce this effect. The input noise performance of INAs also need to be carefully selected because the input noise of the first stage amplification determines the smallest detectable EMG signal [21].

In order to increase the capability of the front end amplifier rejecting the common-mode interference, various technologies have been proposed in the literature, including the use of active electrodes, “guarding”, the driven right leg (DRL) circuit, the virtual ground and the digital adaptive filter [21, 44].

2.1.5.2 EMG filters

Due to the limited bandwidth of the surface EMG signal, filtering frequency components outside the band of interest is possible and also required to increase the signal-to-noise ratio and to provide anti-aliasing for A/D conversion. Corresponding to the useful frequency band of 20–500 Hz of the surface EMG signal, the filter cut-off frequencies are usually selected between 10–20Hz for the high-pass filter and between 400–500 Hz for the low-pass filter [52]. The surface EMG signal is spectrally overlapped at the low frequency end with several types of noise sources, especially the movement artefact which is the most troublesome one. Removal of these components renders the surface EMG signal more useful for practical applications. As a result, more research effort has been seen in the determination of the high-pass filter specification. Different cut-off frequencies including 5 Hz, 10 Hz, 10–20 Hz, 20 Hz, and 15–28 Hz, and different roll-off rates including -12dB/Octave, -18dB/Octave, and -24dB/Octave were investigated or employed in literature [20, 38, 60]. However, the selection of these parameters is application and muscle dependant. This requires careful investigation and determination on these parameters for a specified application.

Both analog and digital filters can be used to remove the components out of the surface EMG signal frequency band. In the analog solution, a high-pass filter should be implemented directly following the front end amplifier to remove low frequency components mainly due to the movement artefacts and the instability of the electrode-skin interface. An alternative strategy is to implement an AC-coupled front end amplifier, without immediately introducing the high-pass filter [37, 61, 62]. The voltage offset introduced by the cascaded amplification stages can be removed by an additional high-pass filter placed along the signal processing chain [13, 21]. In the digital solution, with a high resolution analog-to-digital converter (ADC), the low frequency and the offset removal can be done by a computer or microcontroller using a high-pass digital filter or a moving average filter [21, 33]. In both analog and digital solutions, however, a low-pass analog filter is necessary to remove high frequency components for anti-aliasing immediately before the ADC.

Conventionally, a notch filter at 50 Hz (or 60 Hz) is employed to clean the power line noises. However, the majority energy of the EMG signal is within the 30–150 Hz range, and there is no notch filter that can perform to the ideal level to only eliminate 50 Hz (or 60 Hz) noises without leading to the loss of the neighbouring EMG signal components. The use of the notch filter suppresses the power line interference. At the same time, however, it causes the loss of useful information of the EMG signal. Therefore, the notch filter is not recommended for EMG data acquisition circuitry [5, 7, 20]. As an alternative approach, various adaptive filter techniques have been proposed for the power line noise cancellation [63-65] and have shown the potential for specific EMG signal processing, but with much more complexity and computational cost.

There are different active filter realisation topologies detailed in analog filter design textbooks. Among these filter configurations, the Sallen-Key [38] and the multiple feedback (MFB) [39] topologies are two of the most widely used in EMG applications.

2.1.5.3 EMG A/D conversion

The analog signals are sampled and transformed to digital "levels" represented in binary code by analog-to-digital converters (ADCs). The most critical properties of the ADCs are the sampling rate and the resolution, which impact significantly on the overall system performance.

The useful surface EMG signal is limited below 500 Hz. Nyquist theorem dictates that the sampling rate must be at least twice the signal's highest useful frequency for no loss of information. Apart from the finite bandwidth, the selection of the sampling rate involves taking into account more issues, such as the anti-aliasing filter design and the computational cost of data processing. Different sampling rates, e.g., 400–500 Hz [66], 1000 Hz [24, 54, 67, 68], 1024 Hz [69, 70], 2000 Hz [71] and 4000 Hz [72], were found in the literature for the surface EMG A/D conversion.

The minimum resolution of the ADC is determined by the ADC input range and the number of binary digits of the output code. The principle is that the number of chosen binary output code bits renders at least the same order of magnitude of the noise level. With an input voltage range of 10 V and a binary digital code of 12 bits, the distance between two adjacent codes is $10V/(2^{12}-1) = 2.441$ mV. This distance along with an amplification gain of 1000, provide a minimum input-referred resolution of 2.441 μV which is the same order of magnitude of the noise level [21]. However, a 16 or more bit ADC can provide better accuracy and flexibility to the amplifier with different gains [18].

2.1.6 Review outcome

The trend towards smart, compact and lightweight equipment promotes the research on biosignal application, especially on the biosignal-based human machine interface (HMI). The EMG signal is a suitable candidate for developing a HMI control system. As a type of biosignals, the surface EMG signal is the electrical activity of underlying muscles. It is a very weak, non-stationary biosignal, stochastic in nature. The detection of EMG signals is affected by multiple inherent and external factors such as muscle anatomy, physiological process and different types of noises. Therefore, a specifically designed precision EMG system is necessary for the success of an EMG-driven robotic system. Commercially available EMG systems can provide high quality recording of EMG signals but with the drawback of high cost. The lack of a complete and ready-to-use EMG acquisition system design suggests further research on low-cost and customised EMG acquisition. This section reviews the research work on the

characteristics of the EMG signal, the electrode for EMG detection and the electronics design for EMG detection and signal conditioning. Special emphasis is placed on electrode configuration, the design of the front end amplifier, and filter design.

2.2 Human gesture discrimination

Amongst various myoelectric control schemes, the classical methods are based on on/off or proportional techniques that usually do not allow the user to simultaneously control more than one degree of freedom. In contrast, the pattern recognition-based approach offers the multifunctional control ability, hence regarded as the current preferred method for myoelectric control of prosthetic or rehabilitation devices.

The key point of pattern recognition-based methods is to apply an appropriate classifier to discriminate different EMG signal patterns which correspond to the user's motion volition in a limited period. To this end, the pattern recognition-based motion pattern discrimination module needs more functional components or stages than the basic steps—feature extraction and classification which are essential to a classifier—to increase the recognition accuracy and speed. It is generally considered that the instantaneous value of the EMG signal is of little use because of its stochastic nature. Therefore, the EMG data must be segmented into windows from which a representative feature set can extract useful information of the data. In addition, muscle activity onset detection is needed to activate the subsequent classification process [10], and post-processing methods are usually applied after classification to make a smooth output. If the feature set is too high in dimension, dimensionality reduction techniques are necessary before it is fed to the classifier [6, 24].

In summary, the pattern recognition-based motion pattern discrimination module usually consists of motion activity detection, data segmentation, feature extraction, dimensionality reduction, classification, and post-processing. This section will review previous research work on these aspects.

2.2.1 Activity Onset Detection

Onset time is one of the most commonly used temporal characteristics of EMG signals in biomechanical analysis of human movement and myoelectric control [73]. To apply a myoelectric control method, the first problem is the correct detection of the onset of the movement. In fact, because of the stochastic characteristic of the surface EMG, onset detection is a challenging task, especially when surface EMG response is weak. Visual inspection and various computer-based methods that usually compare a variable related to the rectified EMG signals with a pre-set threshold have been employed as the means of onset detection.

Different computer-based onset detection methods were categorised into the single- and double-threshold methods. The single-threshold method compares rectified raw signals with a threshold, whereas the double-threshold method applies single-threshold detection a number of times [74].

Hodges and Bui compared twenty-seven computer-based methods for onset detection by a standard of visual EMG onset determination of an experienced examiner. They found that the most accurate criteria for methods with sliding window, threshold and low-pass filter techniques are 25 ms/3 SD/50 Hz, 50 ms/1 SD/50 Hz, and 10 ms/1 SD/500 Hz, where the three parameters are window length, the threshold that is a multiple of standard deviation (SD), and the low-pass cut-off frequency respectively [75].

To improve the onset detection performance, several novel algorithms have been proposed, e.g. the maximum value detection (MVD) method [73], the sample entropy analysis method [71], the maximum likelihood (ML) with an adaptive threshold technique method [76], the Teager–Kaiser energy (TKE) operator method [77], and the method combining Teager-Kaiser Energy (TKE) operator with morphological close operator (MCO) and morphological open operator (MOO) [78].

2.2.2 Data Segmentation

The instantaneous values of the EMG signal is generally considered to be unsuitable for pattern recognition due to its stochastic nature. Therefore, features are usually extracted from segmented EMG data analysis windows. Either the disjoint or the overlapped windowing schemes (shown in Figure 2-6) can be used for segmentation. In addition, the length of the analysis window must be appropriate, that is, neither too long to introduce an excessive controller delay (more than 300 ms), nor too short to bring about an unreliable decision [74].

Figure 2-6. Windowing schemes (a) disjoint windowing technique (b) overlapped windowing technique [68].

Oskoei and Hu pointed out a segment with a length of 200 ms contains enough information to determine a motion state of the hand since the minimum interval between two distinct contractions is approximately 200 ms. A length more than 200 ms may demand overlapped windowing technique in order to avoid an excessive controller delay [68].

Farrell and Weir investigated the required trade-offs when considering both controller delay and classification accuracy for multifunctional prostheses. They found that the optimal controller delay ranges approximately from 100ms to 125 ms [79]. They also studied the relationship between controller delay and analysis window length for both the disjoint and the overlapped windowing schemes with/without majority voting (MV) (as shown in Table 2-1) [80].

Table 2-1. Controller delay equations for four configurations [80].

WORST-CASE, AVERAGE AND BEST-CASE DELAYS WITH DELAY RANGES

Classifier Type	Worst-case Delay Equation	Average Delay Equation	Best-case Delay Equation	Difference Between the Best and Worst Cases
No overlap , No majority voting	$D=\frac{3}{2}T_a+\tau$	$D=T_a+\tau$	$D=\frac{1}{2}T_a+\tau$	T_a
No overlap, With majority voting	$D=\left(\frac{n}{2}+1\right)T_a+\tau$	$D=\left(\frac{n+1}{2}\right)T_a+\tau$	$D=\left(\frac{n}{2}\right)T_a+\tau$	T_a
Overlap, No majority voting	$D=\frac{1}{2}T_a+T_{new}+\tau$	$D=\frac{1}{2}T_a+\frac{1}{2}T_{new}+\tau$	$D=\frac{1}{2}T_a+\tau$	T_{new}
Overlap, With majority voting	$D=\frac{1}{2}T_a+\left(\frac{n+1}{2}\right)T_{new}+\tau$	$D=\frac{1}{2}T_a+\left(\frac{n}{2}\right)T_{new}+\tau$	$D=\frac{1}{2}T_a+\left(\frac{n-1}{2}\right)T_{new}+\tau$	T_{new}

***D** = Controller Delay; T_a=Analysis Window Length; τ=Processing Time; T_{new}=Analysis Window Increment; **n** = Number of Majority Votes*

Smith et al. explored the relationship between classification error, controller delay, and real-time controllability using pattern recognition of EMG signals. A target achievement control (TAC) test was performed in a virtual reality environment to inspect controllability. EMG data sequences were collected using two or four bipolar electrodes on the proximal forearm for seven motions. Four time domain features (MAV, ZC, WL and SSC) were extracted within different analysis window lengths and fed into a classifier with a linear discriminant analysis algorithm. A linear mixed-effects model in SPSS software was used to determine the relationship between windows length and classification error. They found that the optimal window length ranges from 150 ms to 250 ms [60].

2.2.3 Feature Extraction

Feature extraction is a method to obtain useful information from the EMG signal through the development of a feature set which is selected to preserve class separability. In fact, it has been shown that classification accuracy is more affected by the choice of feature set than by the choice of classifier [7]. Improper feature set selection is prone to the failure of the whole system design whereas a carefully selected feature set is possible to make the classifier directly achieve high performance. Thus, various features used in EMG signal classification were proposed in literature and their properties were widely studied in the past decades [74].

Most EMG features can be grouped into four categories according to the domain wherein they are calculated: time domain (TD), frequency domain (FD), time-scale or time-frequency domain (TFD), and spatial domain (SD) [81].

Hudgins et al. developed five time-domain features, i.e. mean absolute value (MAV), mean absolute value slope (MAVS), zero crossing (ZC), slope sign changes (SSC), and waveform length (WL), and applied them to a multilayer perceptron (MLP) neural network classifier that uses transient myoelectric signals for classification [82]. This successful application of time domain features in real-time environment incited a multitude of ensuing research efforts invested in myoelectric control research. Du et al. proposed a combination of six time domain features, including integral of the EMG (IEMG), waveform length (WL), variance (VAR), zero crossing (ZC), slope sign changes (SSC), and Willison amplitude (WAMP) [83]. There are also many other feature sets proposed in literature, such as the combination of the autoregressive (AR) and the root mean square (RMS), and the combination of mean absolute value (MAV)+ZC+SSC+WL+AR+RMS [84].

Considering that conventional approaches only use features in the time domain and/or frequency domain for EMG pattern recognition, Phinyomark et al. conducted a review of thirty-seven features of both time and frequency domain proposed in literature, including 26 time domain features and 11 frequency domain features. Three criteria were suggested in quantitative evaluation of these features, i.e. maximum class reparability, robustness and complexity. They found that several features are more suitable for pattern recognition-based myoelectric control [85].

The mathematical definitions of the 26 features in time domain that Phinyomark et al. reviewed are summarised as follows:

1. Integrated EMG (IMEG)

IMEG is usually used to detect the beginning of EMG signal, namely used as an onset detection index.

$$IEMG = \sum_{i=1}^{N} |x_i| \tag{2.1}$$

where x_i stands for the i^{th} point of the EMG segment and N is the length of the EMG segment. These symbols have the same meaning in the following EMG feature definitions.

2. Mean absolute value (MAV)

MAV is one of the most popular EMG signal features and also used as an onset index.

$$MAV = \frac{1}{N} \sum_{i=1}^{N} |x_i| \tag{2.2}$$

This feature is also called the other names in previous literature, such as average rectified value (ARV), averaged absolute value (AAV), integral of absolute value (IAV), and the first order of *v*-Order features (V1).

3. Modified mean absolute value type 1 (MAV1)

$$MAV1 = \frac{1}{N}\sum_{i=1}^{N} w_i \left|x_i\right| \qquad w_i = \begin{cases} 1, & \text{if } 0.25N \le i \le 0.75N \\ 0.5, & \text{otherwise} \end{cases} \tag{2.3}$$

where w_i represents the weighted window function. MAV1 is an extension of MAV with a weighted window function to improve robustness.

4. Modified mean absolute value type 2 (MAV2)

$$MAV2 = \frac{1}{N}\sum_{i=1}^{N} w_i \left|x_i\right| \qquad w_i = \begin{cases} 1, & \text{if } 0.25N \le i \le 0.75N \\ 4i/N, & \text{elseif } i < 0.25N \\ 4(i-N)/N, & \text{otherwise} \end{cases} \tag{2.4}$$

MAV2 that is similar to MAV1 is also an extension of MAV but with a continuous function to improve smoothness of the weighted function.

5. Simple square integral (SSI)

$$SSI = \sum_{i=1}^{N} x_i^2 \tag{2.5}$$

6. Variance of EMG (VAR)

$$VAR = \frac{1}{N-1}\sum_{i=1}^{N} x_i^2 \tag{2.6}$$

7. Absolute value of the 3rd (TM3)

$$TM3 = \left|\frac{1}{N}\sum_{i=1}^{N} x_i^3\right| \tag{2.7}$$

8. Absolute value of the 4th (TM4)

$$TM4 = \frac{1}{N}\sum_{i=1}^{N} x_i^4 \tag{2.8}$$

9. Absolute value of the 5th (TM5)

$$TM5 = \left| \frac{1}{N}\sum_{i=1}^{N} x_i^5 \right| \tag{2.9}$$

10. Root mean square (RMS)

$$RMS = \sqrt{\frac{1}{N}\sum_{i=1}^{N} x_i^2} \tag{2.10}$$

11. v-Order (V)

$$x_i = \left(\gamma m_i^{\alpha}\right) n_i \tag{2.11}$$

where m_i is the muscle contraction force, while α and γ are constants, and n_i is a class of the ergodic Gaussian processes.

$$V = \left(\frac{1}{N}\sum_{i=1}^{N} x_i^v \right)^{\frac{1}{v}} \tag{2.12}$$

It is reported the optimal value for v is 2 and this results in the same definition with RMS.

12. Log detector (LOG)

$$LOG = e^{\frac{1}{N}\sum_{i=1}^{N} \log(|x_i|)} \tag{2.13}$$

13. Waveform Length (WL)

$$WL = \sum_{i=1}^{N-1} |x_{i+1} - x_i| \tag{2.14}$$

14. Average amplitude change (AAC)

$$AAC = \frac{1}{N}\sum_{i=1}^{N-1} |x_{i+1} - x_i| \tag{2.15}$$

15. Difference absolute standard deviation value (DASDV)

$$DASDV = \sqrt{\frac{1}{N-1}\sum_{i=1}^{N-1}\left(x_{i+1}-x_i\right)^2} \tag{2.16}$$

16. Amplitude of the first burst (AFB)

AFB is the first maximum point of the squared and filtered EMG signal.

17. Zero crossing (ZC)

$$\begin{aligned} ZC &= \sum_{i=1}^{N-1}\left[\operatorname{sgn}\left(-x_i \times x_{i+1}\right) \cap \left|x_i - x_{i+1}\right| \geq threshold\right] \\ \operatorname{sgn}(x) &= \begin{cases} 1, & \text{if } x > 0 \\ 0, & \text{otherwise} \end{cases} \end{aligned} \tag{2.17}$$

18. Myopulse percentage rate (MYOP)

$$\begin{aligned} MYOP &= \frac{1}{N}\sum_{i=1}^{N}\left[f(x_i)\right] \\ f(x) &= \begin{cases} 1, & \text{if } \ x \geq threshold \\ 0, & \text{otherwise} \end{cases} \end{aligned} \tag{2.18}$$

19. Willison amplitude (WAMP)

$$\begin{aligned} WAMP &= \sum_{i=1}^{N-1}\left[f\left(\left|x_i - x_{i+1}\right|\right)\right] \\ f(x) &= \begin{cases} 1, & \text{if } \ x \geq threshold \\ 0, & \text{otherwise.} \end{cases} \end{aligned} \tag{2.19}$$

20. Slope sign change (SSC)

$$\begin{aligned} SSC &= \sum_{i=1}^{N-1}\left[f\left[\left(x_i - x_{i+1}\right) \times \left(x_i - x_{i+1}\right)\right]\right] \\ f(x) &= \begin{cases} 1, & \text{if } \ x \geq threshold \\ 0, & \text{otherwise.} \end{cases} \end{aligned} \tag{2.20}$$

21. Mean absolute value slope (MAVS or MAVSLP)

MAVSLP is simply the difference between sums in adjacent segments k and $k+1$:

$$MAVSLP_k = MAV_{k+1} - MAV_k; \qquad k=1,\cdots,K\text{-}1 \tag{2.21}$$

where MAV_k is the MAV of the k^{th} segment, and K is the total number of segments over the entire sampled signal.

22. Multiple hamming windows (MHW)

$$MHW_k = \sum_{i=0}^{N-1}\left(x_i w_{i-i_k}\right)^2, \qquad k = 1,\cdots,K \tag{2.22}$$

where w is the Hamming windowing function.

23. Multiple trapezoidal windows (MTW)

$$MTW_k = \sum_{i=0}^{N-1}\left(x_i^2 w_{i-i_k}\right), \qquad k = 1,\cdots,K \tag{2.23}$$

where w is the trapezoidal windowing function.

24. Histogram of EMG (HIST)

HIST is an extension version of ZC and WAMP.

25. Auto-regressive coefficients (AR)

The coefficients a_p of the auto-regressive (AR) model have been used as EMG features. The AR model is expressed as:

$$x_i = \sum_{p=1}^{P} a_p x_{i-p} + w_i \tag{2.24}$$

where P is the order of the AR model, and w_i is a white noise error term.

26. Cepstral coefficients (CC)

Coefficients of the Cepstral analysis have been used as EMG features. The Cepstral coefficients can be derived from the AR model.

$$\begin{aligned} c_1 &= -a_1 \\ c_p &= -a_p - \sum_{l=1}^{p-1}\left(1-\frac{l}{p}\right)a_p c_{p-l} \end{aligned} \tag{2.25}$$

where a represents the coefficients of the AR model.

The 11 features in frequency domain that Phinyomark et al. reviewed are defined as follows:

1. Mean frequency (MNF)

$$MNF = \sum_{j=1}^{M} f_i P_i \Big/ \sum_{j=1}^{M} P_i \tag{2.26}$$

where f_j is frequency of the spectrum at frequency bin j, P_j is the EMG power spectrum at frequency bin j, and M is length of the frequency bin. The same meanings are applied to subsequent definitions.

2. Median frequency (MDF)

$$\sum_{j=1}^{MDF} P_j = \sum_{j=MDF}^{M} P_j = \frac{1}{2}\sum_{j=1}^{M} P_j \tag{2.27}$$

3. Peak frequency (PKF)

$$PKF = \max(P_j), \qquad j = 1, \cdots, M \tag{2.28}$$

4. Mean power (MNP)

$$MNP = \sum_{j=1}^{M} P_j / M \tag{2.29}$$

5. Total power (TTP)

Zero spectral moment (SM0) is another name for it.

$$TTP = \sum_{j=1}^{M} P_j = SM0 \tag{2.30}$$

6. The 1st spectral moments (SM1)

$$SM1 = \sum_{j=1}^{M} P_j f_j \tag{2.31}$$

7. The 2nd spectral moments (SM2)

$$SM2 = \sum_{j=1}^{M} P_j f_j^2 \tag{2.32}$$

8. The 3rd spectral moments (SM3)

$$SM3 = \sum_{j=1}^{M} P_j f_j^3 \tag{2.33}$$

9. Frequency ratio (FR)

$$FR = \sum_{j=LLC}^{ULC} P_j \Big/ \sum_{j=LHC}^{UHC} P_j \tag{2.34}$$

where ULC and LLC are the upper- and lower-cutoff frequency of the low frequency band and UHC and LHC are the upper- and lower-cutoff frequency of the high frequency band, respectively.

10. Power spectrum ratio (PSR)

$$PSR = \frac{P_0}{P} = \sum_{j=f_0-n}^{f_0+n} P_j \Big/ \sum_{j=-\infty}^{\infty} P_j \tag{2.35}$$

where f_0 is a feature value of the PKF and n is the integral limit.

11. Variance of central frequency (VCF)

$$VCF = \frac{1}{SM0} \sum_{j=1}^{M} P_j \left(f_j - f_c \right)^2 = \frac{SM2}{SM0} - \left(\frac{SM1}{SM0} \right)^2 \tag{2.36}$$

In the experiment of Phinyomark et al., two data sets were collected and the dataset 1 was used to evaluate redundancy of EMG feature sets. The scatter plot was used as the evaluation method for redundancy evaluation. Based on the results of scatter plots and mathematical properties, time domain features were further separated into four groups, i.e. energy and complexity information methods that are calculated based on amplitude values of the EMG signal, frequency information methods that are calculated in time domain but contain frequency information, prediction model methods, and time-dependence methods. There is much redundancy in these four groups of time domain features. Frequency domain features were found not suitable for EMG pattern recognition. Moreover, the dataset 2 was utilised for finding optimal representative EMG feature sets. Linear discriminant analysis (LDA) classifiers were used for searching the optimal features. The recommended features are MAV and WL in energy and complexity information group, WAMP in frequency information group, AR in prediction model group, and MAVS in time-dependence group respectively. All of these EMG features are in time domain. Frequency domain features were found not as good as time domain features in EMG pattern recognition. However, MNF and PSR were recommended to be used for increasing classification accuracy [85]. Furthermore, two EMG feature sets were investigated for redundancy. The first set (MAV, WL, ZC and SSC) used by Hudgins et al. [82] was recommended to keep MAV, WL, and SSC whereas in the second feature set (IEMG, VAR, WL, ZC, SSC, and WAMP) which is used by Du et al. [83], IEMG and WAMP were recommended [85].

Except for the time domain and the frequency domain, EMG features in time-scale or time-frequency domain have also attracted much attention. Signal processing has a long history of using various

transformation techniques. The Fourier transform (FT) represents a signal by a sum of continuous sinusoids that last for all the time, thus being inefficient to transient signals. Wavelet transform (WT) represents a signal by the sum of a series of weighted, shifted and scaled versions of a "mother wavelet" function, enabling better representation of signals that includes fast changing components. Many biomedical electrical signals such as the EMG signal are non-stationary and with transient characteristics. Therefore, WT methods have potentials for better performance when applied to EMG applications. Phinyomark et al. studied the usefulness of wavelet transform (WT) to extract features from partial wavelet components for the EMG signal. The assessment of class separability is based on two criteria, i.e. scatter graph, and the ratio of a Euclidean distance to a standard deviation index (RES). The seventh order of Daubechies wavelet and the forth-level wavelet decomposition were found to be the optimal wavelet decomposition (Figure 2-7). Experiment results showed that only the EMG features extracted from the first-level and the second-level detailed coefficients or their reconstructed EMG signals facilitate class separability in feature space [69, 86].

Figure 2-7. Discrete wavelet transform decomposition tree from the decomposition level 4 [86].

Khushaba et al. proposed a new feature extraction method that extracts a set of power spectrum characteristics directly from the time-domain to reduce the impact of limb position on EMG pattern recognition [87].

There are also researchers using discrete wavelet transform (DWT) or wavelet packet transform (WPT) combined with other techniques for feature extraction, such as [45, 88]. Xing et al. extracted time and frequency information using wavelet packet transform (WPT) and selected the node energy of the WPT coefficients as the EMG feature. They developed a supervised feature selection method based on a depth recursive search algorithm to reduce the high dimension of features [89].

Higher order statistics or higher order spectra (HOS) can detect deviations from linearity, stationarity or Gaussianity in the signal. HOS was also used in myoelectric control research for feature extraction [90-93]. Other techniques of feature extraction that have been tried to use include fractal analysis, the first difference of EMG time series [94, 95] etc.

Another progress area in EMG is that the advances in electronics provide the possibility of high-density EMG measurement to collect not only temporal and spectral but also spatial information, which can be used for feature extraction in EMG motion identification tasks [56, 96].

2.2.4 Dimensionality Reduction

The dimensionality problem, i.e. the "curse of dimension", arises when increasing EMG features or the number of EMG channels. Therefore, dimensionality reduction is an essential technique in EMG applications with high dimensional feature sets, especially when using time-frequency domain features or high-density EMG.

In general, two categories of dimensionality reduction methods exist in literature, i.e. feature selection and feature projection [45, 97]. Feature projection utilises specified transformation to obtain a new dimension-reduced feature space from the original one, whereas feature selection picks out a subset of the features available from the original set.

Compared to other dimensionality reduction techniques, feature projection has reported exhibiting better performance, thus becoming a popular way to reduce the dimensions of the EMG feature vector. Linear discriminant analysis (LDA) and principal component analysis (PCA) [98] are two main linear methods used for feature projection. LDA linearly transforms a high-dimensional feature vector to a lower-dimensional vector space, meanwhile minimising the within-class distance and maximising the between-class distance. LDA is more efficient due to its less computational complexity but with the still comparable classification performance relative to nonlinear discriminant analysis (NLDA) [99]. Phinyomark et al. compared a total of seven methods, including six LDA-based feature projection methods and a PCA method, with a baseline (BS) system that uses all features without any dimensionality reduction. It is reported that orthogonal LDA (OLDA), uncorrelated LDA (ULDA), and orthogonal fuzzy neighbourhood discriminant analysis (OFNDA) are able to achieve good performance with an optimal feature set (RMS, IEMG, MAV, SKW, WL, SSC, ZC, and 6^{th}-order AR). Their experiments showed the reduced feature vector with five elements caused only slight loss of classification accuracy [100].

On the other hand, Liu reported a filter-based feature selection approach which is independent of the type of classification algorithms and features. This means it is possible to perform EMG feature dimensionality reduction without any change to existing classification algorithms [97]. Mesa et al. developed a multivariate variable selection filter method to find the most informative and least redundant combination of EMG channels and features that is able to provide an accurate classification rate in a static-hand task of 14 different gestures [101].

2.2.5 Classification

Pattern recognition attempts to assign each input value to one of a given set of categories or classes. Most of modern statistical classification algorithms have been applied to myoelectric control applications, e.g. decision tree algorithm [88], Gaussian mixture models [84], artificial neural networks

[102, 103], discriminant analysis, K-nearest neighbour (KNN) and Support Vector Machine (SVM). Discriminant analysis uses training data to determine the parameters of discriminant functions of the classifier [7, 99]. KNN is a special case of instance-based learning and also an example of a lazy learning technique. KNN finds a group of k nearest neighbours of the test pattern in the training set, then assigning the test pattern to the class with the maximum number of samples in the group of k nearest neighbours [104]. SVMs are "a system for efficiently training linear learning machines in kernel-induced feature spaces, while respecting the insights of generalisation theory and exploiting optimisation theory" [105]. SVMs combine three important ideas, that is, optimisation algorithms, implicit feature transformation using kernels, and control of over-fitting by maximising the margin [105].

Alkan and Günay implemented classifiers using five different discriminant analysis methods, including linear, diaglinear, quadratic, diagquadratic and Mahalanobis discriminant analysis, along with support vector machine (SVM) respectively. These classifiers were applied to the EMG signals generated by biceps and triceps muscles for four different movements. Mean absolute value (MAV) were employed to extract the feature vectors. The classification accuracy rate was tested by using 10-fold cross validation. They found the SVM classifier achieved a very good average accuracy rate (99%) and discriminant analysis classifiers gave a range of accuracy rate from 98% to 96% in the experiment [106].

Oskoei and Hu introduced and evaluated a SVM-based classification scheme to classify five limb motions and a rest state using four-channel EMG data collected from four locations on a forearm. They found that the SVM performed exceptional accuracy, robustness, and low computational load, compared to LDA and multilayer perception (MLP) [68].

Hargrove et al. proposed a novel multiple binary classifier (MBC) scheme for improved controllability of a powered prosthesis based on the ULDA algorithm. ULDA results in at most C-1 discriminatory dimensions, where C is the number of classes. Consequently, when feeding multidimensional feature data from only two classes to the ULDA algorithm, the output feature vector has a single dimension. Then it is able to be separated using a threshold. The threshold could be computed automatically based on certain criteria; however, it is left to let users or clinicians configure the class threshold in order to improve controllability. For the discrimination of more than two classes, MBC is used to form the final class decision through recombination in some way. A clothespin usability test in a virtual environment showed the proposed control system using MBC had more controllability but with a higher classification error. It suggested that false activations were an important factor of system controllability [24].

Liu presented an adaptive unsupervised classifier based on support vector machine (SVM) to provide a self-correction mechanism for improving classification performance [107].

2.2.6 Post-processing

Overlapped segmentation offers a dense stream of decisions. Postprocessing is used to remove spurious misclassification in the decision stream, producing more reliable and smooth decisions.

Majority voting (MV) is a conventional postprocessing technique. A majority voting is performed using the current decision and decisions made in previous windows [74, 108]. MV improves the robustness of the controller by producing more stable output during classification. However, it does not consider the actual probabilities of misclassification. Instead of MV, Khushaba et al. proposed a novel Bayesian fusion postprocessing method to improve effectiveness by maximising the probability of correct classification [72].

Another post-processing approach is to remove the decisions made from the EMG data windows acquired during movement transition periods [45]. For real-time applications, however, this method requests real-time transition detection, resulting in more complexity.

2.2.7 Review outcome

A reliable movement intention discrimination method is one of the key points for the success of a biosignal-based HMI control system. Pattern recognition-based myoelectric control is a promising method for such a HMI system. The research to develop appropriate algorithms for different modules of pattern recognition-based myoelectric control has attracted many scientists devoting their effort to it for several decades. Most of publications in this area concentrate their interest on the study of representative classification feature sets, high accurate classifiers and effective dimensionality reduction methods. Some pay attention to other relevant techniques, such as activity detection or postprocessing technology. The majority of endeavours carry out the development of individual approaches based on classification accuracy in offline tests that use EMG data sets recorded beforehand. Some papers attempt to use surface EMG data acquired in real-time and verify the proposed methods in a virtual reality environment. However, accuracy cannot directly imply reliability and robustness. A reliable pattern recognition-based multifunctional myoelectric control system with acceptable robustness over time and condition changes still has a long way to go. Therefore, more research is needed to seek such a system.

2.3 Anthropomorphic robotic system design and control

Since the early 1970s, a large amount of effort and attention has been paid by many researchers to issues related to the construction and control of anthropomorphic robotic systems such as robotic arms, legs, humanoids etc. Examining the human body and comparing the construction of legs, arms, feet and

hands, the human hand with five fingers has dexterous joints and is a complicated system to mimic and control. This could be the reason why many researches in literature focus on the human hand, which is widely studied and imitated for robotic system design, control methodology study and testing. This section presents a study on robotic hand construction and control, to give a clear picture of the current status of robotic hand design, and provides useful information for anthropomorphic robotic hand design.

2.3.1 The development of robotic hands and exoskeletons

Many robotic hand devices such as prosthetic hands and anthropomorphic exoskeletons have been developed for research or commercial purposes over several decades. A group of researchers published a few review articles that summarise the advances in this area.

The authors of [109] investigated both common commercial prostheses and anthropomorphic research devices from a perspective of performance characteristics. Five prosthetic hands and eleven research hands were reviewed. Table 2-2 and Table 2-3 summarise their generic characteristics.

Table 2-2. General characteristics of five current prosthetic hands [109].

	Developers	Number of Joints	Degrees of Freedom	Number of Actuators	Actuation Method	Joint Coupling Method	Adaptive grip	Overall Size	Weight
Hosmer Hook [7,8]	Hosmer Corp.	1	1	1	Body Powered	-	No	124 mm long	113-312 grams
SensorHand [9,10]	Ottobock inc.	2	1	1	DC Motor	Fixed pinch	No	Fits inside glove	350-500 grams
Becker Hand (1968) [11,8]	Becker Mechanical Hands Inc.	5	5	1	Body Powered	Spring fingers (act like trunk)	Yes	143 mm long	382-467 grams
i-Limb (2009) [12,13]	Touch Bionics	11	11	5	DC Motors	Tendon Linking MP to PIP	Yes	180-182 mm long, 80-75 mm wide, 35-41 mm thick	450-615 grams
Bebionic (2011) [14]	RSL Steeper	11	11	5	DC Motors	links spanning MP to PIP	Yes	198 mm long, 90 mm wide	495-539 grams

(-) Data not applicable to hand

Table 2-3. General characteristics of eleven research hands [109].

	Developers	Number of Joints	Degrees of Freedom	Number of Actuators	Actuation Method	Joint Coupling Method	Adaptive grip	Overall Size	Weight
TBM Hand (1999) [22]	University of Toronto	15	6	1	DC Motor with Linear Ball Screw	Complient Springs	Yes	146 mm long, 65 mm wide, 25 mm thick	280 grams **
Remedi Hand (2000) [17]	University of Southampton	14	6	6	dc motor (maxon)	Coupled MP, DIP, PIP	No	Simialar to human hand	400 grams
RTR II (2002) [23]	ARTS/Mitech Lbs Pusa Italy	9	9	2	DC Motors	Tendon and free-spinning pulleys	Yes		350 grams
MANUS-Hand (2004) [15]	Spain/Belgium/Isreal	9	3	2	Brushless DC Motors	Fixed Coupling of MP, PIP, and DIP	No[1]		1200 grams
DLR/HIT I (2004) [24]	DLR German Space Agency, Harbin Institute of Technology	17	13	13	Brushless DC Motors with planetary drive	1:1 coupling of two distal flexion joints	No	1.5 X Human hand	2200 grams
DLR/HIT II (2008) [24,25]	DLR German Space Agency	20	15	15	Brushless DC motors with harmonic drive	1:1 coupling of two distal flexion joints	No	Human hand size	1500 grams
UB Hand 3 (2005) [26]	University of Bologna, Italy	18	16	16	HiTec Servos	PIP and DIP coupled in ring, little, and thumb	No		
FluidHand III (2009) [21]	Forschungszentrum Karlsuhe GmbH (KIT)	8	8	1 pump, 5 valves	Pressurized fluid	Distrubuted Pressure	Yes	Fits inside glove	400 grams
Smarthand (2009) [2, 27]	ARTS Lab, Pontedera Italy	16	16	4	DC Motors	Tendon/Spring based	Yes	12 mm longer and 8 mm thicker than 50% male	520 grams
Keio Hand (2008) [28]	Keio University, Yokohama Japan	15	15	1	Ultrasonic motor	Single tendon for each finger	Yes	320 mm length (with motor), 120 mm fingers	730 grams
Vanderbilt Hand (2009) [29]	Vanderbilt University	16	16	5	Brushed DC servomotors mounted in forearm	Single cable for each finger	Yes	190 mm long, 330 mm with motors, 75 mm wide	580 grams

(**) Designed for Children, ([1]) Two DOF of the Thumb controlled through single motor, (blank) Information unavailable

Similarly, six commercially available myoelectric prosthetic hands (Figure 2-8), including Vincent hand by Vincent Systems, iLimb hand by Touch Bionics, iLimb Pulse by Touch Bionics, Bebionic hand by RSL Steeper, Bebionic hand v2 by RSL Steeper, and Michelangelo hand by Otto Bock, were reviewed in the aspects of mechanical design and performance [110]. Moreover, 13 prototype research prosthetic hands from publications were also surveyed in the same paper by collecting their general characteristics to help compare, analyse and find recommended design specifications.

Figure 2-8. Six commercial myoelectric prosthetic hands [110].

The review article [111] proposed some design considerations based on the analysis of kinematical structures, actuators, and sensing technologies used in relevant robotic hand research projects. A task-based design process was then established and recommended.

The authors of [112] presented an anthropomorphic prosthetic hand with a design explicitly providing both precision and conformal grasp capability, as shown in Figure 2-9. A total of four motor units are incorporated for nine degrees of freedom (DoFs). The precision grasps are fully actuated (DOA 1 – DOA 3), while the conformal grasp is performed by using only one motor for three fingers with six DoFs.

Figure 2-9. A prosthetic hand providing both precision and conformal grasps [112].

As with the common prosthetic or research robotic hands, other types of hand-like devices, such as soft robotic hands [113-115] and exoskeletons [116, 117] are also reported in literature.

2.3.2 Anthropomorphism and kinematics

2.3.2.1 Anthropomorphism

It is broadly accepted that the human hand is a reward of nature to human beings, and a result of a long period of evolution. In robotic hand design, one of the most useful methodologies is to obtain inspiration from human hand biomechanical studies. Anthropomorphism refers to the capability of a device to mimic the human hand in general aspects, such as size, weight, degrees of freedom (DoFs), shape etc. The term dexterity reflects the ability of the device to perform highly precise operations using all of the DoFs with feedback information from sources such as vision, perception, and/or tactility. Although anthropomorphism is not necessary to achieve a high dexterity level, it is desirable in rehabilitation, prosthetics, or other human-oriented environments [118].

The human hand is a complex biomechanical structure, composed of bones, joints, muscles, ligaments etc. Its skeletal structure is shown as Figure 2-10. Each of the four fingers consists of three phalanges, whereas the thumb has only two phalanges. The distal interphalangeal (DIP) joint and the proximal interphalangeal (PIP) joint of each finger are able to exercise flexion or extension, but only the metacarpophalangeal (MCP) joint can also move with abduction or adduction in addition to flexion or extension. The thumb, which has the most complex structure in all five digits, shows the versatile movement abilities of flexion/extension, abduction/adduction, and rotation around the axis of the metacarpal joint on the metacarpal phalange.

Figure 2-10. Human hand skeletal structure [119].

The primary aspects involving anthropomorphic robotic hand design include [118]:

- The presence of the main hand's morphological features, such as the palm, the opposite thumb, and the number of phalanges.
- The way in which contact is made with objects over the entire hand surface.
- The robotic hand size resemblance to the human hand real size and the correct size ratio between all hand links.

These can be depicted as Figure 2-11.

Figure 2-11. Robotic hand anthropomorphism level [118].

2.3.2.2 Kinematics

The human hand operations can be generally classified into two different types: grasping and manipulation. The purpose of grasping is to hold an object in a static state with respect to the palm. Manipulation can be regarded as a generalisation of grasping and it is a kind of dynamic grasping to manipulate the object within the hand using collaborative finger movements [120]. Most grasping types further fall within two groups: power grasp and precision grasp. The power grasp holds the object between the finger surfaces and the palm mainly for force, while the precision grasp holds the object with the tips of the fingers and the thumb for high precision and less force [119].

The authors of [121] pointed out that anthropomorphic kinematics should simulate the human hand in four aspects:

- Joint arrangement
- Finger link length and length ratio
- Opposable thumb workspace
- The palm and fingers on a plane

From a kinematic point of view, the minimum number of fingers in a robotic hand is three for grasping operation, while a minimum of four fingers are needed if targeting manipulation with repeated grasping motions [120]. The level of redundancy and flexibility of the fourth and fifth fingers can increase the chances of a stable contact with the gripped object in an unstructured environment, even though effective manipulation can be conducted with only three digits [122].

The opposable thumb is one of the most critical features that contribute to the human hand dexterous manipulation ability. It is estimated that the loss of the thumb corresponds to a loss of 40% of hand functions [109, 119]. A review of research work on biomechanics of the human thumb to understand the evolution and morphology of the human thumb was presented in [119], which also investigated the

robotic thumb design in some of the biologically inspired anthropomorphic robotic hands developed so far. It was found that the kinematic model of the thumb was one of the main variation sources of the robotic hand kinematic model, the total DoFs of which could vary from 15 to 25. It is necessary to incorporate an opposable thumb and a desired number of DOFs to successfully enhance the preferable features of a robotic hand. Various robotic thumb models with different design and control strategies found in the literature were summarised in [119], mainly in four groups of anthropomorphic robotic hand design:

- Multi-fingered robotic hand
  A total of 10 selected robotic thumb designs were outlined. Thumb kinematics adopted in this group vary based on thumb base inclination towards the palm, joint axis orientations and locations, number of actuated DOFs, etc.
- Prosthetic hand
  The thumb implementation in 11 prosthetic hands was discussed. It is more than a challenge to design a prosthetic hand with dexterity and at the same time making sure that its weight is comparable to the human hand (the average weight of a human hand varies from 0.4 kg to 0.6 kg [109, 119, 121]). Therefore, existing prosthetic hands are mainly designed only for grasping objects, but not for manipulating these objects, in order to reduce the number of active DoFs and avoid mechanical complexity. However, present prosthetic hands are considered not to be dexterous enough mainly due to the lack of functional thumbs. A thumb kinematics design having more than one DoF can significantly improve hand functionality.
- Adaptive/soft hand
  Four characteristic thumb mechanisms in adaptive/soft hands were investigated. Soft robotic hands outperformed their conventional rigid counterparts by their adaptability in unstructured environments. The concept of kinematic synergy was adopted in developing soft hands. The human hand can grasp using coordinated time-varying muscle activation patterns (synergies). These muscular synergies can be identified and modelled to implement hardware synergies for a robotic hand. The synergy-based models can contribute to less sophisticated robotic hand design by providing better understanding of force distribution and control.
- Exoskeleton/hand assistive device
  Only a few thumb-assistive mechanisms were found, and most of them included only thumb flexion-extension motion.

According to the allowed kind of motions, the hand configuration can be classified into four types as shown in Figure 2-12.

Figure 2-12. Kinematic configuration of artificial hands [123].

Figure 2-13 shows the anatomical structure of the human index finger. The motion of the PIP and DIP joints are interdependent as the lateral bands of the natural finger couple the rotation of the DIP to that of the PIP joint. The ratio of the DIP joint rotation angle with respect to the PIP joint is approximately a constant, 2:3 [124-126].

Figure 2-13. Anatomy of the index finger [125].

A four-bar linkage or a tendon coupling mechanism can be utilised to achieve the passive rotation interdependence of the DIP and PIP joints. Therefore, the kinematic architecture of an artificial finger can be illustrated as in Figure 2-14.

Figure 2-14. Kinematic architecture of an artificial finger [125].

A mechanical design approach of a prosthetic compliant underactuated finger was proposed in [127]. It was based on the idea of human hand synergy from neuroscience. Principal components analysis (PCA) was used to decompose human hand movements into two groups—primary and secondary motion. In the anthropomorphic robotic hand design, actuators were only used for the primary motion, while the secondary motion was implemented with mechanical compliance. In this way, the number of actuators could be greatly reduced, and the control strategy could be simplified as shown in Figure 2-15.

Figure 2-15. A finger design with one actuator and embedded mechanical compliance [127].

2.3.2.3 High biomimicry design

Effort has also been made to better understand the intrinsic features of biomechanics and control mechanisms in the human hand by developing anatomically correct [128] or highly biomimetic [129] anthropomorphic robotic hands for achieving dexterous, versatile, and robust operations in robotic hand design.

In the paper [128], an anatomically correct testbed (ACT) hand was constructed to identify the critical factors that lead to dexterity in the human hand for a better understanding of functionality towards human-like robotic hand dexterity. The ACT hand closely imitated the biomechanical features of the human hand, including bone structures and tendon arrangements. The ACT control was also inspired by the human hand neuromuscular control system. The robotic finger bones were built using laser-scanned 3D models of human left-hand bones to replicate the biological shapes of the human finger bones, providing accurate moment arms for the tendons. The finger joints were implemented as one or two carefully aligned hinge joints that can approximate complex human joint motion. A tendon string system along with DC motors were used to mimic the human hand muscular structure.

Figure 2-16. The anatomically correct testbed hand [128].

Xu et al. designed a two degree of freedom matacarpophalangeal (MCP) joint of an index finger that consists of three parts: a ball joint which directly deploys unique articulated shapes of human joints, crocheted ligaments to limit the range of motion of the MCP joint, and a silicon rubber sleeve to replicate passive compliance of the musculoskeletal structure (Fig. 2-1). The MCP joint has demonstrated that its dynamic characteristics are similar to that of human index finger [130].

Fig. 2-1 Compliant artificial finger joint with true to life bone shapes [130].

In the paper [129], artificial joint capsules, crocheted ligaments and tendons, laser-cut extensor hood, and elastic pulley mechanisms were used to closely mimic the human hand counterparts instead of the hinge or gimbal type joints used in [128].

Figure 2-17. The highly biomimetic robotic hand [129]

Despite higher imitation to the human hand anatomical structure and kinematic mechanism, the high biomimicry approach requires more actuators to drive joint movements. This makes it difficult to implement using current actuation technologies in practical applications.

2.3.3 Actuation and transmission

Since 1980s, actuation technology has been acknowledged to be the main limit to dextrous robotic hand development. This is still true although novel technologies or materials, such as various artificial muscles, have thrown some light on prospective solutions.

2.3.3.1 Level of actuation

According to the number of actuators and the number of DoFs, a robotic hand can be implemented as:

- Fully actuated (with the same number of actuators and DoFs) ;
- Redundantly actuated (with more actuators than DoFs);
- Underactuated (with fewer actuators than DoFs).

In most development cases, a redundant actuation mechanism is neither desired nor useful and hence usually not considered [118].

The technological limitation of artificial actuation approaches has always been the main barrier to a lightweight dextrous robotic hand design. Two solutions can be used when a bulky hand is unacceptable. The first one utilises fewer actuators than the actual number of degrees of freedom of the hand, i.e. an underactuated hand, whereas the other uses actuators placed in the forearm where a tendon system is routed from the actuators to the hand joints to transmit motion [120]. Some reported research hand platforms have used a tendon motion transmission system having a part of its driving muscles in the forearm [129, 131], just like the human hand. For a prosthetic hand, however, this may be impractical due to different levels of forearm loss in individual patients. A device constructed in this way is more

appropriately referred to as an anthropomorphic robot rather than a prosthesis, and thus of little clinical use or significance [122]. This leads to the underactuated solution more desirable under some circumstances. A theoretical analysis of underactuated hands was conducted with a focus on force distribution for the establishment of the underactuated grasping theory [123]. The grasping stability was analysed mainly in terms of the contact force distribution and the overall grasp stability.

Two different kinds of underactuation can be identified in the robotic hand design: the inter-phalange underactuation within a finger, and the inter-finger underactuation between fingers [118]. It is worth noting here: if the motion of all phalanges of a finger is coupled in such a way that the trajectory can be entirely predetermined, then the finger has only one DoF and is not an underactuated device but a fully actuated one because a single actuator suffices to follow it [123]. The same philosophy happens to the entire hand design. With the help of underactuation mechanical intelligence, a single actuator was designed to be able to drive an anthropomorphic robotic hand with 15 DoFs [132].

Underactuation can be obtained through the use of coupling mechanisms including passive mechanical devices, usually springs and mechanical limits, within a finger or between fingers for grasping [132]. This approach can lead to a mechanical adaptation of the hand to the shape of the grasped object. Therefore, the hand can be named as a shape adaptive hand [118].

Three classes of underactuated mechanisms have been proposed, i.e. differential mechanisms, compliant mechanisms, and triggered mechanisms [123, 133]. Xu and Liu also pointed out in their paper [134] that instead of the differential mechanism, other configurations such as spring-biased linkage, biased cable routing, biased gear transmission, and compliant structures can be used to design underactuated grippers or hands.

Differential mechanism is the most common element used in underactuation. According to the IFToMM terminology (IFToMM 1991), a differential mechanism may resolve a single input into two outputs and vice versa. Typical structures of differential mechanisms include [134, 135]:

- pulley-based forms;
- linkage-based forms;
- gear-based forms;
- fluidic T-pipe-based forms.

The common mechanical mechanisms that can be employed in the finger movement coupling for the use of the underactuation concept include [118, 136, 137]:

- Linkage-driven Mechanism
  The principle of a linkage-driven mechanism can be shown using a two-phalange underactuated finger. Figure 2-18 illustrates the closing sequence of the two-phalange underactuated finger.

There exist two DoFs but only one actuator and one elastic element (a spring), along with a mechanical limit used to drive the closing sequence to adapt to the shape of the object.

Figure 2-18. The closing sequence of an underactuated finger with two phalanges [136].

- Cable-driven mechanism

  Most prototype robotic hands aiming at the imitation of human hand functionality have used the combination of tendons and pulleys for propagating the actuation to the joints. However, very few of them were successfully commercialised [123]. The pulleys share the same axis with corresponding phalanx joints. In order to make the finger underactuated, the pulleys can freely rotate around the respective axis without transmitting this rotation to the phalanges [118, 137, 138]. This kind of mechanism can be very effective for small forces, and the elasticity and friction from tendons can be compensated with appropriate control. It is useful for lightweight prosthesis development.

Figure 2-19 demonstrates the mechanism of a three-phalanx underactuated finger using either four-bar linkage or tendon-pulley coupling mechanism without the indication of springs for legibility. The equivalence between the four-bar linkage and tendon-pulley coupling mechanism has been proven in [139].

(a) (b)

Figure 2-19. A three-phalanx finger (a) using linkages; (b) using tendons [136].

Mechanisms in a similar form to the four-bar linkage were found in commercial prosthetic hands [110], as shown in Figure 2-20.

Figure 2-20. Commercial finger images (top) and kinematic models of finger joint coupling (bottom): (a) Vincent (Vincent Systems), (b) iLimb and iLimb Pulse (Touch Bionics), (c) Bebionic v2 and Bebionic (RSL Steeper), and (d) Michelangelo (Otto Bock). θ1 = angle of MCP joint, θ2 = angle of PIP joint [110].

A soft gripper that can conform to objects of any shape and hold them with uniform pressure was proposed in [140]. The connected differential mechanism of this soft gripper (Figure 2-21) was employed by different robotic hand applications for inter-phalange underactuation [138, 141-144].

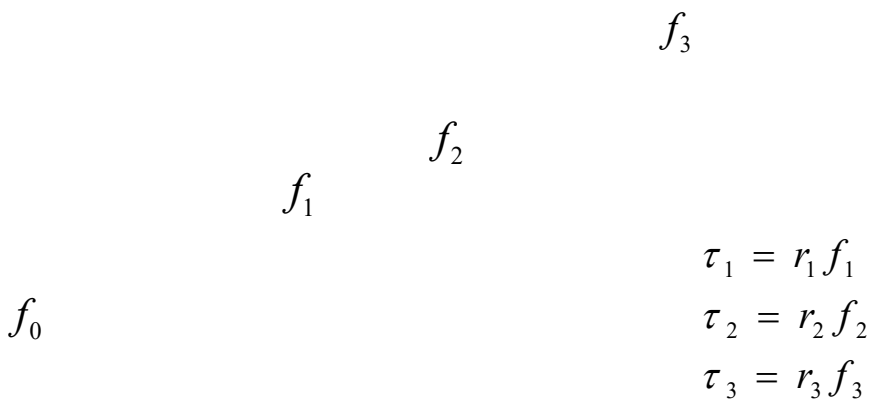

Figure 2-21. Soft gripper mechanism modified from [138].

Two types of tendon-pulley configurations can be used for the soft gripper mechanism, as depicted in Figure 2-22.

Figure 2-22. Two types of tendon-pulley configurations for the soft gripper mechanism [140].

The inter-finger underactuation can be achieved by using a compliantly coupled differential mechanism as shown in Figure 2-23 [145]. A linear slider pulls or releases three tendons by means of three compression springs, thus obtaining adaptive grasp via the adoption of the compression springs.

Figure 2-23. Differential mechanism with compression springs [145].

2.3.3.2 Type of actuation

Biological muscles offer a means of linear actuation and have advantages for providing intermittent displacements and adaptable stiffness, although they can be outperformed in many respects by artificial actuators. The main characteristics of mammalian skeletal muscles are summarised in Table 2-4 and can be used for comparison with other technologies.

Table 2-4. Mammalian skeletal muscle characteristics [146].

PROPERTY	TYPICAL	MAXIMUM
Strain (%)	20	> 40
Stress (MPa)	0.1 (sustainable)	0.35
Work Density ($kJ \cdot m^{-3}$)	8	40
Density ($kg \cdot m^{-3}$)	1037	
Strain Rate ($\%\cdot s^{-1}$)		> 50
Specific Power ($W \cdot kg^{-1}$)	50	284
Efficiency (%)		40
Cycle Life		$> 10^9$
Modulus (MPa)	10 - 60	

The actuation system exerts forces in a robotic system by converting a type of energy, such as electric, hydraulic or pneumatic, to the kinetic energy of rotational or linear movement. The different types of actuators that have been used as energy sources in robotics can be classified in two groups as per the motion generation principle [118]:

- Conventional actuators

  Electric motors, hydraulic actuators, and pneumatic actuators are categorised into this group because of their broad use and relatively longer history. The advantages and disadvantages of each of these actuator types are summarised in Table 2-5.

Table 2-5. The characteristics of conventional actuators [118].

Features\types	Electrical	Hydraulic	Pneumatic
Working Principle	Electricity. Application of magnetic fields to a ferrous core and thereby inducing motion.	By changes of pressure in High Quality Oil Base with Additives, Water Based Solutions, and Synthetic liquids.	Use a compressible gas as the medium for energy transmission.
Basic System	Solid State Logic, Power Amplifiers, DC motors (brushed and brushless, low inertia, geared and direct drive, permanent magnet) or AC motors, Gear	Pump, Sump, Regulators, Filters, Heat Exchangers, Servo Valves, Motors, Actuators, Accumulators	Compressor, interstage Coolers, Pressure Controls, Filter, Dryers, Mufflers, valves, Actuators, Snubbers.

	Boxes, Ball Nuts, Coolers.		
Efficiency	Over 90 % for Large Systems	Seldom over 60 %	Seldom over 30 %
Advantages	Energy easily stored and re-supplied. Control flexibility of the mechanical system. Easy to install and clean. Lower cost.	Very quick movements with great force. Low noise level.	Cleaner and non-flammable. Easy installation, operation and maintenance. Lower cost. Light weight.
Disadvantages	Produce very small torques compared to their size and weight.	Susceptibility to Contamination, High Temperature Sensitivity due to viscosity changes	Less force capability than hydraulic actuators. Lower force and speed.
Principal Applications	The most common choice with a huge number of applications in the robotic industry.	Nuclear and underwater applications, remote operated vehicles	Walking machines and haptic systems

- The non-conventional actuators

  Advances in material sciences have resulted in the advent of smart materials that have similar behaviours to biological muscles. Although the natural muscle functionality and working process cannot be exactly reproduced, such smart materials can replicate part of natural muscle functions [147]. Artificial muscle is a generic term used for materials that have muscle-like properties of reversibly contracting, expanding, or rotating. The most common types of artificial muscles include shape-memory alloys (SMAs), electroactive polymers (EAPs) etc. SMAs and EAPs have been the most promising materials, which exhibit functional characteristics similar to biological muscles. There are also other types of artificial muscles, such as the ones mentioned in [146] and [148].

EAPs are a type of polymers that exhibit a change in size or shape when stimulated by an electric field. EAPs are able to emulate the features of biological muscles, offering resilience, toughness, large actuation strain and inherent vibration damping. EAPs can be used as actuators, especially for the situation of large deformation and low forces [147]. EAP actuators are the least developed technology, and are still too far away from the mature stage [149].

Shape memory alloys (SMAs) are a group of metallic alloys that can return to their original form (shape or size) when subjected to certain stimulus such as thermomechanical or magnetic variations. This phenomenon is known as the shape memory effect (SME). SMAs can be found existing in two different phases associated with three different crystal structures, a total of three combined states, i.e. twinned martensite, detwinned martensite, and austenite. There exist six possible solid-solid transformations between them [150, 151]. The behaviours of SMAs can be characterised by three shape change effects, i.e. one-way shape memory effect, two-way shape memory effect, and pseudoelasticity (PE) or superelasticity (SE). In the one-way shape memory effect, the material can be deformed by applying an external force, and then retains the deformed shape after the removal of the external force. It contracts or recovers to its original form when heated beyond a certain temperature either by internal (Joule or resistive heating) or external heating. Usually, the one-way shape memory effect can be applied commercially in developing actuators. Amongst SMAs, nickel–titanium (NiTi) alloys are the most preferable for the majority of applications. Table 2-6 shows the typical properties of thermal shape memory alloys. The advantages of SMA are the features of large forces per unit area, very high strain rates, relatively large deformations, high peak energy density, and high power per unit mass. However, the practical usage of SMA is limited by its several characteristics: the difficulty of controlling the length, a limited cycle life, and the low efficiency [146].

Table 2-6. Properties of thermal shape memory alloys [146].

PROPERTY	MIN.	TYP.	MAX.
Strain (%)		5	8
Stress (MPa)			200
Work Density (kJ/m^3)		1,000	10,000
Strain Rate (%/s)		300	
Power (W/kg)		1,000	>50,000
Life (cycles) at a amplitude strain of:	300 ~ 5 %		10^7 ~ 0.5 %
Efficiency (%)			< 5
Modulus (GPa)	20		83
Tensile Strength (MPa)		1,000	
Density (kg/m^3)		6,450	
Applied Potential (V)		4	
Conductivity (S/cm)		12500	14250
Cost (US$/kg)		300	

2.3.3.3 Transmission

The approaches employed in robotic hands to transmit actuation power to the joints can be roughly categorised into two groups [121]:

- Rigid connection

  Different gear or articulated mechanisms, such as harmonic drive, spur and worm gears, flexible shafts, and leverages, have been adopted. This kind of rigid transmission mechanism can render better performance in terms of friction but with increased weight to the device. In cases where the actuators can be placed in the palm or in the fingers, a classical gear mechanism can be an appropriate method due to the short power transmission distance needed. However, high cost custom miniaturised gears and parts may be necessary because of the limited housing space. Figure 2-24 shows an example of gears used in power transmission.

Figure 2-24. Internal structure of the actuator module [152].

- Flexible transmission

  Tendons and pulleys or sheaths can be used to create flexible transmission in robotic hand development. A benefit from the flexible transmission is that the actuators can be placed remotely and the number of the required linkage components can be reduced. In addition, the flexible transmission can offer some compliance due to the elasticity of the tendon. Pulleys or sheaths are used to guide the tendon routes. There can be many solutions of the tendon route configuration that can drive the robotic hand performing required tasks. However, it is by no means trivial to get an optimised tendon route network.

As a means of flexible transmission, tendon-based mechanisms have long been researched and utilised in the power transmission of robotic manipulators or robotic hands. The number of tendons per joint is one of the measures used to categorise tendon transmission systems, as schematically depicted in Figure 2-25:

- n-tendon system, as shown by Figure 2-25 (a) and Figure 2-25 (b);
- 2n-tendon system, as shown by Figure 2-25 (c);
- (n+1)-tendon system, as shown by Figure 2-25 (d).

Figure 2-25. Kinematics of tendon systems: (a) One tendon-actuator against extension spring, (b)Two opposed tendons and one actuator, (c) 2n-tendon system and (d) n+1-tendon system [120].

The *n*-tendon system can be implemented using two different structural approaches, as shown by Figure 2-25 (a) and Figure 2-25 (b). The principles of both of them were employed in [112] and called the unidirectional tendon configuration and the bidirectional tendon configuration respectively, as illustrated in Figure 2-26.

Figure 2-26. The tendon-driven configurations: (a) the bidirectional tendon configuration; (b) the unidirectional tendon configuration [112].

There is one difference between Figure 2-25 (a) and Figure 2-26 (b). The *n*-tendon system structure of the Figure 2-25 (a) uses a tension spring in series, while the unidirectional tendon configuration in Figure 2-26 (b) employs a torsion spring in parallel at the joint.

In [153], the *2n*- and *(n+1)*-tendon configurations of robotic finger tendon driving (as in Figure 2-27, *n* is the number of DoFs of the finger) were explored to investigate the optimisation method for force transmission capability to achieve the same range of forces as the human finger.

Figure 2-27. The *2n*- and *(n+1)*-tendon configurations of robotic finger tendon driving [153].

For tendon routing, there can be indefinite solutions. Figure 2-28 and Figure 2-29 depict two of them for tendon-pulley transmission found in literature.

Figure 2-28. Diagram of the finger showing pulleys and cable routing [154].

Figure 2-29. Layout of sliding wheel and tendon [155].

A underactuated prosthetic hand prototype developed in [124] uses tendon-pulley underactuation, joint coupling, and a series of joint locking mechanisms. The transmission and joint coupling mechanism of the four fingers and the thumb are illustrated in Figure 2-30 and Figure 2-31, respectively.

Figure 2-30. The finger subsystems (1) tendon-pulley transmission; (2) joint locking mechanism; (3) four-bar coupling; (4) tactile sensor array [124].

Figure 2-31. The thumb subsystems (1) tendon-pulley actuation; (2) tendon coupling; (3) urethane rubber tip [124].

Tendon-sheath transmission systems are another type of tendon-based systems and are also found applied in research. A conference paper [156] presents a soft prosthetic research hand using an embedded tendon driven underactuated mechanism and compliant joints to make up one continuous part that can deform similarly to a deflected spring as shown in Figure 2-32. Synovial sheaths of the flexible plastic tubing Tygon® from Saint-Gobain Performance Plastics were embedded inside phalanges to route tendon networks. A DC motor with a gearbox and a power-off brake housed in the palm offers actuation power by pulling five tendons, one for each finger. The adaptive grasping is achieved through a simple cable-based differential mechanism. Only two sensors were used: one for monitoring the displacement of the tendon and the other for the DC motor current.

Figure 2-32. The cosmetic prosthetic hand with tendon-driven underactuated mechanism and compliant joints [156].

The UB Hand 3, an anthropomorphic robot hand as in Figure 2-33, was developed using coil springs as elastic hinge joints [157]. It is actuated by sheath-routed tendons. This five-fingered robotic hand has 20 degrees of freedom (DoFs) but only 16 actuators, i.e. 16 degrees of actuation (DoAs. The remaining 4 Dofs are locked or coupled using mechanical mechanisms. Two types of sensors, i.e. strain gaged-based load cells and position sensors, are exploited for the measurement of tendon forces and joint angles respectively.

Figure 2-33. The UB Hand 3 [157].

The transmission characteristics of a tendon-sheath driving system that considers both compliance and friction effects, were investigated in [158], and then a control strategy that is able to remove the direct-dependent response was introduced. Also, the force transmission characteristics of tendon-sheath transmission were analysed in [159, 160]. Tendon-sheath transmission can reduce structure size and mechanical complexity, thus increasing the reliability of the overall system compared to tendon-pulley transmission. However, the tendon compliance and the friction between tendon and sheath may cause some side effects in force control, such as direction-dependent behaviour, hysteresis and dead zone. A lumped parameters tendon model was used in simulation for the analysis of tendon compliance and

friction, with the consideration of a static friction model (Coulomb friction) which can be corrected by a dynamical friction model (Dahl model). A simple force control algorithm with feedforward friction compensation was described for addressing the nonlinear behaviour of tendon-sheath transmission. The lumped parameters tendon model of tendon-sheath transmission was further experimentally validated by comparing the measured tendon tension data with the theoretical tension distribution given by the mathematical model in [161], and then a control scheme based on a sliding-mode controller with a boundary layer for the compensation of the nonlinear friction effect was proposed.

A new type of actuation mechanism was proposed in [126] for driving robotic finger joints. Two strings were twisted on each other to produce a pulling force on a driven object. Figure 2-34 shows the principle of two twisted strings converting rotation to linear motion. Obviously, the electrical motor is still necessary in such an actuation system that uses two twisted strings to drive the object.

Figure 2-34. The principle of twisted strings [126].

A five-fingered robotic hand prototype (Figure 2-35) was constructed to demonstrate the concept of the twisted string actuation mechanism.

Figure 2-35. The five fingered robotic hand prototype [126].

Similarly, two sets of the twisted string actuation mechanism, referred to as “Twist Drive”, are inserted into a finger directly to drive the MCP and PIP joints independently, while the DIP joint is coupled with

the PIP joint by using a four bar linkage type coupling that is particularly designed using a string instead of a classical rigid link, as shown in Figure 2-36 and Figure 2-37.

Figure 2-36. Schematic drawing of finger's cross-section [126].

Figure 2-37. PIP and DIP coupled joint design [126].

Research found that the DIP and PIP joints of a human finger usually move in a coupled manner when without any constraint and special effort. The ratio of the DIP and PIP joint coupling seems linearly in their most range of motion and is to be approximately a constant coupling ratio, mostly in the range of 1.5 to 2. By adjusting the attachment points of the string of the four bar linkage coupling mechanism, it is possible to closely approach a constant value of coupling. This way, the DIP and PIP joint motion of the robotic finger can simulate that of a human one [126].

A similar twisted string actuation was developed in [162] and [163]. Instead of using two strings twisted on each other in the aforementioned "Twist Drive", the twisted string actuation reported in [162] and [163] uses a very thin long string with two or more parallel strands. One end of the string is directly connected to a rotational electrical motor without a mechanical speed reducer such as a gearhead, and the other end is connected to the load to be actuated. The basic concept and schematic configuration of the twisted string actuation system is shown in Figure 2-38. This twisted string actuation allows for the

use of very small and lightweight high-speed electrical motors due to its high speed reduction ratio, suitable for applications where space and weight are of crucial importance.

Figure 2-38. The basic concept and schematic representation of twisted string actuation [162].

The kinetostatics of the twisted string actuation was proposed to take the elasticity of the string into account, while its dynamic model was simplified by assuming the use of rigid strings. An algorithm for controlling the force applied by the twisted string actuation system was developed on the basis of these models and its effectiveness was proven by both simulation and experiments [162, 163]. The twisted string actuation was used in the development of the DEXMART hand robotic finger [164], as shown in Figure 2-39.

Figure 2-39. The finger actuation module of the DEXMART hand [164].

The finger structure of the DEXMART hand was built using 3D printing technology and integrated with position, force and tactile sensors. Four active and one passive transmission tendons are utilised for driving and coupling a total of four DoFs in the three joints [165], as shown in Figure 2-40.

Figure 2-40. The (*n+1)*-type tendon network of the finger [164].

A similar transmission tendon network arrangement (Figure 2-41) was applied to the further development of the UB Hand 3, i.e. the UB Hand IV, which has a total of 20 DoFs, 4 DoFs for each of the 5 identical fingers.

Figure 2-41. The tendon network of the UB Hand IV [166].

2.3.3.4 Non-conventional actuation and transmission

Compared to conventional actuators, such as electrical motors, the artificial muscles, including shape memory alloy (SMA) and Electroactive Polymers (EAPs), can play the role of both actuator and transmission mechanism at the same time due to their direct linear motion characteristics, eliminating the necessity of power transfer from mechanical rotation to linear motion.

Matsubara et al. developed a prosthetic hand using the shape memory alloy (SMA) type artificial muscle (AM). Figure 2-42 shows the configuration of a prosthetic finger that mimics a human index finger.

Two SMA type AM wires are installed inside the finger to generate effective torque for joint movement; a spring with a wire allows extension of the finger [167].

Figure 2-42.Human finger and prosthetic finger [167].

Bundhoo et al. proposed and evaluated a new biomimetic tendon-driven actuation system which combines compliant tendon cables and one-way shape memory alloy (SMA) wires [125]. A set of agonist–antagonist artificial muscle pairs was formed for flexion/extension and abduction/adduction. The novel contribution was that they used a spring-slack element connected to each SMA wire to mimic the nonlinear stiffness of the natural tendon. The modelling and control of the proposed tendon-driven actuation system was further studied in a companion paper by Gilardi et al. [168]. A biomimetic artificial finger was constructed to demonstrate its actuation mechanism as shown in Figure 2-43.

Figure 2-43. Artificial finger with six tendon cables routing through the finger core and attached to the corresponding six remotely placed SMA actuators [125].

Price, Jnifene and Naguib developed a nine-DoF SMA-based robot hand (Figure 2-44) [169]. Finger links are built using Teflon® due to its high melting point and electrical insulation properties, given the high value of electrical current supplied to the SMA wires when actuating. Precision steel shafts and miniature ball bearings were used to construct low-friction revolute joints. The range of motion of the

PIP and DIP joints is precisely limited in their fully extended position using adjustable stops installed within the distal end of the proximal and middle phalanges.

Figure 2-44. A SMA actuated artificial hand [169].

Unlike the traditional tendon network arrangement that is only on one side of all links as Figure 2-45 (a), the SMA wires used in the SMA-based robot hand are fixed at one end near the anterior distal end of each link, then pass along the link surface (toward the base of the finger) and across the interphalangeal joint where they are fixed to the posterior proximal end of the next link, as shown in Figure 2-45 (b). The first advantage is that this arrangement minimises the artificial muscle interference within the work envelope compared to the traditional tendon arrangement. Additionally, the maximum joint deflection for a given strain is increased as a longer SMA wire is needed to cross through the interphalangeal joint, meaning that a larger contraction length can be obtained at the same contraction rate.

Figure 2-45. SMA routing in (a) a traditional linear arrangement and

(b) the implemented joint traversing arrangement [169]

Electroactive Polymers are another promising type of artificial muscles. Jain et al. designed an ionic polymer metal composite (IPMC) artificial muscle-based finger that is controlled using EMG signals from a human index finger (Figure 2-46). Electrodes were located on the index finger skin to collect EMG signals that were amplified and filtered, and then directly sent to a proportional-integral-derivative (PID) controller to produce stable signals for controlling the IPMC-based finger [53].

Figure 2-46. Control of IPMC based artificial muscle finger through EMG signal [53].

2.3.4 Robotic hand operation control

2.3.4.1 Sensing technology in robotic hand operation control

Humans have the capability of performing spontaneous and rapid hand operation planning and execution, even in an unstructured environment, which come from the fusion of feedback information from sensory systems such as tactile, visual and thermal sensors, along with an active intention. The tactile sensors of the skin covering the hand can offer feedback on the amount of applied force and the contact region on the target objects, while the skin's thermal sensors may help to identify the objects, especially in an environment without visual information. Visual feedback from human eyes is essential for image scene segmentation, object and obstacle recognition, object distance estimation, movement tracking etc.

Motion control of anthropomorphic robot hands is one of the active research fields. The reactive planning and execution of robotic hand operation in a certain environment, necessitate closed loop control on finger actuation and drive mechanisms, supported by the measurements of finger joint position, torque, velocity etc.

The sensor types having been used in robotic hand operation control incorporate [121]:

- motor torque sensor
- motor position sensor
- joint torque sensor

- joints position sensor
- tactile sensor
- camera
- temperature sensor

The integration of tactile, force, temperature, texture or other types of sensors and the combination of information acquired using these sensors for the hand and individual finger action control are still a challenge of current research. Compliance or stiffness control schemes can be further implemented to improve force control algorithms [120]. In some cases, a different measurement, instead of a variable with a direct link to the controlled target state, can be utilised as an implicit control parameter. Motor current sensing, for instance, is a method to imply finger grip strength [144]. There is a growing demand for sensors due to the development of prosthetic or research anthropomorphic hands with multiple degrees of freedom that require finger coordination in different postures [170]. The autonomous control of these hands entails the sensing of position, force, temperature, object-slip etc.

Position and torque are the most frequently used feedback information for robotic hand motion control. There are usually two kinds of solutions that integrate sensors into the mechanical structure; one, directly couples the sensors with the joint mechanisms, and the other, places the sensors at the actuator side and then decouples the effects of transmission to reconstruct the desired measurements [121]. The major restriction to obtain kinematic information like position or velocity in a robotic hand is associated with the limited mounting space for the sensors and wires. Hall Effect sensors and encoders can be utilised as compact, precise and reliable alternatives in the case of remote actuation.

The literature study found that strain gauges, optical components, current sensing, and tactile sensors were typical choices to measure forces or torques in robotic hands, whereas motor encoders were the simplest and most often utilised tool for gathering position information.

The authors of [171] conducted a survey of different force or pressure sensor techniques, including load cell, pressure indicating film, and tactile pressure mapping in robotic hand applications. The underlying physical transduction principles, namely piezoresistive, capacitive, and piezoelectric effect, were also discussed. They found that piezoresistive and polymer transducers held the potential to improve the sensing sensitivity for grasping mechanisms.

Tactile sensors are employed to detect and measure various parameters of an object or contact event through physical touch between the object and the tactile sensors. Typical measured parameters include pressure, temperature, normal and shear forces, vibrations, slip, and torques. Tactile sensing, which emulates the human skin sensory characteristics, is considered as an important constituent part for robotic applications. The article [149] reviews some recent bio-inspired developments that are useful for articulated robotic hands in terms of hand tactile sensing. One example proposed by Takahashi T.

et al, is a new robust force and position control method for property-unknown objects during grasping using information from a tactile sensor in coordination with a 6-axis force sensor [172].

Tactile sensing can be based on different physical principles. Typical types of tactile sensor are summarised in Table 2-7. A recent review of tactile sensing technologies with applications in biomedical engineering can be found in [173].

Table 2-7. Tactile sensor types [118].

Modality	Sensor type	Advantages	Disadvantages
Normal Pressure	Piezoresistive array	Simple signal conditioning design and suitable for mass production	Temperature sensitive, fail and signal drift
Capacitive Array	Good sensitivity	Complex circuitry	
Optical	No interconnects to break	Requires PC for computing applied forces	
Skin Deformation	Optical	Compliant membrane and no electrical interconnects to be damaged	Complex computations and hand to customise
Magnetic	Array to hall-effect sensors	Complex computations and hand to customise	
Resistive Tomography	Robust construction	Posed inverse problems	
Piezoresistive (curvature)	Directly measure curvature	Frailty of electrical interconnects	
Dynamic Tactile Sensing	Piezoelectric (stress rate)	High bandwidth	Frailty of electrical junctions
Skins Acceleration	Simple	No spatially distributed content	

2.3.4.2 Application of typical sensing technology

The sensing techniques presented in the previous section are reported to apply to robotic hand control at different levels using different sensor combinations. Some examples of typical applications found in literature are listed below.

The UB Hand 3 prototype in [157] has a total number of 20 degrees of mobility, 16 of which are actively actuated. Each actuator is composed of a very low-cost DC-brushed motor equipped with a position sensor and a tendon force sensor that are based on the strain gauge sensing principle. Experiments were conducted to demonstrate the capability of the robotic hand to perform both grasping operations and manipulation tasks by developing suitable control strategies with information from these sensors.

A miniaturised optical force sensor was proposed to measure tendon tension using optoelectronic components [174]. Experiments of a robotic joint position control loop on a tendon-driven mechanism similar to the one used in the UB hand 3 or UB hand IV showed that the optical sensor was suitable to replace traditional strain gauge-based load cells for the measurement of tendon forces, and that the optoelectronic component-based load cell was better at rejecting electromagnetic noise.

The control of the developed prosthetic hand prototype in [124] required finger position and force information. Position information was provided by a set of angle sensors placed on each joint, and the forces applied to the fingers were measured by a tactile sensor array that was integrated into the fingertip.

An anthropomorphic artificial hand with three articulated underactuated fingers was designed in [142]. The control of this artificial hand was supported with incremental encoders, three-component force sensors, and Hall effect switches that are used for the encoder calibration.

The anthropomorphic 16 degrees of freedom, 4 degrees of mobility prosthetic hand of [145] is equipped with 15 Hall effect sensors integrated in all the joints, with 5 cable tension sensors measuring the grasping force of each finger, 4 current sensors each of which is for one driving motor, and 4 optical-based tactile/pressure sensors in the intermediate and proximal phalanxes of the thumb and index.

The control of a shape memory alloy based robot hand relies on the joint deflections measured by flexible bend sensors installed at each joint [169]. A sigmoid based control algorithm for the position control of SMA elements has been proposed and evaluated, minimising overshoot to avoid the slow time response inherent to the passive cooling of SMA.

2.3.5 Material selection and manufacturing consideration

There are two categories of materials that can be used in the construction of an artificial hand, i.e. metals and composite materials. The constraints pertaining to the selection of materials for artificial hand

construction are mainly cost, availability, strength, durability, weight, manufacturing approach etc. Aluminium, steel and titanium are common metal materials used in robotic hand designs. Titanium has the best mechanics performance, but it is the most expensive option and also very difficult to manufacture with required shapes. Therefore, aluminium or steel is more often the choice due to their low cost, high availability and moderate performance. Alternatively, different composite materials, such as nylon, Teflon and ABS plastic, can be used in artificial hand structural construction, but usually with less strength and durability.

Conventional manufacturing processes incorporate milling, turning, boring, drilling, sawing, shaping, broaching, reaming, tapping etc., using cutting tools to remove material from a stock to achieve a desired geometry. In contrast, 3D printing [164], also known as additive manufacturing (AM) [175], refers to processes in which material is solidified or joined to create a three-dimensional object under computer control. 3D printing can almost create objects with any desired shape or geometry by successively adding or fusing material layer by layer, and has been a popular method of creating prototypes since the 1980s. It is quickly becoming the fastest, most affordable way to create customised consumer goods. The producing processes are controlled using digital model data from a 3D model or another electronic data source, such as an additive manufacturing file (AMF) (usually in sequential layers). Fused deposition modelling (FDM) or fused filament fabrication (FFF) is now the most popular process of 3D printing, using a thermoplastic filament which is heated to its melting point and then extruded, layer by layer, to create a three-dimensional object.

Thermoplastics can endure mechanical stress, heat, and chemicals, which makes them an ideal material for printing prototypes that must withstand testing. FDM is also commonly used by engineers who need to test parts for form and fit since it can print highly detailed objects.

2.3.6 Review outcome

A physical testing environment is critical for the development of a biosignal-based HMI control system. Specifically, an anthropomorphic robotic hand is an ideal control target for demonstrating and evaluating a HMI system based on the human upper limb surface EMG signal. This section examines the state-of-the-art robotic hands developed for both commerce and research. Reported research work in anthropomorphic robotic hand development focuses on issues related to the imitation of size and kinematics, the actuation level and type, the transmission mechanisms, feedback sensing, and manufacturing material and method. Each issue involves different techniques and considerations. Many parallel methods can be used to build an anthropomorphic robotic hand. However, there is no established guide for anthropomorphic robotic hand construction. Trade-offs must be made for a specific application scenario. This is the motivation to carry out a deep research on anthropomorphic robotic hand design to build a physical testing prototype for the EMG-based HMI system.

Chapter 3
Research on EMG acquisition for EMG-based robotic hand control

This chapter starts with an introduction to the framework of EMG acquisition systems and possible implementation configurations. Then, it proceeds to a detailed investigation in each of technical aspects of EMG acquisition, particularly for electrode placement, analog front end amplifier construction, and filter layout and parameter determination. As a result, a single-ended signalling approach that utilises instrumentation amplifiers to capture EMG signals for the applications of EMG-driven robotic systems is first proposed to determine proper analog EMG signal processing chain structure and specifications. The EMG acquisition design finally evolves into a fully differential EMG detection and conditioning method.

The literature review shows that obtaining accurate EMG signals is still a challenging research topic although many attempts are reported in literature. Many of researchers in myoelectric control use commercial multi-channel surface EMG systems available on the market, such as the products from DelSys Incorporated [30], to obtain the targeted EMG data sets. However, their extremely high cost is often beyond the reach of many other research peers or laboratories. To specifically design a system using common commercial electronic components for collecting targeted surface EMG signals is a feasible and affordable option. Therefore, complete and detailed precision surface EMG acquisition system designs are useful and desirable to EMG-driven system development. However, only a few designs [13, 37-39], which can be used as reference for certain parts of the surface EMG acquisition, were found by the literature study. Most of the publications concern various aspects of electrode such as shape, size, interspace and placement, or circuit parameters such as the filter cut-off frequency, filter roll-off rate, and sampling rate. The lack of ready-to-use and low-cost precision surface EMG measurement solutions has motivated this thesis to conduct an in depth research of EMG acquisition.

3.1 EMG data acquisition framework and configuration

Based on the outcome of the literature study, this research proposes an EMG data acquisition module. The block diagram of the proposed EMG system is illustrated in Figure 3-1.

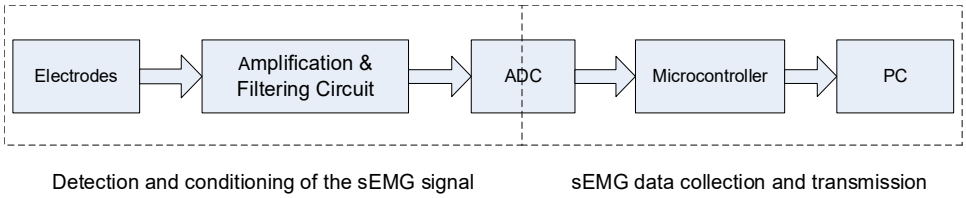

Figure 3-1. Block diagram of the EMG data acquisition module.

The surface EMG data acquisition module is usually composed of two parts jointed with a mixed-signal device, namely an analog-to-digital converter (ADC). The first part is the analog EMG signal detection and conditioning circuit, followed by the digital part for EMG data collection and transmission.

The analog surface EMG signal detection and conditioning circuit can be implemented by using three configurations:

- The discrete monolithic instrument amplifier (INA or IA) configuration
  This method uses discrete monolithic INAs as the analog front end. Its drawback is that the INA converts differential input signals to single-ended outputs that are more likely subject to external noise coupling which can be more easily rejected in a differential configuration, thus compromising the ability of noise rejection.

- The fully differential configuration
  In this configuration, all stages including the front end, subsequent amplification and filtering sections are completely constructed by using discrete op-amps in a symmetrical manner, thus leading to the advantage of this approach—relatively remote external noise sources can be regarded as common-mode signals and rejected as much as possible.

- The integrated analog front end configuration
  An integrated analog front end monolithic chip such as ADS1292 and RHA2216 [176] for biopotential measurements can greatly simplify the design process of an EMG data acquisition system. The ADS1292 offers an integrated front end PGA, a DRL amplifier, internal test functions, lead off detection, and an ADC for every input channel. By using a high-resolution ADC, a lower gain provided by the PGA is able to guarantee the same noise-free dynamic range at the ADC output as the combination of a high gain and a low-resolution ADC. There is no need for a second amplification stage, which may give rise to the saturation problem by magnifying the DC voltage between electrodes too much. Therefore, the high-pass filter immediately following the front end is no longer necessary [177]. Compared to the preceding two approaches, however, this method lacks the ability to customise power, sampling, and filtering characteristics in the ADC driver circuit based on certain system requirements.

The drawback of the integrated analog front end solution is that it relies much more on digital signal processing techniques, such as digital filtering, which require a larger computational capacity. Therefore, the following sections will present the investigation on the first and second proposals. The next section will start to delineate the research work on the first proposed solution—a discrete monolithic INA EMG data acquisition approach, followed by the description of the second proposed solution—a fully differential configuration in the subsequent section.

3.2 Proposed solution 1: the discrete monolithic INA approach for surface EMG signal detection and conditioning

3.2.1 System framework

EMG detection and conditioning circuit design is the key element of the EMG acquisition. The quality of an EMG signal from the electrodes is partially dependent on the properties of the amplifiers. Because of the weak amplitude of the EMG signals typically in the order of tens to thousands μV, it is necessary that the gain of the amplifiers used in EMG applications is in the range from a few hundreds to several thousands and even more. Consequently, the amplification process commonly incorporates several stages. Figure 3-2 illustrates the block diagram of the amplification and filtering for a single channel implemented in this research. The most important stage, namely the first stage which is most close to the electrodes, is conventionally called pre-amplifier or front end amplifier. The consideration to incorporate a pre-amplifier is to have a high common-mode rejection ratio (CMRR), a high input impedance, a short distance to the signal source, and a strong direct current (DC) signal suppression [17]. The driven right leg (DRL) and the "shielding" techniques are used with the pre-amplifier for common-mode voltage and interference reduction. There is also a low-pass filter before the inputs of the pre-amplifier for common-mode and differential mode electromagnetic interference (EMI) or radio-frequency interference (RFI) rejection. The output from the pre-amplifier is then processed by a high-pass and a low-pass filter before entering into the second amplification stage that amplifies signals again to attain an expected EMG signal level. The second amplification stage is a simple inverting or noninverting amplifier and its gain is easily adjusted by choosing different resistor values. To further suppress high frequency noises introduced by the previous circuit stages and provide anti-aliasing, a low-pass filter follows the second amplification stage. Finally, the output signal from the amplification and filtering circuit is fed into an ADC.

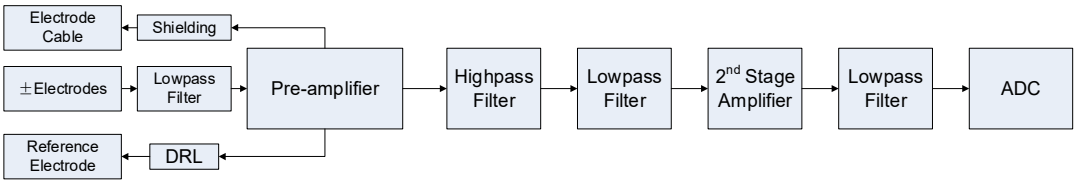

Figure 3-2. Block diagram of the amplification and filtering for a single channel.

3.2.2 The surface EMG electrode

3.2.2.1 Electrode selection

As mentioned in Section 2.1.4, the selection of electrodes is one of the most critical aspects in EMG electronics design [51]. The wet Ag–AgCl electrode with conductive gel is currently preferred for surface EMG applications. There are three configuration methods for using electrodes: monopolar, differential or high-density [21]. For the sake of reducing or eliminating common-mode noise and simplicity, a single differential configuration was used in this research. The pairs of electrodes were set with an inter-electrode spacing about 3-4 cm [178]. The sEMG snap cable with three protected pin snap style leads (1 positive, 1 negative and 1 ground) and the pre-gelled disposable sEMG electrodes both from Thought Technology (Figure 3-3) were completely satisfactory for the requirement of this research.

Figure 3-3. The sEMG snap cable and electrodes.

3.2.2.2 Electrode placement

Electrode placements directly affect the quality of the EMG signals. This research aims to successively collect two channels of EMG signals from two pairs of electrodes placed on the flexor carpi radialis muscle and the extensor carpi radialis longus muscle respectively as illustrated in Figure 3-4.

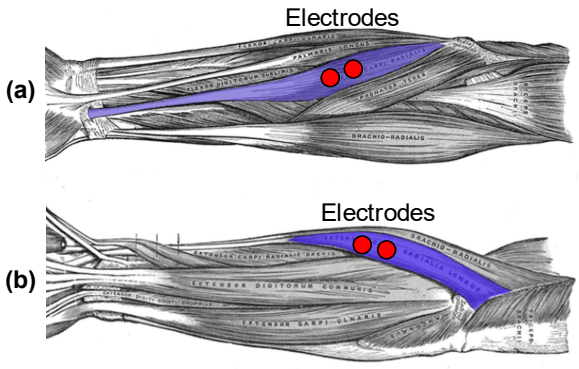

Figure 3-4. The placement of electrodes. (a) the anterior view of the left forearm with the flexor carpi radialis visible in blue; (b) the posterior view of the left forearm with the extensor carpi radialis longus visible in blue (modified from [179]).

3.2.2.3 Electrode-skin impedance model

During all processes of circuit design, an analog electronic circuit simulator such as TINA-TI™ SPICE can be used for the analysis of signal integrity, transient response, stability or noise characteristics [180]. It is common to use an electrical equivalent circuit of the electrode-skin impedance when using an analog electronic circuit simulator such as TINA-TI™ SPICE to check the integrity of circuit design and to predict circuit behaviour, especially for circuit stability examination. This research used an impedance model presented in Figure 3-5. The V_{dc} voltage can reach ±300mV over time and with varying external conditions [181].

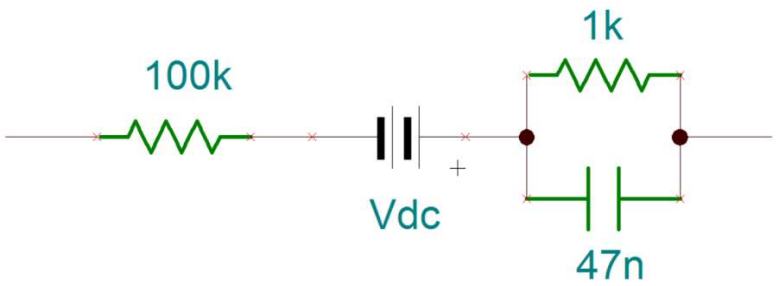

Figure 3-5. The impedance model used in the TINA-TI™ SPICE circuit analysis.

3.2.3 The EMI/RFI rejection filter

A differential signal represents the difference between two physical quantities. In a strict sense, all voltage signals are differential, as a voltage can only be measured with respect to another electric potential level, i.e. a voltage. “Balanced signal” is a more accurate term of the traditional terminological form—“differential signal”. For the single differential electrode configuration adopted in this research, the electrode voltage model can be represented as Figure 3-6, where V_p and V_n are the voltages of the positive and negative electrode with respect to the reference electrode, respectively.

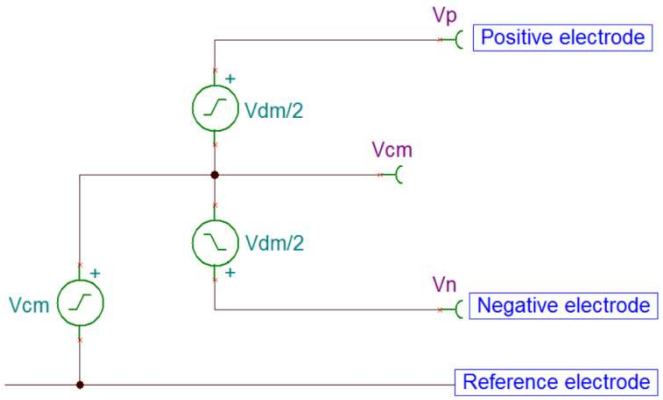

Figure 3-6. Differential signaling model.

The differential signal value is the difference between the individual voltages of V_p and V_n :

$$V_{dm} = V_p - V_n \tag{3.1}$$

and the average voltage of V_p and V_n is refered to as the common-mode component:

$$V_{cm} = \frac{V_p + V_n}{2} \tag{3.2}$$

Therefore the voltages of V_p and V_n can be represented as :

$$V_n = V_{cm} - \frac{V_{dm}}{2} \tag{3.3}$$

$$V_p = V_{cm} + \frac{V_{dm}}{2} \tag{3.4}$$

For better noise performance, low-pass filters are added before the analog inputs of the front-end amplifiers to provide high frequency electromagnetic interference (EMI) or radio-frequency interference (RFI) attenuation. Figure 3-7 shows the first-order low-pass RC filter used in this research for both differential and common-mode voltage signals [182, 183].

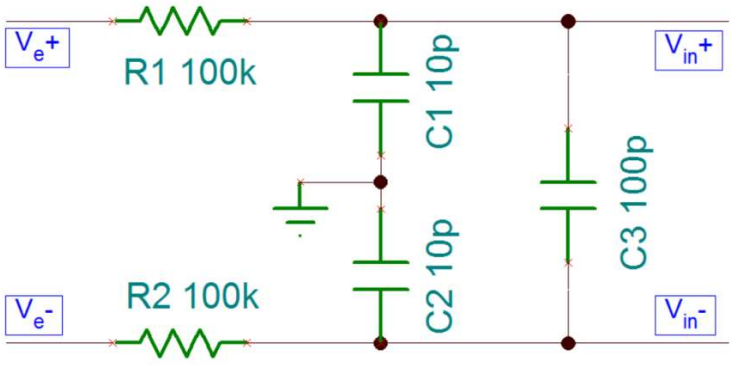

Figure 3-7. A first-order low-pass filter for EMI/RFI rejection, where capacitances $C1 = C2$.

The V_e+ and V_e- are connected to the positive and negative leads of the sEMG snap cable respectively, and V_{in}+ and V_{in}- are similarly connected to the positive and negative input pins of the pre-amplifier respectively. For the common-mode signal, the voltages at the two ends of C_3 are at the same potential level, thus there is no common-mode current flowing through C_3. When determining the common-mode cut-off frequency, C_3 can be thought of as being removed; therefore the common-mode cut-off frequency can be expressed as

$$f_{cm} = \frac{1}{2\pi R_1 C_1} = \frac{1}{2\pi R_2 C_2} \tag{3.5}$$

On the other hand, for the differential mode signal, the C_3 can be thought of as two separate capacitors C_3' and C_3'' with the same value of $2\times C_3$ as shown in Figure 3-8. The differential mode cut-off frequency can be calculated by

$$f_{dm} = \frac{1}{2\pi R_1 (C_1 + 2C_3)} = \frac{1}{2\pi R_2 (C_2 + 2C_3)} \tag{3.6}$$

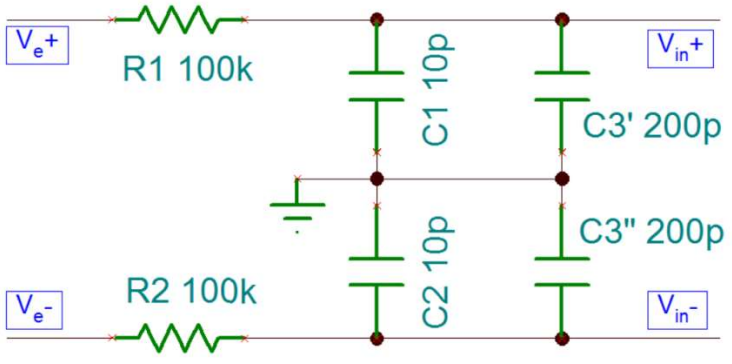

Figure 3-8. Differential mode low-pass filter equivalent circuit.

To prevent any capacitive mismatch between C_1 and C_2 from reflecting itself as an in-band signal error, the value of C_3' or C_3'' is usually at least 10 times larger than the value of C_1 or C_2. Meanwhile, in order

to keep useful EMG frequency information, the differential mode cut-off frequency should be at least a decade greater than the highest component of interest, which is 500 H_z in this research. Furthermore, in the low-pass EMI/RFI rejection filter, the resistors R_1 and R_2 act also as a means of protection to minimise the amount of current that can be delivered from the electric circuitry back into the patient body in a failure mode. The value of R_1 and R_2 is usually 100 KΩ. In this research, the value of C_1 and C_2 is selected at 10 pF, C_3 at 100 pF. The differential mode and common-mode cut-off frequencies are about 7.5 kH_z and 159 kH_z respectively, as computed in Equation (3.7) and (3.8), which are safe enough.

$$f_{cm} = \frac{1}{2\pi R_1 C_1} = \frac{1}{2\pi \times 100\text{k}\Omega \times 10\text{pF}} \approx 159\ \text{kHz} \gg 7.5\ \text{kHz} \tag{3.7}$$

$$f_{dm} = \frac{1}{2\pi R_1 (C_1 + 2C_3)} = \frac{1}{2\pi \times 100\text{k}\Omega \times (10\text{pF} + 2 \times 100\text{pF})} \approx 7.5\ \text{kHz} \gg 500\ \text{Hz} \tag{3.8}$$

3.2.4 The surface EMG front end amplifier

The nature of surface EMG signal acquisition requires a biosignal front-end amplifier, i.e. an instrumentation amplifier—a differential amplifier with a fixed differential gain, a high input impedance, a high common-mode rejection ratio (CMRR) and low noise [184-186]. As mentioned in Section 2.1.5.1, high input impedance, high CMRR, and low noise are the essentials for the surface EMG front end amplifier. The input impedance of the surface EMG amplifier is recommended greater than 100 MΩ, but 1000 MΩ is preferable in case of small dry electrodes. This requirement leads to the choice among only three basic types of circuit configuration [52]:

- Op-amps in voltage follower configuration
- The classic three op-amp instrumentation amplifier configuration
- The classic two op-amp instrumentation amplifier configuration

Additionally, the finite CMRR and the unbalance of impedance at two inputs of the front end amplifier can generates a differential voltage due to the common-mode voltage. Instead of costing much higher in increasing CMRR and impedance balance performance, reducing the common-mode voltage on the subject is a better choice. This technique is initially designed for ECG recordings, referred to as “driven right leg” (DRL), and later applied to other biopotential recordings. Another technique, “shielding”, can be further applied to minimise the coupling noise induced into the electrode wires. The proposed front end amplifier in this research employs the three op-amp configuration instrumentation amplifier INA128 (Texas Instrument, Inc.) and the coupling-reducing techniques DRL and “shielding”, as shown in Figure 3-9. INA128 is a low power, general purpose instrumentation amplifier offering excellent accuracy with very low offset voltage, drift and high common-mode rejection. The gain is adjustable from 1 to 10,000 according to the Equation (3.9):

$$G = 1 + \frac{50k\Omega}{R_G} \tag{3.9}$$

where R_G is an external resistor [187].

Since the DC or slowly changing voltages presented between two electrodes can reach as high as ±300 mV, the DC gain of the front end amplifiers must be limited to prevent saturation [21]. This can be done by setting the INA gain resistor to get a small gain or by using the AC coupled approaches [13, 61, 62]. For the pre-amplifier designed in this research, the gain was calculated using Equation (3.9) and set at 6.3:

$$G = 1 + \frac{50k\Omega}{R_G} = 1 + \frac{50k\Omega}{4.7k\Omega + 4.7k\Omega} = 6.3 \tag{3.10}$$

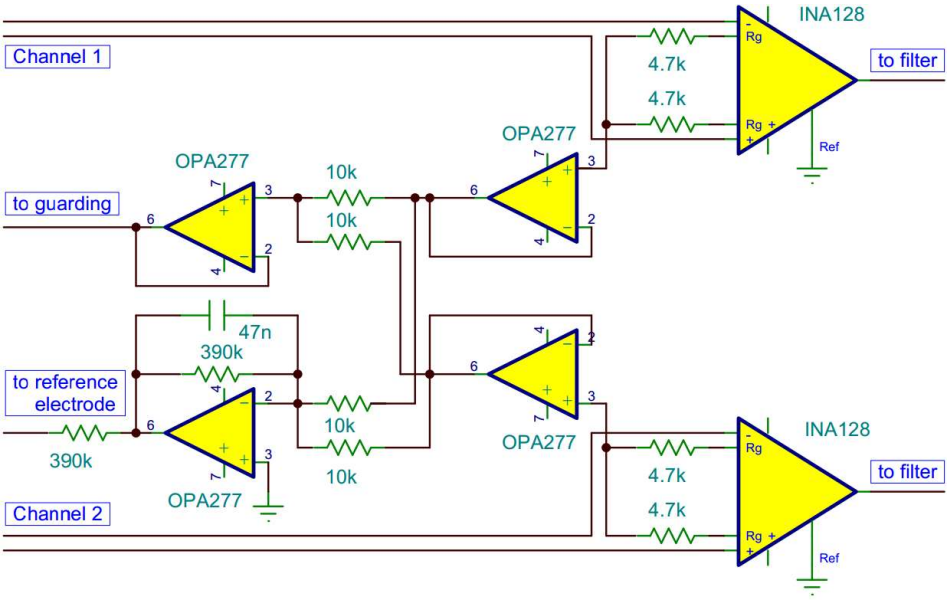

Figure 3-9. The two channel surface EMG front end amplifier with the DRL and guarding circuit.

The positive and negative inputs of INA128 are connected to the corresponding $V_{in}+$ and $V_{in}-$ of the first-order low-pass EMI/RFI rejection filter for each channel. Except for three pins connected to the three electrodes, there is an extra pin in the sEMG snap cable connector for the use of "shielding". In this research, a method called "guarding" is implemented, which involves driving a shield with a potential essentially equal to the common-mode voltage on the signal wire that is enclosed within the shield [188]. The common-mode voltage of each EMG channel can be obtained from the midpoint of the gain resistor which is formed by two equal-valued resistors connected to the R_g pins of the INA128. All common-mode voltages from two channels are buffered to prevent any influence to the instrumentation amplifier and then averaged to drive the lead wire shields [37]. An electrode located on

the wrist is connected to the DRL circuit to provide the reference. The common-mode voltages are fed back to the trial subject after being inversely amplified and summed. The DRL circuit creates a negative feedback loop which restricts the common-mode voltage to a narrow range, depending on the loop gain. The resultant common-mode voltage can theoretically be reduced by an amplification factor not greater than 100 [21].

3.2.5 The EMG filtering

As mentioned in Section 2.1.5.2, the limited frequency bandwidth of the surface EMG signal make filtering out of band noises possible and necessary to get high fidelity. According to the recommendation of De Luca et al., 20 Hz and 500 Hz were selected as the cut-off frequencies of high-pass and low-pass filter respectively [20].

Once the frequency selectivity characteristics are decided, the next task of the filter design is to make the choice between the analog and digital implementation. The digital filter is much easier to get better passband flatness, roll-off, stopband attenuation and linear phase response, whereas its analog counterpart is advantageous in term of response speed, amplitude and frequency dynamic range [189]. Theoretically, both analog and digital filter formats can fulfil certain required specifications. The digital filter, however, is more dependent on the digital computational and storage capacity, which are both limited on an embedded microcontroller in any practical apparatus such as a prosthetic hand. On the other hand, the analog filter approach uses analog hardware to carry out filtering at the expense of a more complicated analog configuration. Although analog implementation uses more components, the software computation for a digital filter may consume more power than that for hardware components. Therefore, this research is inclined to the analog approach.

3.2.5.1 The determination of the analog EMG filter topology

Inspired by the literature reviewed, the Sallen-Key and the multiple feedback (MFB) topologies were investigated for the purpose of eliminating the out-of-band noises. The Sallen-Key configuration, also known as a voltage control voltage source (VCVS), was first introduced in 1955 by R. P. Sallen and E. L. Key of MIT's Lincoln Labs. It is one of the most widely used filters, mainly because of it having the least dependence of filter performance on the performance of the op-amps. This is due to the fact that the op-amp is configured as an amplifier, as opposed to an integrator, which minimises the gain bandwidth requirements of the op-amp. Another advantage of this configuration is that the low ratio of the largest component value to the smallest component value is a benefit for manufacturability. On the contrary, the MFB filter uses an op-amp as an integrator, thus resulting in more dependence on the op-amp parameters and requiring higher ratios of the maximum to minimum component value than in the Sallen-Key realisation [190]. Therefore, the Sallen-Key filter is preferable to the MFB topology due to these advantages, and it becomes the first candidate in this thesis if possible.

One of the most important specifications that should be initially considered when selecting an op-amp for active filters is the gain bandwidth product (GBWP) of the op-amp. For the Sallen-Key configuration, the GBWP should be equal to or greater than $100*G_{CLN}*f_C$, where G_{CLN} is equal to the non-inverting closed-loop gain of the filter and f_C is the cut-off frequency; whereas the GBWP should be equal to or greater than $100*(-G_{CLI} + 1)*f_C$ for the MFB configuration, where G_{CLI} is equal to the inverting closed-loop gain [191].

3.2.5.2 High-pass filter design

The complexity of the filter, defined by its "order", is related to the number of energy storage elements such as capacitors or inductors used in filter design. The order of the filter defines the asymptotic roll-off rate of the amplitude response with respect to frequency. A simple first-order filter has a standard roll-off rate of -20 dB/decade or -6 dB/octave and the n^{th} order filter subsequently has a roll-off rate of -20n dB/decade or -6n dB/octave. An octave is a doubling or halving of the frequency whereas a decade is a tenfold increase or decrease of frequency. Higher-order filters are usually formed by cascaded first-order and second-order filter sections because of the fact that the sensitivities to component values and the interaction effects of the components on the frequency response will increase dramatically when a three-order or higher-order filter is built within a single active stage [192].

The literature study found the determination of the high-pass filter characteristics has been a focus of attention in conditioning surface EMG signals. Regarding the roll-off rate of the high-pass EMG filter, -12dB/Octave, -18dB/Octave, and -24dB/Octave were employed by different previous work. To determine an appropriate high-pass filter roll-off rate for making a trade-off between complexity and performance, a second-order Sallen-Key high-pass filter (Figure 3-10) and a fourth-order Sallen-Key high-pass filter, which is built by cascading two second-order Sallen-Key filters (Figure 3-11), were studied and compared. The former has a slope of -12dB/Octave and a 20 Hz corner frequency, whereas the latter has a slope of -24dB/Octave and the same corner frequency.

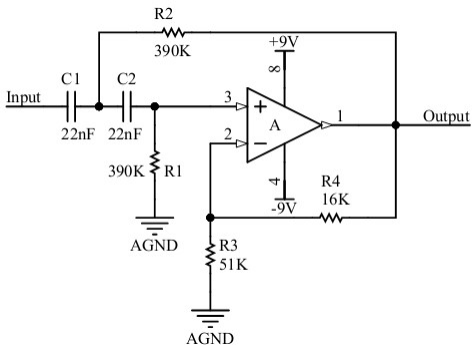

Figure 3-10. The 2nd-order Sellen-Key high-pass active filter with a corner frequency of 20 Hz.

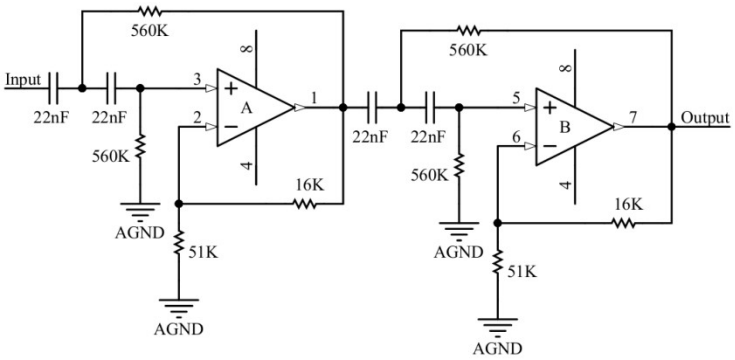

Figure 3-11. The 4th-order Sellen-Key high-pass active filter with a corner frequency of 20 Hz.

The corner frequency and the passband gain of the second-order Sellen-Key high-pass filter are given by Equation (3.11) and (3.12) respectively [193]:

$$f_c = \frac{1}{2\pi\sqrt{R_1 R_2 C_1 C_2}} \tag{3.11}$$

$$G_{pass} = 1 + \frac{R_4}{R_3} \tag{3.12}$$

where f_c is the corner frequency and G_{pass} is the passband gain.

3.2.5.3 Low-pass filter design

Since the noises coupled into the circuit from electromagnetic radiation are mainly in the high frequency band, in this research, every amplification stage is followed by a second-order Sallen-Key low-pass filter (Figure 3-12). The corner frequency and the passband gain can also be calculated using Equation (3.11) and (3.12), similar to high-pass filter design. The two second-order low-pass filters have the same properties and are placed immediately before and after the second amplification stage (Figure 3-2). The total frequency response of these two second-order low-pass filters is equivalent to a fourth-order low-pass filter with a corner frequency of 500 Hz.

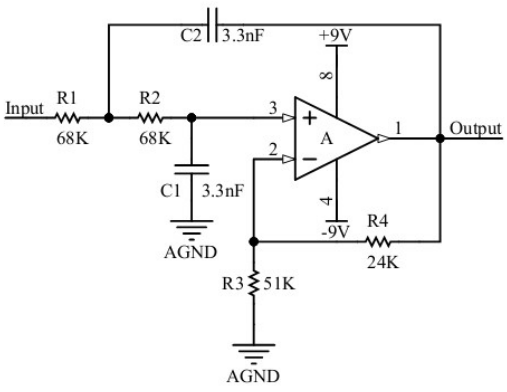

Figure 3-12. The 2nd-order Sellen-Key low-pass active filter with a corner frequency of 709 Hz.

An issue related to low-pass filter design is the selection of the sampling rate that is of importance in data acquisition systems. There is not an identical sampling rate which is exclusively recommended in literature. It has been found that different sampling rates, e.g., 400-500 Hz [66], 1000 Hz [24, 67, 68], 1024 Hz [69, 70], 2000 Hz [71] and 4000 Hz [72] were used to convert analog EMG signals to digital data.

It is true that using a high sampling rate could reduce the requirements on analog anti-aliasing filter, but at the expense of increasing the computational workload and processing time. According to the Nyquist–Shannon sampling theorem, when digitising a band-limited signal, the sampling rate has to be two times higher than its band-limit otherwise aliasing may happen. Theoretically, as the highest useful frequency component of the EMG signals from an upper limb is less than 500 Hz, a 1000 Hz sample rate is sufficient. The issue, however, is more complicated than it looks since the suitable sampling rate is also dependent on the roll-off rate of the anti-aliasing filter [194, 195]. Only when using an ideal low-pass anti-aliasing filter with a brick wall response, there happens to be a sampling rate of 1000 Hz that is sufficient for collecting the EMG signals with the maximum frequency less than 500 Hz. In other words, the low-pass anti-aliasing filter must have an ideal property, that is, an infinite roll-off rate. In reality, however, this is impossible. As a result, the selection of the sampling rate has to consider also the roll-off rate of the anti-aliasing filter, which is determined by the order of the low-pass filter.

In the first version of circuit design, two low-pass filters with a corner frequency of 709 Hz and a slope of -12dB/Octave were cascaded to form a fourth-order low-pass filter with a 500 Hz corner frequency and a slope of -24dB/Octave. The two low-pass filters are able to remove the noises above 500 Hz. Meanwhile, the two low-pass filters also work as an anti-aliasing filter for analog-to-digital conversion [196]. As shown in Figure 3-13, the fourth-order low-pass filter (Line C) has a higher possibility of using a lower sampling rate f_{s1} than the second-order low-pass filter (Line D), by achieving the same attenuation to spectral alias at 500 Hz or even higher attenuation within 0-500 Hz, without causing aliasing. In other words, if the same sampling rate f_{s2} is used, the fourth-order low-pass filter (Line E) can introduce a lower amplitude of spectral alias in the spectral baseband (0-500 Hz) than the second-order low-pass filter (Line D). Figure 3-13 also reveals that, when using a Nyquist rate ADC for converting signals with the maximum 500 Hz component, a sampling rate of 1000 Hz may not provide the necessary aliasing rejection from the fourth-order low-pass filter (Line F).

In an experiment to verify the filtering circuit design, a sampling rate of 2000 Hz was chosen to avoid aliasing. The detailed configuration of the design validation experiment is described later. The experimental results show that the fourth-order low-pass filter along with the 2000 Hz sampling rate attenuate effectively the components above 500 Hz to alias back into the signal bandwidth. However, the size of the dataset is increased as the sampling rate gets higher. Therefore, in real applications, the selection of a high sampling rate may pose more storage and computation burden to hardware.

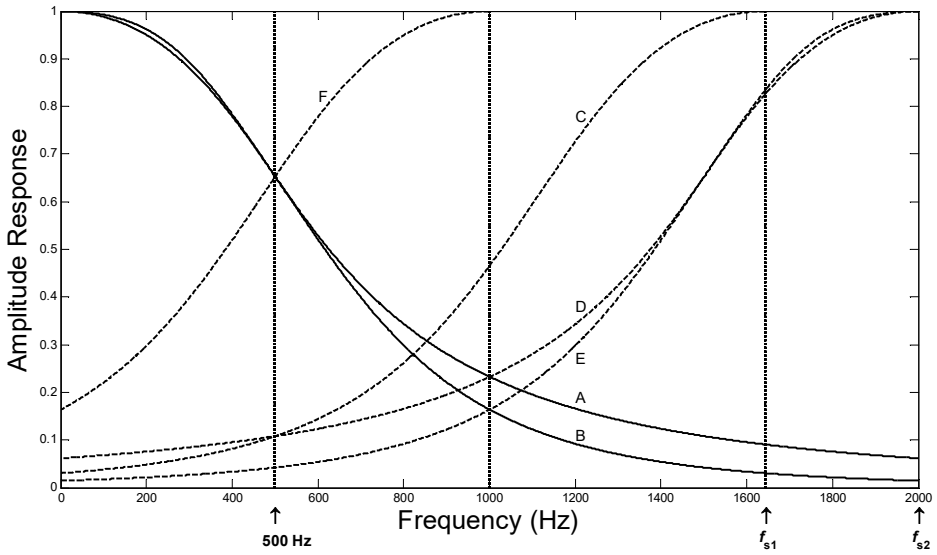

Figure 3-13. The amplitude responses and spectral replications of Sellen-Key low-pass filters:
Line A – the amplitude of the second-order low-pass filter;
Line B – the amplitude of the fourth –order low-pass filter;
Line C – the replication of the fourth-order low-pass filter at sampling rate of f_{s1};
Line D – the replication of the second-order low-pass filter at sampling rate of f_{s2};
Line E – the replication of the fourth-order low-pass filter at sampling rate of f_{s2}.
Line F – the replication of the fourth-order low-pass filter at sampling rate of 1 kHz

3.2.6 Amplification and filtering design validation

3.2.6.1 Experiment configuration

In order to validate the preliminary amplification and filtering circuit design, an experiment was devised and conducted. The high-pass filter roll-off rate is one of the important parameters awaiting determination. To compare the effect of a fourth-order and a second-order high-pass filter on the low frequency components, the experimental circuit was implemented as showed in Figure 3-14. The EMG signal from the detective electrodes first get pre-amplified and then separated into two paths, obtaining filtering and further amplification before being fed to a SCB-68 connector (National Instrument). The difference between the two approaches is in the high-pass filter section. The first approach uses a second-order high-pass filter as in Figure 3-10, whereas the other is a fourth-order high-pass filter (Figure 3-11). The amplified and filtered EMG signals from the two approaches were simultaneously sampled and recorded. Hence, the two EMG signals fed into the connector SCB-68 are actually the same signal from the same original source and in the same period of time, until separated to get through different filtering and amplification paths.

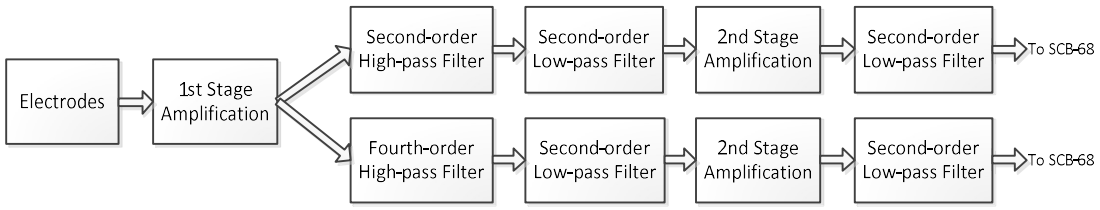

Figure 3-14. Block diagram of the amplification and filtering.

The two paths of EMG signals from SCB-68 were digitalised and collected using a PCI-6229 (National Instrument) data acquisition card and the software platform LabView (National Instrument). The amplified and filtered EMG signals were fed into the 68-pin shielded connector SCB-68 which is connected to the 16-Bit PCI-6229 DAQ card plugged into a computer (Figure 3-15). A programme was developed in LabView to log the EMG data. The EMG signals were recorded at a sampling rate of 2000 Hz. Matlab (MathWorks Inc.) was employed to analyse the spectra of the EMG signals.

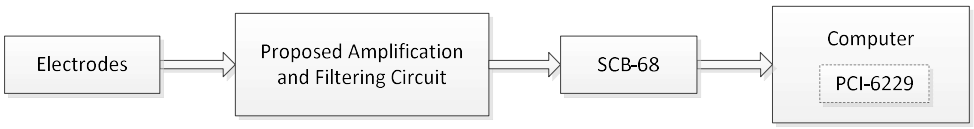

Figure 3-15. Experiment configuration.

In the experiment, the high-pass and low-pass corner frequency of the amplification and filtering circuit were set as follows:

- The high-pass corner frequency is 20 Hz;
- The low-pass corner frequency is 500 Hz.

The human upper limb is able to perform sophisticated movements due to the multiple degrees of freedom it has. However, it is still a challenge for researchers to model and control human hand movement. In most cases, only certain hand gestures are studied. In this experiment, two upper limb movements were used to analyse and test the proposed amplification and filtering design. The first one is ball squeezing, which is the spherical grasping from the six basic hand grasping proposed by N. Fukaya [197], and another one is forearm flexion from two common movements in everyday life as illustrated in Figure 3-16.

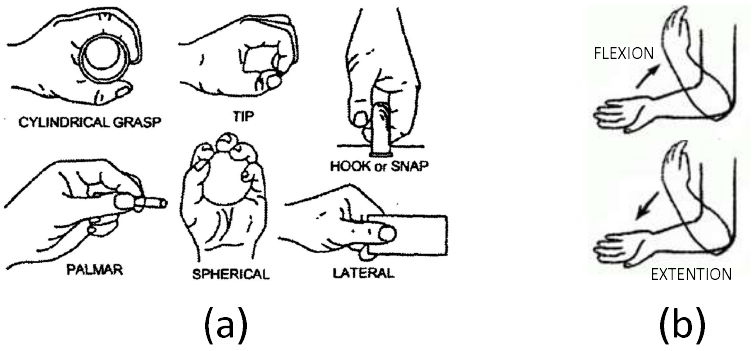

Figure 3-16. Hand and forearm motions (a) six types of hand grasping; and (b) two forearm motions.

The spherical grasping is tested to squeeze a rubber ball and the forearm flexion to hold a bottle of water suspended from the hand. For each hand movement, the test was repeated five times with five sets of data collected. Each test run had a 2-second rest at the beginning followed by a 2-second activation and then a further 2-second rest pattern. The experimental data was stored in datasheet files using LabView and then transferred to Matlab to carry on the time-frequency analysis.

3.2.6.2 Experiment results and discussions

The analysis of the experimental data and the evaluation of the proposed EMG amplification and filtering circuit were performed in the Matlab environment. First the EMG signal waveforms were graphically displayed in Matlab. Then the activating EMG data segments of the two upper-limb movements, that is, the recorded EMG data subsets in the contracting period of the target muscles, were manually identified from the graphics. As shown in Figure 3-14, each test had two sets of data. One is the result of using a fourth-order high-pass filter, while the other is the output from the second-order high-pass filter.

1) Experimental results of ball squeezing

Spectral analysis was conducted for activating EMG data segments using Fourier transformation. Figure 3-17 and Figure 3-18 show the amplitude response of a randomly selected activating EMG data segment of the two channels of EMG data on the same graph with the same scale for comparison.

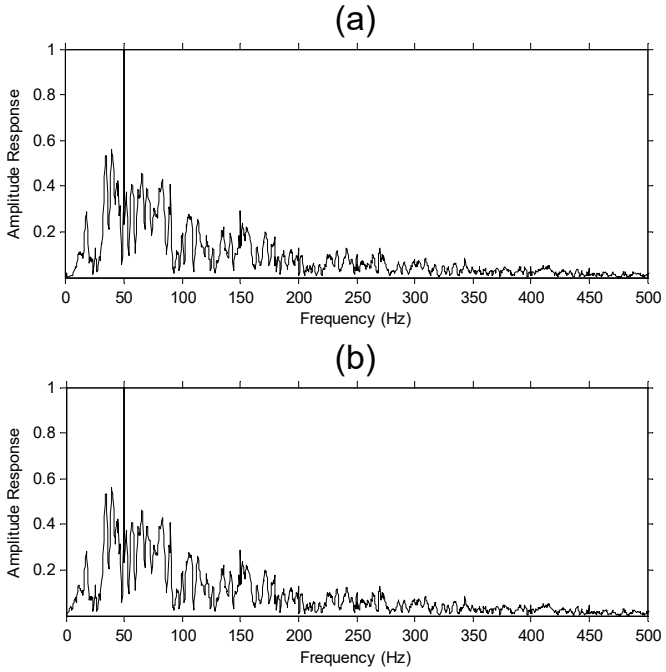

Figure 3-17. The amplitude response of the EMG signal of ball squeezing (0-500 Hz):

(a) using the fourth-order high-pass filter; (b) using the second-order high-pass filter.

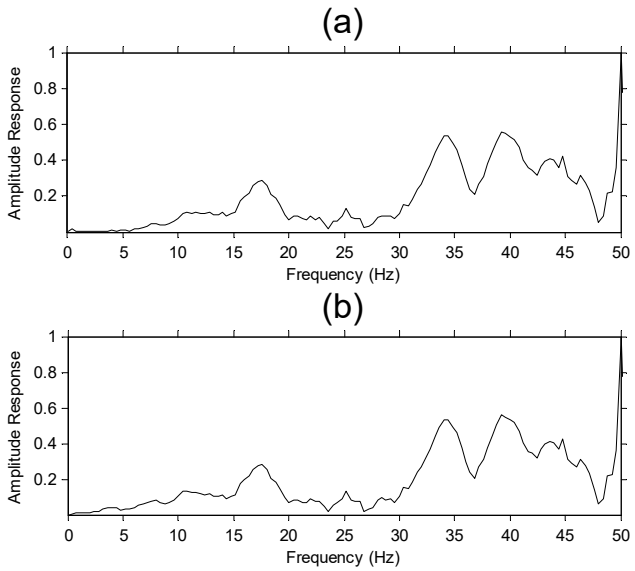

Figure 3-18. The amplitude response of the EMG signal of ball squeezing (zoomed in 0-50 Hz): (a) using the fourth-order high-pass filter; (b) using the second-order high-pass filter.

2) Experimental results of forearm flexion

Similar to the ball squeezing movement, the amplitude response of the forearm flexion motion is presented in Figure 3-19 and Figure 3-20.

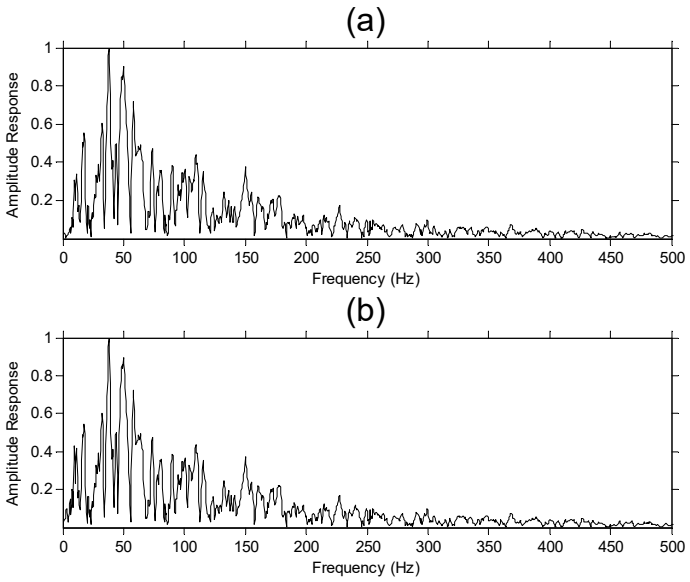

Figure 3-19. The amplitude response of the EMG signal of forearm flexion (0-500 Hz): (a) using the fourth-order high-pass filter; (b) using the second-order high-pass filter.

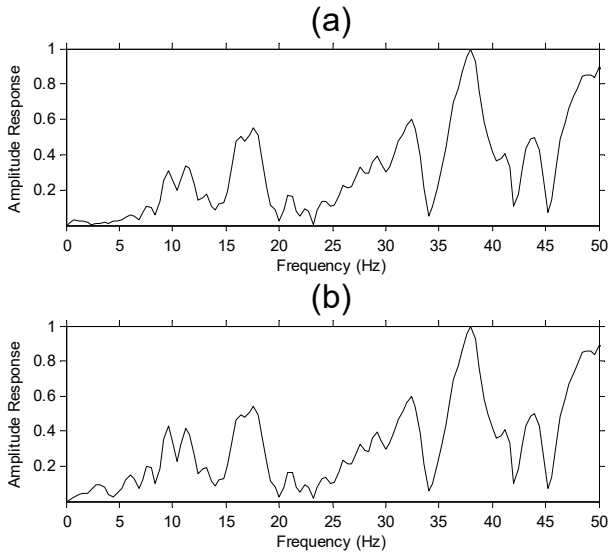

Figure 3-20. The amplitude response of the EMG signal of forearm flexion (zoomed in 0-50 Hz): (a) using the fourth-order high-pass filter; (b) using the second-order high-pass filter.

As can be seen from Figure 3-17, Figure 3-18, Figure 3-19 and Figure 3-20, there is only little improvement in terms of suppression of low frequency noises within the range of 0-20 Hz, when the high-pass roll-off rate was doubled from -12dB/Octave to -24dB/Octave. This suggests that the second-

order high-pass filter can almost perform as well as the fourth-order high-pass filter in the tested EMG filtering circuit design.

3.2.6.3 The first version of amplification and filtering design

Based on the aforementioned experiments and analyses, the first version of the EMG amplification and filtering circuit consists of a pre-amplifier, a second-order high-pass filter, a second-order low-pass filter, an inverting amplifier, and another second-order low-pass filter. Figure 3-21 is the schematic of the circuit. The EMG signals collected from ball squeezing and forearm flexion movements using this circuit are presented in Figure 3-22.

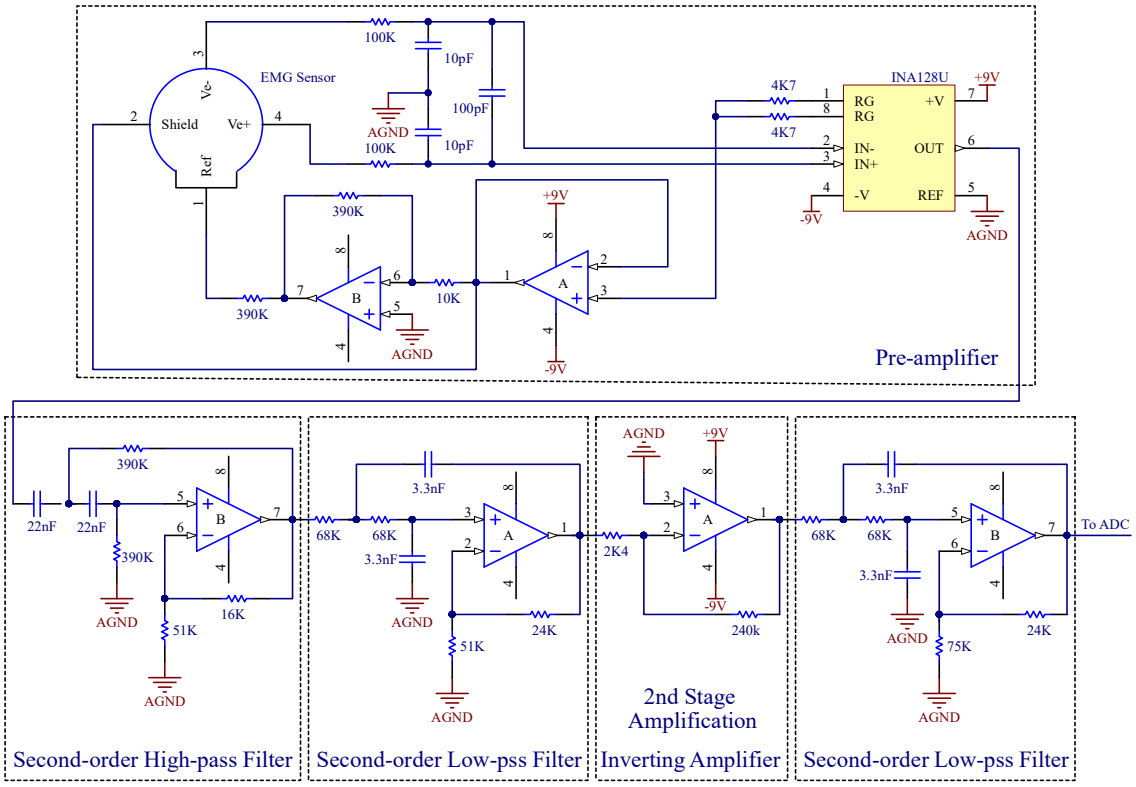

Figure 3-21. The first version of the amplification and filtering circuit.

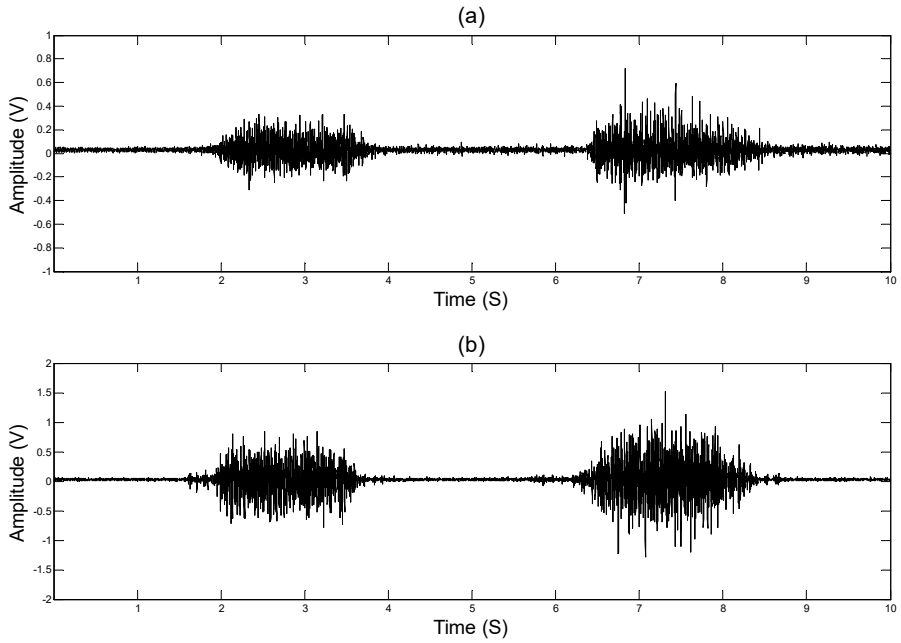

Figure 3-22. The EMG signal waveforms in time domain: (a) ball Squeezing; (b) forearm flexion.

The experiments also showed that, even when the limb keeps completely relaxed, the signal collected from the EMG circuit has some obvious noise signals. The frequency spectrum of the noise signals is displayed in Figure 3-23, which clearly reveals that the noise from the power line interference includes a base component of 50 Hz and its harmonics. These kind of noises from the power line coupling or radiation are usually the primary noise source. As described in the literature review chapter, a notch filter at 50 Hz (or 60 Hz) can be employed to clean the power line noises. At the same time, however, some important adjacent components of 50 Hz (or 60 Hz) in the surface EMG frequency range could be suppressed as well. In addition, the notch filter at 50 (or 60) Hz is still unable to attenuate its harmonics introduced by the nonlinearity of electronic components. Therefore, the notch filter was not used in this research.

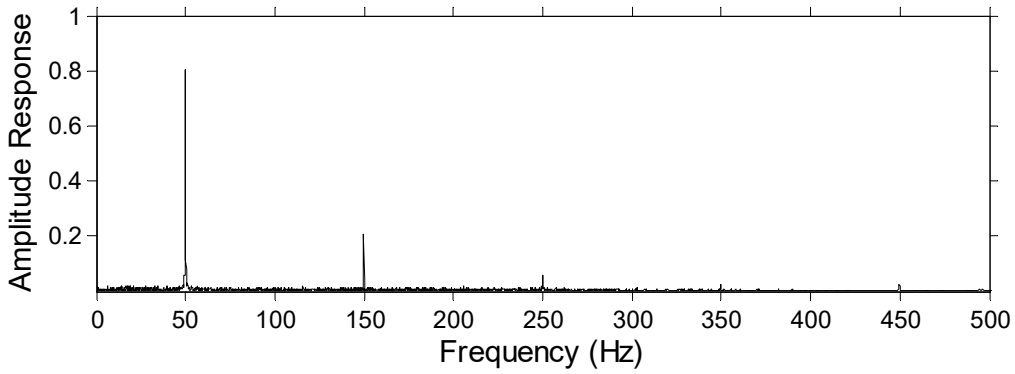

Figure 3-23. The amplitude response of the noise signals acquired using the proposed amplification and filtering circuit when the limb in the completely relaxed status.

3.2.7 Analog-to-digital conversion design

To integrate an EMG acquisition module into an EMG-controlled robotic hand, it is necessary to develop an analog-to-digital conversion circuit with the performance of multichannel and simultaneous sampling, instead of using a commercial data acquisition card such as the PCI-6229 used previously. The selection of a proper ADC plays a key role in analog-to-digital conversion design for a particular application. During this process, the main considerations include ADC architecture, sampling rate, resolution, latency, power consumption, power supply voltage, cost, etc. As mentioned in the literature review, the ADC architecture, sampling rate and resolution are essential properties to first be determined.

Among miscellaneous methods of implementing an ADC, the most common ways fall within three categories, that is, successive-approximation (SAR), sigma-delta (Σ-Δ), and pipelined ADCs. Figure 3-24 shows in a general way how the three most popular architectures and four typical types of contemporary application scenarios, relate to the ADC sampling rate and resolution.

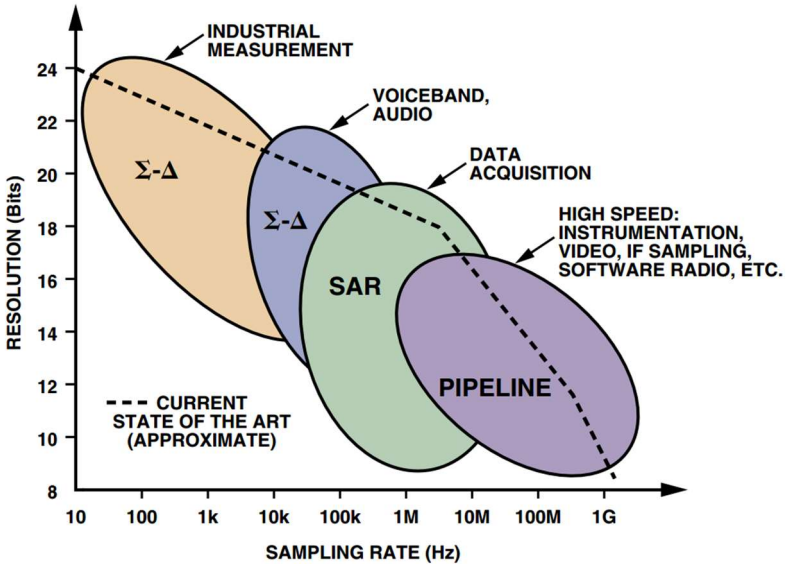

Figure 3-24. ADC architectures, applications, resolution, and sampling rates [198].

As can be seen from this figure, the best choice of EMG application appears to be the sigma-delta (Σ-Δ) ADC architecture, which applies oversampling and digital filtering techniques, given the 20–500 Hz useful bandwidth of the EMG signal and the recommendation of using a 16 or more bits of resolution as described in the literature review chapter.

Unlike conventional Nyquist rate ADC, the sigma-delta (Σ−Δ) ADC uses oversampling, noise-shaping, decimation and digital filtering technologies [199]. At the analog input end, a sampling rate, which is much greater than the Nyquist rate, is used. Through decimation and digital filtering, the sampling rate is reduced down to the Nyquist rate at the digital output end. Sigma-delta (Σ−Δ) conversion technology minimises the size of the dataset and simultaneously reduces the requirements on the analog anti-

aliasing filter. It means that using a sigma-delta (Σ−Δ) ADC, EMG signals with the highest useful frequency component of 500 Hz can be recorded at an output sampling rate of 1000 samples per second (SPS).

ADS1292 is an integrated monolithic analog front end for biopotential measurements from Texas Instruments Inc. It incorporates 2-channel, simultaneous sampling, 24-bit, sigma-delta (Σ-Δ) ADCs with a built-in programmable gain amplifier (PGA), internal reference, and an on-board oscillator [200]. The ADS1292 can operate at data rates up to 8000 SPS which will be more than enough for the surface EMG application, when considering it employs the oversampling and decimation technology. The input is internally sampled at 128 kHz by a sigma-delta modulator of the ADS1292, and this means that when a 1000 SPS of output sampling rate is used, the oversampling ratio is 128, which significantly reduces the noise level and the complexity of the analog anti-aliasing filter. Due to its high levels of integration and exceptional performance, the ADS1292 was selected to serve as the ADC in this research.

To match the input range of the built-in ADC of the ADS1292, a PGA gain of 3 can be used together with a gain of 333 provided by aforementioned two amplification stages and three filter sections, that is, a total gain of about 1000 was utilised to amplify the raw EMG signal.

Following the ADS1292, an Arduino UNO board which includes an 8-bit AVR microcontroller is used to collect and transmit the EMG data to a computer through a USB Virtual COM Port. Experiments proved that the Arduino UNO board using the USB Virtual COM Port was able to transmit 2 channels of EMG signals which were simultaneously sampled by a rate up to 4000 SPS yet without losing any data when the ADS1292 using its internal oscillator. As a result of using oversampling and digital filtering technology by the ADS1292, the sampling rate was set at 1000 Hz which can fulfil all tasks well in this research [18]. Moreover, the digital part of the ADS1292 operates at a voltage of 3.3 V whereas the Arduino UNO runs at 5 V; therefore, a bidirectional logic level translator ADG3308 (Analog Devices Inc.) is necessary between them. Figure 3-25 shows the configuration of the analog-to-digital conversion design.

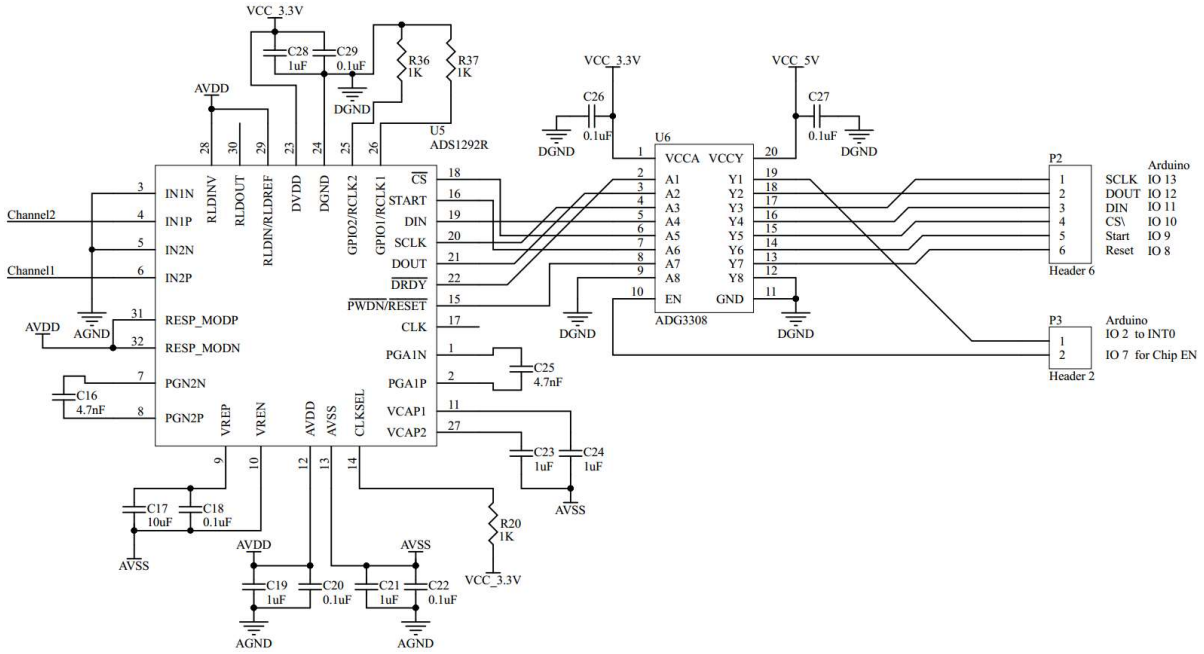

Figure 3-25. Analog-to-digital conversion and collection configuration.

On the computer side, a program was developed in Microsoft Visual Studio environment to store the EMG data, perform offline training and execute real-time myoelectric control tasks.

3.2.8 The modification of filtering design

In Section 3.2.5, inspired by [38, 201], the electronic component values of both low and high pass filters are calculated according to Equation (3.11) and (3.12). The experiments described in Section 3.2.6 verified the effectiveness of this method for the selection of filter component values. The further literature study, however, revealed that the filter with component values calculated in this way was not guaranteed to be optimised in terms of any individual specification. The ideal filter is with the characteristics of a brick wall amplitude and linear phase response that are physically unattainable. Practical filters in either analog or digital format can only approach the ideal attribute, and there are a variety of methods of approximation based on different criteria. Trade-offs must be made to maximise the performance on one specific aspect of the filtering characteristics but only at the expense of some other. The most popular and commonly-used methods include Butterworth, Bessel, Chebyshev and Elliptic approximation function, so are called the Butterworth, Bessel, Chebyshev and Elliptic filter respectively [202, 203].

A non-linear phase response can cause phase distortion by introducing different amounts of phase delay to different spectral components. In some circumstances, where phase distortion becomes a problem, the Bessel filter with the best phase linearity may be the choice [21]. For the surface EMG signal, however, the non-linear phase response is usually not a concern compared to the amplitude response,

since the nature of the surface EMG detection process does not allow for phase preservation. The Butterworth filter, which is with a maximally flat amplitude response in the passband and also a very smooth phase response at the expense of a relatively wide transition region from pass band to stop band and average transient characteristics, is best suited for applications requiring preservation of passband amplitude linearity, thus making an ideal candidate for conditioning the EMG signal [18].

Analog filter design is generally a two-step process to individually determine the filter transfer function and the circuit implementation topology. The analog filter theory has developed a set of systematic design approaches which are based firmly on long-established and arduous equations and tables of theoretical results; however the filter design and verification process can be tedious and time-consuming. Fortunately, there are computer programs developed to aid in the design of active filters. FilterPro™ from Texas Instruments Incorporated is one of them. It should be also noted that a 4th-order Butterworth filter cannot be obtained simply by calculating the components for a 2nd-order filter and then cascading two such stages as the Figure 3-12 in Section 3.2.5. So the component values of the two stages of the 4th-order low-pass Butterworth filter should be calculated in one design of FilterPro™. The Butterworth filters designed by using FilterPro™ are shown in Figure 3-26 and Figure 3-27.

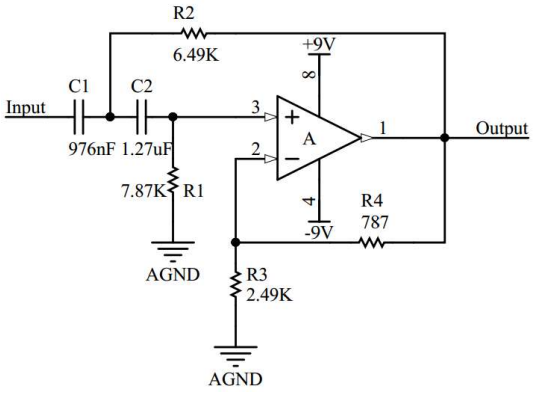

Figure 3-26. The Butterworth 2nd-order Sellen-Key high-pass active filter with a corner frequency of 20 Hz.

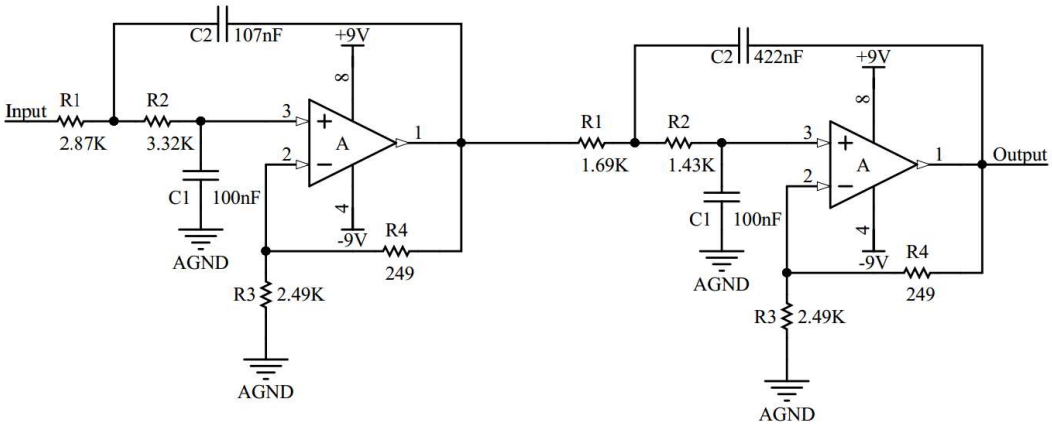

Figure 3-27. The Butterworth 4th-order Sellen-Key low-pass active filter with a corner frequency of 500 Hz.

The experiments also found that a certain level of DC voltage offset was introduced into the EMG signal chain by the cascaded amplification and filtering stages. Therefore, in the final design shown as Figure 3-28, a capacitor of 10 μF is placed in front of the input resistor of the 2nd amplification stage to form a first-order high-pass filter for removing the DC offset, the cut-off frequency of which is calculated as per:

$$f_c = \frac{1}{2\pi RC} = \frac{1}{2\pi \times 5.1\text{k}\Omega \times 10\mu\text{F}} = 3.12\ \text{Hz} \tag{3.13}$$

The cut-off frequency of 3.12 Hz is much less than 20 Hz, leading to little effect on the high-pass filtering characteristics of the whole signal chain.

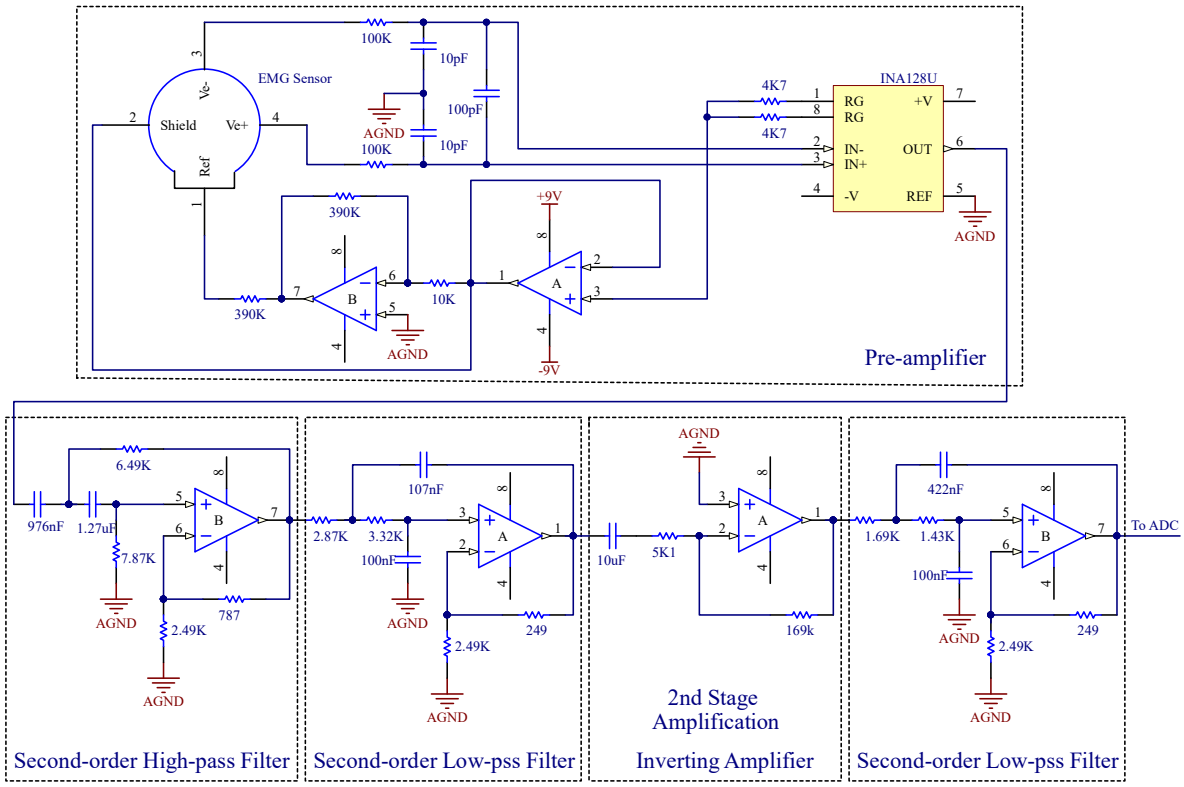

Figure 3-28. The modified amplification and filtering circuit using Butterworth filters.

3.3 Proposed solution 2: The fully differential approach for surface EMG signal detection and conditioning

Differential signalling has many attractive attributes such as common-mode rejection from a balanced signal path and matched filter response, immunity from single-ended component parasitic effects, decoupling the signal from requiring a ground reference, twice the output swing for a given voltage limit when compared to single-ended systems, and rejection of even-order harmonics. It is commonly

used for implementation of differential biopotential amplifiers [204, 205]. As described in the introduction section of this chapter, the discrete monolithic INA approach converts differential signals to single-ended outputs, compromising the overall performance. Therefore, it is desirable to utilise a fully differential EMG signal detection and conditioning circuit that can take advantage of the inherent ability of balanced signalling. However, the literature study has not found any easily-used solution that implements all amplification and filtering stages of the EMG signal processing chain using fully differential methods, although some ASIC-based EMG acquisition methods were reported in [33-36]. This is also the reason that a single-ended approach using the classical instrumentation amplifier configuration was first designed to determine and evaluate an appropriate EMG signal amplification and filtering architecture and suitable parameters. Actually, in this research, a fully differential EMG signal detection and conditioning solution has a similar block structure to the discrete monolithic INA one shown as Figure 3-2, except for the two amplification and three filter stages that need to use differential design instead. This is based on the fact that the EMG detection electrode configuration, the EMI/RFI rejection filter and the ADC ADS1292 employed in the discrete monolithic INA approach, are all differential design. Figure 3-29 depicts the circuit structure that is suitable for fully differential EMG signal detection and conditioning.

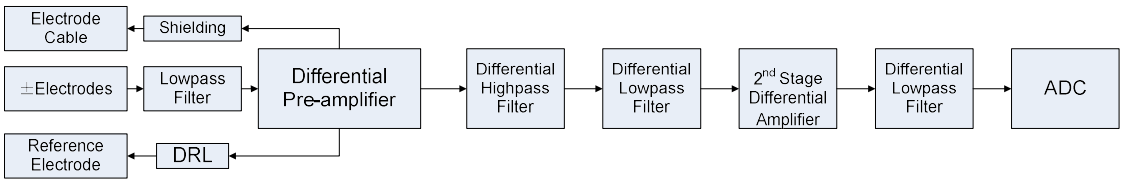

Figure 3-29. Block diagram of the fully differential version of the amplification and filtering for a single channel.

3.3.1 The fully differential front end amplifier

Two options can be used to realise an amplifier with both differential input and output, that is,

- The dual op-amp configuration;
- The integrated fully-differential amplifier (FDA) configuration.

Figure 3-30 and Figure 3-31 show the basic configuration of these two methods respectively.

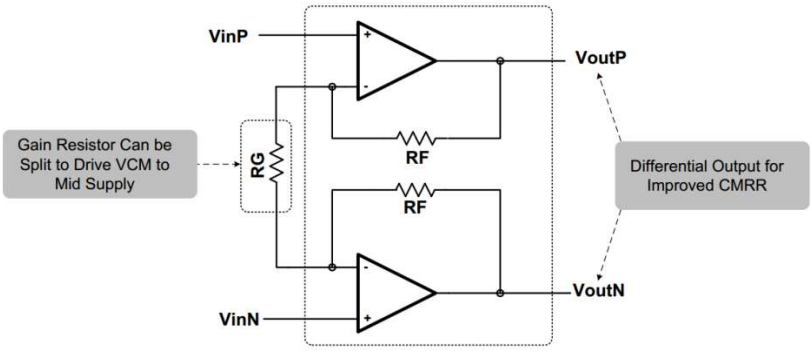

Figure 3-30. Differential-in and differential-out front end amplifier topology [181].

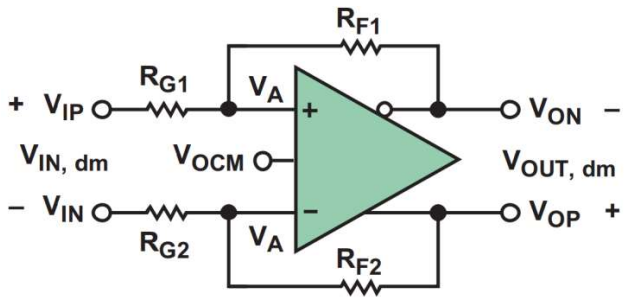

Figure 3-31. Fully differential amplifier (FDA) [206].

Although either of the two methods can be used in the design of fully differential amplification, there are differences between them. While the dual op-amp configuration can also serve as an analog front end in addition to an ordinary amplifier because of its high impedance provided by setting the two op-amps in a voltage follower manner, the integrated FDA method can only be used in further amplification or filter sections. Therefore, the dual op-amp configuration was used to implement the fully differential EMG front end amplifier as shown in Figure 3-32. As described in Section 3.2.4, the gain of the front end amplifier is set in such a way that the electrode DC offset does not saturate the front end itself so that 150kΩ and 56kΩ have been decided to be the values of the gain resister R_F and R_G, respectively. This means that the front end amplifier has a low gain of 6.36 which is hardly to cause the saturation problem.

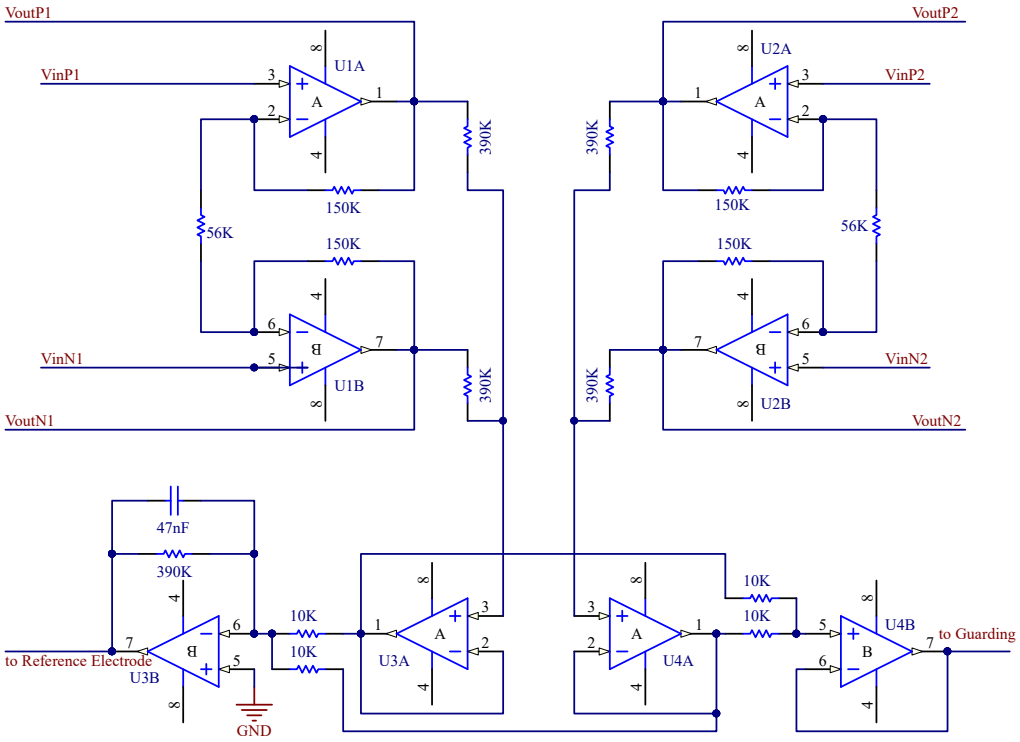

Figure 3-32. Fully differential EMG front end amplifier and DRL circuit of two channels.

The same guarding and DRL principle as the single-end INA approach described in Section 3.2 can also be applied to the dual op-amp fully differential design, except that the common-mode voltage is obtained by averaging all positive and negative outputs of two channels, instead of averaging the midpoint voltages of the gain resistors.

3.3.2 The second differential amplification stage

The second stage of differential amplification can be converted from its single-ended counterpart as Figure 3-28, by using the fully differential amplifier configuration as Figure 3-31. The same frequency and amplitude characteristics as the single-ended can be obtained with the design as Figure 3-33.

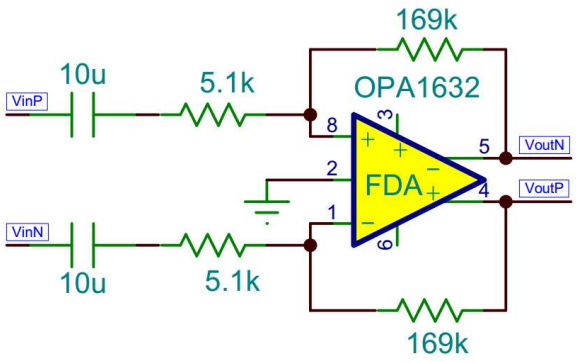

Figure 3-33. The fully differential AC-coupled second amplification stage.

3.3.3 The fully differential filter design

It seems that the fully differential filter design is daunting at first. However, a differential filter can be obtained by converting from the corresponding single-ended filter in a few steps [183, 207-209]:

- First mirror the single-ended filter design around GND and removing the GND;
- Then combine the circuit element and its mirror that connect to GND and recalculate these circuit component values;
- Finally, for the active filter, replace the op-amp and its mirror with a fully differential operational amplifier.

The inverting input end is usually used as the return point of a negative feedback path in most of op-amp applications, including active filter implementation. This leaves the only choice of the noninverting input end for establishment of a common-mode voltage, between an op-amp and its mirror, but not for signal input or positive feedback return. The converting process indicates only certain double pole topologies are suitable to implement a differential active filter, excluding those topologies with both positive and negative feedback, or those with only negative feedback but employing the noninverting end for signal input. This leads to only few utilitarian options [210]:

- Multiple feedback (MFB) filter (using one op-amp)
- Akerberg Mossberg filter (using two op-amps)
- Biquad filter (using two op-amps)

The MFB configuration is a simple and commonly used topology that is ready to support fully differential active filter design. The software program FilterPro can be used for differential MFB filter design in a similar way as for single-ended filter design. The schematics of the proposed fully differential high-pass and low-pass filter are presented in Figure 3-34 and Figure 3-35 respectively.

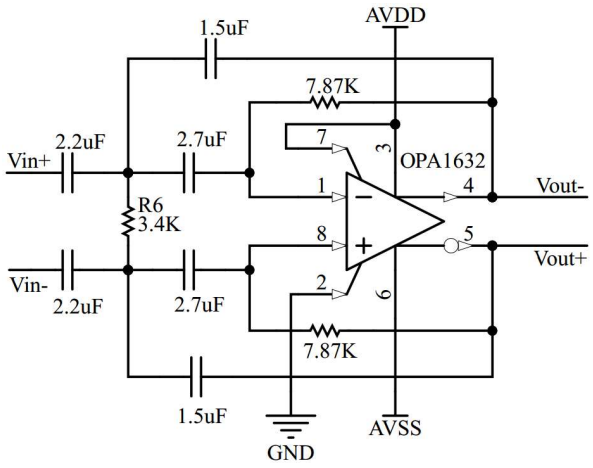

Figure 3-34. The fully differential MFB Butterworth 2nd-order high-pass active filter with a corner frequency of 20 Hz.

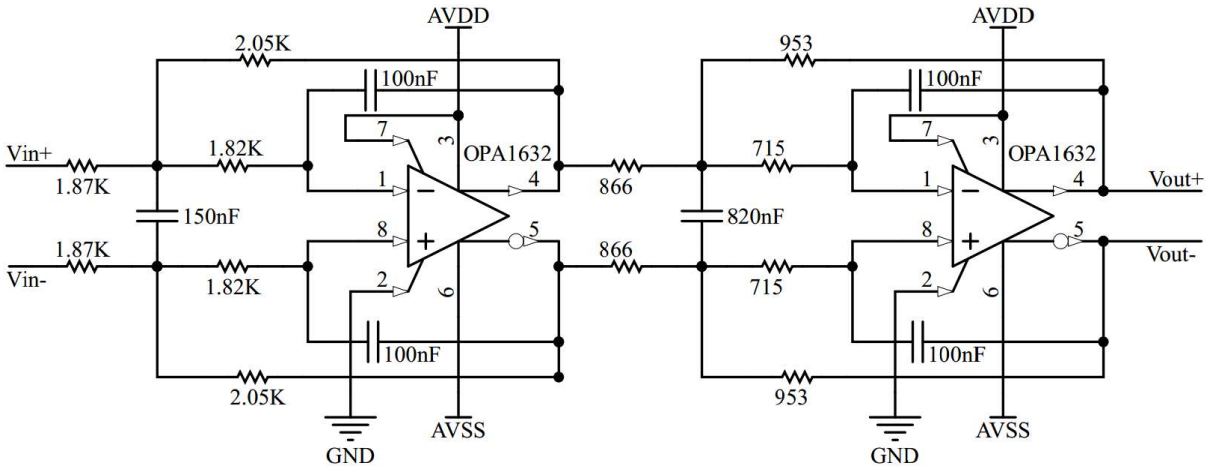

Figure 3-35. The fully differential MFB Butterworth fourth-order low-pass active filter with a corner frequency of 500 Hz.

The other differences from the single-ended approach are the ADS1292's IN1N and IN2N pins that are connected to V_{out}- pins of their corresponding channel low-pass filter instead of being led to GND as shown in Figure 3-25. At this point, all circuit blocks shown in Figure 3-29 are designed and implemented in the fully differential design manner, thus forming a complete fully differential surface EMG signal detection and data acquisition system.

The fabricated EMG signal acquisition circuit PCB is shown in Figure 3-36. All schematics are attached in appendices.

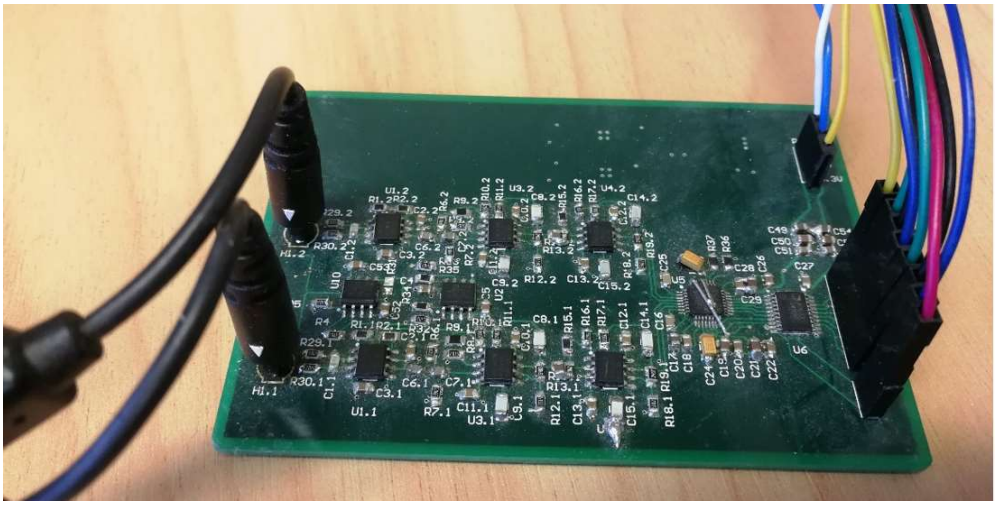

Figure 3-36. The fabricated EMG signal acquisition circuit PCB.

Chapter 4
Pattern recognition-based hand gesture discrimination

This chapter focuses on robust pattern recognition-based real-time myoelectric control schemes that could be applied to drive a robotic hand with fingers, which will be discussed in next chapter. The overall framework of myoelectric control algorithms will be studied first, followed by the elaborations of the approaches and methods for myoelectric control.

4.1 Myoelectric control framework

As mentioned in Chapter 1, various schemes have been researched for the implementation of myoelectric control. The early approaches work only on one or two degrees of freedom (DOFs), usually mapping an estimated parameter such as the amplitude or the change rate of the EMG signal to a targeted DoF of a prosthetic hand. In contrast to these primitive methods, pattern recognition has the potential to be used for more DOFs. Indeed, pattern recognition has been the preferred method for multi-functional myoelectric control. Up until now, however, research in myoelectric control systems based on pattern recognition is still mainly limited to the laboratory environment. Very few products based on EMG pattern recognition are commercially available. The flexibility, reliability and robustness of such systems still remain as challenging issues. As a result, these products are facing a considerable rejection rate especially in real-life applications.

The pattern recognition-based myoelectric control can consist of different functional stages or steps, including data segmentation, feature extraction, dimensionality reduction, classification, and post-processing. For real-time applications, EMG activity detection is a necessary step added at the beginning to trigger the running of following steps. On the contrary, dimensionality reduction and post-processing can be ignored from the myoelectric control scheme, determined by specific system design specifications. The overall framework can be illustrated as in Figure 4-1, where occurrence of the blocks enclosed in dashed rectangles is dependent on applications. From the next section, the methods for each step of the pattern recognition-based real-time myoelectric control scheme developed by this research will be presented.

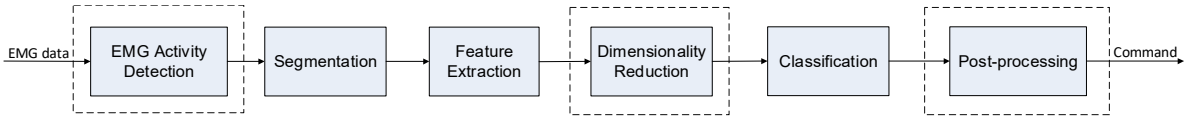

Figure 4-1. Framework of pattern recognition-based myoelectric control.

4.2 Muscle activity detection via EMG signal recognition

Despite the usefulness of the manual visual inspection method that is used in activity detection for EMG offline analysis and algorithm testing result comparison, a real-time control scheme necessitates automatic EMG onset and duration detection. Onset detection is a challenging task due to the stochastic characteristic of the EMG signal, especially when considering the weak surface EMG response.

To use EMG signals to automatically and precisely identify muscle activity starting and ending point, the basic idea involves the comparison between certain specific parameters calculated from the signal data and one or two pre-defined thresholds. Various computer-based methods have been proposed for muscle activity detection. Most of them are related to EMG signal amplitude. Although the activity detection methods associated with the amplitude of EMG signals are sensitive to noises, the algorithmic implementation of these methods is straightforward and computationally efficient. To improve the detection accuracy, there are different novel algorithms proposed in literature, e.g. the maximum value detection (MVD) method [73], the sample entropy analysis method [71], the maximum likelihood (ML) method [76], the approximated generalized likelihood ratio (AGLR) method [211], and the Teager–Kaiser energy (TKE) operator method [77]. However, these novel approaches are more complex and time-consuming than those amplitude-related counterparts.

The literature study has shown that amplitude-based methods are the most utilised choice for activity detection due to their simplicity and low computational cost. A simple moving average method that calculates energy using signal amplitude values [212] is a feasible option for this research. The average signal energy is computed in windows with a certain length and then compared with a predefined threshold that is chosen beforehand. The threshold is set as the value of average energy calculated at the activity starting point of EMG data recorded in offline experiments with the same setting as the real-time test. The activity starting point of offline EMG data is determined by using the manual visual inspection method.

In this research, the average amplitude value of the EMG signals from two channels is first calculated, and then the square of the average is regarded as the instantaneous energy of the EMG signal. Two adjacent windows (leading and trailing) slide through the EMG instantaneous energy data series to evaluate the average energy in these two sliding windows. The calculation process of the average energy in either window consists of three steps as follows:

1) Calculate the average of the EMG signals from all channels

$$\overline{s}(t) = \frac{1}{C}\sum_{c=1}^{C} s_c(t) \tag{4.1}$$

where $s_c(t)$ is the c -th channel EMG signal; C is the total number of the EMG channels and in this research $C = 2$.

2) Compute the transient signal energy

$$E(t) = \overline{s}^2(t) \tag{4.2}$$

3) Evaluate the average of the transient signal energy in moving windows

$$E_{MA}(t) = \frac{1}{W}\sum_{i=t-W+1}^{t} E(i) \tag{4.3}$$

where W is the width of the moving windows.

Once the average energy is determined in the leading and trailing windows, they are compared with a predefined threshold to detect the start point or end point of the EMG signal. Starting from a rest state, when the energy averages in both the leading window and the trailing window are greater than the predefined threshold, the EMG activity is considered started. On the contrary, when the energy averages in both the leading window and the trailing window are less than the predefined threshold and the EMG is previously active, it begins to stop activity.

The advantage of using two adjacent moving windows is that this method can prevent spurious start or end point detection when a pulse noise signal is mainly distributed in only one of them. It is worth noting that the minimum interval between two distinct human muscle contractions is approximately 200 ms [68]. This also suggests that the duration of any muscle contraction may not likely be less than 200 ms. Therefore, if the interval between any pair of detected start point and end point is less than 200 ms, this period of signal is most likely caused by noise or artefacts and should be discarded.

The length of the moving average windows in this thesis was set as 25 ms, leading to an activity detection response time of 50 ms that is two times the moving average window length due to the two adjacent sliding windowing scheme.

4.3 Data segmentation

Because of the stochastic nature, it is generally acknowledged that the instantaneous values of the myoelectric signal do not contain proper information that can be directly used in pattern recognition. Instead, EMG data segments are usually used to estimate features for classification, based on the statistical parameters from each segment.

Three points must be carefully considered during EMG data segmentation, i.e. segment length, the state of data, and the data windowing technique [6, 68].

Normally two states can be observed in recorded EMG signals, i.e. the transient state emanating from a burst of fibres when a muscle goes from rest to a voluntary contraction level, and the steady state emanating during a constantly maintained contraction in a muscle. Although the transient state shows a capability for classification [82], higher classification accuracy can be obtained from the steady state [213]. In addition, given the weakness of a request to start a motion from rest for transient state classification, the steady state is preferred in myoelectric control.

The first consideration of designing a real-time robotic control system is the real-time constraint—with a delay less than 300 ms between muscle contraction and physical robotic system movement. A smaller segment length is helpful to reduce the response delay, which depends mostly on the segment length. On the other hand, classification error increases as the segment length declines because of the raised deviation and variance of features in accordance with the decreased segment length.

The controller delay can be calculated by using equations in Table 2-1 for different system configurations in connection with the selection of segmentation windowing scheme and postprocessing technique. The difference of the real-time constraint 300 ms and the computation processing time, is the longest permissible time period that can be used for segmentation and postprocessing. Considering the computational capacity of modern microprocessors or CPUs such as ARM Cortex-M3 or Cortex-M4 series, 50 ms is much more than the necessary time for finishing the computational task of a segment. This means at least 250 ms can be left for segmentation, postprocessing and other factors such as a short time of mechanical inertia.

Two windowing techniques, i.e. the disjoint and the overlapped windowing, were proposed for data segmentation in literature. Disjoint windowing has only one variable parameter—segment length, whereas overlapped windowing is determined by length and increment. The increment is the time interval between two adjacent segments. It should be less than the segment length, and more than the computational processing time for a segment. The use of a segment length longer than 200 ms requires overlapped segmentation in order to avoid failure in real-time. Research shows that real-time controllability is dependent not only on classification accuracy but also on controller delay, and in turn

on the segment length, the windowing scheme and the post-processing technique, as detailed in the literature review section 2.2. It is found that the optimal controller delay ranges approximately from 100 ms to 125 ms [79], and the optimal window length is between 150 ms and 250 ms for the overlapping window technique [60].

Aiming for a real-time myoelectric control system, the overlapped windowing scheme was considered and selected in this research. The delay of the hand gesture discrimination module relates to multiple factors, which also includes the post-processing technique used, such as majority voting, rather than simply analysis window parameters and computation processing time. Therefore, the analysis window length and increment were determined accordingly with the majority voting scheme in the experiments.

4.4 Feature extraction

The success of EMG pattern recognition is heavily dependent on the choice of discriminative features that are used to represent the corresponding pattern categories [82]. It is widely accepted that the choice of a representative feature set is more effective and efficient than the attempt to design a complicated classifier that could theoretically achieve higher accuracy. It is reported that a carefully selected EMG feature set is possible to make a classifier directly achieve high performance [85].

Many EMG feature sets have been proposed and studied due to the important role they play in pattern recognition-based myoelectric control. The majority can be divided into four groups: time domain (TD) features, frequency domain (FD) features, time-scale or time-frequency domain (TFD) features, and spatial domain (SD) features [81]. Three indicative measures, i.e. class separability, robustness and complexity, can be used to evaluate feature performance.

EMG features in time domain are usually easy to implement and computationally efficient since their calculation is based on raw EMG data time series—the digital discrete EMG signal amplitude values, without the necessity of any type of mathematical transformation. A disadvantage of time domain features is that they cannot capture the non-stationary property of the EMG signal, which may lead to situations in which some statistical parameters of the analysis window change over time. Additionally, more interference may be introduced because their calculation is only based on EMG signal amplitudes that are more likely affected by noise. However, features in this group can reach acceptable classification performance in low noise environments, hence being widely used in both medical and engineering researches and practices. Time domain features can be further grouped into four subsets: energy and complexity information, frequency information, prediction model, and time-dependence. Features from the same subset often result in redundancy [85].

Frequency domain features are computed based on statistical parameters of power spectral density (PSD) and are mostly used to study muscle fatigue, force production, and changes in motor unit recruitment and firing patterns [81]. Although some frequency domain features show similar separability to time domain features, features in frequency domain are considered unsuitable for EMG recognition application. However, specified frequency domain features may be combined with successful time domain features to improve system robustness.

Modern signal processing technology has developed new mathematical transformation techniques, including short time Fourier transform (STFT), continuous wavelet transform (CWT), discrete wavelet transform (DWT), wavelet packet transform (WPT) and stationary wavelet transform (SWT). Coefficients of these transformations can be selected or combined as time-frequency domain (TFD) features for classification. TFD features can constitute a high-dimensional feature vector that necessitates dimensionality reduction to increase the speed and accuracy of the classification.

Spatial domain (SD) features come from the spatial information that high-density surface EMG (HD-sEMG) measurements can provide. SD features can be used to provide information about the spatial distribution of the MUAPs and the load-sharing between muscles.

Literature study found recommended EMG features in myoelectric control including:

1) MAV, WL, WAMP, AR, CC, RMS and MAVS from the time domain;

2) MNF and PSR from the frequency domain;

3) Sample entropy (SampEn) [29].

Based on the extensive preceding work in literature, given the consensus of the effectiveness and efficiency of the time domain features, together with concerns about the effect of long-term usage, five features were considered in this research for the proposed real-time myoelectric control system development. The mathematical expressions of these features are listed below. The parameter values used in this research for feature computation are also pointed out.

1) Root mean square (RMS)

RMS is a measure of the signal energy in a time segment.

$$\mathrm{RMS} = \sqrt{\frac{1}{N}\sum_{i=1}^{N} x_i^2} \tag{4.4}$$

where x_i stands for the EMG signal instantaneous amplitude voltage and N is the length of a signal segment [85].

2) Waveform length (WL)

WL is a measure of complexity of the myoelectric signal, representing the cumulative length of the EMG waveform over a data window [85].

$$\mathrm{WL} = \sum_{i=1}^{N-1} \left| x_{i+1} - x_i \right| \tag{4.5}$$

3) Cepstral coefficients (CC)

CC is the coefficient set of the inverse Fourier transform of the logarithmic power spectrum magnitude of the signal data, and can be calculated from the parameters of the auto-regressive (AR) model for the same signal data [85].

$$c_1 = -a_1 \tag{4.6}$$

$$c_p = -a_p - \sum_{l=1}^{p-1} \left(1 - \frac{l}{p} \right) a_P c_{p-l} \tag{4.7}$$

where c_p is the p-th order coefficient of Cepstral analysis and $1 \le l \le P$; P is the order of the AR model; a_1 and a_p are the coefficients from AR model:

$$x_i = \sum_{p=1}^{P} a_p x_{i-p} + w_i \tag{4.8}$$

The fourth-order AR and in turn the fourth-order CC were suggested in previous studies [85], thus selected and implemented in this research.

4) Sample entropy (SampEn)

SampEn represents the complexity and regularity of a system [214]. It is defined as:

$$\mathrm{SampEn}(m, r, N) = -\ln[A^m(r) / B^m(r)] \tag{4.9}$$

where $B^m(r)$ and $A^m(r)$ are the probability that two series will match for m and $m+1$ points, respectively [29]; m was set as 2 in this research [214]; and r is the global tolerance, set as $c \times \sigma$, where σ is the standard deviation of the EMG time series for all non-rest states of each subject, and c is an adjustable coefficient for finding a proper global tolerance to avoid the occurrence of $\ln(0)$. The computational algorithm implemented in [215] was employed to determine sample entropy values.

5) Willison amplitude (WAMP)

$$\mathrm{WAMP} = \sum_{i=1}^{N-1} \left[f\left(\left| x_i - x_{i+1} \right| \right) \right] \tag{4.10}$$

$$f(x)=\begin{cases}1, & \text{if} \quad x \geq threshold \\ 0, & \text{otherwise.}\end{cases} \tag{4.11}$$

The threshold can be selected from a series of candidates through experiments such that a classifier can reach the highest accuracy when using a single WAMP feature. The suitable threshold value is normally in a range corresponding to an input-referenced EMG signal voltage variation span between 10 – 100 μV [216]. Since the total gain value of the EMG signal recording circuit was set as 1000 in this research, the typical threshold value of WAMP is between 10 – 100 mV. A threshold of 5 mV would correspond to an input signal of 5 μV, which is close to the system noise level that is about a few μV. An experiment was conducted to chosen a suitable threshold in this research. The experiment employed the single WAMP feature of two channels of EMG signals and a built-in LDA classifier function *Classify* from Matlab. The threshold was chosen based on the experimental results. Figure 4-2 shows the classification error rates produced in the WAMP threshold examination experiment. The 10 mV of threshold corresponds to the least error rate and thus was selected as the threshold of WAMP in this research.

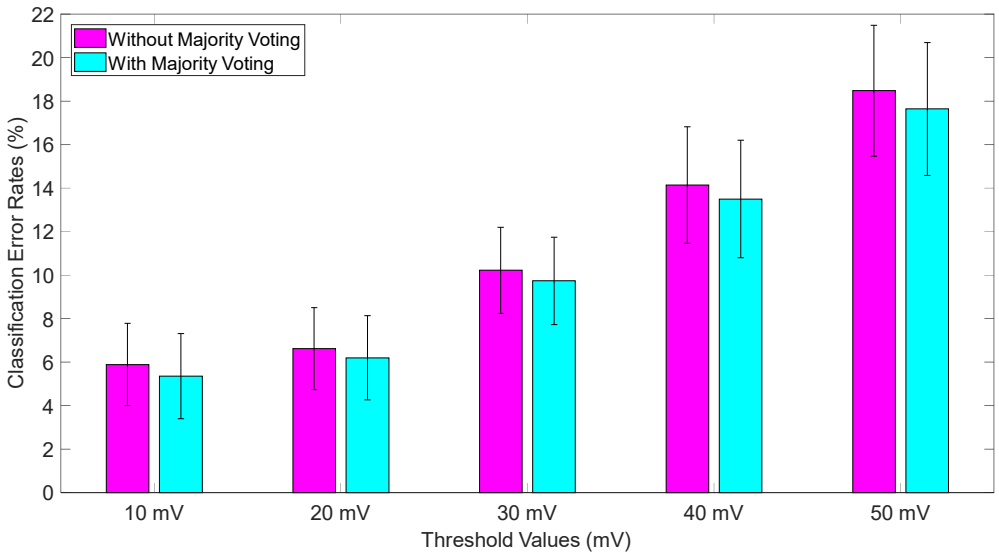

Figure 4-2. WAMP threshold examination experiment results.

The final feature set for classification in this research is composed of 8 quantities, i.e. RMS, WL, SampEn, WAMP, and four CC coefficients (c_1, c_2, c_3, and c_4). A total of 8 scalar parameters can be calculated from each channel of EMG signals. Taking account of two channels of EMG signals used in this research, a total of 16 parameters can be obtained. These 16 parameters can be concatenated as a feature vector fed into the pattern recognition classifier in the next processing step. The feature vector dimension in this research is 16 and can be considered unable to cause the high dimensionality problem. This eliminates the necessity of further dimension reduction before classification. Therefore, dimension reduction methods are not studied and implemented in this research.

4.5 Classification

Classification is the process to identify the category that a new observation belongs to, within a set of categories, on the basis of a set of observations whose category membership is known. There are two phases in classification, i.e. training to determine classifier parameters using the membership-known specimen set, and testing to predict the membership of new instances.

Previous studies on myoelectric control have made comparisons on most modern classification methods [24]. In principle, all classifiers similarly use a set of training data to define a decision boundary in the feature space, but with different boundary shapes allowed and with different ways the boundary is placed on the basis of the training data [217]. Literature study shows that support vector machine (SVM) [68] and linear discriminant analysis (LDA) [29] have been considered the most robust and thus the two most popular classifiers for myoelectric control.

4.5.1 Linear discriminant analysis (LDA)

Linear discriminant analysis assumes linear decision boundaries between classes and uses training data to determine the weights of discriminant functions of the classifier so as to optimally discriminate two classes with the equal-covariance Gaussian distribution attribute.

A general idea for supervised classification is to use a discriminant function to lead to a classification rule. A linear discriminant function is defined as

$$g(\mathbf{x}) = \mathbf{w}^T \mathbf{x} + w_0 \tag{4.12}$$

where $\mathbf{w}$ is a weight vector and w_0 is a threshold; $\mathbf{x}$ is one of the training patterns $\{\mathbf{x}_i,\ i = 1,\ \cdots,\ n\}$.

In the binary classification problem, the discriminant function approach of classification is to seek a weight vector $\mathbf{w}$ and a threshold w_0 such that

$$\mathbf{w}^T \mathbf{x} + w_0 \begin{cases} > 0 \\ < 0 \end{cases} \quad \Rightarrow \quad \mathbf{x} \in \begin{cases} \omega_1 \ \ with\ corresponding\ numeric\ value,\ y_i = +1 \\ \omega_2 \ \ with\ corresponding\ numeric\ value,\ y_i = -1 \end{cases} \tag{4.13}$$

Thus, all training patterns can be correctly classified if

$$y_i(\mathbf{w}^T \mathbf{x}_i + w_0) > 0 \ \text{ for all } i \tag{4.14}$$

In this research, the LDA classifier function *classify*—a built-in function implemented in Matlab Statistics and Machine Learning Toolbox for discriminant analysis [218], as shown in Equation (4.15), was selected for offline experiments to compare classification accuracy with the SVM classifier.

$$class = classify(sample, training, group, 'type') \tag{4.15}$$

Where *type* is 'linear' to fit a multivariate normal density to each group, with a pooled estimation of covariance (this means each group with an equal variance).

4.5.2 Support vector machine

SVM is a kernel-based machine learning approach, which has increasingly become popular since the 1990s. SVM trains linear learning machines in high-dimension linearly separable feature spaces that are implicitly transformed from low-dimension linearly inseparable spaces using kernels in order to maximise the margin by applying optimisation algorithms to control over-fitting [3, 99, 105, 219].

The idea behind SVM requires not only that the training patterns are subject to Equation (4.14), but also that the margin is maximised for a better generalisation capability, i.e.

$$y_i(\mathbf{w}^T\mathbf{x}_i + w_0) \geq b \quad \text{where } b \text{ is a constant and } \; b > 0 \tag{4.16}$$

Without loss of generality, a value $b = 1$ may be taken, thus

$$\begin{aligned} \mathbf{w}^T\mathbf{x}_i + w_0 &\geq +1 \quad \text{if } \mathbf{x}_i \in \omega_1 \\ \mathbf{w}^T\mathbf{x}_i + w_0 &\leq -1 \quad \text{if } \mathbf{x}_i \in \omega_2 \end{aligned} \tag{4.17}$$

The seperating hyperplane is defined by Equation (4.18).

$$\mathbf{w}^T\mathbf{x}_i + w_0 = 0 \tag{4.18}$$

Equation (4.19) defines two canonical hyperplanes.

$$\begin{aligned} \mathbf{w}^T\mathbf{x}_i + w_0 &= +1 \\ \mathbf{w}^T\mathbf{x}_i + w_0 &= -1 \end{aligned} \tag{4.19}$$

The distance between the two canonical hyperplanes, i.e. the margin, is $2/|\mathbf{w}|$. Therefore, maximising the margin is equivalent to seeking a solution that minimises $|\mathbf{w}|$ subject to the constraints:

$$y_i(\mathbf{w}^T\mathbf{x}_i + w_0) \geq 1 \quad i = 1, \; \cdots, \; n \tag{4.20}$$

The objective function of the above optimisation problem can be written as:

$$J(\mathbf{w}) = \frac{1}{2}\mathbf{w} \bullet \mathbf{w} \tag{4.21}$$

For nonlinear separable two-class data, constraints (4.17) can be relaxed by introducing a slack variable ξ_i, leading to a soft margin:

$$\begin{aligned} &\mathbf{w}^T\mathbf{x}_i + w_0 \geq +1-\xi_i \quad \text{if } \mathbf{x}_i \in \omega_1 \\ &\mathbf{w}^T\mathbf{x}_i + w_0 \leq -1+\xi_i \quad \text{if } \mathbf{x}_i \in \omega_2 \\ &\xi_i \geq 0 \qquad\qquad\qquad i = 1,\cdots,n \end{aligned} \tag{4.22}$$

If $\mathbf{x}_i$ is correctly classifed, then $\xi_i = 0$; otherwise $\frac{|\xi_i|}{|\mathbf{w}|}$ is the distance of $\mathbf{x}_i$ from the corresponding canonical hyperplane.

The objective function (4.21) can be replaced by (4.23) to incorporate the additional cost due to nonseparability:

$$J(\mathbf{w}) = \frac{1}{2}\mathbf{w}\bullet\mathbf{w} + C\sum\nolimits_i \xi_i \tag{4.23}$$

where *C* is a regularisation parameter to adjust the penalty term in the objective function. A large value of *C* will lead to a lower misclassification rate on training data and a smaller margin thus a lower generalisation capability, while a small value of *C* will result in a better generalisation capability by a larger margin but misclassifying more training samples.

By introducing the slack variables, the classification margin of SVM is softened and thus this method is called soft margin SVM or *C*-SVM, which is the standard configuration for a typical SVM classification problem. There is also another implementation of the soft margin SVM, called *v*-SVM. The soft-margin SVM classifiers are sensible for EMG application since EMG signals are often contaminated by artefacts and noises thus with high levels of outliers. The possibility to have adjustable margins is beneficial to consider the effect of outliers [3].

The choice of *C* is critical in that a too high value of *C* will lead to overfitting whereas a too low value of *C* will result in underfitting. No optimal criteria exist to select a value for *C*, but a method of "grid-search" using cross-validation can be considered [3, 220].

Soft-margin allows for an acceptable misclassification level so as to obtain a linear approach for non-linearly separable problems. For circumstances inherently nonlinearly separable, however, a nonlinear method may lead to a better outcome. Except for being applied to the original variables, the algorithms developed for using linear discriminant functions can also be utilised in a transformed feature space defined by nonlinear transformations of the original variables. The discriminant function can be rewritten from Equation (4.12):

$$g(\mathbf{x}) = \mathbf{w}^T \phi(\mathbf{x}) + w_0 \tag{4.24}$$

with decision rule

$$\mathbf{w}^T \phi(\mathbf{x}) + w_0 \begin{cases} > 0 \\ < 0 \end{cases} \quad \Rightarrow \quad \mathbf{x} \in \begin{cases} \omega_1 \ \textit{with corresponding numeric value,} \ y_i = +1 \\ \omega_2 \ \textit{with corresponding numeric value,} \ y_i = -1 \end{cases} \tag{4.25}$$

The objective function optimisation and subsequent classification can be deduced only by relying on dot products $\phi(\mathbf{x}_i)^T \phi(\mathbf{x}_j)$ between transformed feature vectors and it can be replaced by a kernel function

$$K(\mathbf{x}, \mathbf{y}) = \phi(\mathbf{x})^T \phi(\mathbf{y}) \tag{4.26}$$

In this way, explicitly computing the transformation $\phi(\mathbf{x})$ can be avoided and the dot product can be replaced with $K(\mathbf{x}, \mathbf{y})$ instead. The whole procedure is referred to as the kernel trick.

The most used kernel functions include:

- Radial Basis Function (RBF), $K(\mathbf{x}_i, \mathbf{x}_j) = e^{-\frac{\|\mathbf{x}_i - \mathbf{x}_j\|^2}{2\sigma^2}}, \quad \sigma \neq 0$
- Polynomial, $K(\mathbf{x}_i, \mathbf{x}_j) = (\mathbf{x}_i \cdot \mathbf{x}_j + 1)^d, \quad d > 0$
- Sigmoidal, $K(\mathbf{x}_i, \mathbf{x}_j) = \tanh(k\mathbf{x}_i \cdot \mathbf{x}_j - \delta)$
- Cauchy, $K(\mathbf{x}_i, \mathbf{x}_j) = \left(1 + \frac{\|\mathbf{x}_i - \mathbf{x}_j\|^2}{2\sigma^2}\right)^{-1}, \quad \sigma \neq 0$
- Logarithmic, $K(\mathbf{x}_i, \mathbf{x}_j) = -\log(\|\mathbf{x}_i - \mathbf{x}_j\|^d + c, \quad d > 0$

As with the regularisation parameter *C*, kernel function parameters can also be set using a grid-search approach.

SVMs are stable classifiers due to the SVM decision rule prescribed by a simple linear function in the kernel space. SVMs also consist in low variance that reflects the low sensitivity of the classifier to the training data. Low-variance classifiers, such as SVM, can deal with non-stationary signals, such as EMG, with features that change over time, better than others [3]. In general, it is found SVM is a more robust technique for classification than the LDA-based method. The SVM focuses on the data at the boundary of the classes for extracting group differences that are less perceivable on the original space,

but more important for classification. Conversely, the LDA-based method can capture variations within each group which is useful for extracting discriminative information [221].

Multiclass SVM classifiers can be converted from binary classifiers either in a one-against-all or in a one-against-one manner. In one-against-all (OAA), *M* binary classifiers are constructed for *M*-class problem. The *k*-th classifier is trained to separate instances in class ω_k from all the others. A new observation is classified to the class whose corresponding classifier generates the highest score. Similarly, in one-against-one (OAO) for *M*-class problem, *M**(*M* − 1)/2 classifiers are built. Each classifier discriminates one class from another. A new observation is assigned according to a majority voting result of all classifiers' responses.

LibSVM [222] is one of the most famous software libraries of SVM algorithm implementation. In this research, the source codes of LIBSVM in C/C++ programming language were utilised for the implementation of SVM classifier in both offline and real-time situations. The RBF is the first option of kernel functions. The RBF kernel function of LIBSVM is described in a form of

$$K(\mathbf{x},\mathbf{y}) = e^{-\gamma\|\mathbf{x}-\mathbf{y}\|^2} \tag{4.27}$$

Scaling is an important data preprocessing step before applying SVM for avoiding features in greater numeric ranges dominating those in smaller numeric ranges and also avoiding numerical difficulties during calculation [220]. In this research, each feature of training EMG data was linearly scaled to the range [−1, +1] or [0, 1] according to Equation (4.28).

$$f_{new} = B_{lower} + (f_{old} - f_{\min}) \times \frac{B_{upper} - B_{lower}}{f_{\max} - f_{\min}} \tag{4.28}$$

where

B_{upper} and B_{lower} are the upper and lower boundaries of each feature after scaling respectively and they are -1, 1 or 0 in this research;

$f_{\max}$ and $f_{\min}$ are the maximum and minimum of each feature before scaling, respectively;

f_{old} and f_{new} are the values of each feature before and after scaling, respectively.

In addition, the scaling factor $\frac{B_{upper} - B_{lower}}{f_{\max} - f_{\min}}$ calculated using the training data set must be applied to the testing data set and real-time application for getting a better accuracy.

Unlike LDA, the SVM classifier demands several mathematical model parameters determined beforehand. As used in [72], *C*-SVM was also selected as the SVM classifier type in this research. For *C*-SVM, the required parameters consist of the regularisation parameter C and the RBF kernel parameter γ. The best values of C and γ can be found by a grid-search method using cross-validation (CV) [220]. A parameter selection tool *grid.py* using Python programming language is provided in the LIBSVM package for C-SVM classification using the RBF kernel. It uses cross-validation technique to estimate the accuracy of each parameter combination in a specified range and helps to decide the best parameters for a specific problem. In this research, these two parameters were chosen to be the same as used in [72], i.e. $C = 8$, and γ = 12/(number of features). As stated in the segmentation section, the number of features in this research, namely the dimension number of the classification feature vector, is 16. Therefore, γ = 12/(number of features) = 12/16 = 0.75.

4.6 Post-processing

The density-increased decision stream due to the overlapping windowing scheme, provides possibility and also necessitates post-processing to reduce the number of commands sent to the output device. Majority voting (MV) is a conventional post-processing method used after classifier outputting decisions. MV has shown that it can eliminate spurious classification results and smooth the output decision stream [108], avoiding abrupt device movement changes. The number of decisions utilised in a MV queue can be determined by the acceptable control delay, analysis window length and increment, and the computational processing time [60, 79, 80].

For the overlapped windowing scheme with majority voting, the average decision-making delay can be calculated according to Equation (4.29) from Table 2-1. In this research, a variable was purposely designed in the software program to allow the adjustment of the decision number in majority voting.

$$D = \frac{1}{2}T_a + (\frac{n}{2})T_{new} + \tau \tag{4.29}$$

Where $D = Controller\ Delay$; $T_a = Analysis\ Window\ Length$; $\tau = Processing\ Time$;

$T_{new} = Analysis\ Window\ Increment$; $n = Number\ of\ Majority\ Votes$.

To utilise more information in a window, a longer window length is preferable but may lead to a unacceptable delay according to Equation (4.29). The same logic happens to the analysis window increment and the number of votes in majority voting. Trade-offs must be made between these three parameters to get balanced performance. In this research, the analysis window length and increment were selected as 200 ms and 25 ms respectively; the typical number of votes in a majority voting queue

can be 5, 7, and 9 corresponding to an average delay value of 163, 188, and 213 ms respectively, given the negligible processing time demanded on a modern desktop computer [80]. An example of calculating the controller delay for using 7 votes in majority voting is shown in Equation (4.30).

$$D = \frac{1}{2}T_a + (\frac{n}{2})T_{new} + \tau = \frac{1}{2}\times 200 + (\frac{7}{2})\times 25 + \tau \approx 188 \text{ ms} \tag{4.30}$$

4.7 Final structure of the real-time hand gesture discrimination module

The proposed pattern recognition-based real-time hand gesture discrimination module is finally composed of five blocks: EMG activity detection using a moving average method, overlapped windowing segmentation, feature extraction (5 features), SVM classifier, and majority voting, as shown in Figure 4-3.

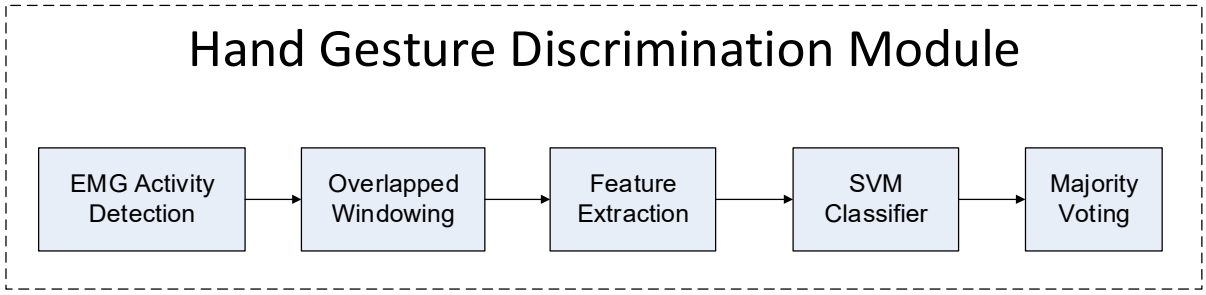

Figure 4-3. Block diagram of the real-time hand gesture discrimination module.

The activity detection for triggering the running of following function steps uses an amplitude-based method because of its computational efficiency. Once it detects targeting muscles on a rest state, all other functional blocks except activity detection, terminate execution to reduce computational consumption. Overlapped windowing segmentation combined with majority voting is conducive to using more information in a longer data window, but at the same time generates an acceptable delay and smooths the output decision stream. The feature set consists of EMG features mainly from the time domain for low computational demand, low dimension, and in turn, the elimination of dimension reduction. The SVM classifier is utilised in real-time application because of better robustness and the convenience of the LIBSVM C/C++ library.

Chapter 5
EMG-driven robotic hand construction and control system design

The EMG acquisition and hand gesture discrimination methods proposed in previous chapters can be used to build a novel human-machine interface—a myoelectric control system that can be used for various applications. Without a physical testing device, the performance of the myoelectric control system can merely be evaluated using those criteria, such as the offline classification accuracy and online virtual prosthesis control, that are unable to consider the coupling influence with output devices. However, many factors from the combination with output equipment, such as weight and inertia, have a significant impact on the controllability and reliability of the entire system. Therefore, a physical device, which is close to a practical application, is needed for the evaluation of the myoelectric control method.

Among available options, a robotic hand is a suitable choice of output equipment for myoelectric control since the human hand gestures and the corresponding robotic hand responses can be directly compared visually. Robotic hand design has a long history. Various robotic hands, ranging from the simplest robotic manipulators used in an industrial environment to the one as complex as a dexterous anthropomorphic hand, have been developed for the purposes of industrial task, tele-manipulation, prosthesis, or domestic service [121]. The industrial manipulators largely focus on the customised end effectors that are capable of autonomously performing specific manufacturing and handling tasks. They have greatly increased productivity, but lack the ability of performing general object manipulation. Inspired by the dexterity and versatility of the human hand, however, an anthropomorphic multi-fingered robotic hand is likely to be applied to applications beyond mass production, such as a compact yet fully functional prosthetic hand used by an amputee in everyday life, and a complex tele-manipulator used by an operator in health or dangerous or other remote applications [169]. Therefore, it was decided to develop an anthropomorphic robotic hand for myoelectric control validation in this research.

Issues relevant to the development of dexterous robot hands generally include kinematics, mechanisms, actuation, sensing etc. This chapter presents the development of an anthropomorphic robotic hand driven by biosignal control. The design work started with the palm and finger structure construction of

the robotic hand, followed by the development of an actuation and transmission system based on the analysis of available approaches for robotic finger movement. Then, a robotic hand controller was designed with feedback using electric current and position sensing techniques. A prototype physical anthropomorphic robotic hand was finally built.

5.1 Anthropomorphic robotic hand design

One of the early aims of robotic hand design was for disabled people. This is why prosthetics is one of the most important application areas of robotic hands. Despite the desire for dexterity in prosthetics, the most commonly used prosthetic hand is still a mechanically controlled hook-like prosthesis as shown in Figure 5-1, a design dating from over a century ago. It is quite possible that such a design surviving until now is because of the relatively higher effectiveness, robustness and simplicity of the prosthetic hook. However, the hook-like prosthesis brings patient convenience at the cost of a conspicuous stigma, and thus is undesirable in some circumstances. In addition, multifunction and dexterity are always desired for a robotic hand. Human hand structure and functionality are the result of a long evolutionary period involving the use of tools. The human hand is therefore the best source to imitate the human-like grasp and manipulation capability. Moreover, the target objects being grasped or manipulated by prosthetic hands in daily life are usually made for use by human beings. Although a hook-like hand, or a hand with three digits, is able to perform basic grasp tasks, one or two extra fingers can provide supplemental stability and flexibility. Therefore, most of the developmental effort for multifunctional terminal devices has been towards creating fully anthropomorphic hands [122]. This means that the robotic hand will possess five digits and the shape, size and mass of this device need to be constructed as similar to a natural human hand as possible. The development of an anthropomorphic robotic hand with five fingers was thus the choice of this research.

Figure 5-1. A body-powered prosthetic hook.

As described in Section 2.3.2, the human hand skeletal structure is composed of the palm and five digits—four fingers and a thumb. The palm and digits are further constituted by separate bones or phalanges. Using contemporary technologies and materials, however, it is hard to build a robotic hand

that is thoroughly same as the human hand. Therefore, for simplicity, the robotic hand was built using different strategies for palm and digit design.

5.1.1 Robotic hand palm design

The human palm is composed of thirteen bones including eight carpals and five metacarpals, providing a base to hold the fingers. It is impossible to completely mimic the anatomical structure of the human palm for an artificial hand. Anthropomorphism in robotic hand palm design largely means an imitation of the shape and dimensions of the human palm.

The palm is a vital part of the human hand. It offers an articular surface to share forces with fingers, constituting one of the three distinctive force-sharing pairs identified in object grasping. The other two force-sharing pairs are between the pads of the fingers and the thumb, and between the thumb and the side of the index finger respectively. Studies also reveal that the foldable palm, along with the human thumb, contribute to making oblique arches that help to stabilise orientations and positions of the fingers during in-hand object manipulation [119].

For the sake of an aesthetic purpose, an anthropomorphic palm with the same shape as the human one would be the better choice to mimic human hand structure and link with the fingers. To obtain a real human hand shape, a 3D laser scanner can be used to scan a human hand and import the geometric data into a CAD system to establish a model of the palm.

In this research, an existing 3D scanned human right hand palm model in the STL format downloaded from the internet [223], as shown in Figure 5-2, was utilised as the origin of work. This model is permitted under a license that allows free sharing and adaptation for any purpose.

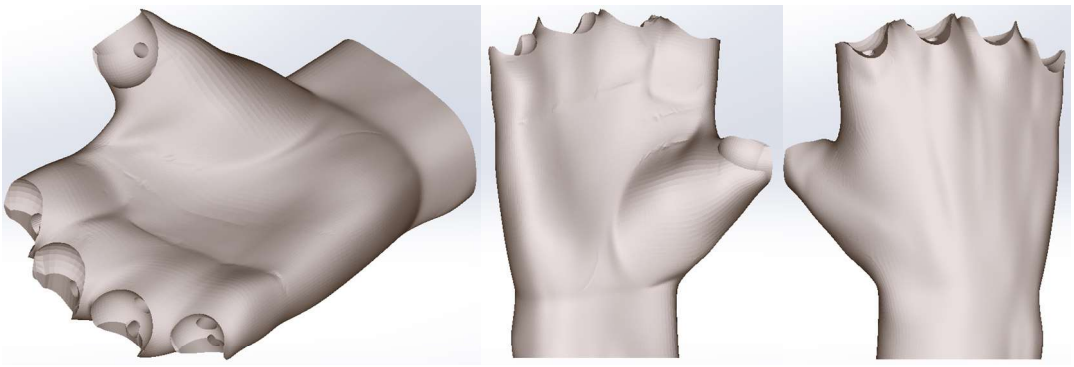

Figure 5-2. The STL model of a right human hand palm in the (a) isometric view; (b) front view, (c) back view.

Through the investigation on the available materials and corresponding manufacturing technologies, additive manufacturing, also known as 3D printing process, was identified as the suitable way to produce the prototype because of the advantages stated in Section 2.3.5. The final decision of this

research was made to use FDM 3D printing in ABS plastic for construction of the hand architecture. The process to create objects with an FDM printer starts from building computer-aided design (CAD) files. These CAD files must then be converted to a format that a 3D printer can understand, usually the STL format, before an object can be printed.

The first step of 3D printing is to build the 3D model of a target object in a specific software program. SolidWorks® (Dassault Systems SolidWorks Corporation) is a popular CAD system used in industry and educational organisations and was used for hand modelling in this research. SolidWorks is a parametric CAD modelling tool with both solid and surface modelling capability. The underlying technology of its surface modelling is based on non-uniform rational b-spline (NURBS). NURBS modelling is great at combining shapes via Boolean and feature operations, as well as at refining shapes with operations such as filleting, blending and face editing [224]. However, it is not the best choice to create 3D models such as a human palm with irregular curved surfaces.

There are other alternative technologies to NURBS surface modelling, i.e. T-splines, subdivision surfaces, and polygon meshes. The strength of subdivision (Sub-D) modelling is at producing and modifying complex freeform or organic shapes with smooth surfaces, which is the weakness of NURBS modelling. Power Surfacing is a plugin product that adds Sub-D modelling capability to SolidWorks in addition to its native NURBS modelling paradigm. The demo version of Power Surfacing can be downloaded from the website www.npowersoftware.com. Being able to use both modelling paradigms together in the modelling process provides huge productivity advantages in both the design and revision process.

Starting from the palm STL file imported as a reference mesh, reverse engineering work was conducted by using PowerSurfacing RE tools to convert the STL file to a revisable 3D solid palm CAD model. Resurfacing an existing model by using quad-based subdivisions (Sub-Ds) is the method of choice to reverse engineer non-mechanical freeform or organic shapes in Power Surfacing RE. The resurfacing procedure of the palm STL mesh was done as follows:

- Import the palm STL file as a reference mesh;
- Create the new Sub-Ds on top of the palm mesh;
- Interpolate to maintain the reference mesh details;
- Convert the result to CAD.

Figure 5-3 shows the Sub-Ds created on the top of the STL reference mesh after the second step. Figure 5-4 is the final 3D CAD model revisable in the SolidWorks history tree, which can be modified for further functional usage such as cutting the palm into a few parts, and digging a housing cavity to mount actuators or other mechanisms inside the palm that are able to be assembled from these separated parts or units.

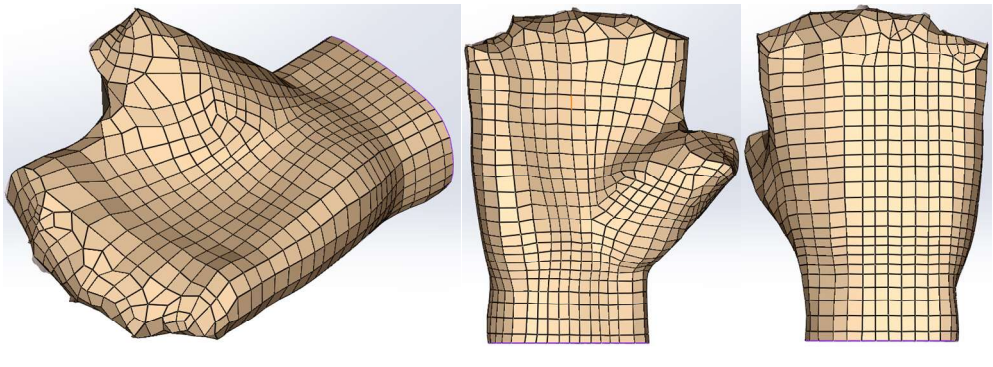

(a) (b) (c)

Figure 5-3. The Sub-Ds on the top of the STL reference in the (a) isometric view; (b) front view, (c) back view.

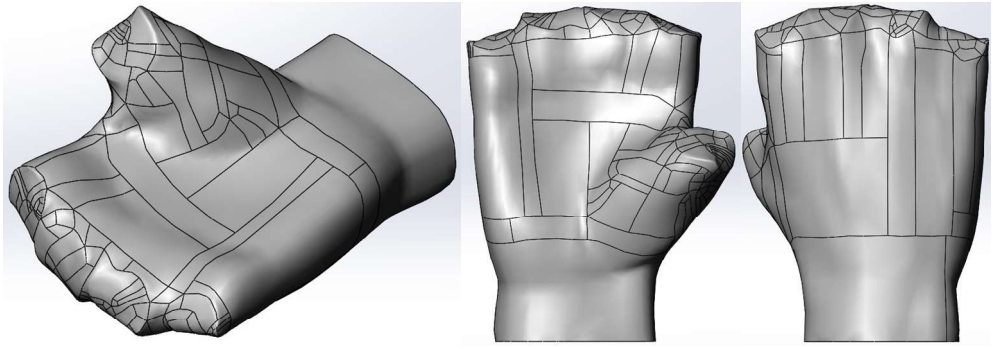

(a) (b) (c)

Figure 5-4. The 3D CAD model of the palm in the (a) isometric view; (b) front view, (c) back view.

5.1.2 Digit design

To study and resemble the human hand kinematics, an effective method is to imitate its natural anatomical structure. Besides an anthropomorphic palm design coming from a 3D scanned human hand, all digits of the robotic hand, i.e. the four fingers and thumb, need to be designed with an anthropometric size and anthropomorphic shape to mimic human finger movement as close as possible.

5.1.2.1 Finger design

Each of the four human fingers is designed by following the three intercalated bony segments, i.e. the proximal, middle, and distal phalanges. These three phalanges along with the metacarpal bones create the metacarpophalangeal (MCP), proximal interphalangeal (PIP) and distal interphalangeal (DIP) joints from the proximal to the distal end in order.

The fingers of the robotic hand were designed referencing the dimensions related to the index finger obtained from [125], as shown in Table 5-1 and Table 5-2. The whole data set describing the kinematics of the human hand is available in [225].

Table 5-1. Phalangeal length estimates

Phalange	Length (mm)
Proximal	44.8
Middle	26.2
Distal	17.7

Table 5-2. Phalangeal depth and breadth estimates

Joint	Depth (mm)	Breadth (mm)
MCP	22.3	19.8
PIP	16.0	17.4
DIP	13.5	16.0

Since the joint contacting surface is composed of the convex and concave topologies of bone extremities, the human finger joint can be regarded as a ball-type joint, which can have a 6 degrees of freedom motion in space. However, the muscles, tendons and ligaments that span the finger joints introduce constraints to the range of motion, resulting in simplified kinematic models that can be replicated using common mechanical components. A universal joint is usually used to realise the 2 degrees of freedom (DoFs) motion of abduction/adduction and flexion/extension for the MCP joints, while a hinge joint, also called a pin joint or revolute joint, is an appropriate choice for the 1 degree of freedom (DoF) flexion/extension of the PIP and DIP joints.

A single pin joint structure along the flexion/extension axis was implemented for all finger PIP and DIP joints in this research. Although a universal joint can offer more flexibility to the artificial finger MCP joints, the same single pin joint structure as the PIP and DIP joints was used in MCP joint design for simplicity. The fingers' 3D models were built in SolidWorks. Figure 5-5 shows the assembly 3D model of the index finger without a fingertip.

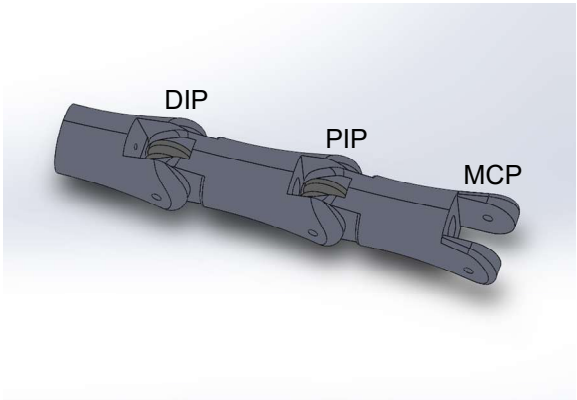

Figure 5-5. The 3D model of the index finger.

5.1.2.2 Thumb design

The human thumb has two phalanges and one metacarpal bone forming three joints, i.e. the carpometacarpal (CMC), metacarpophalangeal (MCP), and interphalangeal (IP) joints. It has the ability of performing more complicated movements than the other four fingers. Research on human hand movement indicates that the opposable thumb is the key point of performing most everyday life grasping and manipulation functions [119, 226].

In most of the anthropomorphic artificial hand mechanical designs reported in literature, the thumb is actuated along thumb flexion and circumduction rotation axes. The circumduction rotation of the thumb is to alternate between a lateral grasp and a power or precision grasp. By angling the axis properly, however, the two rotation axes can be jointly approximated in a single DoF, i.e. a single joint axis [110]. This can be conducive to achieving desired thumb functional movements while still keeping complexity low.

In this research, the robotic hand thumb was implemented with IP and MCP joints and both of them have only 1 DoF around the flexion/extension axis. The thumb base that corresponds to the human thumb metacarpal bone was mounted in a fixed offset angle to the palm plane for the resemblance of the opposable thumb. Figure 5-6 shows the final 3D hand assembly model and the 3D printed and fabricated robotic hand including the palm and all digits.

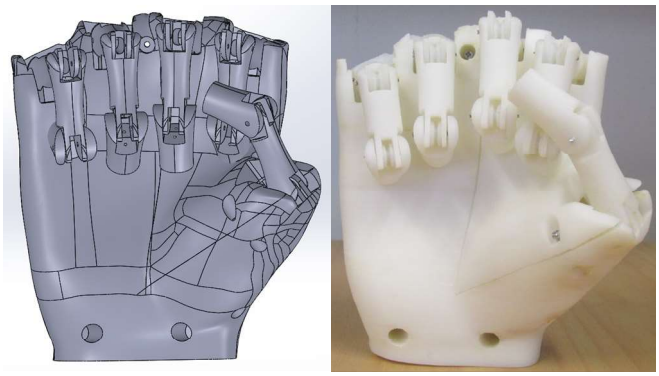

Figure 5-6. The proposed robotic hand (a) the 3D assembly model; (b) the printed and fabricated robotic hand.

5.2 Actuation and transmission design

The design of a proper actuation and transmission system is regarded as one of the most critical and challenging issues in the mechanical design of an articulated robotic hand. It is especially crucial when considering the installation of pertinent mechanisms and components into a small space with constrained and limited dimensions.

Fundamental issues in relation to the mechanical design of actuation and transmission for an artificial hand generally include:

- the type of actuators
- the actuation architecture or the level of actuation, i.e. the number of directly or indirectly driven joints and the organisation of the actuators
- the location of the actuators
- the type of transmission systems

In following sections, the issues pertaining to the development of an effective actuation and transmission system for the proposed anthropomorphic robotic hand will be discussed in detail.

5.2.1 Actuator selection

The functionality of an actuator is to convert energy from an input modality such as electricity or chemical fuel into a useful mechanical motion to deliver work in a certain amount of time according to a signal or stimulus in a controllable manner [227]. Selecting actuators is currently no trivial task, given the diversity of actuation technologies and the large amount of actuators with different configurations available. A series of studies have developed and recommended actuator selection and evaluation methods to accommodate task requirements [227-230]. To develop an actuator selection method, the ways that actuators may be categorised are first considered. One of the most common approaches is to classify actuators according to the working principles. Generally speaking, two categories, i.e. the conventional and non-conventional types, of actuators can be found in artificial hand applications reported in literature. The former includes electromagnetic motors, hydraulic, and pneumatic actuators, whereas the latter consists of shape memory alloy (SMA) actuators, ultrasonic motors (USM), pneumatic artificial muscles (PAM), and flexible fluidic actuators (FFA) [230, 231]. Recently emerging materials have provided the possibility of the promising human muscle-like linear actuators, e.g. the ionic polymer metal composite (IPMC) artificial muscle [53]. Among all these available options, SMA actuators and electromagnetic motors are representative of the two categories of actuators, hence being examined in the following sections for making use of one of them to deliver the energy conversion.

5.2.1.1 Shape memory alloy (SMA) actuator

Aiming at developing an anthropomorphic hand, the biological muscle-like non-conventional actuators were the first to be investigated in this research. The SMAs and the EAPs are two types of the most common artificial muscles. Despite the attractive features that the EAPs can offer, the EAP actuators are the least developed technology and their application is still in a premature stage. Therefore, only the SMA actuators were researched in detail for their applicability in the proposed artificial hand.

Since the 1980s, SMA actuators have been used in robotics. Examples can be found in [125, 146, 151, 167, 169, 231-233]. In the development of artificial hands, the advantages and limitations of SMA actuators can be summarised below.

Advantages:

- direct-drive configuration, eliminating the demand for complex transmission systems
- a high power to weight ratio, leading to the design of compact, lightweight systems
- silent operation because only using phase transformation for actuation

Limitations:

- activation is relatively fast but relaxation governed by the cooling rate of the SMA wire which is a passive process dependent on external heat transfer parameters, limiting the actuator bandwidth
- limited life cycle
- low efficiency
- nonlinear operation due to hysteretic behaviour
- low actuation strains

To better understand the characteristics of SMA actuators, an SMA-based artificial muscle, BMX150 from TOKI Corporation, was tested in the Mechatronics Laboratory of Massey University for developing biomimetic prosthetic fingers [234]. BMX150 elongates at room temperature and contracts to its original length when an electrical current is fed through it. The details about BMX150 are attached in appendices. As BMX150 is a micro coil-type linear actuator with a wire diameter of 0.15 millimetres and a coil diameter of 0.62 millimetres, it can produce a small practical force only up to 30 gram-force, which is not large enough for the use in the robotic hand application of this research. In addition, compared to conventional electric motors, the high cost of BMX150 is another concern that may prevent its use in low-cost robotic hand systems, such as the one developed in this research.

Given the shortcomings of SMAs outweighing the advantages they can provide, SMA actuators were regarded as an undesirable solution in the robotic hand development of this thesis. Instead of SMAs, conventional electric motors were investigated for their feasibility in providing actuation to robotic finger movements.

5.2.1.2 Electrical motor

Electrical motors, hydraulic and pneumatic actuators have long been power sources, thus being considered conventional actuators. In prosthetics today, the most common choice of externally-powered actuators is the electrical direct current (DC) motor, mainly due to its practicality. An example of its practicality is the easily rechargeable energy source, the batteries, for DC motors. This advantage has

increased over recent decades in the wake of the continuous advance of technology. With increased capacity and peak power output from batteries, miniature DC motors are lightweight and small-sized and can be housed inside the artificial hand or forearm, whereas other alternative actuation technologies remain less practical. The functionality of electric motors can be enhanced by using various mechanisms. Gearing may be needed in order to reduce the speed and increase the output torque from motors. Non-backdriveable or locking mechanisms can be employed to maintain grip on an object without motors continuously drawing current from the battery and creating heat [109, 110, 154].

There are also drawbacks with motors, one being that electrical motors are most efficient with rotation at a constant rate and maintaining one direction. However, frequent or repeated start and stop, and slow motion are more often found in biological systems. Hence a motor is not the best choice from the perspective of efficiency in a biological sense [122]. Another known issue related to permanent magnet DC motors is the cogging torque, which manifests torque and speed ripples at very low speeds. The effect of cogging torque can result in jerky finger motions and finger position errors, especially during low speed operations. A method to reduce the effect of cogging torques is known as magnet step skewing [128, 235].

Taking into account all considerations such as availability, cost, easiness and feasibility, the electrical motor becomes most practical and in turn the most preferable solution in this research. The low cost micro high power brushed DC motor with a 298:1 metal gearbox and an extended motor shaft from Pololu Corporation, as shown in Figure 5-7, was selected to provide actuation for moving mechanisms of the proposed robotic hand.

Figure 5-7. The micro high power brushed DC motor with a 298:1 metal gearbox and an extended motor shaft.

At the rated voltage 6 V, the motor can output a torque up to 5 kg•cm with a 1.6 A current at stall, and a speed 100 RPM by a 120 mA current with no load. Considering the constrained space for housing motors, a total of three motors were mounted inside the hand cavity, one of them for the thumb, another for the index and middle fingers, and the remaining one for the ring and little fingers. The micro DC motor can be fixed in position by using mounting bracket as shown in Figure 5-8.

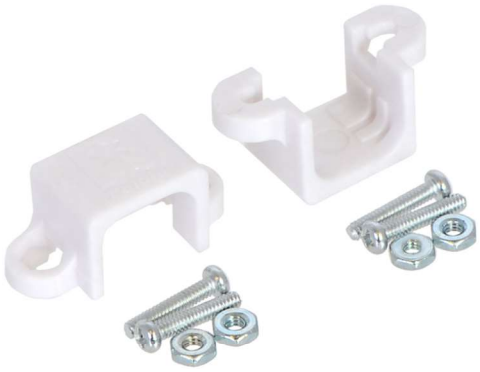

Figure 5-8. The motor mounting bracket.

5.2.2 Actuation architecture

For a hand with *m* actuators and *n* joints, the three alternative implementation schemes of the actuation architecture include:

- The underactuated approach ($m<n$) where some joints are passive, or kinematically coupled in a fixed or variable way to a controlled joint;
- The fully-actuated approach ($m = n$) where each joint has its own actuator;
- The overactuated approach ($m>n$) where more than one actuator acts on a joint [230].

A redundant actuation mechanism is neither necessary nor desired in development [118]. Therefore, only fully-actuated or underactuated methods can usually be found in literature. Most commercially available prosthetic hands have used fully-actuated finger designs, such as Vincent (Vincent Systems), iLimb and iLimb Pulse (Touch Bionics), Bebionic v2 and Bebionic (RSL Steeper), and Michelangelo (Otto Bock), mentioned in Chapter 2. The finger joints of these hands are actuated neither independently nor in an underactuated and compliant manner, but they have a fixed movement relative to each other. A mechanism in a similar form to the four-bar linkage described in Chapter 2 but distinct for each of these hands, is used to couple the motion of the PIP to the motion of the MCP joint, defining the fixed relationship between the joint motions.

Despite the usefulness of the fully-actuated methodology, building fully-actuated multi-finger hands requires multiple actuators, one for each degree of freedom. This would lead to a design with increased complexity, weight and cost. A probable solution is to reduce the degree of freedom while keeping essential hand functions. This is implemented by the six commercial hands aforementioned. Five of them were designed with two joints for each finger, unlike the human one with three joints, whereas the remaining one, the Michelangelo (Otto Bock) hand, has only one joint for each finger.

Another solution to reducing actuator numbers is the use of the underactuated approach, i.e. using less actuators than the degrees of freedom. An extra benefit in addition to actuator quantity reduction is that, when applied to artificial hands, the underactuated mechanisms lead to an adaptive grasp of the finger

to accommodate to the shape of the target object, in a manner closer to the human grasping than the independent actuation solution [136, 156]. Compared with rigidly linked hands, underactuated adaptive fingers can interact with the grasped object over more locations and thereby distribute the grasping force on more contact points, leading to the joint torques comparable with the joint torques of human hands. They can also adapt to various grasp patterns for the same number of actuators [110, 119].

The concept of underactuation presented in robotic systems usually means a manipulator with one or more unactuated joints. Different from this, however, underactuation in robotic fingers is usually implemented by using elastic or passive elements, e.g. springs and mechanical limits, to kinematically constrain the finger and ensure the shape adaptation of the finger to the grasped object [133, 139]. It is more suitable to consider the joints of underactuated fingers uncontrollable or passively driven rather than unactuated. The actuation is transmitted to joints through proper mechanical design, e.g. four-bar linkages, pulley-tendons, and gears, in which the elastic or passive elements are incorporated. The equivalence between the four-bar linkages, pulley-tendons, and gears has been proven in [139]. The tendon-pulley actuation may be preferable than linkage actuation due to suffering less from mechanical singular configurations, but it may leads to smaller forces applied with tendons than with linkages.

In this research, the underactuated method became the choice to build the actuation and transmission system for the proposed hand, given the advantage of the underactuated approach along with the constrained space for electrical motor mounting.

5.2.3 Transmission design

As described in previous sections, the proposed hand has a total of 14 degrees of freedom, 3 for each of four fingers and 2 for the thumb. The actuation system was decided to use 3 brushed electrical DC motors. This results in a highly underactuated hand, 14 degrees of freedom (DoFs) versus 3 degrees of actuation (DoAs). Therefore, an effective transmission system is critical for the proposed robotic hand.

The transmission system in robotic hand design can be roughly categorised into two parts according to functionality, the main transmission that deliver forces or torques from the power sources to active joints, and the mechanism that couple passive joints to active joints. Of the thirty-six robotic hand projects reviewed in [230], the majority utilise gears or tendons for the main transmission, while the most common methods for the coupling mechanism include rigid linkages, tendon-pulleys, and tendon-pulley-springs. The article [128] and [110] also list some examples of robotic hands driven by gears or tendons. Considering the constraints on construction, especially the limited space for installation, the methods to build a transmission system using tendons, pulleys and springs were scrutinised. On this basis, the transmission mechanism for joint movement of the proposed robotic hand was created.

5.2.3.1 Tendon transmission

The human hand movements are controlled by two types of muscles, the intrinsic muscles located in the palm, and the extrinsic muscles located in the forearm. As with the anatomy of the index finger demonstrated in Figure 2-13, muscle contractions are transmitted to fingers through long tendons that pass over the joints and terminate at the insertion points on the finger bones, resulting in hand movement and force generation. The tendons are restricted by sheaths (biologically called retinacula) that act as pulleys and maintain a moment arm from the joint axis [169]. The tension of a small displacement in the tendons can induce a moment to actuate the joint. Similarly, actuators can be placed remotely from the fingers or the hand by using tendon transmission in robotic hand design. The use of tendon sheaths can also reduce interference between the transmission medium and the work envelope. In addition to the imitation of the human anatomy, tendon-driven transmission can simplify control by providing zero-backlash compliant transmission [120]. Additional advantages for tendon transmission systems are low inertia, low friction, high flexibility, and low cost.

Tendon-based transmission is an appropriate solution for the proposed robotic hand, considering the advantages of the tendon-driven system and the inspiration from human hand anatomy. Both tendon-pulley and tendon-sheath transmission can be found in literature. However, a tendon-sheath transmission mechanism, where cables running in synovial sheaths, channels or tunnels work as the Bowden cable [143, 236], may suffer more from friction, requiring more analytical efforts on friction and its compensation [159, 160]. Therefore, tendon-pulley transmission was the preferable option in this research.

5.2.3.2 Tendon configuration

As described in Chapter 2, tendon systems can be classified into three types according to the number of tendons per joint:

- n-tendon system, including unidirectional and bidirectional configuration;
- 2n-tendon system;
- (n+1)-tendon system.

All 2n-tendon and (n+1)-tendon systems are bidirectional. One of the advantages of the bidirectional tendon configuration is that full kinematic controllability can be obtained by incorporating it for a finger with only one joint. Different from bidirectional tendon systems, the unidirectional n-tendon configuration needs to use passive springs to provide reverse forces. Either parallel or series springs can be utilised for this purpose. Compared to the unidirectional tendon configuration, the bidirectional tendon configuration can eliminate the demand for parallel or series springs, thus being able to generate greater maximum grasp forces.

In this research, the bidirectional n-tendon configuration was used to implement transmission for all five digits due to its least use of tendons and better controllability. The flexion tendon and the extension tendon are wound on two pulleys that are mounted onto the same motor output shaft, but in the opposite winding directions.

5.2.3.3 Tendon transmission for inter-phalange underactuation

There are two types of underactuation in the proposed robotic hand, i.e. the inter-phalange underactuation within a finger because of the multiple joints driven by one motor, and the inter-finger underactuation between fingers due to motor sharing between two pairs of digits (the pair of the index and middle fingers, and the pair of the ring and little fingers for the proposed robotic hand design).

The proposed robotic hand implements a connected differential mechanism, the soft gripper mechanism [138, 140-142] as shown in Figure 2-21, sometimes called moment isotropy [143, 144], to resolve inter-phalange underactuation. In this mechanism, links that represent finger phalanges are connected with joints in series. Pulleys which can freely rotate around the joint are mounted on these joint axes. A tendon is fixed on the distal link tip at one end and then wound around pulleys mounted on every joint in the same winding direction, extending to the proximal end of the finger. When pulling the proximal end of the tendon, a torque proportional to the radius of the pulley at a joint is applied to the joint, causing the link rotation around the joint axis. In this way, the traction of tendons is transferred to the torques of all the joints. An advantage of this mechanism is that it only introduces a small degree of friction, especially when the pulleys are supported by miniature ball bearings, since the mechanism only consists of rotational motion and doesn't include any sliding motion.

The pulleys of the soft gripper mechanism play two roles. One drives the rotational motion of the phalanges with their proximal end mounted on the same joint as the driving pulley, and the other rotates freely around the joint axis and delivers tension along the tendon after the phalanges have conformed to the grasped object. Since the rotational friction of pulleys is negligible, all forces can be regarded as equivalent.

According to the theory of belt friction in the statics of engineering mechanics, the relationship between the forces on two sides of a driven pulley can be determined by Equation (5.1).

$$\frac{T_1}{T_2} = e^{\mu\theta} \tag{5.1}$$

where

T_1 = Force in the belt on the tight side,
T_2 = Force in the belt on the slack side,
μ = Coefficient of friction,

θ = Angle of contact in radians, i.e. the angle subtended by the arc formed by the tendon segment that contacts the surface of the driven pulley.

In the soft gripper mechanism, the tendon is wound around every pulley by at least one circle in the configuration of Figure 2-22 (a). This means that the smallest value of θ is 2π in this configuration. The typical static friction coefficient between polythene and steel is 0.2.

$$T_1 = T_2 \times e^{\mu\theta} = T_2 \times e^{0.2\times 2\times\pi} \approx 3.5 \times T_2$$
$$\text{The static friction force} = T_1 - T_2 \approx 0.71 \times T_1 \quad (5.2)$$

Therefore, the torque produced by the static friction force between the tendon and the pulley groove surface would be much greater than the torque caused by the rotational friction force between the contact surfaces of the pulley and the pin joint, especially when supporting the pulleys using miniature ball bearings. This eliminates the slipping motion between the tendons and pulleys, only allowing for rotational motion for both pulleys and phalanges around joint axes.

When the soft gripper mechanism is applied to the bidirectional tendon configuration, two groups of pulleys are necessary, one for flexion and the other for extension. This might lead to a bulky and clumsy design unsuitable to the limited space. Therefore, a modified mechanism from the soft gripper mechanism, as shown in Figure 5-9, is used for the proposed robotic hand in this research.

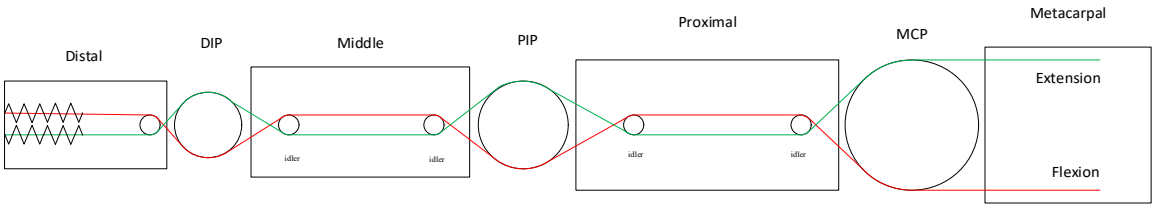

Figure 5-9. Tendon routing configuration.

The bidirectional tendon configuration in this research uses two tendons that are routed in a symmetrical manner along phalanges as in Figure 5-9, where the tendon in the red colour is for flexion and the tendon in the green colour is for extension. The pins between the adjacent two joints are used as idlers to guide and tension the tendon. The first version of tendon routing design in this research did not employ the idlers between joints, leading to unmatched tendon path lengths for flexion and extension. This in turn caused tendon tension loss at the side of the slave driving pulley that was mounted on the same motor output shaft as the master driving pulley. The roles of these two driving pulleys alternate for flexion and extension.

The desired finger motion is a cascading joint movement pattern, as in the movement of the human finger. This means the MCP joint moves first, followed by the PIP and then DIP joint. This cascading joint movement pattern can be achieved by designing pulleys at these three joints with different radii,

i.e. the MCP joint with the largest radius and the DIP joint with the smallest one [112]. Calculated by using the equation $\tau = rf$, the torque acting at the MCP joint will greater than at other joints even when not considering the loss of tendon force induced by pulley friction, causing the MCP joint to rotate first. Then the PIP and DIP joint rotate in the expected sequence based on the same principle.

5.2.3.4 Tendon transmission for inter-finger underactuation

The inter-finger underactuation is achieved by using a compliantly coupled differential mechanism. The mechanism coming from [145], as shown in Figure 2-23, uses a linear slider to pull or release three tendons by means of three compression springs, thus obtaining adaptive grasp via the adoption of the compression springs.

Instead of using compression springs at the proximal end, the proposed robotic hand finger employs compression springs at the distal end for inter-finger underactuation, as shown in Figure 5-9. At the same time, the compression springs maintain a pre-tension on the tendons and eliminate backlash by imposing series elasticity. A simplified schematic is depicted in Figure 5-10.

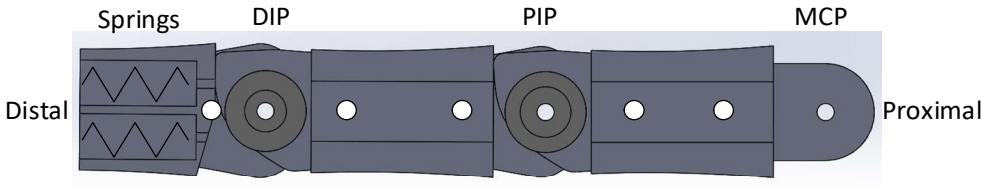

Figure 5-10. Schematic of compliantly coupled differential mechanism.

A simplified system using one electrical motor to actuate two fingers was built for verifying the design concept, as shown in Figure 5-11. This system showed the feasibility and effectiveness of the proposed tendon-pulley underactuation transmission mechanism.

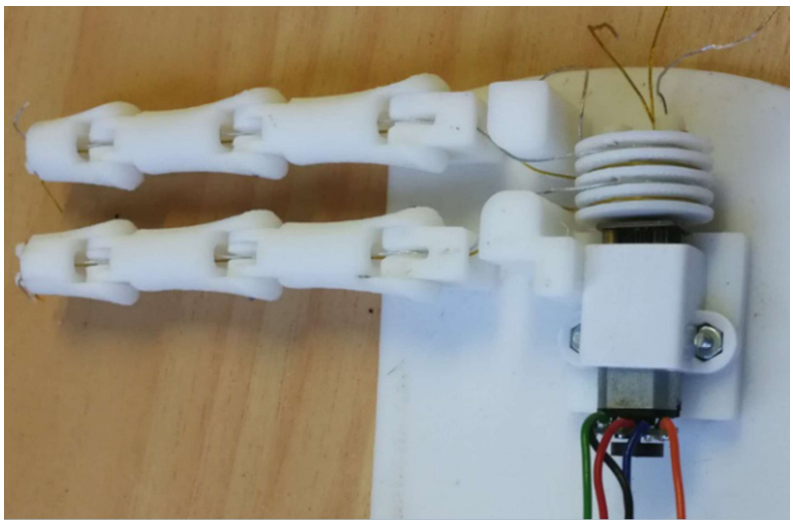

Figure 5-11. The underactuated tendon-pulley mechanism.

5.3 Sensory system and control

Once the user's hand moving intention is deciphered by the hand gesture discrimination module described in previous chapter, a device controller is necessary to convert the intention to device control commands, according to the specific configuration of the motor driving scheme. To perform grasping or manipulation reactively to the environment, a control scheme that can act according to real-time feedback is needed. This means the device controller will yield specified action commands based on the feedback information from a certain types of sensors. The parameters acquired from these sensors, about position, torque, pressure, temperature, or shape, reveal the state the targeted object is holding. As mentioned in the literature review chapter, both direct and indirect sensing approaches are useful for control variable measurement. The advantage of the indirect method is based on its simplicity and convenience to implement.

A control scheme, where two of the most common feedback measurements—position and torque—are measured indirectly, is implemented in this research. The block diagram of the control unit is illustrated in Figure 5-12.

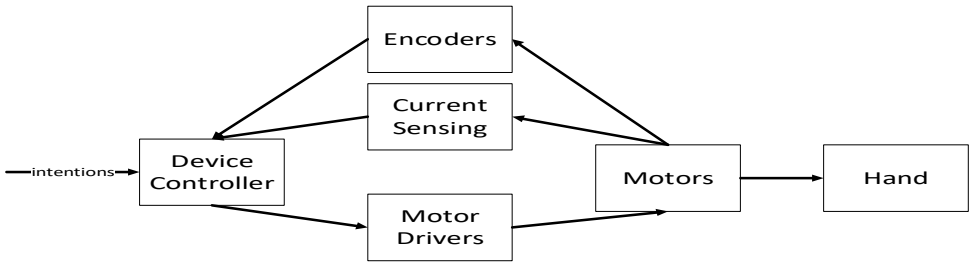

Figure 5-12. The hand control unit diagram.

5.3.1 Motor driver

The rotational direction and speed of the motor are controlled by adjusting the current through it. This is usually achieved by feeding a pulse-width modulated (PWM) voltage across the motor using an H-bridge circuit. There can be various solutions for the motor driver circuitry at different integration levels, e.g. a microcontroller directly coupled with an integrated H-bridge such as NJM2670; a microcontroller working with an integrated monolithic motor driver such as TB6612FNG; or a microcontroller working with an H-bridge PWM motor driver that features current-control PWM circuitry such as DRV8829. A higher integration level may be able to considerably reduce the burden on the microcontroller and the workload of control logic implementation.

In this research, a compact motor controller board, the Pololu Qik 2s9v1 Dual Serial Motor Controller as shown in Figure 5-13, was selected for its convenience. This motor controller can receive motor movement commands from a microcontroller through an UART module to drive two small, brushed DC motors with full direction and speed control. A total of two Pololu Qik 2s9v1 controllers were used for driving three brushed DC motors.

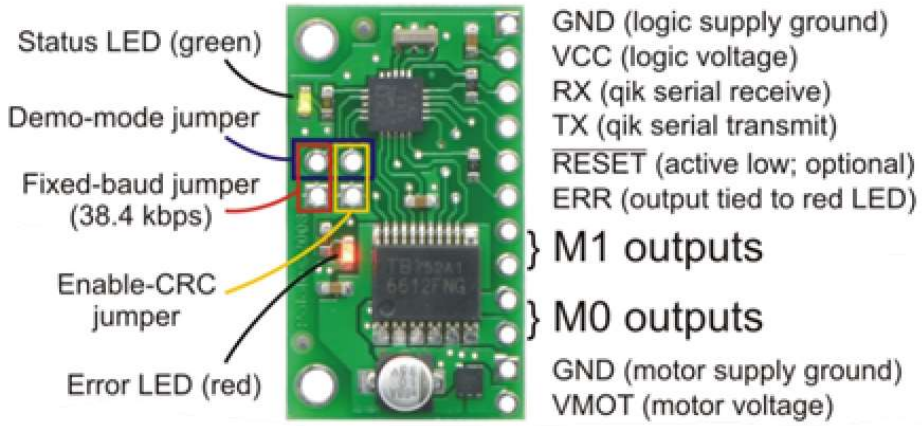

Figure 5-13. Pololu Qik 2s9v1 Dual Serial Motor Controller.

Main features of the Qik 2s9v1 include:

- simple bidirectional control of two DC brush motors
- logic-level, non-inverted, two-way serial control for easy connection to microcontrollers
- a robust, high-speed communication protocol with user-configurable error condition response
- optional automatic baud rate detection from 1200 bps to 38.4 kbps
- variable speeds achieved with 7-bit or 8-bit pulse width modulated (PWM) outputs at a frequency of 31.5 kHz, 15.7 kHz, 7.8 kHz, or 3.8 kHz

The highest achievable PWM frequency of 31.5 kHz is ultrasonic, which can result in quieter motor control at the expense of more power losses due to switching.

5.3.2 Torque sensing

The torque of motors was measured in an indirect manner, i.e. by sensing the electrical currents feeding through these motors. The actuation module of the proposed robotic hand is backdriveable, which helps torque control with current sensing. Also, these current values can serve as a measurement for protecting the motors from damage caused by overcurrent.

Current sensing is widely used in power electronic applications such as dc-to-dc power converters and adjustable-speed motor drives [237-239]. Most of the current measurement approaches can be classified as a resistive-based or an electromagnetic-based technique.

The most common method of resistive-based current sensing is to use an external sense resister (sometimes called shunt resistor) added in series with the motor to measure the current through it. The sense resistor functions as a current-to-voltage converter. The current is measured by sensing the voltage across the sensing resistor. Sense resistors are selected on the criteria related to accuracy, cost, voltage drop, power dissipation, efficiency, and parasitic inductance. The shunt resister current sensing method is widely used due to its low cost, simplicity and accuracy. The drawbacks of this technique are

associated with the power loss incurred by the sense resistor, the lack of measurement isolation from transient voltage potentials on the load, and the requirement for a noise filter to reduce the noise in the output signal.

Three options are available for current sensing according to where the sense resistor is placed:

- between the supply voltage and load (high-side current sensing),as shown in Figure 5-14 (a);
- between the load and ground (low-side current sensing), as shown in Figure 5-14 (b);
- on the motor (output current sensing), as shown in Figure 5-14 (c).

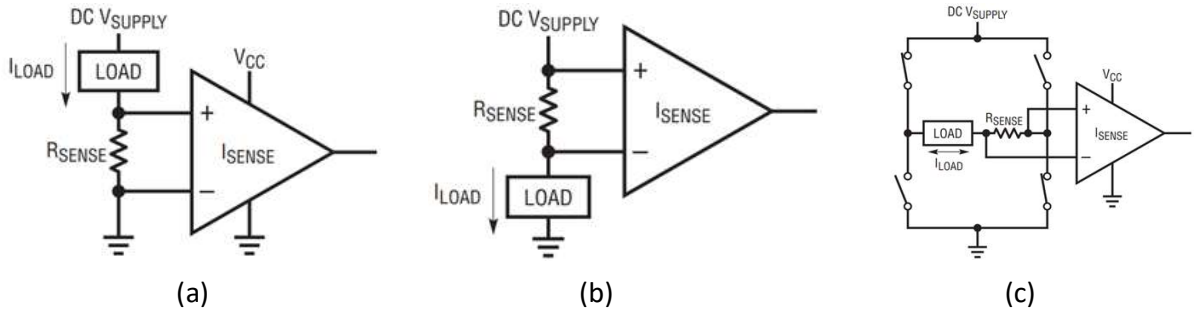

Figure 5-14. Current sensing configuration, (a) high-side current sensing, (b) low-side current sensing, (c) output current sensing.

The low-side approach is desirable with a near ground common-mode voltage. However, it lacks the diagnostic ability to detect high load current caused by short circuit, and adds extra resistance in the ground path, disturbing the system load's ground potential. High-side sensing is capable of detecting high load current caused by a short-to-ground fault but its input common mode voltage may be in excess of the load's power supply voltage, necessitating the use of amplifiers that allow for common-mode voltages outside their voltage supply range. Output current sensing is convenient for bidirectional sensing with only one sense resistor. The challenges for output current sensing are related to dealing with the input common-mode voltages that swing all the way from ground to the power supply voltage, and high frequency accuracy when used in PWM applications. This entails stringent performance constraints on the current-sense amplifier, i.e. a high range of input common-mode voltage and an excellent CMRR at the switching frequency and at its harmonics.

The voltage across the sense resistor can usually be measured by using differential amplifiers including operational amplifiers (op-amps), instrumentation amplifiers (IAs), difference amplifiers (DAs), and current shunt monitors (CSMs). However, the requirement of a high range input common-mode voltage excludes the use of op-amps and IAs that demand an input common-mode voltage within their power supplies, since only the output current sensing technique is available in this research due to the use of the Pololu Qik 2s9v1 Dual Serial Motor Controller that exposes only the H-bridge output pins to access.

A high-accuracy, wide common-mode range and bidirectional current shunt monitor, INA282, has become the final solution for the current sensing amplifier. INA 282 features a wide common-mode voltage range from –14V to +80V, which is independent of the supply voltage, a gain of 50V/V, and a CMRR of 140dB, making it an excellent candidate.

For making more accurate measurements, the current sensing solution of this research uses a 20 mΩ precision current sense resistor with Kelvin terminals (four wires) that uses separate pairs of current-carrying and voltage-sensing electrodes. Kelvin-connection, i.e. using short and balanced input traces, as shown in Figure 5-15, was also implemented between the sense resistor and INA282 input pins for PCB layout since parasitic resistances either in series with the sense resistor, or in series with the input pins of INA282, can induce measurement errors.

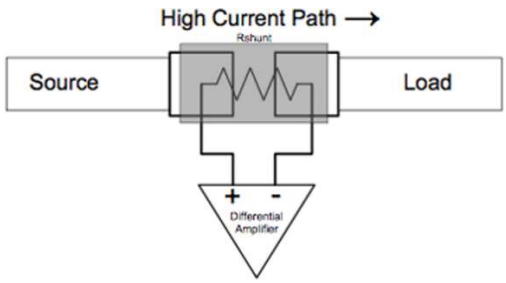

Figure 5-15. Kelvin-connection.

The torque and speed of a motor are dependent on the average current through it. A typical waveform of the motor current is depicted in Figure 5-16 if the motor torque and speed are controlled by using PWM.

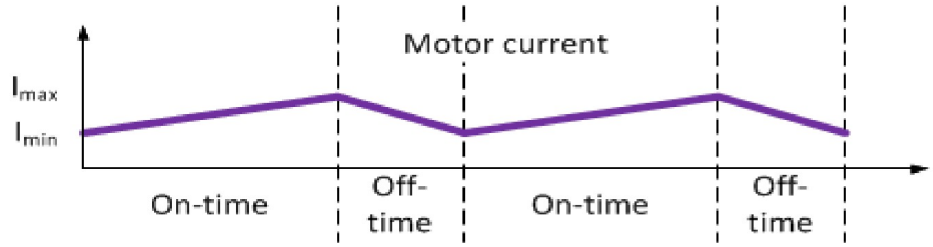

Figure 5-16. The motor current waveform of a PWM controlled motor.

The current mean can be obtained by using a first-order low-pass filter, provided that the filter's time constant τ is much longer than the PWM switching period T. For example, the output fluctuation in a PWM period will be limited in a range of 9.52% of the peak value when $\tau = 10T$. This can be explained below.

For a first-order linear time-invariant (LTI) system, the output response to a step input can be described by Equation (5.3).

$$V_{(t)} = V_0 e^{-t/\tau} + A\tau(1 - e^{-t/\tau}) \tag{5.3}$$

where

$V_{(t)}$ = output;
t = time (generally t > 0);
V_0= initial value;
τ = time constant;
A = step input amplitude.

Since

$$\begin{aligned} e^{-t/\tau} &= e^{-0.1} \approx 90.48\% \quad \text{when} \quad t = 0.1\tau \\ e^{-t/\tau} &= e^{-0.01} \approx 99.01\% \quad \text{when} \quad t = 0.01\tau \end{aligned} \tag{5.4}$$

as a first-order LTI system, the output fluctuation of the first-order filter can be regarded negligible in one PWM period, subject to $\tau \geq 10T$. The cut-off frequency of the first-order low-pass filter used to get the average current value must meet Equation (5.5). In addition, it is worth noticing that the selection of the low-pass filter cut-off frequency should retain the capability of reacting sensitively to the desired current changing.

$$f_c = \frac{1}{2\pi\tau} \leq \frac{1}{2\pi \bullet 10T} = \frac{1}{20\pi} f_{PWM} \qquad \text{IF } \tau \geq 10T \tag{5.5}$$

This research is inclined towards using the 31.5 kHz PWM frequency for quieter operation. Therefore, the low-pass filter should have a cut-off frequency

$$f_c \leq \frac{1}{20\pi} f_{PWM} = \frac{1}{20\pi} \times 31.5 \text{ kHz} = 501 \text{ Hz} \tag{5.6}$$

The first-order low-pass filter can be implemented by either analog or digital means. When using the digital option, a digital infinite-impulse-response (IIR) first-order low-pass filter in the form of $y_i = \alpha x_i + (1-\alpha) y_{i-1}$, or a simple moving average method can be used to calculate the average current value from measured samples. Instead of the simple moving average method, there is also a modified moving average method for reducing the overheads of computation [240]:

$$MA_i = MA_{i-1} + \frac{1}{n}(P_i - MA_{i-1}) \tag{5.7}$$

where

n = number of samples,

MA_i = current moving average value,

MA_{i-1} = previous moving average value,

P_i = current sample.

This research, however, prefers a first-order low-pass analog filter to average the current in order to lower the computational demand. This filter is composed of a 16 kΩ resistor and a 0.22 μF capacitor and its cut-off frequency is computed as:

$$f_c = \frac{1}{2\pi RC} = \frac{1}{2\pi \times 16\text{k}\Omega \times 0.22\mu\text{F}} = 45.2 \text{ Hz} \tag{5.8}$$

Current changing rates less than 45 Hz can be well detected, which is fast enough considering the mechanical inertial property of the Pololu brushed DC motor.

5.3.3 Position sensing

As with torque sensing, position sensing was also carried out indirectly for simplicity in this research. The revolution numbers measured by using motor encoders were used to represent the finger positions. A quadrature motor encoder from Pololu using a magnetic disc and two Hall Effect sensors, as shown in Figure 5-17, was attached to a brushed DC motor, providing 12 counts per revolution of the motor shaft.

Figure 5-17. The magnetic encoder from Pololu attached to a Pololu brushed DC motor.

Since the motor rotation direction is controlled by the device controller actively, one of the two quadrature signal channels provided by the Pololu quadrature encoders is adequate for position sensing.

5.3.4 Device controller

An Arduino Mega 2560 board was used as the device controller to translate the recognised user's intentions to corresponding motor driver commands, while the device controller performs the overall control law according to information provided by motor current sensors and motor encoders. There will be a calibration process each time the robotic hand is switched on. All five digits will go to their most extended positions, which can be regarded as the zero positions, until the motors are stalled by

geometrical limits, which are intentionally designed as mechanical stops for finger movement, and this in turn causes a motor current over a predefined threshold detected by current sensing. When motors rotate forward or backwards, the Arduino Mega 2560 obtains the number of counts generated by the motor encoders. In this way, the device controller is always aware of the rough position information for each finger. The ultimate torque control of fingers was achieved by comparing the current values of three motors with predefined thresholds, which were determined through experiments for appropriate contact forces on objects.

The fabricated motor driving and current sensing circuit PCB and the Arduino Mega 2560 board are shown in Figure 5-18. The schematic of the motor driving and current sensing circuit are attached in appendices.

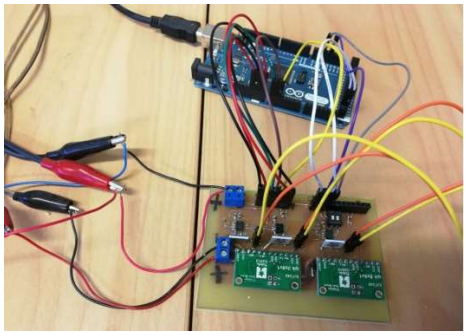

Figure 5-18. The fabricated motor driving and current sensing circuit PCB and the Arduino Mega 2560 board.

5.4 Hand prototype fabrication

The 3D palm model was divided into 3 pieces. Then the mechanical structures for housing actuators and installing the driving mechanisms were built internally as shown in Figure 5-19.

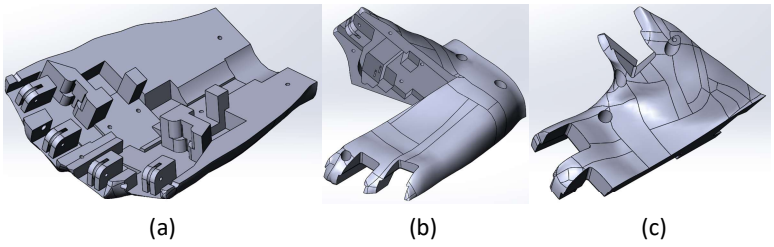

Figure 5-19. The split palm part 3D models.

Figure 5-20 shows the 3D printed palm parts along with the fabricated actuation and transmission system and fingers.

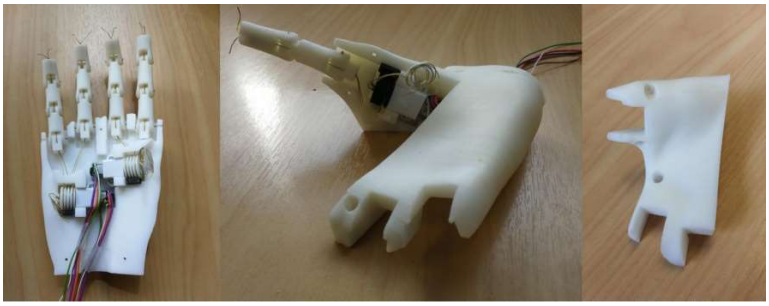

Figure 5-20. The 3D printed palm parts and fabricated actuation and transmission system.

The final assembly of the five-fingered robotic hand is presented in Figure 5-21. This robotic hand has the following features.

- The hand control can be easily integrated with different control systems driving by EMG or other types of signals
- Can perform hand gestures and hold objects with different shapes
- Individual fingers can move adaptively to the shape of the grasped object
- Can grasp objects using different finger configurations, i.e. three or more fingers.

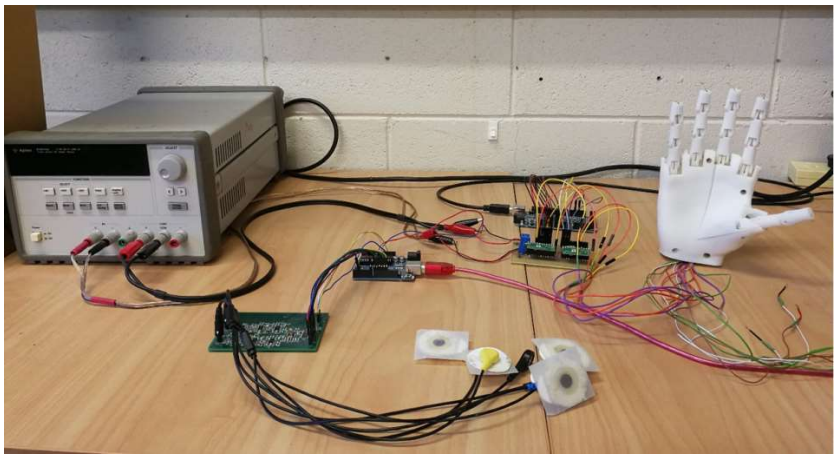

Figure 5-21. The EMG real-time pattern recognition-based five-fingered robotic hand system.

Chapter 6
Experimental design, testing and discussion

To evaluate the proposed EMG signal capturing and data processing methods, control methodologies and the robotic system, two types of experiments were designed. One is offline and the other is in real time. This chapter covers the experiment set up, testing, data analysis, and discussions.

6.1 Offline experiment 1

The purpose of this thesis is to investigate the approaches and algorithms of myoelectric control and to construct a robotic system that could be driven by myoelectric signals. Such a robotic system has potential to evaluate or test the proposed EMG signal processing methods and EMG-based control methodologies. It can also serve as a platform for learning and designing biosignal-driven robotic systems, or even for prosthesis design evaluation and design. The offline experiment was the first step to validate the effectiveness and suitability of the methods proposed by this research for pattern recognition-based myoelectric control. Then a real-time myoelectric control experiment was conducted on the five-fingered robotic hand designed in Chapter 5.

6.1.1 Experimental setting

6.1.1.1 EMG data collection

In this offline experiment, all EMG data were collected in static states. The subjects were asked to sit on a chair and put their arms on a desk, keeping relaxed. Electrodes were placed on the positions described in Section 3.2.2. When the subjects heard the operator's instruction, the subjects performed corresponding movements in sequence with an interval. The EMG system operator controlled the system to collect EMG data during the period that a specific gesture was constantly kept. This was repeated several times and all EMG data sets were stored in data files for further analysis of individual gestures. EMG data for all other gestures were obtained in the same way. Collecting EMG data in this way eliminates the need to detect the start and end of EMG activity and is suitable for offline experiments. It is actually equivalent to the visual EMG activity inspection mentioned in Section 2.2.1.

The experiment was designed to collect data from six subjects, three females and three males including a male amputee. In the experiment, each subject was asked to perform five upper limb movements: hand open (HO), hand close (HC), wrist extension (WE), wrist flexion (WF), and rest state (RS). Each movement was held for 5 seconds and repeated for six times. A relaxed interval of about 5 seconds was arranged between two hand movements.

Figure 6-1 shows an example of the experiments collecting EMG data from an amputee's residual forearm.

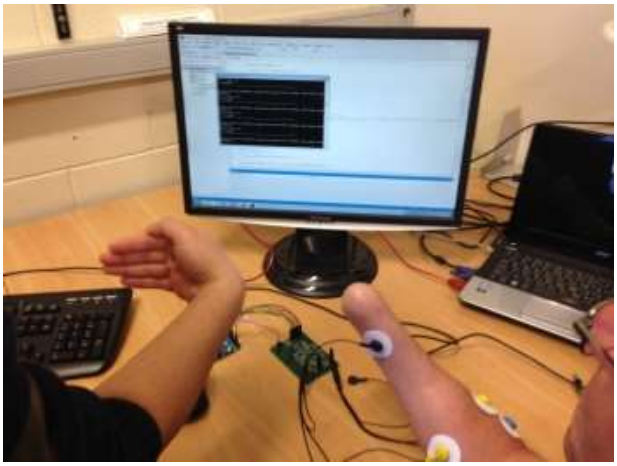

Figure 6-1. Collecting EMG data from an amputee's residual forearm.

Figure 6-2, Figure 6-3 and Figure 6-4 present two channels of EMG data segment examples collected from an able-bodied male, an able-bodied female and a male amputee, respectively, when performing these five hand gestures. Each segment consists of 1000 EMG data points. All EMG data segments of the five hand gestures are displayed on the same horizontal axis to obtain an amplitude comparison. It can be clearly seen that there are some apparent interrupts within the amputee's EMG signals when he was imagining performing and keeping these gestures. Perhaps, this is because he has not performed these movements for a long time after amputation. This suggests that some difficulties may exist in gesture recognition for amputees when acquiring EMG data from their residual arms. Therefore, it is possible that the training process for amputees using a myoelectric-controlled device needs to take longer than for someone who is able-bodied.

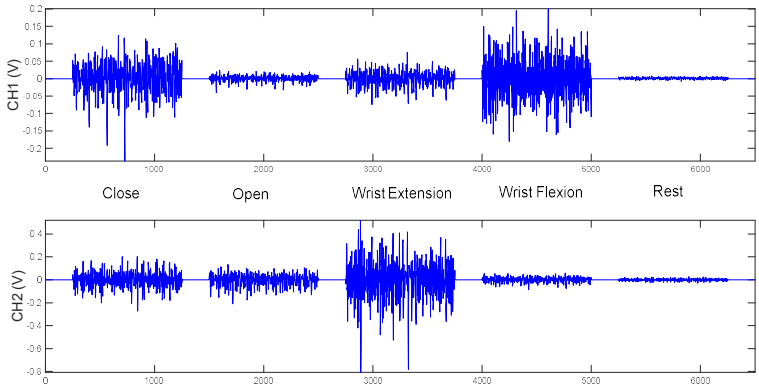

Figure 6-2. Two-channel EMG segments of the five hand gestures from an able-bodied male (the horizontal axis represents data points).

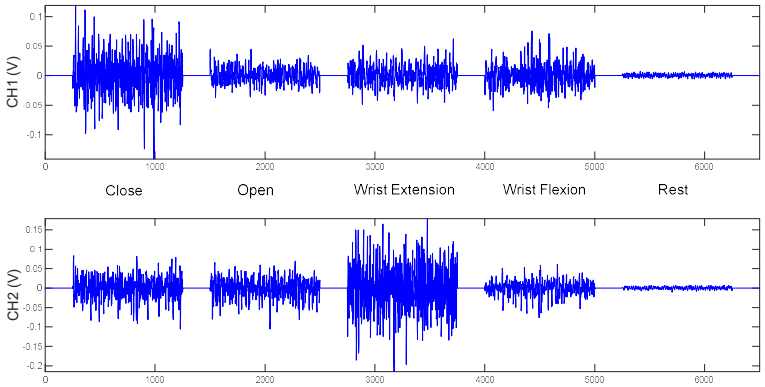

Figure 6-3. Two-channel EMG segments of the five hand gestures from an able-bodied female (the horizontal axis represents data points).

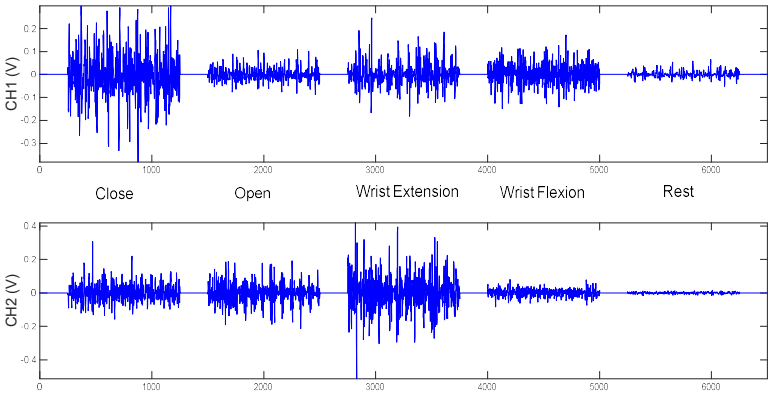

Figure 6-4. Two-channel EMG segments of the five hand gestures from a male amputee (the horizontal axis represents data points).

Figure 6-5 shows the two channels of EMG signals lasting 2.5 seconds for all five gestures from the able-bodied male subject. All subplots in this figure are depicted in the same proportion to give a unique impression in signal amplitude.

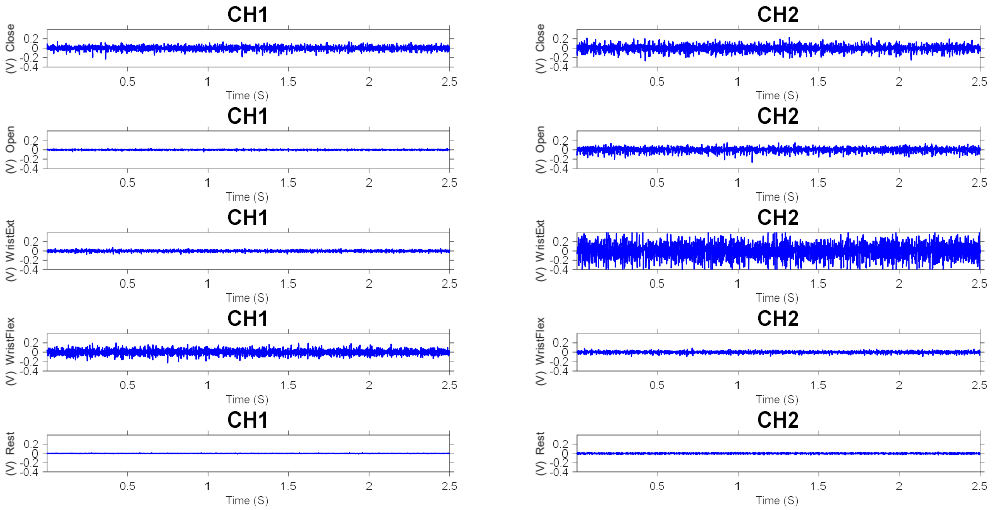

Figure 6-5. EMG signals from an able-bodied male subject.

Figure 6-6 is the spectra of the EMG signals displayed in Figure 6-5, showing the relative relationship of amplitude for different frequency components.

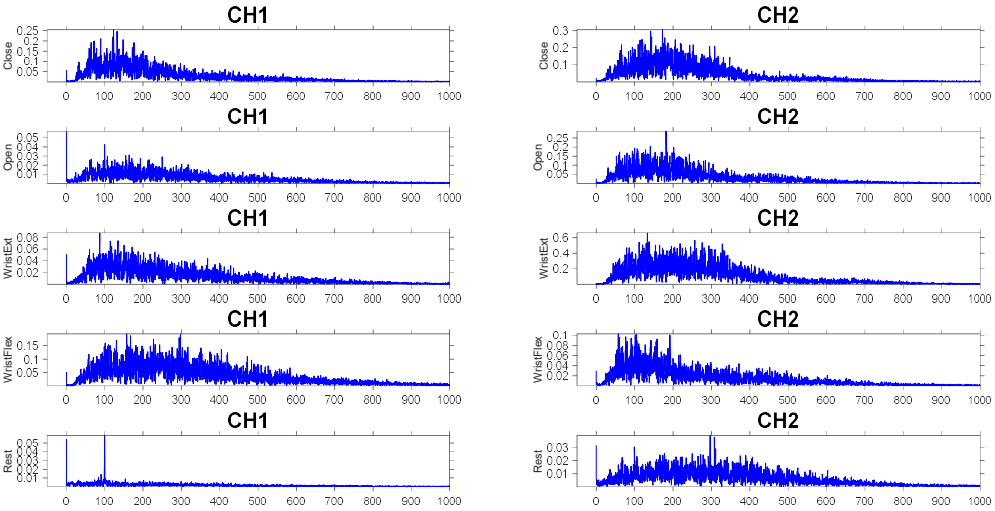

Figure 6-6. Corresponding spectra of the EMG signals displayed in Figure 6-5.

To evaluate the data finally obtained by this research is a challenge as there are very limited data and information available in literature. Pizzolato et al. published a paper in 2017 [14]. It provides a

comparison between professional EMG acquisition systems and the Myo armband. Their outcome was used to judge the result of this research. Figure 6-7 is the comparison between a professional EMG system, the Delsys Trigno, and the Myo armband produced by Pizzolato et al. It shows the spectra of EMG signals obtained by the Delsys Trigno and Myo armband. It is clear that the signals obtained by these two systems have big differences. The Myo armband has a sampling rate of 200 Hz. This means it cannot detect information contained in signal frequency components higher than 100 Hz. Therefore, its usage may be limited. Although the Myo armband was used in research [241-244], it was pointed unsuitable to existing myoelectric control methods [15, 245].

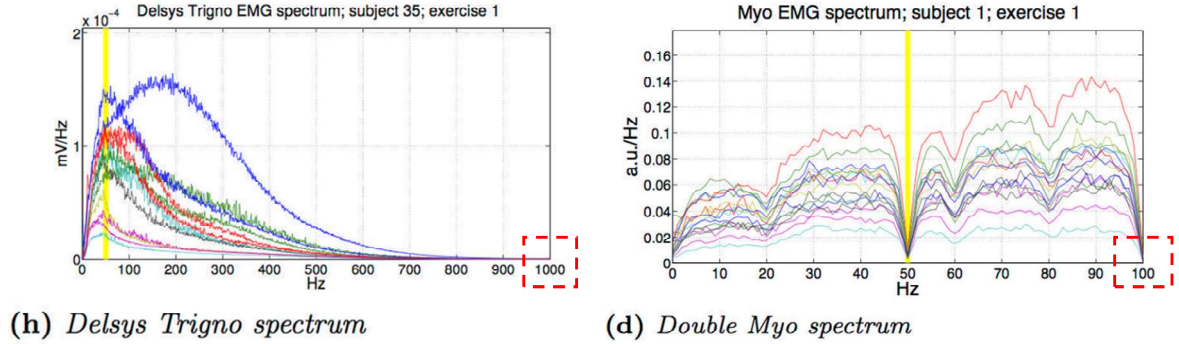

(h) *Delsys Trigno spectrum* (d) *Double Myo spectrum*

Figure 6-7. The acquired EMG signal spectra of the Delsys Trigno and the Myo armband [14].

Figure 6-8 shows EMG signal frequency spectrum comparison between the Delsys Trigno and the system developed by this research. It clearly exhibit that the spectra of the EMG signals obtained using the system developed by this research are very similar to the EMG signals obtained by Delsys Trigno.

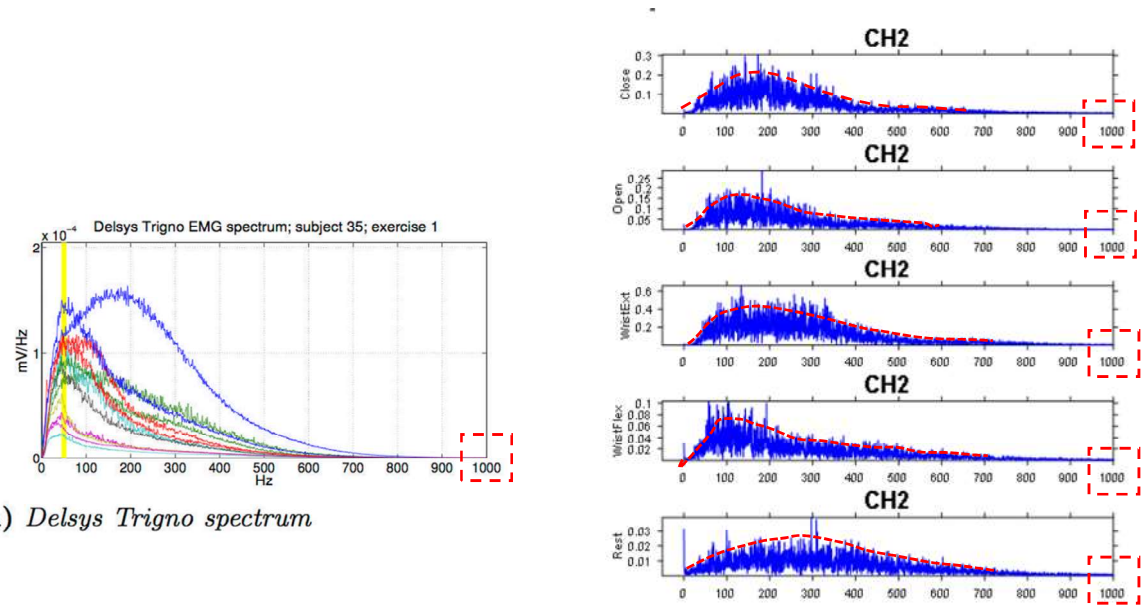

(h) *Delsys Trigno spectrum*

Figure 6-8. The acquired EMG signal spectra of the Delsys Trigno and the system developed by this research.

6.1.1.2 Hand gesture discrimination configuration

The four steps of the pattern recognition-based hand gesture discrimination developed in Chapter 4 are involved and validated in the offline experiment, i.e. overlapped windowing segmentation, feature extraction (5 features), LDA or SVM classifier, and majority voting, as shown in Figure 6-9. The EMG data were imported from the data files that were stored in the computer hard drive as described in the Section 6.1.1.1. The decision results were exported to files for hand gesture identification and comparison.

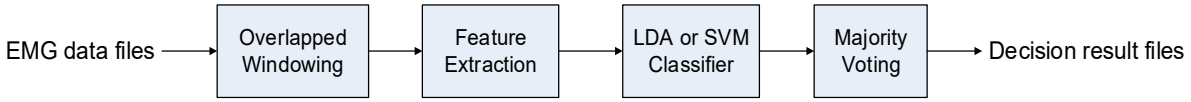

Figure 6-9. Steps involved in the offline experiment.

The hand gesture discrimination module itself was entirely implemented using software on a Windows platform computer using C++, C# and C in Visual Studio. The final Visual Studio program solution implementing hand gesture discrimination contains three program aspects.

1) The native C++ project, including LIBSVM library, SampEn calculation algorithm, and AR parameter estimation algorithm source codes;

2) The C++/CLI project, as a intermediate project to compute and construc all data structures that the native C++ codes need and to call corresponding C++ algorithms;

3) The C# project, as the startup entry of the program for front end coding.

6.1.2 Experimental results and discussions

6.1.2.1 Classification accuracy

In the experiment for testing offline classification accuracy, EMG data were manually selected from the collected data and then divided into two sets for each subject: the first four trials for classifier training and the remaining two trials for accuracy testing. This process was repeated for all possibilities of selecting two trials from the six trial collection. In this way, a method similar to the k-fold cross verification [219] could be performed. The number of 2-combinations from a six element set is calculated as per Equation (6.1).

$$\binom{n}{k} = \frac{n!}{k!(n-k)!} = \frac{6!}{2!(6-2)!} = 15 \tag{6.1}$$

Therefore, for each of the six subjects, total 15 testing trial combinations were considered.

The data segmentation and feature extraction were carried out by algorithms implemented in Visual Studio and the calculated EMG features of RMS, WL, WAMP, SampEn and CC were stored in files for the comparison of SVM and LDA — the two of the most popular classifiers in myoelectric control.

A renowned SVM algorithm implementation using C/C++ programming language, the LIBSVM [222] library, was selected in this research because it has been validated and recommended by many other researchers in this area. Based on the similar consideration of ensuring the algorithm implementation correctness, a Matlab built-in function *Classify* was utilised for LDA, as described in Section 4.5.1.

As an effective means to smooth the output decisions and decrease the time delay for overlapped windowing scheme, the majority voting technique is recommended. In this research, the number of decisions in majority voting is 7 and both the approach with majority voting and the one without majority voting were computed for evaluations.

Figure 6-10 shows the classification error rates obtained individually using each of the five features and the result obtained by combining the five features for both SVM and LDA classifiers without using MV.

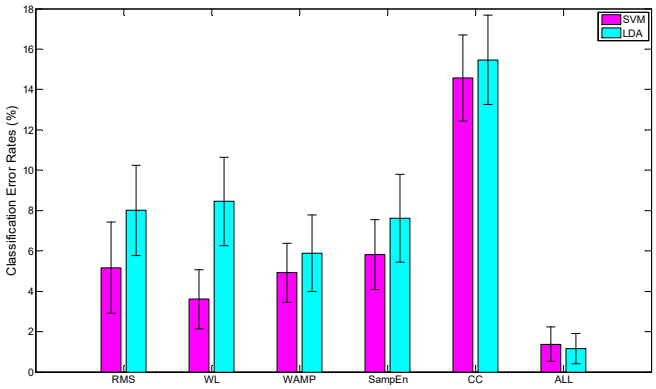

Figure 6-10. Classification Error Rates of individual features and the combination feature set using SVM and LDA without the contribution of MV, where "ALL" stands for the combination of five features.

Figure 6-11 shows the outcomes of the same system configuration with the contribution of MV including seven decisions in the MV queue.

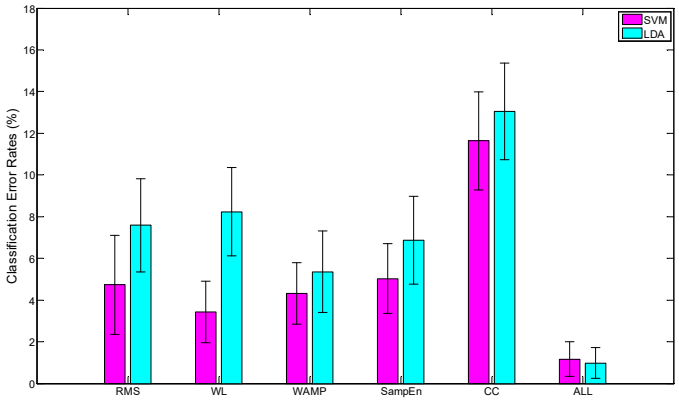

Figure 6-11. Classification Error Rates of individual features and the combination feature set using SVM and LDA with the contribution of MV (the decision number of MV queue is 7), where "ALL" stands for the combination of five features.

6.1.2.2 Discussion

Both Figure 6-10 and Figure 6-11 clearly show that combining the five features could make both SVM and LDA classifiers produce higher accuracy, in particular for LDA. The experimental results also revealed that using MV with the seven decisions could only achieve slightly higher accuracy. As the response time delay is also affected by the decision number of MV queue, the selection of the decision number could be considered after the window length/increment is determined, which might not significantly degrade system performance. Therefore, a proper decision number in MV queue can be examined for an acceptable response delay before finalising the system configuration in a real-time situation.

The offline classification accuracy experimental result also showed that SVM had better performance when it was used with each single EMG feature of RMS, WL, WAMP, SampEn and CC, whereas LDA achieved slightly higher accuracy when using the combined feature set (RMS + WL + WAMP + SampEn + CC). This might be because that when using the combined feature set, as the dimensionality grows, the degree of nonlinearity between class boundaries diminishes. Therefore, the linear algorithm of LDA can get similar or even better performance under certain circumstances than the nonlinear algorithm of SVM that uses a RBF kernel function [45].

Based on analysing the experiment results, this research was decided to use the five EMG feature set (RMS, WL, WAMP, SampEn and CC) for feature extraction. In addition, the overlapped windowing, SVM classifier, and majority voting were selected for respective steps.

6.2 Offline experiment 2

This offline experiment was carried out to compare the proposed methods with other available methods. Two renowned EMG feature sets reported in literature, the Hudings' feature set and Du's feature set [85], were used in this experiment to make a comparison with the methods proposed by this research.

The Hudings' feature set includes four EMG features, i.e. mean absolute value (MAV), waveform length (WL), zero crossing (ZC), and slope sign changes (SSC). The Du's feature set consists of six EMG features, i.e. integral of the EMG (IEMG), variance (VAR), WL ZC, SSC, and Willison amplitude (WAMP). The EMG feature set proposed by this research is composed of RMS, WL, WAMP, SampEn and CC.

The same overlapped windowing, SVM classifier, and majority voting methods were implemented for hand gesture discrimination in this experiment.

6.2.1 Experimental setting

In this experiment, the EMG data was recorded in two consecutive days and two times each day, in the morning and afternoon respectively. Electrodes were detached during the lunch time and night. In each morning or afternoon, two sessions with a resting interval of at least 30 minutes were conducted. Each session includes six trails as the previous offline experiment.

Unlike the previous offline experiment, this experiment involved only one subject and nine hand gestures, including hand open (HO), hand close (HC), wrist extension (WE), wrist flexion (WF), rest state (RS), ulnar deviation (UD), radial deviation (RD), pronation (PN), and supination (SN).

6.2.2 Experimental results and discussions

A cross validation method similar to the one used in the previous experiment was first performed to compare the classification error rates produced by using the three EMG feature sets. The outcome is shown in the Table 6-1. The proposed feature set obtained better performance than the other two.

Table 6-1. Classification error rates in cross validation

EMG data collected in	Hudgins's set		Du's set		The proposed set	
	Error rate	SD*	Error rate	SD*	Error rate	SD*
2 days	9.20%	4.52%	7.16%	3.36%	5.92%	3.58%
First day	7.77%	3.61%	5.87%	2.90%	3.69%	2.66%
First morning	6.38%	3.62%	4.77%	2.74%	2.03%	1.29%
First afternoon	5.54%	4.27%	4.52%	3.75%	3.85%	3.40%
Second day	7.16%	3.36%	6.27%	2.96%	5.28%	3.59%
Second morning	6.77%	4.53%	6.89%	4.45%	6.24%	4.40%
Second afternoon	5.87%	2.98%	4.91%	2.83%	3.42%	2.18%

*SD stands for standard deviation.

Table 6-2 shows the classification error rates for prediction, namely using EMG data recorded in the previous time frame for training and in the next time frame for testing. The proposed feature set also got better outcome compared with the other two.

Table 6-2. Classification error rates for prediction

Training data collected in	Testing data set collected in	Hudgins's set error rate	Du's set error rate	Proposed set error rate
First day	Second day	17.11%	15.82%	13.36%
Frist morning	First afternoon	25.23%	23.75%	19.12%
Second morning	Second afternoon	16.98%	14.86%	13.19%
First session in the first morning	Second session in the first morning	13.75%	12.43%	8.34%
First session in the first afternoon	Second session in the first afternoon	22.52%	24.01%	21.11%
First session in the second morning	Second session in the second morning	25.71%	25.26%	14.18%
First session in the second afternoon	Second session in the second afternoon	9.43%	7.65%	6.57%

As can be seen from the Table 6-1 and Table 6-2, the classification accuracies computed by using the cross validation method are generally better, sometimes with a large difference, than that in prediction. This suggests that using the cross validation method may not be able to evaluate the actual performance of the pattern recognition-based myoelectric control method.

It can also be seen from the Table 6-2 that the classification accuracies vary significantly when using different EMG data set combinations for training and testing respectively. This is perhaps caused by different variations, such as the contract force level change, electrode shift and arm posture change. This also implies the necessity of further research to improve the robustness of the pattern recognition-based myoelectric control method in varying conditions.

6.3 Real-time experiment

6.3.1 Experimental setting

The real-time experiment was conducted on the anthropomorphic robotic hand designed in Chapter 5 to evaluate the proposed myoelectric control methodologies as well as the software and hardware developed for this real-time myoelectric-controlled robotic system. Different from the offline experiment, the real-time experiment demands connecting the hardware and software units in a chain, as shown in Figure 6-12. In the offline experiment, the EMG data was recorded in a static period when a certain gesture was being held. In the real-time experiment, however, the trial subjects could randomly perform the five hand gestures. The system will obtain required EMG data and identify corresponding gestures dynamically with only an acceptable time delay. Therefore, the hand gesture discrimination

algorithm needs to automatically detect the moment the muscle begins to start or to stop contractions, without manual intervention. This leads to an activity detection step being placed before the step segmenting EMG data into windows.

Only the SVM classifier was employed in the real-time experiment due to its higher robustness and the convenience of integrating the ready-to-use LIBSVM library into the main program developed in the Visual Studio environment. For the experiment, the SVM classifier was first trained using previously recorded and stored EMG data. The computed supporting vectors of SVM were stored and used for real-time pattern recognition afterwards.

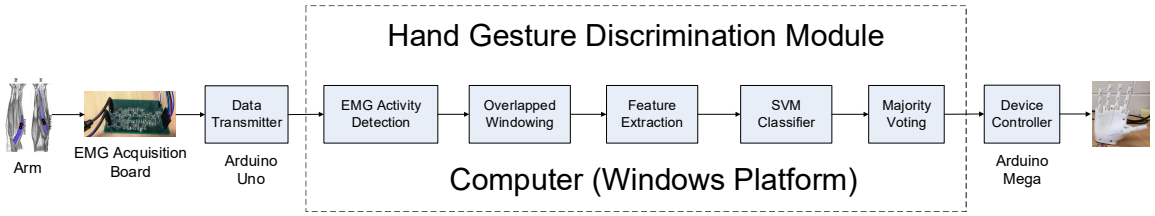

Figure 6-12. Real-time experiment configuration.

Prior to the EMG activity detection is a data transmitter, which uses an Arduino Uno board to obtain digitalised EMG signal data from a SPI serial interface of the analog-to-digital converter and then transfers the EMG data to the following computer through a USB serial port. The traditional RS-232, a serial communication protocol, is convenient for programming, even though it is actually on top of a hardware USB connection. Similarly, an Arduino Mega board is connected to the Windows computer via another USB serial port to generate control instructions to the actuator control circuit, by receiving the recognised hand motion intentions from the majority voting program.

At the same time, the recognised hand gestures' names were displayed on the computer screen for observing the presence or absence of any mechanical delay. The success of performing desired gestures and the behaviour of the robotic hand were observed to evaluate the effectiveness of the myoelectric control system proposed by this research. The integrated system configuration is shown in Figure 6-13.

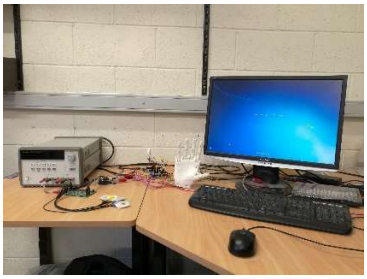

Figure 6-13. The pattern recognition-based real-time EMG-driven five-fingered robotic hand system.

6.3.2 Experiment result and discussion

The real-time experiment showed that the developed EMG acquisition and myoelectric control system was able to identify these five hand gestures and to control the robotic hand manipulations in real-time. Figure 6-14 shows some examples of the system used to hold various objects.

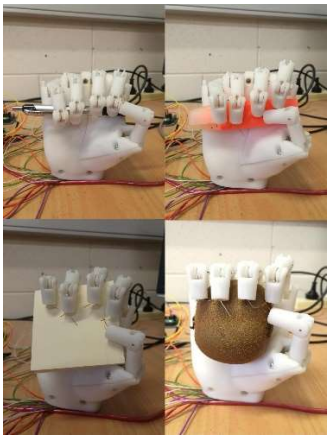

Figure 6-14. The robotic hand was controlled to hold objects with different shapes.

The experiment also observed a phenomenon that the transition period between two hand gestures had huge influence on the recognised decision outcomes. During transition periods, the gesture discrimination algorithm is more likely to generate misclassified results because the transition states do not actually belong to any class of gestures. Although transition periods are often a short time compared to activity durations, the accordingly generated device commands by misclassification induce the robotic hand movement hesitation. This suggests that further research in myoelectric control is necessary to improve EMG-driven system reliability.

Chapter 7
Conclusion and future research

This chapter summarises the research work conducted by this research, concludes the major contributions of this research and gives the recommendations for further research in this area.

7.1 Conclusion

This thesis proposed a novel biosignal-based human-machine interface (HMI) system—a pattern recognition-based myoelectric control system for biosignal-driven robotic systems. To verify and demonstrate the effectiveness of the proposed myoelectric control methods, an anthropomorphic robotic hand was developed as a testing platform that is close to a practical application environment for improving myoelectric control reliability and robustness.

Contributions of this research have been made in the fields of EMG data acquisition, hand gesture identification and the development of robotic systems driven by biosignals such as EMG. Specifically, two surface EMG capturing and recording methods, a pattern recognition-based real-time gesture discrimination method, and an approach of anthropomorphic robotic hand construction and control for myoelectric control validation, as described below, were developed.

- EMG data acquisition
  A single-ended signalling method using discrete monolithic instrument amplifiers (INAs) and a fully differential biosignal acquisition approach were proposed in Chapter 3.
  Despite the research on individual signal conditioning functional blocks in literature, it is hard to find a complete EMG data acquisition reference design that can be easily applied to myoelectric control applications. Therefore, this research first proposed a surface EMG signal detection and data collection method based on the discrete monolithic INA configuration. The proposed method uses EMI/RFI rejection low-pass filters to remove both common-mode and differential-mode noises, and wet Ag–AgCl electrodes to detect surface EMG signals. The amplification chain includes a three op-amp instrumentation amplifier INA128 for extracting and amplifying the differential signal between each pair of electrodes and translating it to a

single-ended signal, a filtering and amplification block with a bandwidth from 20 Hz to 500 Hz for de-noising and further amplification. Then, after the EMG signal is digitised, via an analog-to-digital converter, the EMG data is transferred to a computer for conducting pattern recognition-based hand gesture discrimination algorithms.

However, in the above EMG acquisition method, the differential or balanced EMG signal between a pair of electrodes is translated to a single-ended signal, compromising the ability of noise rejection that is otherwise inherent in a fully differential or balanced design. Therefore, a fully differential EMG acquisition method is also proposed in Chapter 3 for making full use of its inherent noise rejection capability.

Instead of using a classical three op-amp instrument amplifier INA128, the symmetrical discrete dual op-amp configuration is the only option for the differential-in and differential-out analog front end amplifier. Additionally, the subsequent filtering and amplification stages used in the aforementioned single-ended signal approach are substituted with their fully differential counterparts converted from corresponding single-ended filters or amplifiers. Different from the single-ended signal approach that utilises the Sallen-Key active filter, the multiple feedback (MFB) topology becomes the preferable choice in the fully differential solution, since the MFB configuration is the simplest among a few topologies that are ready to support fully differential active filter designs. Finally, the differential ability of the ADC, which is popular for almost all modern analog-to-digital converters, can be totally realised in the fully differential design. To the best of my knowledge, the literature study has not found similar methods that implement the entire analog sEMG amplification and filtering chain in a fully differential way by using common commercial electronic components.

- Pattern recognition-based real-time gesture discrimination

  The interpretation of the user's intention is the key point for various human machine interfaces, and this is also true in myoelectric control of robotic hand application where an effective, reliable and robust method is necessary to discriminate specific hand motions from collected surface EMG data of particular muscles. A pattern recognition-based real-time hand gesture discrimination approach is proposed in Chapter 4 for the purpose to control an anthropomorphic robotic hand.

  This approach consists of different functional steps, including EMG activity detection, data segmentation, feature extraction, classification, and post-processing. An amplitude-related algorithm is utilised to detect the EMG signal activity start and end point, using two moving adjacent windows to calculate the average energy and compare it with a predefined threshold. The data segmentation employs an overlapped windowing technique with a window length of 200 ms and an increment of 25 ms for getting a real-time output decision flow. A novel feature set, consisting of four features from the time domain and the sample entropy, is proposed for effectiveness, efficiency and long-term usage in feature extraction. The SVM and LDA

classifiers are compared in classification accuracy of EMG hand gesture identification in this research using the proposed EMG feature set. The SVM classifier is finally realised using the LIBSVM toolbox for real-time control application due to SVM's better generalisation capability, versatility and robustness with non-stationary data. As a post-processing technique, the majority voting (MV) is used to eliminate spurious classification and smooth the output decision stream.

- Anthropomorphic robotic hand construction and control
  A real-time myoelectric control system, using the proposed EMG acquisition and hand gesture discrimination methods, can be used as a research base for evaluating robotic systems with hand manipulating functions, or integrating it with automatic systems requiring robotic grippers driven by biosignals such as EMG. To validate the proposed real-time myoelectric control method, a physical testing platform—a five-fingered anthropomorphic robotic hand is proposed in Chapter 5. Experiments show the feasibility of the proposed system, the effectiveness of the human machine interface and the good response of the robotic hand.
  This robotic hand features 14 degrees of freedom and 3 degrees of actuation, thus being a highly underactuated mechanism. To resemble the human hand kinematically, the robotic hand is designed to imitate the human hand anatomical structure in an anthropomorphic manner. The mechanism of the human hand finger joints is simplified and implemented by using a hinge joint in the robotic hand design. A comparison of actuation methods is made between the classical electric motor and the non-traditional shape memory alloy (SMA) artificial muscle. The actuation and transmission system is implemented by using electric DC motors and the combination of tendons and pulleys. A soft gripper technique and a compression spring mechanism are used for realising the inter-phalange and inter-finger underactuation respectively. For simplicity, motor encoders and current sensors are employed for indirect position and torque sensing, which constitutes the whole control loop for the robotic hand.

This research also produced some publications both in journal and international conferences such as:

J. Wang, L. Tang, and J. E. Bronlund, "Surface EMG Signal Amplification and Filtering," International Journal of Computer Applications, vol. 82, pp. 15-22, November 2013, dio: 10.5120/14079-2073.

J.Wang, L. Tang, and J. E. Bronlund, "A pattern recognition system for myoelectric based prosthesis hand control," IEEE Explore, doi: 10.1109/ICIEA.2015.7334225.

J.Wang, L. Tang, and J. E. Bronlund, "Pattern recognition-based real time myoelectric system for robotic hand control," IEEE Explore, ICIEA 2019.

7.2 Recommendations for further research

It is obvious there is a long way to go before having a robust, accurate and fast biosignal-driven robotic system. However, based on the knowledge and experience gained from this research, five aspects could be considered for further research to improve the performance of myoelectric control.

- The EMG feature set selection is most important for classification and in turn for pattern recognition-based myoelectric control. The research of other novel feature extraction methods or feature combinations is still very attractive, which may be capable of offering a more reliable, robust and usable EMG-driven robotic control scheme in the future.
- The lack of simultaneous control and proportional control is a major limitation of pattern recognition-based myoelectric approaches. The research on proportional and simultaneous control using pattern recognition methods, or using other newly developed algorithms such as regression, is worth further investigation in the future.
- To facilitate the algorithm research of myoelectric control, a good method is to establish a standard EMG database for offline algorithm performance testing and comparison. The Ninapro database is an example of this attempt [14].
- This research only studied a simple sensory system for robotic system control. However, the fusion of multiple modalities of feedback such as tactile or visual information to the device controller or to the user's central nervous system, would provide great potential for further improvement on device controllability.
- The robustness of pattern recognition-based myoelectric control is affected by different variations. Using representative samples from varying conditions for training is a means to improve system robustness [11]. In addition, integrating this method with other sensing technologies, such as inertial measurement units (IMUs) [246] and computer vision, is a promising approach to increase system reliability.

Appendix A Low risk notification

MASSEY UNIVERSITY
TE KUNENGA KI PŪREHUROA

30 October 2013

Jingpeng Wang
[redacted]

Dear Jingpeng

Re: Biosignal-Based Artificial Muscle-Driven Robotic System Design

Thank you for your Low Risk Notification which was received on 2 October 2013.

Your project has been recorded on the Low Risk Database which is reported in the Annual Report of the Massey University Human Ethics Committees.

The low risk notification for this project is valid for a maximum of three years.

Please notify me if situations subsequently occur which cause you to reconsider your initial ethical analysis that it is safe to proceed without approval by one of the University's Human Ethics Committees.

Please note that travel undertaken by students must be approved by the supervisor and the relevant Pro Vice-Chancellor and be in accordance with the Policy and Procedures for Course-Related Student Travel Overseas. In addition, the supervisor must advise the University's Insurance Officer.

A reminder to include the following statement on all public documents:

> *"This project has been evaluated by peer review and judged to be low risk. Consequently, it has not been reviewed by one of the University's Human Ethics Committees. The researcher(s) named above are responsible for the ethical conduct of this research.*
>
> *If you have any concerns about the conduct of this research that you wish to raise with someone other than the researcher(s), please contact Professor John O'Neill, Director (Research Ethics), telephone 06 350 5249, e-mail humanethics@massey.ac.nz".*

Please note that if a sponsoring organisation, funding authority or a journal in which you wish to publish requires evidence of committee approval (with an approval number), you will have to provide a full application to one of the University's Human Ethics Committees. You should also note that such an approval can only be provided prior to the commencement of the research.

Yours sincerely

J. O'Neill

John G O'Neill (Professor)
Chair, Human Ethics Chairs' Committee and
Director (Research Ethics)

cc Dr Liqiong Tang
School of Engineering and Advanced Technology
PN456

Prof Don Cleland, HoS
School of Engineering and Advanced Technology
PN456

Massey University Human Ethics Committee
Accredited by the Health Research Council

Research Ethics Office
Massey University, Private Bag 11222, Palmerston North 4442, New Zealand **T** +64 6 350 5573 +64 6 350 5575 **F** +64 6 350 5622
E humanethics@massey.ac.nz animalethics@massey.ac.nz gtc@massey.ac.nz **www.massey.ac.nz**

Appendix B EMG acquisition circuit

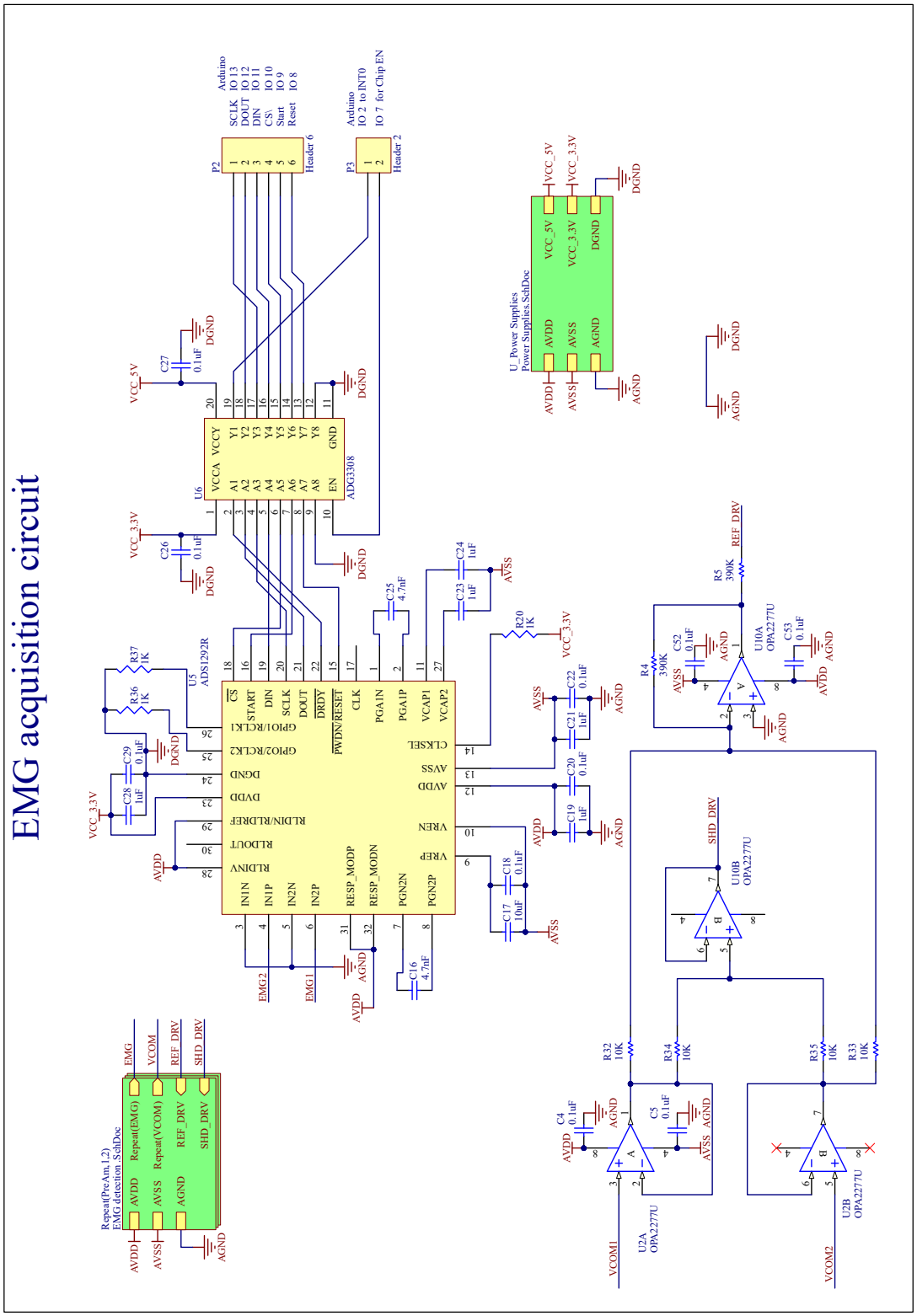

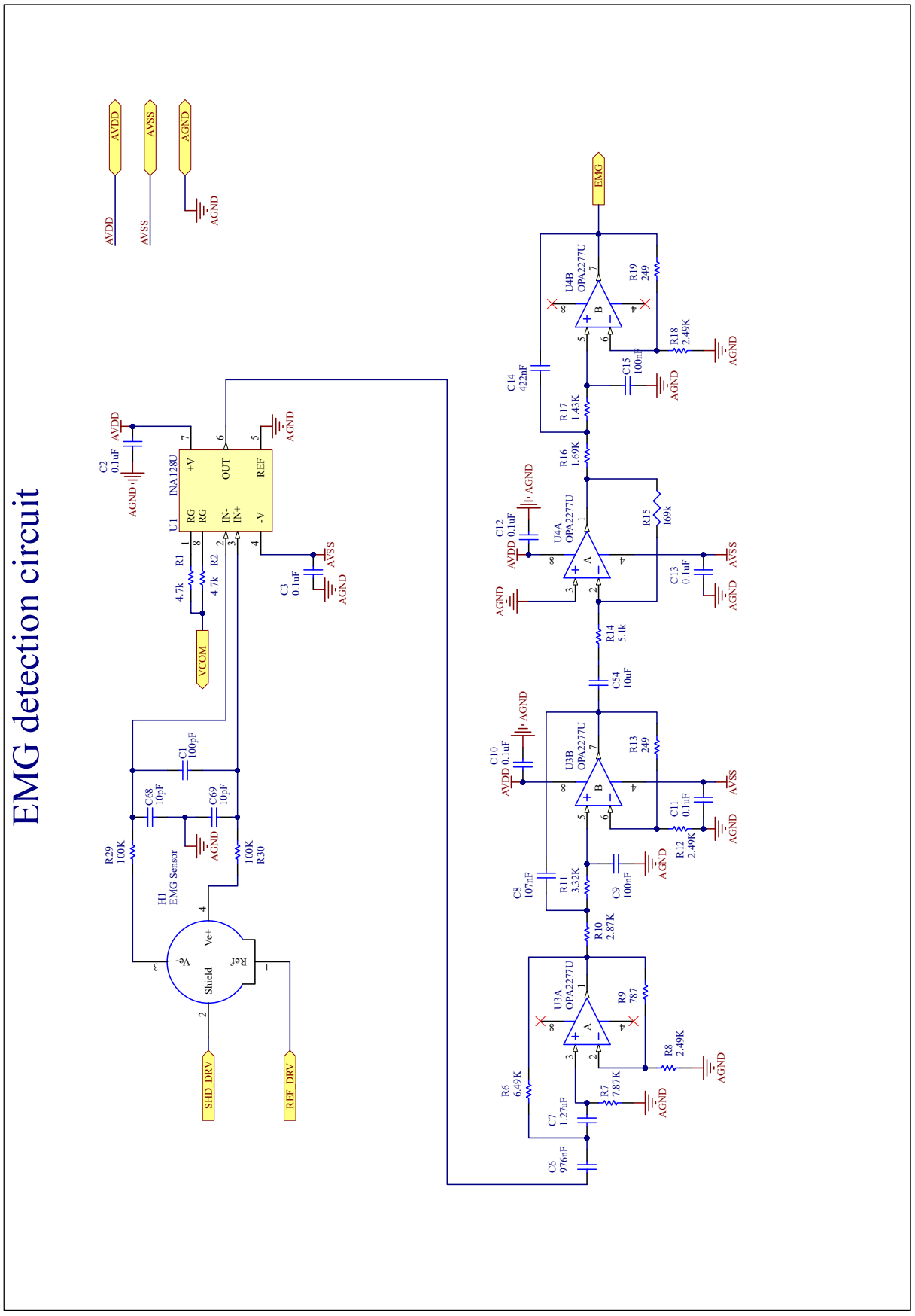
EMG detection circuit
AVDD
AVSS
AGND
INA128U
OPA2277U
EMG Sensor
SHD_DRV
REF_DRV
VCOM
EMG

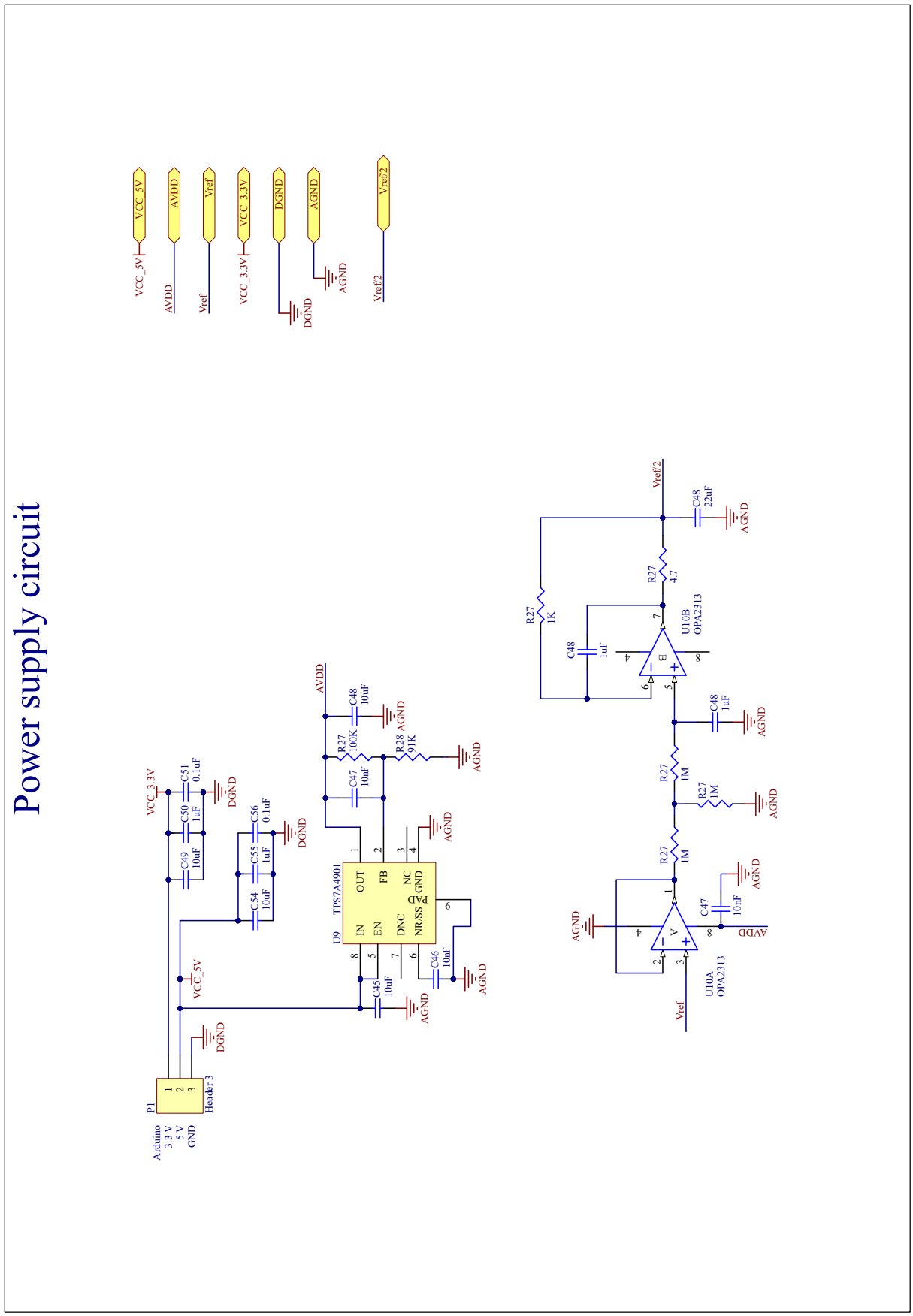
Power supply circuit
VCC_5V
AVDD
Vref
VCC_3.3V
DGND
AGND
Vref/2
P1
Arduino
3.3 V
5 V
GND
Header 3
C49 10uF
C50 1uF
C51 0.1uF
C54 10uF
C55 1uF
C56 0.1uF
U9
TPS7A4901
IN
EN
DNC
NR/SS
OUT
FB
NC
GND
C45 10uF
C46 10nF
C47 10nF
C48 10uF
R27 100K
R28 91K
U10A
OPA2313
U10B
OPA2313
R27 1K
R27 4.7
R27 1M
C48 1uF
C48 22uF
C47 10nF

EMG detection circuit

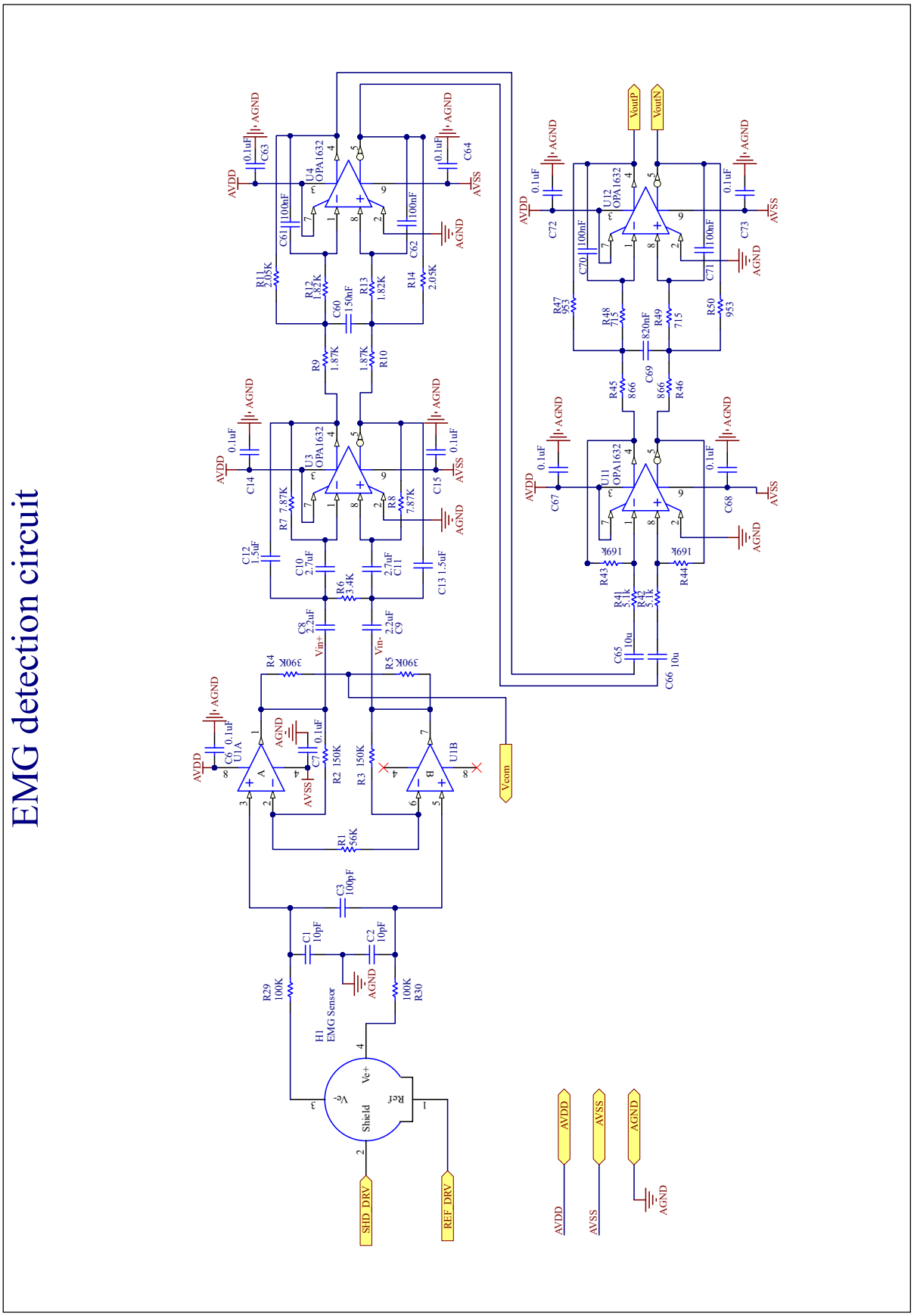

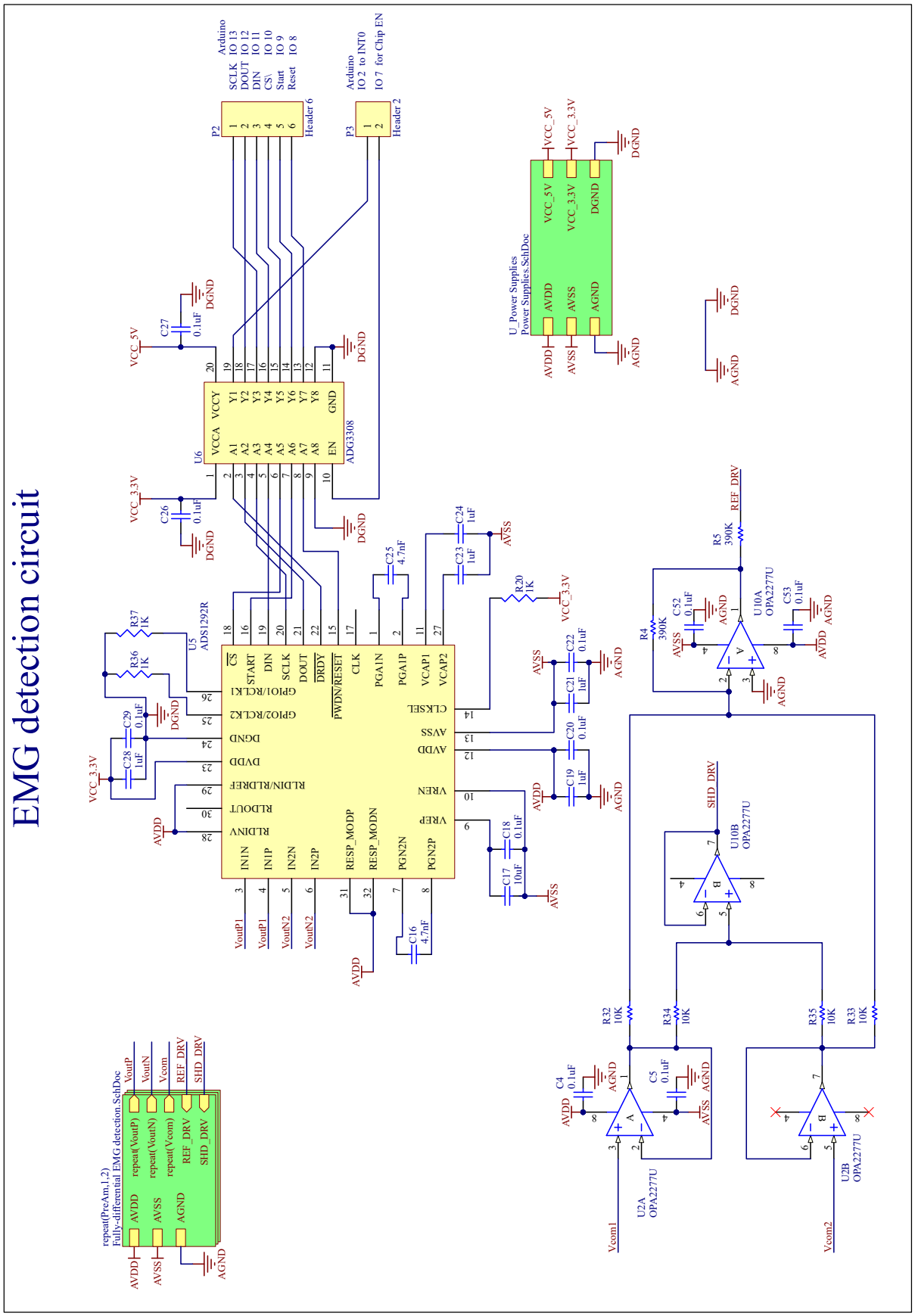
EMG detection circuit
repeat(PreAm,1,2)
Fully-differential EMG detection.SchDoc
AVDD
AVSS
AGND
VoutP
VoutN
Vcom
REF_DRV
SHD_DRV
U5
ADS1292R
U6
ADG3308
P2
Header 6
P3
Header 2
U_Power Supplies
Power Supplies.SchDoc
U10A
OPA2277U
U10B
OPA2277U
U2A
OPA2277U
U2B
OPA2277U
VCC_5V
VCC_3.3V
DGND
Vcom1
Vcom2

Appendix C Current sensing and motor driving circuit

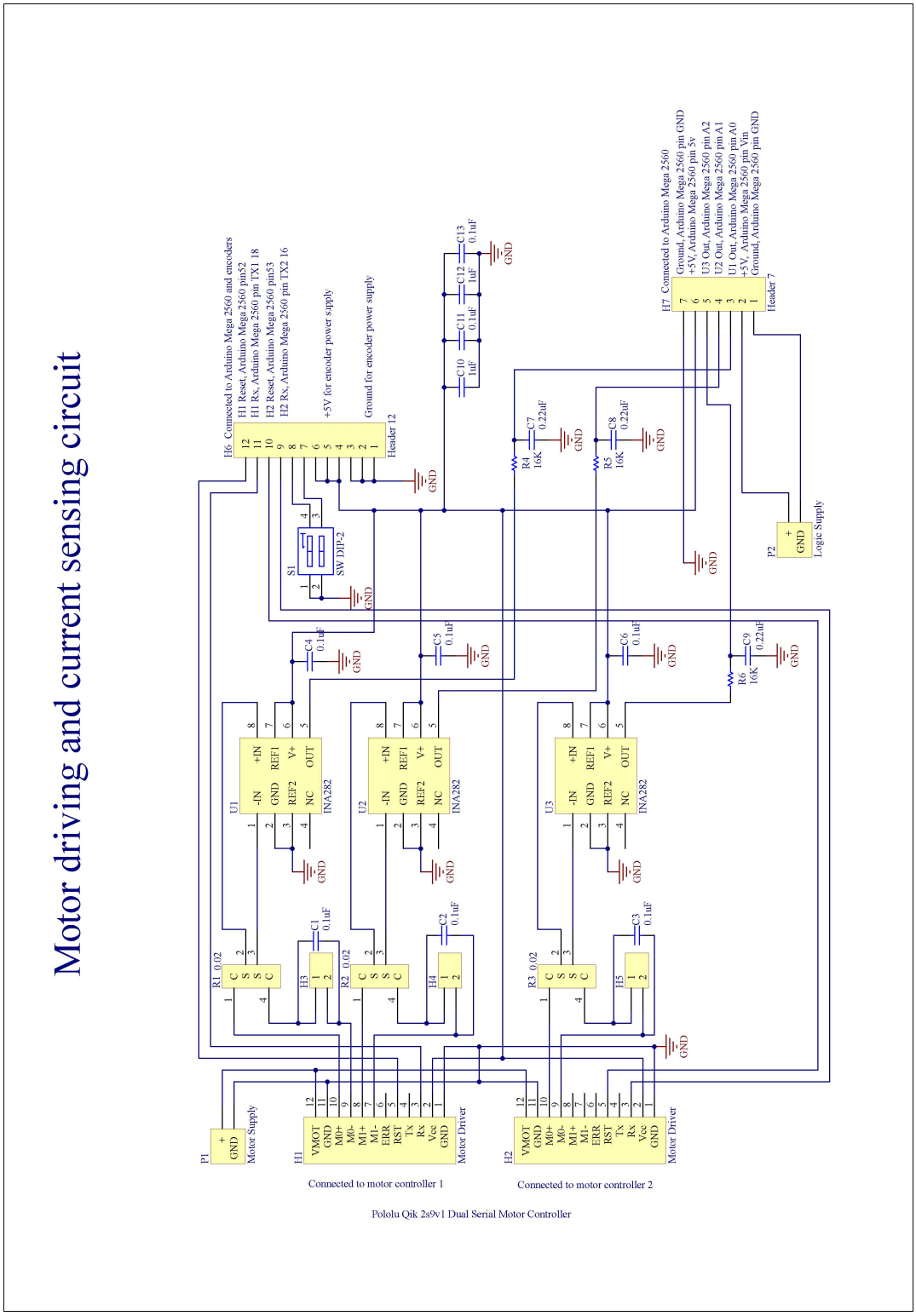

Appendix D Guide for hardware and software set-up and data capturing

The entire system developed is shown below. Following is a brief guide to set up and run the system.

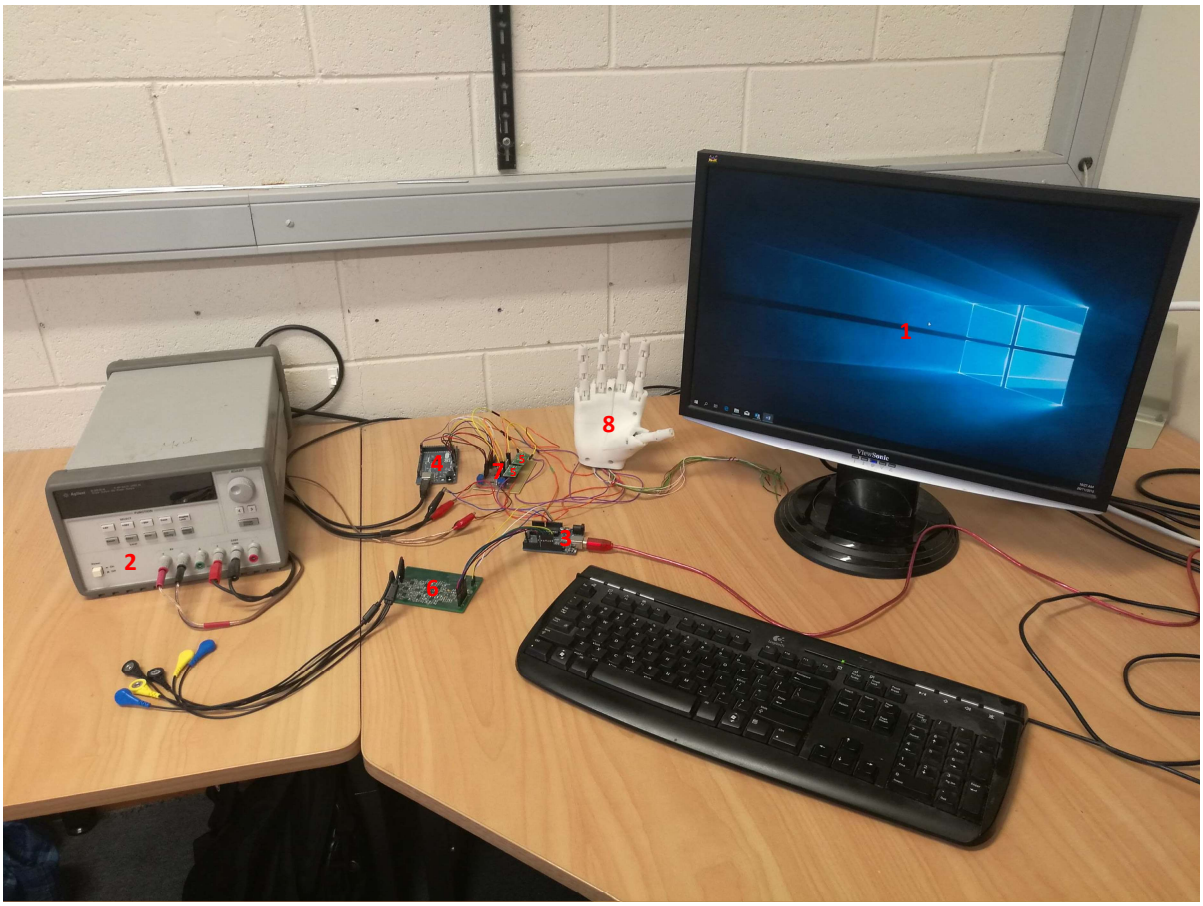

1 PC
2 DC power supply
3 Arduino Uno
4 Arduino Mega 2560
5 Pololu Qik 2s9v1
6 EMG acquisition board
7 Current sensing and motor driving board
8 Robotic hand

1. Preparing hardware devices

- One PC installed Windows 7 or later version
- One DC power supply such as Agilent E3631A Triple Output DC Power Supply
  - +6V (current limit 3A)
  - +9V (current limit 0.5A)
- One Arduino Uno board
- One Arduino Mega 2560 board
- Two Pololu Qik 2s9v1 dual serial motor controller
- One EMG acquisition board developed by this research (described in Chapter 3)
- One current sensing and motor driving board developed by this research (described in Chapter 5).
- One robotic hand developed by this research (described in Chapter 5) or use other similar robot hand

2. System set up

Connect the hardware devices as instructed below and check carefully before running.

Note: the Arduino Uno board and Arduino Mega 2560 board provide +5V DC voltage for the EMG acquisition board and the current sensing and motor driving board respectively. If the Arduino boards are powered through USB cables, the total current drawn from a computer USB port may exceed its maximum current limit. This may cause computer USB port damage. Therefore, it is recommended to use a separate DC power supply to provide the Arduino boards with +9V voltage through their Vin and GND pins and then connect the Arduino boards to computer USB ports. When shut down the system, detach the USB cables from computer USB ports first before switching off the separate DC power supply.

Arduino Uno

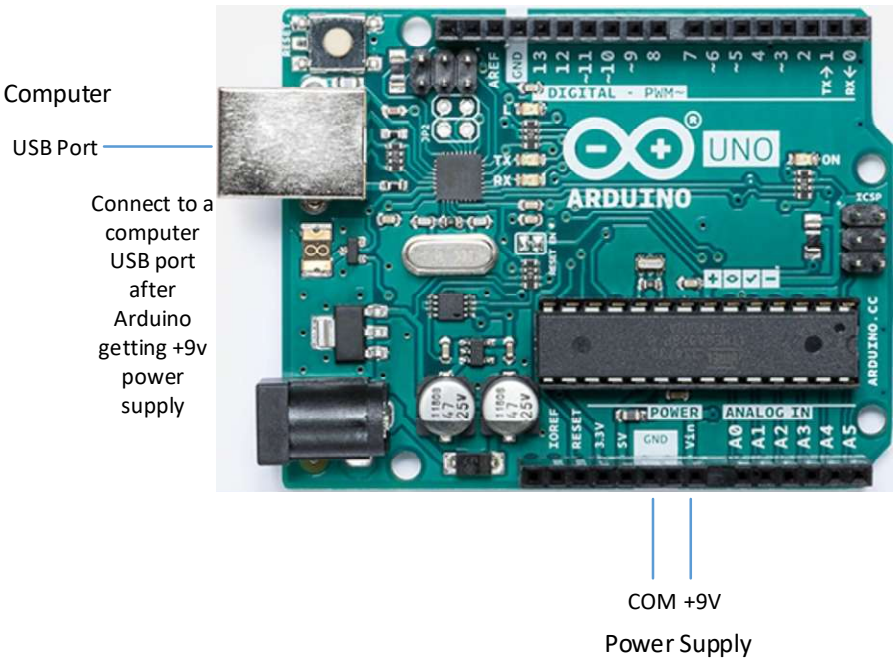

Arduino Mega 2560

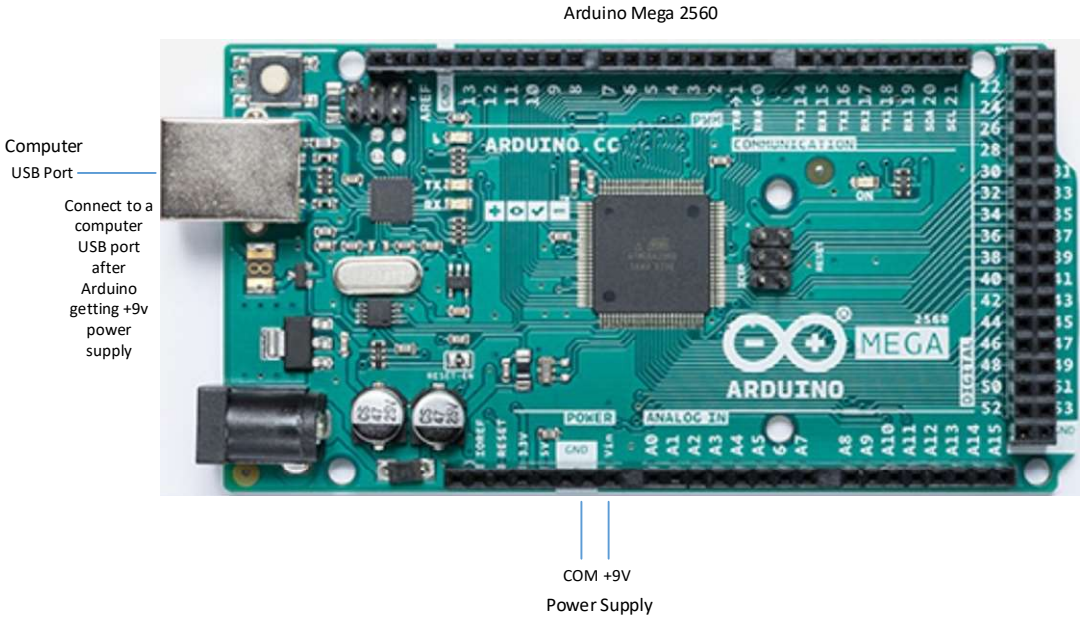

EMG Acquisition Board

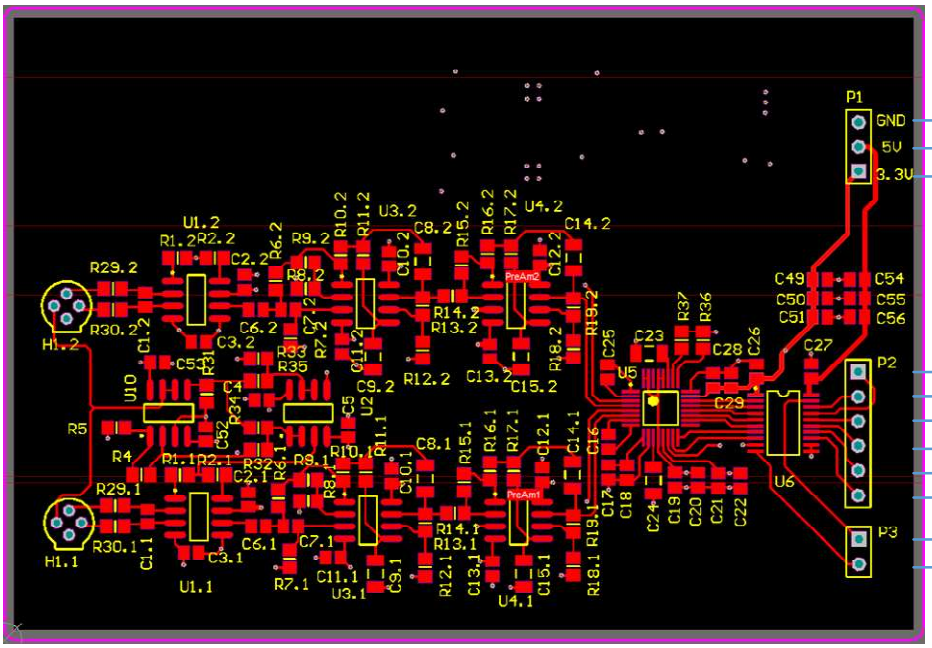

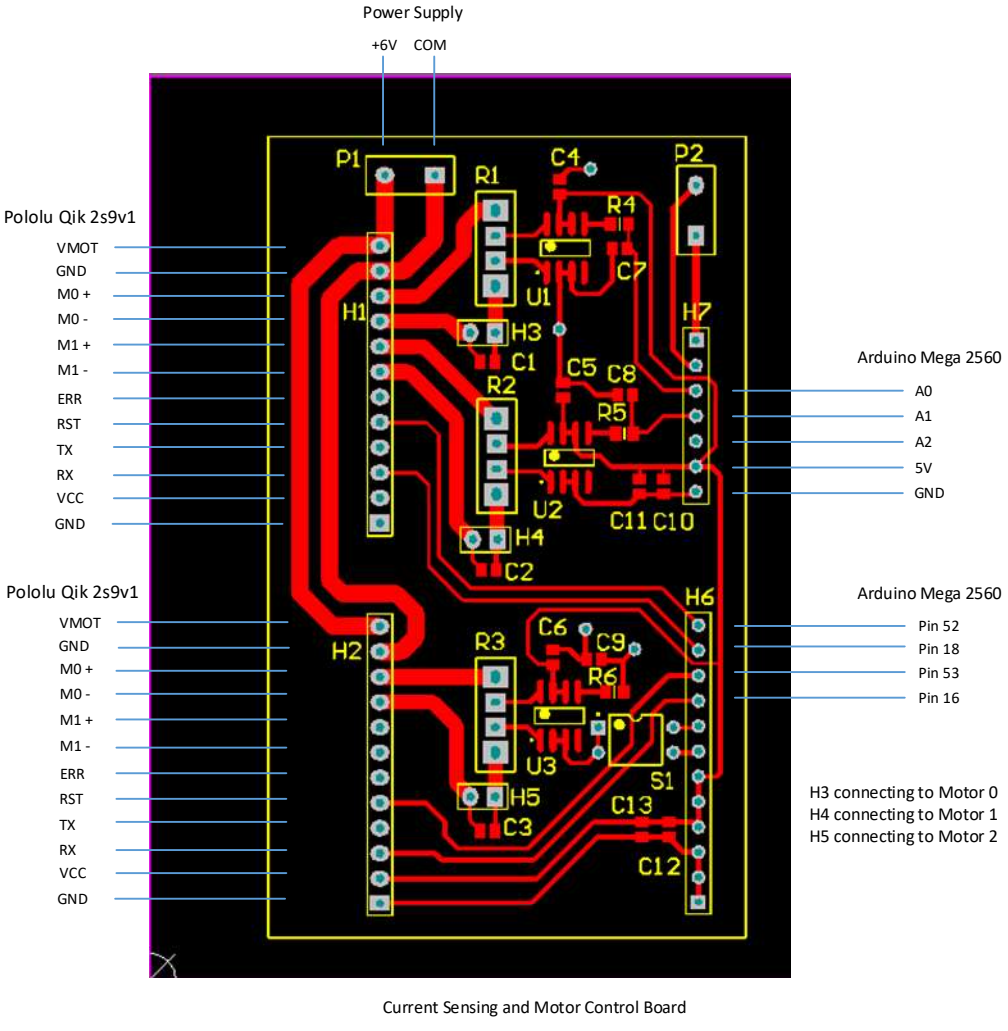

Current Sensing and Motor Control Board

3. Preparing software programs

- The EMG data collection program
  This program was developed in Arduino IDE and downloaded to Arduino Uno board.
- The motor control program
  This program was developed in Arduino IDE and downloaded to Arduino Mega 2560 board.
- The main program
  This program was developed in Visual Studio 2012 environment. The Visual Studio solution file includes three projects:
  1) The C# project, as the start-up entry of this program for front end coding;
  2) The C++/CLI project, as an intermediate project to construct and compute all data structures that the native C++ code needs and to call corresponding C++ algorithms;
  3) The native C++ project, including LIBSVM library, SampEn calculation algorithm, and AR parameter estimation algorithm.

4. Software environment set up

Before starting experimental operation, configure execution parameters on the main program GUI:

- File location
  The base folder storing experimental data and result files, e.g. C:\EMG_Data.
- Subject
  The name of the current trial subject, e.g., James.
- Port to Arduino Uno
  The name of the virtual USB port connecting to Arduino Uno, e.g., COM4.
- Port to Arduino Mega 2560
  The name of the virtual USB port connecting to Arduino Mega 2560, e.g., COM6.

EMG data and training result files will be stored in the folder "File location\Subject\", e.g., "C:\EMG_Data\James\".

5. Running the system

For each trial subject, the experiment is conducted in three steps, i.e. training data acquisition, training and real-time robotic hand control.

- Training data acquisition
  Collecting and saving EMG data of five gestures, i.e. hand open (HO), hand close (HC), wrist extension (WE), wrist flexion (WF), and rest state (RS), according to instructions displayed on the main program GUI. The process is described in Chapter 6 in detail.

- Training

  Using the stored EMG data to train the SVM classifier and save training results for further use.

- Real-time robotic hand control

  Using the training results to control the robotic hand in real-time.

Appendix E BMX150 artificial muscles

BioMetal®

Artificial Metal-Based Muscle for Long Strke Actuators

BioMetal Helix
BMX series

The BioMetal Helix (BMX Series) is a biometal micro coil. It is a linear actuator (linear-motion drive unit) featuring wide-range expansion and contraction. At room temperature, it is soft and can be elongated with ease. The BMX, elongated at room temperature, becomes stiff and sharply contracts to its original length when a current is fed through it. It is again softened by stopping the flow of current. It also contracts if heated by hot air. The BMX produces a by far greater force when it contracts than does it when it extends at room temperature. The change in length is nearly 200% of the length of the contracted BMX. It can be repeatedly used any number of times. It is ideally suited for millimeter and micrometer size actuators for use in narrow spaces where it is impossible to use motors and pneumatic cylinders.

Features of the BMX Series

Long stroke and production of strong force

A remarkably long stroke, 100%-200% of the length of the contracted BMX. Although being a very thin actuator, this product produces a very strong force. Since a wide-range movement can be brought by its simple mechanism, it can be easily incorporated into the design of systems for a wide variety of applications.

The BMX150 is lifting a 30 g weight.

Wide-range movement of the BMX

Smooth, pliable operation

The BMX moves without generating any vibration or sound. Unlike the solenoid (electromagnet), it produces the greatest force at the start point and the force produced changes only slightly over the long displacement interval. Its capability can be fully utilized when it is used for the resetting mechanism of latches and locks and for micro servo actuators.

The force produced by the BMX is the strongest at the start and it changes only slightly.

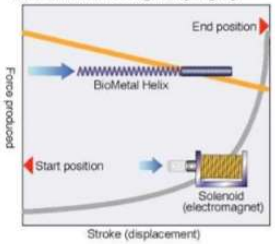

Operation at low voltage and low power

The BMX can be moved merely by connecting it to a cell after stretching it lightly. No special drive circuit is necessary. It can be safely used because it can be driven by a low voltage. The drive current required is very small. Fine adjustment of motion can be made by using a PWM power control circuit. The BMX, which moves responding to temperature changes, can also be utilized as a thermostat-like actuator. Needless to say, it can also be moved by heating it by a hot air blower.

Ideal for milli and micro size mechanisms

The forced produced by the BMX is directly proportional to its cross-sectional area. Although small in size, the BMX is capable of producing a strong force and less susceptible to friction and viscosity than motors and solenoids.
The BMX's material itself is an actuator. It can be used even when cut short. Since being small, thin, and simple in construction, it is ideally suited for use in milli and micro size mechanisms. It is the only powerful actuator available that can be incorporated in thin IC cards and chips.

The BMX operates at low voltage.

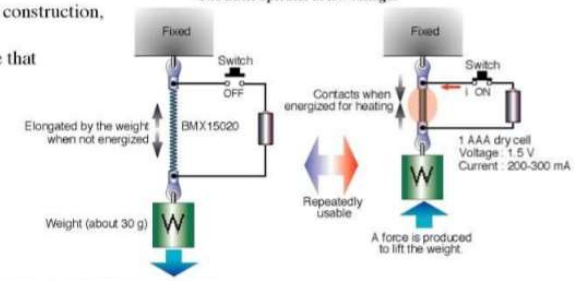

TOKI CORPORATION

BioMetal Helix BMX series

Applications of the BMX Series

■Ultra-small actuators
■Ultra-thin actuators
■Ultra-small temperature switches
■Flexible actuators
■Actuators for toys and models

Basic uses of the BMX

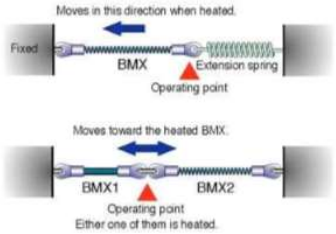


Micro plunger

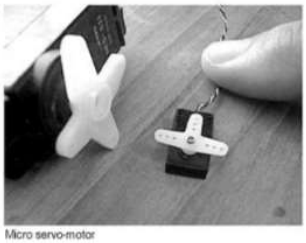
Micro servo-motor

NOTE:The BMX series is not suited for the following applications.
●Applications where high-speed repetitive operations are required (The BMX can move at high speed only in the contracting direction.) ●Movement of a heavy load ●Mechanism of a size allowing the use of a motor ●Applications where the temperature can rise to above 55℃ ●Prolonged use in water
※Where high reliability in produced force and service life is required, consider using the BioMetal Helix BMX series.

Major Characteristics and Specifications of the BMX Series

	BMX50	BMX75	BMX100	BMX150
Standard coil diameter D (mm)	0.2	0.32	0.4	0.62
Wire diameter d (mm)	0.05	0.075	0.1	0.15
Coil diameter-to-wire diameter ratio D/d	4.0	4.3	4.0	4.1
Practical maximum force produced (gf)	3~5	5~10	10~20	20~40
Kinetic displacement (change in length) (%)	200	200	200	200
Standard drive current (mA)	50~100	70~120	100~150	200~300
Standard electric resistance (Ω/m)	3600	1600	900	400
Allowable upper temperature limit (℃)	—	—	—	50~60
Service life (times)	—	—	—	10^6

※The number following BMX in the product name is the value of its diameter expressed in micrometer. For example, the BMX100 has a diameter of 0.1 mm. For any type of BMX, the coil diameter-to-wire diameter ratio is about 4.
※The BMX is uniform in the longitudinal direction. For this reason, most of the numerical data in the table are determined with reference to the unit length (1 m) of the BMX.
※The kinetic distortion is represented by the ratio in percentage of the displacement (contraction or expansion) of the BMX to its total length.
※The numerical data in the table are standard values used as a guide for device design. The actual performancecharacteristics may differ from them, depending on the operating conditions.
※The numerical data in the table are not guaranteed values but reference values. The actual numerical data may be varied by improvement of the BMX. There are also slight variations between lots.

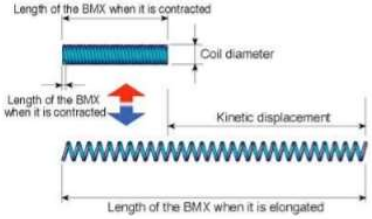

■The service life of the BMX is closely associated with the magnitude of the load and the kinetic distortion. It has atrack record of having made more than five millicn reciprocating motions under appropriate load and movement conditions (Example: BMX150. Eight million motions completed at the load of 30 gf and at the kinetic distortion of 50%.)
■The BMX makes non-linear, asymmetric motions (contractions and expansions). It can be quickly contracted if it is heated in an adiabatic manner by feeding a large current through it. However, it cannot be quickly elongated without forced cooling because the rate of elongation depends on cooling speed. In the case of self-cooling the BMX is affected by the ambient temperature and the wind. The data shown in the table beloware those obtained at the room temperature of 20℃ under the windless condition.
■The upper limit of operating temperature varies with the load condition. This limit can be increased to some extent by increasing the bias. In that case, however, the service life of the BMX may be shortened. There is no lower limit of operating temperature. The current required for driving by heat increases with decreasing ambient temperature.

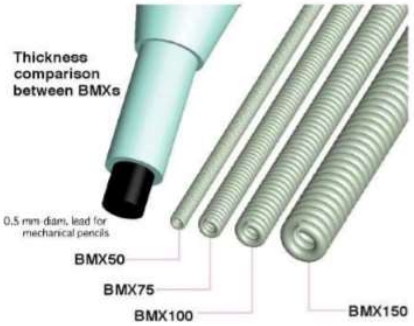

■Line-up of BioMetal Helix BMX Series Sample Set

Product No.	Coil diameter
BMX5020	φ0.20㎜
BMX7520	φ0.32㎜
BMX10020	φ0.40㎜
BMX15020	φ0.62㎜

CONTENTS
BioMetal Helix each 20 mm, 1 pc.
Instruction manual
Biasing spring 4 pcs.
Small-size spectacle terminal 16 pcs.
Ultra small-size eyelet terminal 16 pcs.

TOKI CORPORATION
BioMetal Actuator Department:3-43-15, Omori-kita, Ota-ku, Tokyo 143-0016, Japan
Phone: (03)5735-2833, Fax: (03)3742-2701 URL: http://www.toki.co.jp/biometal

●For technical inquiries, please use our inquiry form on our web-site.
We may not be able to answerquestions over the telephone.
●More detailed information on the BMX series will be available on our company's home page.
●Specifications are subject to change without prior notice.

BioMetal® Helix INSTRUCTION MANUAL

The BioMetal Helix (BMX) is a new type of actuator designed to work like muscles.
The BMX,elongated at room temperature, contracts to its original length when a current is fed through it.
It also contracts if heated by hot air. When heated, it contracts with greater force than it extends at room temperature. It can be repeatedly used any number of times.

Section 1 - Unpacking and Use

● BioMetal Helix is shipped on solid wire and must be carefully removed first.

● Elongate the BMX to 40-50 mm. When it is carefully and slowly elongated at room temperature it abruptly becomes difficult to extend any further. This means that it has reached its limit length.
If it is elongated beyond this limit, it will no longer returned to its original length.
However, even in that case, it can extend and contract.

● Each end of the BMX is provided with a crimp terminal for the passage of current through it.It can be made hard to break by heating its crimp terminal parts with a soldering iron to a temperature of about 200-300 °C.
Even if it is bent during the work, it will restore to normal when heated.

● The crimp terminals can be soldered to once they are crimped to the helix.
Hold the crimp with a pliers to act as a heatsink in order to prevent overheating of the helix by the soldering iron.

● Connect one AA cell between the terminals of the BMX to feed a current through itand it will contract to its original length.
It has no polarity. It is heated on the same principle as with nichrome wires when a current is fed through it. The voltage of a dry cell is suitable for it's use.At room temperature (20 °C), it begins to move when the amount "Typ Cur" (from table at end of instructions) in mA of current is fed through it. Even if a greater amperage of current than necessary is fed through it, the contracting force will not increase.
Important Note: Do not overheat. A very hazardous condition might occur.
Since no electrical insulation is provided for its surface, care should be taken to avoid accidental contact.
If it is elongated when it is heated, it will become hard to return to its original length.

● The BMX will also contract when it is directly heated by a dryer.
It may degrade in performance if it is heated to 200 °C or higher. Be careful not to overheat it.

● To move the BMX again, stop energizing or heating it, cool it for a period of 1 to 2 seconds, and then slowly elongate it. When it is sufficiently cooled it may extend on its own with no force applied to it.
However, this does not indicate any abnormality.

● The BMX is made of a very strong material. To cut it, use a pair of nippers with strong edges.
If a pair of scissors is used for cutting it, its edges may chip.

<Preparation for use>

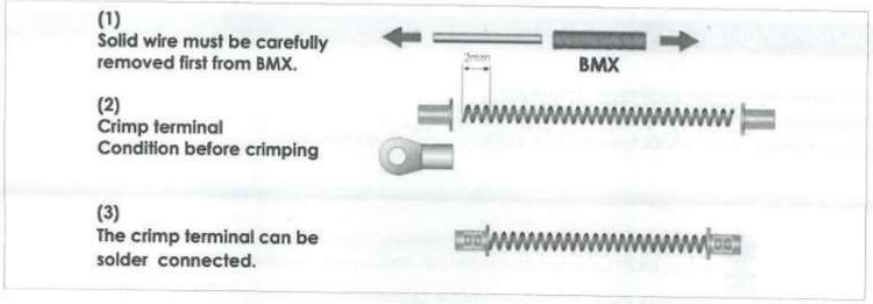

Section 2 - Helix Wire Specification

BioMetal Helix	Helix O.D.	Wire Res	Typ Cur	Wire Dia	Recovery	Activation	Contracted
	mm	Ω / m	mA	μm	Force gr	Temp ° C	length mm
BMX5020	0.20	3,600	50~100	50	3	70	20
BMX7520	0.30	1,600	70~120	75	5	70	20
BMX10020	0.40	900	100~150	100	12	70	20
BMX15020	0.60	400	200~300	150	30	70	20

Section 3 - Applications

A: Hanging a weight on the BMX

Hang a weight on the BMX and then heat it, and it will lift the weight.
Although it can produce a strong lifting force, the suitable weight (up to "recovery force" in table above) ingrams.
With a heavier weight hung on it, it may not return to its original length.
Applying too great force to it during heating will shorten its useful life.
The lighter the load, the longer will be its useful life.

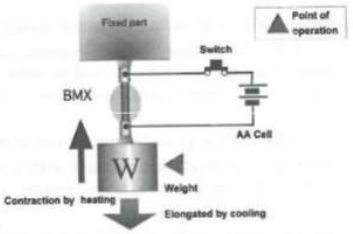

B: Use of a spring

Connect the BMX with the spring supplied so that they pull against each other.
Adjust the spring to a tension weaker than the contracting force of a heated BMX.
When heated, it pulls the spring. When cooled, it is elongated by the spring.
The contracting force of a heated BMX is by far stronger than the force required to elongate it at room temperature.

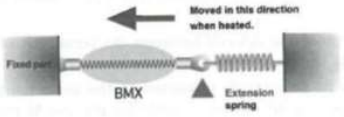

C: Differential System

Connect two BMXs together so that they pull against each other.
Note: Heat only one of these BMXs at time.
No movement can be obtained if both of them are heated.

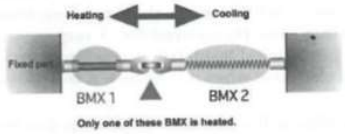

Section 4 - Precautions

- Exercise care not to feed an excessive amount of current through the BMX, or it may be dangerously overheated.
- Do not heat the BMX by the flame of a lighter, or it would be broken or might burn.
- The numerical values given in this instruction manual are only a guide; they are not guaranteed values. We shall not be liable for any damages resulting from the use of this product.
- Although the material of this product is excellent in corrosion resistance, prolonged use of the product in water or in damp places may make it easy to break.
- Specifications are subject to change without prior notice due to improvements in quality or performance.

Requests from Manufacturer

- ○ We cannot answer any technical questions over the telephone.
- ○ For technical inquiries, please use our inquiry form on our web-site.
- ○ More detailed information on the BMX Series will be available on our company's home page.

BioMetal Actuator Department: 3-43-15, Omori-kita, Ota-ku, Tokyo 143-0016, Japan
Phone: (03)5735-2833, Fax: (03)3742-2701 URL: http://www.toki.co.jp/biometal

2008.10

Instructions to install BMX to crimp ring terminal




Bibliography

[1] Hewett, Baecker, Card, Carey, Gasen, Mantei, *et al.* ACM SIGCHI Curricula for Human-Computer Interaction. Available: http://old.sigchi.org/cdg/cdg2.html#2_1

[2] L. R. Quitadamo, M. G. Marciani, G. C. Cardarilli, and L. Bianchi, "Describing Different Brain Computer Interface Systems Through a Unique Model: A UML Implementation," *Neuroinformatics,* vol. 6, pp. 81-96, 2008.

[3] L. R. Quitadamo, F. Cavrini, L. Sbernini, F. Riillo, L. Bianchi, S. Seri, *et al.*, "Support vector machines to detect physiological patterns for EEG and EMG-based human–computer interaction: a review," *Journal of Neural Engineering,* vol. 14, p. 011001, 2017.

[4] R. A. Ramadan and A. V. Vasilakos, "Brain computer interface: control signals review," *Neurocomputing,* vol. 223, pp. 26-44, 2/5/ 2017.

[5] C. J. De Luca, "Electromyography," *Encyclopedia of Medical Devices and Instrumentation,* pp. 98-109, 2006.

[6] M. A. Oskoei and H. Hu, "Myoelectric control systems—A survey," *Biomedical Signal Processing and Control,* vol. 2, pp. 275-294, 2007.

[7] L. J. Hargrove, K. Englehart, and B. Hudgins, "A Comparison of Surface and Intramuscular Myoelectric Signal Classification," *Biomedical Engineering, IEEE Transactions on,* vol. 54, pp. 847-853, 2007.

[8] M. H. Mohd Zaini and S. A. Ahmad, "Surgical and non-surgical prosthetic hands control: A review," pp. 634-637, 2011.

[9] A. D. Roche, H. Rehbaum, D. Farina, and O. C. Aszmann, "Prosthetic Myoelectric Control Strategies: A Clinical Perspective," *Current Surgery Reports,* vol. 2, pp. 1-11, 2014.

[10] M. Zecca, S. Micera, M. Carrozza, and P. Dario, "Control of multifunctional prosthetic hands by processing the electromyographic signal," *Critical Reviews™ in Biomedical Engineering,* vol. 30, 2002.

[11] O. W. Samuel, M. G. Asogbon, Y. Geng, A. H. Al-Timemy, S. Pirbhulal, N. Ji, *et al.*, "Intelligent EMG Pattern Recognition Control Method for Upper-Limb Multifunctional Prostheses: Advances, Current Challenges, and Future Prospects," *IEEE Access,* vol. 7, pp. 10150-10165, 2019.

[12] N. Nazmi, M. Abdul Rahman, S.-I. Yamamoto, S. Ahmad, H. Zamzuri, and S. Mazlan, "A Review of Classification Techniques of EMG Signals during Isotonic and Isometric Contractions," *Sensors,* vol. 16, p. 1304, 2016.

[13] T. G. Supuk, A. K. Skelin, and M. Cic, "Design, development and testing of a low-cost sEMG system and its use in recording muscle activity in human gait," *Sensors,* vol. 14, pp. 8235-8258, 2014.

[14] S. Pizzolato, L. Tagliapietra, M. Cognolato, M. Reggiani, H. Müller, and M. Atzori, "Comparison of six electromyography acquisition setups on hand movement classification tasks," *PloS one,* vol. 12, pp. e0186132-e0186132, 2017.

[15] A. Phinyomark and E. Scheme, "A feature extraction issue for myoelectric control based on wearable EMG sensors," in *2018 IEEE Sensors Applications Symposium (SAS)*, 2018, pp. 1-6.

[16] D. J. Hewson, J. Y. Hogrel, Y. Langeron, and J. Duchêne, "Evolution in impedance at the electrode-skin interface of two types of surface EMG electrodes during long-term recordings," *Journal of Electromyography and Kinesiology,* vol. 13, pp. 273-279, 6// 2003.

[17] S. Day. (2002, Date Accessed: April 4, 2016). Important factors in surface EMG measurement. *Calgary: Bortech Biomedical Ltd*. Available: http://www.bortec.ca/Images/pdf/EMG%20measurement%20and%20recording.pdf

[18] G. De Luca. (2003, Date Accessed: April 18, 2016). Fundamental concepts in EMG signal acquisition. Available: https://www.delsys.com/Attachments_pdf/WP_Sampling1-4.pdf

[19] C. J. De Luca. (2002, Date Accessed: March 16, 2016). Surface electromyography: Detection and recording. Available: http://www.delsys.com/Attachments_pdf/WP_SEMGintro.pdf

[20] C. J. De Luca, L. Donald Gilmore, M. Kuznetsov, and S. H. Roy, "Filtering the surface EMG signal: Movement artifact and baseline noise contamination," *Journal of Biomechanics,* vol. 43, pp. 1573-1579, 2010.

[21] R. Merletti, A. Botter, A. Troiano, E. Merlo, and M. A. Minetto, "Technology and instrumentation for detection and conditioning of the surface electromyographic signal: state of the art," *Clinical biomechanics (Bristol, Avon),* vol. 24, pp. 122-134, 2009.

[22] P. Geethanjali, "Myoelectric control of prosthetic hands: state-of-the-art review," *Medical Devices (Auckland, N.Z.),* vol. 9, pp. 247-255, 07/27 2016.
[23] P. Erik Scheme MSc and P. Kevin Englehart PhD, "Electromyogram pattern recognition for control of powered upper-limb prostheses: State of the art and challenges for clinical use," *Journal of rehabilitation research and development,* vol. 48, p. 643, 2011.
[24] L. J. Hargrove, E. J. Scheme, K. B. Englehart, and B. S. Hudgins, "Multiple Binary Classifications via Linear Discriminant Analysis for Improved Controllability of a Powered Prosthesis," *Neural Systems and Rehabilitation Engineering, IEEE Transactions on,* vol. 18, pp. 49-57, 2010.
[25] N. JIANG and D. Farina, "Myoelectric control of upper limb prosthesis: current status, challenges and recent advances," *Frontiers in Neuroengineering,* 2014.
[26] M. Ortiz-Catalan, F. Rouhani, R. Brånemark, and B. Håkansson, "Offline accuracy: A potentially misleading metric in myoelectric pattern recognition for prosthetic control," in *2015 37th Annual International Conference of the IEEE Engineering in Medicine and Biology Society (EMBC)*, 2015, pp. 1140-1143.
[27] N. Jiang, I. Vujaklija, H. Rehbaum, B. Graimann, and D. Farina, "Is Accurate Mapping of EMG Signals on Kinematics Needed for Precise Online Myoelectric Control?," *IEEE Transactions on Neural Systems and Rehabilitation Engineering,* vol. 22, pp. 549-558, 2014.
[28] I. Vujaklija, A. D. Roche, T. Hasenoehrl, A. Sturma, S. Amsuess, D. Farina*, et al.*, "Translating Research on Myoelectric Control into Clinics—Are the Performance Assessment Methods Adequate?," *Frontiers in Neurorobotics,* vol. 11, 2017-February-14 2017.
[29] A. Phinyomark, F. Quaine, S. Charbonnier, C. Serviere, F. Tarpin-Bernard, and Y. Laurillau, "EMG feature evaluation for improving myoelectric pattern recognition robustness," *Expert Systems with Applications,* vol. 40, pp. 4832-4840, 9/15/ 2013.
[30] D. Incorporated. *DelSys Incorporated*. Available: https://www.delsys.com/
[31] I. Motion Lab Systems. *Motion Lab Systems, Inc*. Available: https://www.motion-labs.com/
[32] B. Bioengineering. *BTS Bioengineering*. Available: www.btsbioengineering.com/
[33] S. Benatti, F. Casamassima, B. Milosevic, E. Farella, P. Schonle, S. Fateh*, et al.*, "A Versatile Embedded Platform for EMG Acquisition and Gesture Recognition," *Biomedical Circuits and Systems, IEEE Transactions on,* vol. PP, pp. 1-1, 2015.
[34] S. Benatti, B. Milosevic, F. Casamassima, P. Schonle, P. Bunjaku, S. Fateh*, et al.*, "EMG-based hand gesture recognition with flexible analog front end," in *Biomedical Circuits and Systems Conference (BioCAS), 2014 IEEE*, 2014, pp. 57-60.
[35] P. Schönle, F. Schulthess, S. Fateh, R. Ulrich, F. Huang, T. Burger*, et al.*, "A DC-connectable multi-channel biomedical data acquisition ASIC with mains frequency cancellation," in *2013 Proceedings of the ESSCIRC (ESSCIRC)*, 2013, pp. 149-152.
[36] A. Nikas, L. Klein, A. Holzberger, J. Hauer, M. Voelker, C. Hoppe*, et al.*, "ASIC design of an implantable system for improved control of hand prosthesis," in *2016 IEEE Biomedical Circuits and Systems Conference (BioCAS)*, 2016, pp. 380-383.
[37] Y. Yao-Ming and L. Rong-Chin, "A Simple and Portable Preamplifier for Multichannel Intracortical Recordings Using Commercial Components," in *Biomedical Engineering and Informatics, 2009. BMEI '09. 2nd International Conference on*, 2009, pp. 1-6.
[38] A. Cosmanescu, B. Miller, T. Magno, A. Ahmed, and I. Kremenic, "Design and Implementation of a Wireless (BluetoothÂ®) Four Channel Bio-Instrumentation Amplifier and Digital Data Acquisition Device with User-Selectable Gain, Frequency, and Driven Reference," *Engineering in Medicine and Biology Society, 2006. EMBS '06. 28th Annual International Conference of the IEEE,* pp. 2053-2056, Aug. 30 2006-Sept. 3 2006 2006.
[39] P. Geethanjali and K. K. Ray, "A Low-Cost Real-Time Research Platform for EMG Pattern Recognition-Based Prosthetic Hand," *Mechatronics, IEEE/ASME Transactions on,* vol. PP, pp. 1-8, 2014.
[40] V. Rama Raju, "Design and Development of Advanced Multi-channel EMG Micro Electrode Recording System," Singapore, 2019, pp. 179-183.
[41] R. M. Rangayyan, *Biomedical signal analysis* vol. 33: John Wiley & Sons, 2015.
[42] T. Moritani, D. Stegeman, and R. Merletti, "Basic physiology and biophycs of EMG signal generation," in *Electromyography: physiology, engineering, and non-invasive applications*, R. Merletti and P. Parker, Eds., ed: John Wiley & Sons, 2004.
[43] D. Farina, N. Jiang, H. Rehbaum, A. Holobar, B. Graimann, H. Dietl*, et al.*, "The Extraction of Neural Information from the Surface EMG for the Control of Upper-Limb Prostheses: Emerging Avenues and Challenges," 2014.
[44] E. Clancy, E. L. Morin, and R. Merletti, "Sampling, noise-reduction and amplitude estimation issues in surface electromyography," *Journal of Electromyography and Kinesiology,* vol. 12, pp. 1-16, 2002.

[45] R. N. Khushaba, "Application of Biosignal-Driven Intelligent Systems for Multifunction Prosthesis Control," University of Technology, Sydney, 2010.

[46] R. G. E. Clement, K. E. Bugler, and C. W. Oliver, "Bionic prosthetic hands: A review of present technology and future aspirations," *Surgeon,* vol. 9, pp. 336-340, 2011.

[47] A. M. Simon, L. J. Hargrove, B. A. Lock, and T. A. Kuiken, "A strategy for minimizing the effect of misclassifications during real time pattern recognition myoelectric control," in *Engineering in Medicine and Biology Society, 2009. EMBC 2009. Annual International Conference of the IEEE*, 2009, pp. 1327-1330.

[48] S. Lewis, M. Friedrich Russold, H. Dietl, R. Ruff, T. Dorge, K. Hoffmann*, et al.*, "Acquisition of muscle activity with a fully implantable multi-channel measurement system," in *Instrumentation and Measurement Technology Conference (I2MTC), 2012 IEEE International*, 2012, pp. 996-999.

[49] E. N. Kamavuako, E. J. Scheme, and K. B. Englehart, "Combined surface and intramuscular EMG for improved real-time myoelectric control performance," *Biomedical Signal Processing and Control,* vol. 10, pp. 102-107, 2014.

[50] J. Xu, S. Mitra, C. V. Hoof, R. Yazicioglu, and K. A. A. Makinwa, "Active Electrodes for Wearable EEG Acquisition: Review and Electronics Design Methodology," *IEEE Reviews in Biomedical Engineering,* vol. PP, pp. 1-1, 2017.

[51] H. J. Hermens, B. Freriks, C. Disselhorst-Klug, and G. Rau, "Development of recommendations for SEMG sensors and sensor placement procedures," *Journal of electromyography and Kinesiology,* vol. 10, pp. 361-374, 2000.

[52] R. Merletti and H. J. Hermens, "Detection and conditioning of the surface EMG signal," in *Electromyography: physiology, engineering, and non-invasive applications*, R. Merletti and P. Parker, Eds., ed: John Wiley & Sons, 2004.

[53] R. K. Jain, S. Datta, and S. Majumder, "Design and Control of an EMG Driven IPMC Based Artificial Muscle Finger," in *Computational Intelligence in Electromyography Analysis - A Perspective on Current Applications and Future Challenges*, ed, 2012, pp. 363-390.

[54] Y. Li, X. Chen, X. Zhang, and P. Zhou, "Several practical issues toward implementing myoelectric pattern recognition for stroke rehabilitation," *Medical Engineering & Physics,* vol. 36, pp. 754-760, 2014.

[55] J. Liu and P. Zhou, "A Novel Myoelectric Pattern Recognition Strategy for Hand Function Restoration After Incomplete Cervical Spinal Cord Injury," *Neural Systems and Rehabilitation Engineering, IEEE Transactions on,* vol. 21, pp. 96-103, 2013.

[56] X. Zhang and P. Zhou, "High-Density Myoelectric Pattern Recognition Toward Improved Stroke Rehabilitation," *Biomedical Engineering, IEEE Transactions on,* vol. 59, pp. 1649-1657, 2012.

[57] E. Mastinu, M. Ortiz-Catalan, and B. Hakansson, "Analog Front-Ends comparison in the way of a portable, low-power and low-cost EMG controller based on pattern recognition EMBC 2015," in *Engineering in Medicine and Biology Society (EMBC), 2015 37th Annual International Conference of the IEEE*, 2015, pp. 2111-2114.

[58] A. W. Wilson, Y. G. Losier, P. A. Parker, and D. F. Lovely, "A Bus-Based Smart Myoelectric Electrode/Amplifier--System Requirements," *Instrumentation and Measurement, IEEE Transactions on,* vol. 60, pp. 3290-3299, 2011.

[59] A. W. Wilson, Y. G. Losier, P. A. Parker, and D. F. Lovely, "A bus-based smart myoelectric electrode/amplifier," in *Medical Measurements and Applications Proceedings (MeMeA), 2010 IEEE International Workshop on*, 2010, pp. 86-91.

[60] L. H. Smith, L. J. Hargrove, B. A. Lock, and T. A. Kuiken, "Determining the Optimal Window Length for Pattern Recognition-Based Myoelectric Control: Balancing the Competing Effects of Classification Error and Controller Delay," *Neural Systems and Rehabilitation Engineering, IEEE Transactions on,* vol. 19, pp. 186-192, 2011.

[61] E. M. Spinelli, R. Pallas-Areny, and M. A. Mayosky, "AC-coupled front-end for biopotential measurements," *Biomedical Engineering, IEEE Transactions on,* vol. 50, pp. 391-395, 2003.

[62] M. J. Burke and D. T. Gleeson, "A micropower dry-electrode ECG preamplifier," *Biomedical Engineering, IEEE Transactions on,* vol. 47, pp. 155-162, 2000.

[63] S. Yacoub, K. Raoof, and H. Eleuch, "Filtering of Cardiac and Power Line in Surface Respiratory EMG Signal."

[64] M. Golabbakhsh, M. Masoumzadeh, and M. F. Sabahi, "ECG and power line noise removal from respiratory EMG signal using adaptive filters," *Majlesi Journal of Electrical Engineering,* vol. 5, 2011.

[65] A. B. Sankar, D. Kumar, and K. Seethalakshmi, "Performance study of various adaptive filter algorithms for noise cancellation in respiratory signals," *Signal Processing: An International Journal (SPIJ),* vol. 4, p. 267, 2010.

[66] G. Li, Y. Li, Z. Zhang, Y. Geng, and R. Zhou, "Selection of sampling rate for EMG pattern recognition based prosthesis control," *Engineering in Medicine and Biology Society (EMBC), 2010 Annual International Conference of the IEEE,* pp. 5058-5061, Aug. 31 2010-Sept. 4 2010 2010.

[67] C. Cipriani, C. Antfolk, M. Controzzi, G. Lundborg, B. Rosen, M. C. Carrozza*, et al.*, "Online Myoelectric Control of a Dexterous Hand Prosthesis by Transradial Amputees," *Neural Systems and Rehabilitation Engineering, IEEE Transactions on,* vol. 19, pp. 260-270, 2011.

[68] M. A. Oskoei and H. Hu, "Support Vector Machine-Based Classification Scheme for Myoelectric Control Applied to Upper Limb," *Biomedical Engineering, IEEE Transactions on,* vol. 55, pp. 1956-1965, 2008.

[69] A. Phinyomark, A. Nuidod, P. Phukpattaranont, and C. Limsakul, "Feature extraction and reduction of wavelet transform coefficients for EMG pattern classification," *Elektronika ir Elektrotechnika,* vol. 122, pp. 27-32, 2012.

[70] C. Jun-Uk, M. Inhyuk, and M. Mu-Seong, "A Real-Time EMG Pattern Recognition System Based on Linear-Nonlinear Feature Projection for a Multifunction Myoelectric Hand," *Biomedical Engineering, IEEE Transactions on,* vol. 53, pp. 2232-2239, 2006.

[71] X. Zhang and P. Zhou, "Sample entropy analysis of surface EMG for improved muscle activity onset detection against spurious background spikes," *Journal of Electromyography and Kinesiology,* vol. 22, pp. 901-907, 2012.

[72] R. N. Khushaba, S. Kodagoda, M. Takruri, and G. Dissanayake, "Toward improved control of prosthetic fingers using surface electromyogram (EMG) signals," *Expert Systems with Applications,* vol. 39, pp. 10731-10738, 2012.

[73] Q. Sun, Y. Sun, X. Ding, and Z. Ma, "Onset determination of muscle contraction in surface electromyography signals analysis," *Information Acquisition, 2005 IEEE International Conference on,* 2005.

[74] M. Asghari Oskoei and H. Hu, "Myoelectric control systems—A survey," *Biomedical Signal Processing and Control,* vol. 2, pp. 275-294, 2007.

[75] P. W. Hodges and B. H. Bui, "A comparison of computer-based methods for the determination of onset of muscle contraction using electromyography," *Electroencephalography and Clinical Neurophysiology/Electromyography and Motor Control,* vol. 101, 1996.

[76] X. Qi, Q. Yazhi, Y. Lei, and H. Jiping, "An Adaptive Algorithm for the Determination of the Onset and Offset of Muscle Contraction by EMG Signal Processing," *Neural Systems and Rehabilitation Engineering, IEEE Transactions on,* vol. 21, pp. 65-73, 2013.

[77] X. Li, P. Zhou, and A. Aruin, "Teager–Kaiser Energy Operation of Surface EMG Improves Muscle Activity Onset Detection," *Annals of Biomedical Engineering,* vol. 35, pp. 1532-1538, 2007/09/01 2007.

[78] D. Yang, H. Zhang, Y. Gu, and H. Liu, "Accurate EMG onset detection in pathological, weak and noisy myoelectric signals," *Biomedical Signal Processing and Control,* vol. 33, pp. 306-315, 3// 2017.

[79] T. R. Farrell and R. F. Weir, "The Optimal Controller Delay for Myoelectric Prostheses," *Neural Systems and Rehabilitation Engineering, IEEE Transactions on,* vol. 15, pp. 111-118, 2007.

[80] T. R. Farrell and R. F. f. Weir, "Analysis window induced controller delay for multifunctional prostheses," *Proceedings of the 2008 MyoElectric Controls/Powered Prosthetics Symposium,* 2008.

[81] M. Hakonen, H. Piitulainen, and A. Visala, "Current state of digital signal processing in myoelectric interfaces and related applications," *Biomedical Signal Processing and Control,* vol. 18, pp. 334-359, 2015/04/01/ 2015.

[82] B. Hudgins, P. Parker, and R. N. Scott, "A new strategy for multifunction myoelectric control," *Biomedical Engineering, IEEE Transactions on,* vol. 40, 1993.

[83] Y.-C. Du, C.-H. Lin, L.-Y. Shyu, and T. Chen, "Portable hand motion classifier for multi-channel surface electromyography recognition using grey relational analysis," *Expert Systems with Applications,* vol. 37, pp. 4283-4291, 2010.

[84] Y. Huang, K. B. Englehart, B. Hudgins, and A. D. Chan, "A Gaussian mixture model based classification scheme for myoelectric control of powered upper limb prostheses," *Biomedical Engineering, IEEE Transactions on,* vol. 52, pp. 1801-1811, 2005.

[85] A. Phinyomark, P. Phukpattaranont, and C. Limsakul, "Feature reduction and selection for EMG signal classification," *Expert Systems with Applications,* vol. 39, 2012.

[86] A. Phinyomark, C. Limsakul, and P. Phukpattaranont, "Application of wavelet analysis in EMG feature extraction for pattern classification," *Measurement Science Review,* vol. 11, 2011.

[87] R. N. Khushaba, M. Takruri, J. V. Miro, and S. Kodagoda, "Towards limb position invariant myoelectric pattern recognition using time-dependent spectral features," *Neural Networks,* vol. 55, pp. 42-58, 2014/07/01/ 2014.

[88] E. Gokgoz and A. Subasi, "Comparison of decision tree algorithms for EMG signal classification using DWT," *Biomedical Signal Processing and Control,* vol. 18, pp. 138-144, 2015/04/01/ 2015.

[89] K. Xing, P. Yang, J. Huang, Y. Wang, and Q. Zhu, "A real-time EMG pattern recognition method for virtual myoelectric hand control," *Neurocomputing,* vol. 136, pp. 345-355, 7/20/ 2014.
[90] K. Nazarpour, A. R. Sharafat, and S. M. P. Firoozabadi, "Surface EMG Signal Classification Using a Selective Mix of Higher Order Statistics," *Engineering in Medicine and Biology Society, 2005. IEEE-EMBS 2005. 27th Annual International Conference of the,* pp. 4208-4211, 2005.
[91] A. Khadivi, K. Nazarpour, and H. S. Zadeh, "SEMG classification for upper-limb prosthesis control using higher order statistics," *Acoustics, Speech, and Signal Processing, 2005. Proceedings. (ICASSP '05). IEEE International Conference on,* vol. 5, pp. 385-388, 2005.
[92] K. Nazarpour, A. R. Sharafat, and S. M. P. Firoozabadi, "Application of Higher Order Statistics to Surface Electromyogram Signal Classification," *Biomedical Engineering, IEEE Transactions on,* vol. 54, pp. 1762-1769, 2007.
[93] K. C. Chua, V. Chandran, U. R. Acharya, and C. M. Lim, "Application of higher order statistics/spectra in biomedical signals-A review," *Medical Engineering and Physics,* vol. 32, pp. 679-689, 2010.
[94] A. Phinyomark, P. Phukpattaranont, and C. Limsakul, "Fractal analysis features for weak and single-channel upper-limb EMG signals," *Expert Systems with Applications,* vol. 39, pp. 11156-11163, 2012.
[95] A. Phinyomark, F. Quaine, S. Charbonnier, C. Serviere, F. Tarpin-Bernard, and Y. Laurillau, "Feature extraction of the first difference of EMG time series for EMG pattern recognition," *Computer Methods and Programs in Biomedicine,* vol. 117, pp. 247-256, 2014/11/01/ 2014.
[96] M. Jordanić, M. Rojas-Martínez, M. Mañanas, J. Alonso, and H. Marateb, "A Novel Spatial Feature for the Identification of Motor Tasks Using High-Density Electromyography," *Sensors,* vol. 17, p. 1597, 2017.
[97] J. Liu, "Feature dimensionality reduction for myoelectric pattern recognition: A comparison study of feature selection and feature projection methods," *Medical Engineering & Physics,* vol. 36, pp. 1716-1720, 2014/12/01/ 2014.
[98] G. R. Naik, S. E. Selvan, M. Gobbo, A. Acharyya, and H. T. Nguyen, "Principal Component Analysis Applied to Surface Electromyography: A Comprehensive Review," *IEEE Access,* vol. 4, pp. 4025-4037, 2016.
[99] S. Theodoridis and K. Koutroumbas, *Pattern recognition*, 4th ed.: Elsevier, 2009.
[100] A. Phinyomark, H. Hu, P. Phukpattaranont, and C. Limsakul, "Application of linear discriminant analysis in dimensionality reduction for hand motion classification," *Measurement Science Review,* vol. 12, pp. 82-89, 2012.
[101] I. Mesa, A. Rubio, I. Tubia, J. De No, and J. Diaz, "Channel and feature selection for a surface electromyographic pattern recognition task," *Expert Systems with Applications,* vol. 41, pp. 5190-5200, 2014/09/01/ 2014.
[102] F. E. R. Mattioli, E. A. Lamounier, A. Cardoso, A. B. Soares, and A. O. Andrade, "Classification of EMG signals using artificial neural networks for virtual hand prosthesis control," in *Engineering in Medicine and Biology Society,EMBC, 2011 Annual International Conference of the IEEE*, 2011, pp. 7254-7257.
[103] L. Feng, Z. Yu, and G. Kening, "Pattern recognition of Finger Motion's EMG signal based on improved BP neural networks," in *Computer Science and Network Technology (ICCSNT), 2011 International Conference on*, 2011, pp. 1266-1269.
[104] X. Wu and V. Kumar, "The top ten algorithms in data mining." vol. 9, ed: Chapman & Hall, 2009.
[105] N. Cristianini and J. Shawe-Taylor, *An introduction to support vector machines and other kernel-based learning methods*: Cambridge university press, 2000.
[106] A. Alkan and M. Günay, "Identification of EMG signals using discriminant analysis and SVM classifier," *Expert Systems with Applications,* vol. 39, pp. 44-47, 2012.
[107] J. Liu, "Adaptive myoelectric pattern recognition toward improved multifunctional prosthesis control," *Medical Engineering & Physics,* vol. 37, pp. 424-430, 2015/04/01/ 2015.
[108] K. Englehart and B. Hudgins, "A robust, real-time control scheme for multifunction myoelectric control," *Biomedical Engineering, IEEE Transactions on,* vol. 50, pp. 848-854, 2003.
[109] J. T. Belter and A. M. Dollar, "Performance characteristics of anthropomorphic prosthetic hands," 2011.
[110] J. T. Belter, J. L. Segil, A. M. Dollar, and R. F. Weir, "Mechanical design and performance specifications of anthropomorphic prosthetic hands: A review," *Journal of Rehabilitation Research and Development,* vol. 50, pp. 599-618, 2013.
[111] J. S. Martell and G. Gini, "Robotic hands: Design review and proposal of new design process," *World Academy of Science, Engineering and Technology,* vol. 26, pp. 85-90, 2007.
[112] D. A. Bennett, S. A. Dalley, D. Truex, and M. Goldfarb, "A Multigrasp Hand Prosthesis for Providing Precision and Conformal Grasps," *Mechatronics, IEEE/ASME Transactions on,* vol. PP, pp. 1-8, 2014.
[113] R. Deimel and O. Brock, "A novel type of compliant and underactuated robotic hand for dexterous grasping," *The International Journal of Robotics Research,* vol. 35, pp. 161-185, 2016.
[114] C. Lee, M. Kim, Y. J. Kim, N. Hong, S. Ryu, H. J. Kim*, et al.*, "Soft robot review," *International Journal of Control, Automation and Systems,* vol. 15, pp. 3-15, 2017/02/01 2017.

[115] M. Ciocarlie, C. Lackner, and P. Allen, "Soft Finger Model with Adaptive Contact Geometry for Grasping and Manipulation Tasks," in *EuroHaptics Conference, 2007 and Symposium on Haptic Interfaces for Virtual Environment and Teleoperator Systems. World Haptics 2007. Second Joint*, 2007, pp. 219-224.
[116] B. Robert, "Exoskeletons and robotic prosthetics: a review of recent developments," *Industrial Robot: An International Journal,* vol. 36, pp. 421-427, 2009.
[117] Q. Meng, S. Xiang, and H. Yu, "Soft Robotic Hand Exoskeleton Systems: Review and Challenges Surrounding the Technology," 2017.
[118] E. N. Gama Melo, O. F. Aviles Sanchez, and D. Amaya Hurtado, "Anthropomorphic robotic hands: a review," *Ingeniería y Desarrollo,* vol. 32, pp. 279-313, 2014.
[119] V. K. Nanayakkara, G. Cotugno, N. Vitzilaios, D. Venetsanos, T. Nanayakkara, and M. N. Sahinkaya, "The Role of Morphology of the Thumb in Anthropomorphic Grasping: A Review," *Frontiers in Mechanical Engineering,* vol. 3, 2017-June-30 2017.
[120] J. L. Pons, R. Ceres, and F. Pfeiffer, "Multifingered dextrous robotics hand design and control: a review," *Robotica,* vol. 17, pp. 661-674, 1999.
[121] U. Scarcia, "Design and Control of Robotic Hands," Alma Mater Studiorum University of Bologna, 2015.
[122] P. Kyberd and B. Jones, "The use of underactuation in prosthetic grasping," 2011.
[123] L. Birglen, T. Laliberté, and C. M. Gosselin, *Underactuated robotic hands* vol. 40: Springer, 2007.
[124] B. Peerdeman, M. Valori, D. Brouwer, E. Hekman, S. Misra, and S. Stramigioli, "UT hand I: A lock-based underactuated hand prosthesis," *Mechanism and Machine Theory,* vol. 78, pp. 307-323, 2014/08/01/ 2014.
[125] V. Bundhoo, E. Haslam, B. Birch, and E. J. Park, "A shape memory alloy-based tendon-driven actuation system for biomimetic artificial fingers, part I: design and evaluation," *Robotica,* vol. 27, pp. 131-146, 2009.
[126] I. Godler and T. Sonoda, "A five fingered robotic hand prototype by using twist drive," *Robotics (ISR), 2010 41st International Symposium on and 2010 6th German Conference on Robotics (ROBOTIK),* pp. 1-6, 2010.
[127] W. Chen, C. Xiong, M. Liu, and L. Mao, "Characteristics analysis and mechanical implementation of human finger movements," in *2014 IEEE International Conference on Robotics and Automation (ICRA)*, 2014, pp. 403-408.
[128] A. D. Deshpande, X. Zhe, M. J. V. Weghe, B. H. Brown, J. Ko, L. Y. Chang*, et al.*, "Mechanisms of the Anatomically Correct Testbed Hand," *Mechatronics, IEEE/ASME Transactions on,* vol. 18, pp. 238-250, 2013.
[129] Z. Xu and E. Todorov, "Design of a Highly Biomimetic Anthropomorphic Robotic Hand towards Artificial Limb Regeneration."
[130] X. Zhe, E. Todorov, B. Dellon, and Y. Matsuoka, "Design and analysis of an artificial finger joint for anthropomorphic robotic hands," *Robotics and Automation (ICRA), 2011 IEEE International Conference on,* pp. 5096-5102, 9-13 May 2011.
[131] G. Palli, G. Borghesan, and C. Melchiorri, "Modeling, identification, and control of tendon-based actuation systems," *Robotics, IEEE Transactions on,* vol. 28, pp. 277-290, 2012.
[132] C. Gosselin, F. Pelletier, and T. Laliberte, "An anthropomorphic underactuated robotic hand with 15 dofs and a single actuator," in *Robotics and Automation, 2008. ICRA 2008. IEEE International Conference on*, 2008, pp. 749-754.
[133] S. Krut, "A Force-Isotropic Underactuated Finger," in *Proceedings of the 2005 IEEE International Conference on Robotics and Automation*, 2005, pp. 2314-2319.
[134] K. Xu and H. Liu, "Continuum Differential Mechanisms and Their Applications in Gripper Designs," *IEEE Transactions on Robotics,* vol. 32, pp. 754-762, 2016.
[135] B. Lionel and M. G. Clément, "Force Analysis of Connected Differential Mechanisms: Application to Grasping," *The International Journal of Robotics Research,* vol. 25, pp. 1033-1046, 2006/10/01 2006.
[136] L. Birglen and C. M. Gosselin, "Geometric design of three-phalanx underactuated fingers," *Journal of Mechanical Design,* vol. 128, pp. 356-364, 2006.
[137] R. Balasubramanian and A. M. Dollar, "Performance of serial underactuated mechanisms: Number of degrees of freedom and actuators," in *2011 IEEE/RSJ International Conference on Intelligent Robots and Systems*, 2011, pp. 1823-1829.
[138] S. Hirose and S. Ma, "Coupled tendon-driven multijoint manipulator," in *Robotics and Automation, 1991. Proceedings., 1991 IEEE International Conference on*, 1991, pp. 1268-1275 vol.2.
[139] L. Birglen and C. M. Gosselin, "Kinetostatic analysis of underactuated fingers," *Robotics and Automation, IEEE Transactions on,* vol. 20, pp. 211-221, 2004.
[140] S. Hirose and Y. Umetani, "The development of soft gripper for the versatile robot hand," *Mechanism and Machine Theory,* vol. 13, pp. 351-359, 1978/01/01/ 1978.
[141] S. Ma, S. Hirose, and H. Yoshinada, "Design and experiments for a coupled tendon-driven manipulator," *IEEE Control Systems,* vol. 13, pp. 30-36, 1993.

[142] L. Zollo, S. Roccella, E. Guglielmelli, M. C. Carrozza, and P. Dario, "Biomechatronic Design and Control of an Anthropomorphic Artificial Hand for Prosthetic and Robotic Applications," *Mechatronics, IEEE/ASME Transactions on,* vol. 12, pp. 418-429, 2007.

[143] S. A. Dalley, T. E. Wiste, T. J. Withrow, and M. Goldfarb, "Design of a Multifunctional Anthropomorphic Prosthetic Hand With Extrinsic Actuation," *IEEE/ASME Transactions on Mechatronics,* vol. 14, pp. 699-706, 2009.

[144] G. Jones, A. Rosendo, and R. Stopforth, "Prosthetic design directives: Low-cost hands within reach," in *Rehabilitation Robotics (ICORR), 2017 International Conference on*, 2017, pp. 1524-1530.

[145] M. Controzzi, C. Cipriani, and M. C. Carrozza, "Mechatronic design of a transradial cybernetic hand," in *2008 IEEE/RSJ International Conference on Intelligent Robots and Systems*, 2008, pp. 576-581.

[146] J. D. W. Madden, N. A. Vandesteeg, P. A. Anquetil, P. G. A. Madden, A. Takshi, R. Z. Pytel*, et al.*, "Artificial muscle technology: physical principles and naval prospects," *Oceanic Engineering, IEEE Journal of,* vol. 29, pp. 706-728, 2004.

[147] P. Tozzi, "Artificial muscle: the human chimera is the future," *Swiss Medical Weekly,* vol. 141, p. 13311, 2011.

[148] C. S. Haines, M. D. Lima, N. Li, G. M. Spinks, J. Foroughi, J. D. W. Madden*, et al.*, "Artificial Muscles from Fishing Line and Sewing Thread," *Science,* vol. 343, pp. 868-872, February 21, 2014 2014.

[149] E. Mattar, "A survey of bio-inspired robotics hands implementation: New directions in dexterous manipulation," *Robotics and Autonomous Systems,* vol. 61, pp. 517-544, 2013.

[150] P. S. Lobo, J. Almeida, and L. Guerreiro, "Shape Memory Alloys Behaviour: A Review," *Procedia Engineering,* vol. 114, pp. 776-783, 2015/01/01/ 2015.

[151] J. Mohd Jani, M. Leary, A. Subic, and M. A. Gibson, "A review of shape memory alloy research, applications and opportunities," *Materials & Design (1980-2015),* vol. 56, pp. 1078-1113, 2014/04/01/ 2014.

[152] D. H. Lee, J. H. Park, S. W. Park, M. H. Baeg, and J. Bae, "KITECH-Hand: A Highly Dexterous and Modularized Robotic Hand," *IEEE/ASME Transactions on Mechatronics,* vol. PP, pp. 1-1, 2016.

[153] N. S. Pollard and R. C. Gilbert, "Tendon arrangement and muscle force requirements for human-like force capabilities in a robotic finger," in *Robotics and Automation, 2002. Proceedings. ICRA '02. IEEE International Conference on*, 2002, pp. 3755-3762 vol.4.

[154] D. Aukes, S. Kim, P. Garcia, A. Edsinger, and M. R. Cutkosky, "Selectively compliant underactuated hand for mobile manipulation," in *2012 IEEE International Conference on Robotics and Automation*, 2012, pp. 2824-2829.

[155] Y. Huang, X. Zhang, J. Zhang, and C. Huang, "Mechanism design of underactuated robotic hand," in *2016 International Conference on Manipulation, Automation and Robotics at Small Scales (MARSS)*, 2016, pp. 1-6.

[156] M. C. Carrozza, G. Cappiello, G. Stellin, F. Zaccone, F. Vecchi, S. Micera*, et al.*, "A Cosmetic Prosthetic Hand with Tendon Driven Under-Actuated Mechanism and Compliant Joints: Ongoing Research and Preliminary Results," in *Robotics and Automation, 2005. ICRA 2005. Proceedings of the 2005 IEEE International Conference on*, 2005, pp. 2661-2666.

[157] F. Lotti, P. Tiezzi, G. Vassura, L. Biagiotti, G. Palli, and C. Melchiorri, "Development of UB Hand 3: Early Results," in *Robotics and Automation, 2005. ICRA 2005. Proceedings of the 2005 IEEE International Conference on*, 2005, pp. 4488-4493.

[158] M. Kaneko, T. Yamashita, and K. Tanie, "Basic considerations on transmission characteristics for tendon drive robots," in *Advanced Robotics, 1991. 'Robots in Unstructured Environments', 91 ICAR., Fifth International Conference on*, 1991, pp. 827-832 vol.1.

[159] G. Palli and C. Melchiorri, "Model and control of tendon-sheath transmission systems," *Robotics and Automation, 2006. ICRA 2006. Proceedings 2006 IEEE International Conference on,* pp. 988-993, 15-19 May 2006 2006.

[160] G. Palli and C. Melchiorri, "Optimal control of tendon-sheath transmission systems," in *Proc. of the IFAC Symposium on Robot Control*, 2006.

[161] G. Palli, G. Borghesan, and C. Melchiorri, "Tendon-based transmission systems for robotic devices: Models and control algorithms," *Robotics and Automation, 2009. ICRA'09. IEEE International Conference on,* pp. 4063-4068, 2009.

[162] Wu, x, T. rtz, C. May, B. Holz, C. Natale*, et al.*, "The twisted string actuation system: Modeling and control," *Advanced Intelligent Mechatronics (AIM), 2010 IEEE/ASME International Conference on,* pp. 1215-1220, 2010.

[163] G. Palli, C. Natale, C. May, C. Melchiorri, and T. Wurtz, "Modeling and Control of the Twisted String Actuation System," *Mechatronics, IEEE/ASME Transactions on,* vol. 18, pp. 664-673, 2013.

[164] G. Palli, S. Pirozzi, C. Natale, G. De Maria, and C. Melchiorri, "Mechatronic design of innovative robot hands: Integration and control issues," in *Advanced Intelligent Mechatronics (AIM), 2013 IEEE/ASME International Conference on*, 2013, pp. 1755-1760.
[165] G. Borghesan, G. Palli, and C. Melchiorri, "Design of tendon-driven robotic fingers: Modeling and control issues," in *Robotics and Automation (ICRA), 2010 IEEE International Conference on*, 2010, pp. 793-798.
[166] F. Ficuciello, G. Palli, C. Melchiorri, and B. Siciliano, "Experimental evaluation of postural synergies during reach to grasp with the UB hand IV," in *Intelligent Robots and Systems (IROS), 2011 IEEE/RSJ International Conference on*, 2011, pp. 1775-1780.
[167] S. Matsubara, S. Okamoto, and J. H. Lee, "Prosthetic Hand Using Shape Memory Alloy Type Artificial Muscle," *Proceedings of the International MultiConference of Engineers and Computer Scientists,* vol. 2, 2012.
[168] G. Gilardi, E. Haslam, V. Bundhoo, and E. J. Park, "A shape memory alloy-based tendon-driven actuation system for biomimetic artificial fingers, part II: modelling and control," *Robotica,* vol. 28, pp. 675-687, 2010.
[169] A. D. Price, A. Jnifene, and H. E. Naguib, "Design and control of a shape memory alloy based dexterous robot hand," *Smart Materials and Structures,* vol. 16, p. 1401, 2007.
[170] P. H. Chappell, "Making sense of artificial hands," *Journal of Medical Engineering and Technology,* vol. 35, pp. 1-18, 2011.
[171] A. M. Almassri, W. Z. Wan Hasan, S. A. Ahmad, A. J. Ishak, A. M. Ghazali, D. N. Talib*, et al.*, "Pressure Sensor: State of the Art, Design, and Application for Robotic Hand," *Journal of Sensors,* vol. 2015, p. 12, 2015.
[172] T. Taro, T. Toshimitsu, K. Takeo, K. Yasunori, S. Satoru, I. Masatsugu*, et al.*, "Adaptive grasping by multi fingered hand with tactile sensor based on robust force and position control," in *2008 IEEE International Conference on Robotics and Automation*, 2008, pp. 264-271.
[173] M. I. Tiwana, S. J. Redmond, and N. H. Lovell, "A review of tactile sensing technologies with applications in biomedical engineering," *Sensors and Actuators A: Physical,* vol. 179, pp. 17-31, 2012/06/01/ 2012.
[174] G. Palli and S. Pirozzi, "A miniaturized optical force sensor for tendon-driven mechatronic systems: Design and experimental evaluation," *Mechatronics,* vol. 22, pp. 1097-1111, 12// 2012.
[175] 3DPrinting.com. (2018, Date Accessed: January, 16). *What is 3D printing?* Available: https://3dprinting.com/what-is-3d-printing/
[176] E. Mastinu, M. Ortiz-Catalan, and B. Håkansson, "Analog front-ends comparison in the way of a portable, low-power and low-cost EMG controller based on pattern recognition," in *2015 37th Annual International Conference of the IEEE Engineering in Medicine and Biology Society (EMBC)*, 2015, pp. 2111-2114.
[177] K. Soundarapandian and M. Berarducci. (2010). Analog front-end design for ecg systems using delta-sigma adcs. *Application Report SBAA160A,* 1-11. Available: http://www.ti.com/lit/an/sbaa160a/sbaa160a.pdf
[178] C. J. De Luca, M. Kuznetsov, L. D. Gilmore, and S. H. Roy, "Inter-electrode spacing of surface EMG sensors: Reduction of crosstalk contamination during voluntary contractions," *Journal of Biomechanics,* vol. 45, pp. 555-561, 2012.
[179] Wikipedia. (2016, Date Accessed: March 2, 2016). *Forearm*. Available: https://en.wikipedia.org/wiki/Forearm
[180] A. Kay, *Operational amplifier noise: techniques and tips for analyzing and reducing noise*: Elsevier, 2012.
[181] M. W. Hann. (2013). Ultra Low Power, 18 bit Precision ECG Data Acquisition system. *Application Report SLAU516*. Available: http://www.ti.com/lit/ug/slau516/slau516.pdf
[182] B. Zhang and A. Buda. (2016, Date Accessed: May 8, 2016). Analog Front-End Design Considerations for RTD Ratiometric Temperature Measurements. *Analog Dialogue 50-03, March 2016 50*. Available: http://www.analog.com/library/analogdialogue/archives/50-03/rtd-ratio.html
[183] K. Chan. (2010). Design of differential filters for high-speed signal chains. *Application Report SLWA053B*. Available: http://www.ti.com/lit/an/slwa053b/slwa053b.pdf
[184] A. M. Van Rijn, A. Peper, and C. Grimbergen, "High-quality recording of bioelectric events Part 1. Interference reduction, theory and practice " *Medical and Biological Engineering and Computing,* vol. 28, pp. 389-397, 1990.
[185] A. van Rijn Metting, A. Peper, and C. Grimbergen, "High-quality recording of bioelectric events. Part 2. Low-noise, low-power multichannel amplifier design," *Medical & biological engineering & computing,* vol. 29, pp. 433-440, 1991.
[186] A. MettingVanRijn, A. Peper, and C. Grimbergen, "Amplifiers for bioelectric events: a design with a minimal number of parts," *Medical and Biological Engineering and Computing,* vol. 32, pp. 305-310, 1994.
[187] Texas Instruments Incorporated. (2005). INA128 Datasheet. Available: http://www.ti.com/lit/ds/sbos051b/sbos051b.pdf
[188] A. Rich, "Shielding and guarding," *Analog Dialogue,* vol. 17, pp. 8-13, 1983.
[189] S. W. Smith, "The scientist and engineer's guide to digital signal processing," 1997.

[190] H. Zumbahlen. (2007, Date Accessed: July 7, 2016). *Basic Linear Design*. Available: http://www.analog.com/library/analogDialogue/archives/43-09/linear_circuit_design_handbook.html
[191] B. C. Baker. (2003, Date Accessed: April 8, 2016). Select the Right Operational Amplifier for your Filtering Circuits. *ANALOG DESIGN NOTE ADN003*. Available: http://ww1.microchip.com/downloads/en/DeviceDoc/adn003.pdf
[192] H. Zumbahlen. (2007). Phase Relations in Active Filters. *Analog Dialogue 41(10)*. Available: http://www.analog.com/library/analogDialogue/archives/41-10/phase_relations.pdf
[193] Texas Instruments Incorporated. (1999). Analysis of the Sallen-Key Architecture. Available: http://www.ti.com/analog/docs/litabsmultiplefilelist.tsp?literatureNumber=sloa024b&docCategoryId=1&familyId=1463
[194] T. Wescott. (2015, Date Accessed: April 7, 2016). Sampling: What Nyquist Didn't Say, and What to Do About It. *Wescott Seminars*. Available: http://www.wescottdesign.com/articles/Sampling/sampling.pdf
[195] W. Kester. (2009). What the Nyquist criterion means to your sampled data system design. *Analog Devices,* 1-12. Available: http://www.analog.com/media/en/training-seminars/tutorials/MT-002.pdf
[196] R. H. Hosking. (2012). Critical Techniques for High-Speed A/D Converters in Real-Time Systems. Available: http://www.pentek.com/pildocs/8363/techother/HIGHSPEEDAD.PDF
[197] N. Fukaya, S. Toyama, T. Asfour, and R. Dillmann, "Design of the TUAT/Karlsruhe humanoid hand," *Intelligent Robots and Systems, 2000. (IROS 2000). Proceedings. 2000 IEEE/RSJ International Conference on,* vol. 3, pp. 1754-1759, 2000.
[198] W. Kester. (2005, Date Accessed: April 14, 2016). Which ADC Architecture Is Right for Your Application? *Analog Dialogue 39(6)*. Available: http://www.analog.com/library/analogdialogue/archives/39-06/architecture.html
[199] S. Park. (n.d.). Principles of Sigma-Delta Modulation for Analog-to-Digital Converters. *Motorola Digital Signal Processors*. Available: http://xanthippi.ceid.upatras.gr/people/psarakis/courses/DSP_APL/demos/APR8-sigma-delta.pdf
[200] Texas Instruments Incorporated. (2012). ADS1292 Datasheet. Available: http://www.ti.com/lit/ds/symlink/ads1292.pdf
[201] T. Instruments, "Analysis of the Sallen-Key Architecture," *Application Report,* 2002.
[202] L. D. Thede, *Practical analog and digital filter design*: Artech House New Jersey, 2005.
[203] L. D Paarmann, *Design and analysis of analog filters: A signal processing perspective*: Kluwer Academic Publishers, 2003.
[204] E. M. Spinelli, N. Martínez, M. A. Mayosky, and R. Pallàs-Areny, "A novel fully differential biopotential amplifier with DC suppression," *Biomedical Engineering, IEEE Transactions on,* vol. 51, pp. 1444-1448, 2004.
[205] J. Jerabek, J. Koton, R. Sotner, and K. Vrba, "Adjustable band-pass filter with current active elements: two fully-differential and single-ended solutions," *Analog integrated circuits and signal processing,* vol. 74, pp. 129-139, 2013.
[206] J. Ardizzoni and J. Pearson. (2015, Date Accessed: January 16th, 2017). High Speed Differential ADC Driver Design Considerations. Available: http://www.analog.com/media/en/technical-documentation/application-notes/AN-1026.pdf
[207] T. Kuehl. (2009). Using the infinite-gain, MFB filter topology in fully differential active filters. *Analog Applications Journal*. Available: http://www.ti.com/lit/an/slyt343/slyt343.pdf
[208] O. Casas and R. Pallas-Areny, "Basics of analog differential filters," *IEEE Transactions on Instrumentation and Measurement,* vol. 45, pp. 275-279, 1996.
[209] M. Massarotto, O. Casas, V. Ferrari, and R. Pallas-Areny, "Improved Fully Differential Analog Filters," *IEEE Transactions on Instrumentation and Measurement,* vol. 56, pp. 2464-2469, 2007.
[210] B. Carter. (2003). A differential op-amp circuit collection. Available: http://www.ti.com/lit/an/sloa064/sloa064.pdf
[211] A. S. Lee, J. Cholewicki, and N. Peter Reeves, "The effect of background muscle activity on computerized detection of sEMG onset and offset," *Journal of Biomechanics,* vol. 40, pp. 3521-3526, // 2007.
[212] X. Chen and Z. J. Wang, "Pattern recognition of number gestures based on a wireless surface EMG system," *Biomedical Signal Processing and Control,* vol. 8, pp. 184-192, 2013.
[213] K. Englehart, B. Hudgin, and P. A. Parker, "A wavelet-based continuous classification scheme for multifunction myoelectric control," *Biomedical Engineering, IEEE Transactions on,* vol. 48, pp. 302-311, 2001.
[214] E. N. Kamavuako, D. Farina, K. Yoshida, and W. Jensen, "Estimation of grasping force from features of intramuscular EMG signals with mirrored bilateral training," *Annals of biomedical engineering,* vol. 40, pp. 648-656, 2012.

[215] A. L. Goldberger, L. A. Amaral, L. Glass, J. M. Hausdorff, P. C. Ivanov, R. G. Mark*, et al.*, "Physiobank, physiotoolkit, and physionet components of a new research resource for complex physiologic signals," *Circulation,* vol. 101, pp. e215-e220, 2000.
[216] A. Phinyomark, C. Limsakul, and P. Phukpattaranont, "A novel feature extraction for robust EMG pattern recognition," *arXiv preprint arXiv:0912.3973,* 2009.
[217] M. Misaki, Y. Kim, P. A. Bandettini, and N. Kriegeskorte, "Comparison of multivariate classifiers and response normalizations for pattern-information fMRI," *NeuroImage,* vol. 53, pp. 103-118, 10/15/ 2010.
[218] MathWorks. *Classify*. Available: https://au.mathworks.com/help/stats/classify.html?searchHighlight=classify&s_tid=doc_srchtitle
[219] A. R. Webb and K. D. Copsey, *Statistical pattern recognition*, 3rd ed.: John Wiley & Sons, 2011.
[220] C.-W. Hsu, C.-C. Chang, and C.-J. Lin, "A practical guide to support vector classification," 2010.
[221] C. E. Thomaz, P. S. Rodrigues, and G. A. Giraldi, "Using face images to investigate the differences between lda and svm separating hyper-planes," in *II workshop de visao computacional*, 2006.
[222] C.-C. Chang and C.-J. Lin, "LIBSVM: A library for support vector machines," *ACM Trans. Intell. Syst. Technol.,* vol. 2, pp. 1-27, 2011.
[223] bqLabs. (2015, Date Accessed: March 16, 2016). *Jointed Hand*. Available: http://www.thingiverse.com/thing:906098/#files
[224] M. Lombard, *SolidWorks surfacing and complex shape modeling bible* vol. 485: John Wiley & Sons, 2011.
[225] B. Buchholz, T. J. Armstrong, and S. A. Goldstein, "Anthropometric data for describing the kinematics of the human hand," *Ergonomics,* vol. 35, pp. 261-273, 1992/03/01 1992.
[226] D.-p. Yang, J.-d. Zhao, Y.-k. Gu, X.-q. Wang, N. Li, L. Jiang*, et al.*, "An anthropomorphic robot hand developed based on underactuated mechanism and controlled by EMG signals," *Journal of Bionic Engineering,* vol. 6, pp. 255-263, 2009.
[227] A. D. Poole and J. D. Booker, "Design methodology and case studies in actuator selection," *Mechanism and Machine Theory,* vol. 46, pp. 647-661, 2011.
[228] J. E. Huber, N. A. Fleck, and M. F. Ashby, "The selection of mechanical actuators based on performance indices," *Proceedings of the Royal Society of London. Series A: Mathematical, Physical and Engineering Sciences,* vol. 453, pp. 2185-2205, 1997.
[229] M. Zupan, M. F. Ashby, and N. A. Fleck, "Actuator Classification and Selection—The Development of a Database," *Advanced Engineering Materials,* vol. 4, pp. 933-940, 2002.
[230] M. A. Saliba and C. Ellul, "Dexterous actuation," *Mechanism and Machine Theory,* vol. 70, pp. 45-61, 2013.
[231] V. O. D. Cura, F. L. Cunha, M. L. Aguiar, and A. Cliquet Jr, "Study of the Different Types of Actuators and Mechanisms for Upper Limb Prostheses," *Artificial Organs,* vol. 27, pp. 507-516, 2003.
[232] S. M., N. T., S. M., Z. M., and M. R., "Critical review of current trends in shape memory alloy actuators for intelligent robots," *Industrial Robot: An International Journal,* vol. 34, pp. 285-294, 2007.
[233] L. Chee Siong, H. Yokoi, and T. Arai, "New Shape Memory Alloy Actuator: Design and Application in the Prosthetic Hand," in *Engineering in Medicine and Biology Society, 2005. IEEE-EMBS 2005. 27th Annual International Conference of the*, 2005, pp. 6900-6903.
[234] J. Stuart and L. Tang, "The Design and Construction of a Biomimetic Prosthetic Hand," Massey University2013.
[235] N. Bianchi and S. Bolognani, "Design techniques for reducing the cogging torque in surface-mounted PM motors," *IEEE Transactions on Industry Applications,* vol. 38, pp. 1259-1265, 2002.
[236] G. Stellin, G. Cappiello, S. Roccella, M. C. Carrozza, P. Dario, G. Metta*, et al.*, "Preliminary Design of an Anthropomorphic Dexterous Hand for a 2-Years-Old Humanoid: towards Cognition," in *The First IEEE/RAS-EMBS International Conference on Biomedical Robotics and Biomechatronics, 2006. BioRob 2006.*, 2006, pp. 290-295.
[237]A. Patel and M. Ferdowsi, "Current Sensing for Automotive Electronics - A Survey," *Vehicular Technology, IEEE Transactions on,* vol. 58, pp. 4108-4119, 2009.
[238] F. Briz, D. Diaz-Reigosa, M. W. Degner, P. Garcia, and J. M. Guerrero, "Current sampling and measurement in PWM operated AC drives and power converters," in *Power Electronics Conference (IPEC), 2010 International*, 2010, pp. 2753-2760.
[239] C. M. Wolf, M. W. Degner, and F. Briz, "Analysis of Current Sampling Errors in PWM VSI Drives," *Industry Applications, IEEE Transactions on,* vol. 51, pp. 1551-1560, 2015.
[240] P. J. Kaufman, *The New Commodity Trading Systems and Methods*. New York: John Wiley & Sons, 1978.
[241] I. Mendez, B. W. Hansen, C. M. Grabow, E. J. L. Smedegaard, N. B. Skogberg, X. J. Uth*, et al.*, "Evaluation of the Myo armband for the classification of hand motions," in *2017 International Conference on Rehabilitation Robotics (ICORR)*, 2017, pp. 1211-1214.
[242] M. Tavakoli, C. Benussi, P. Alhais Lopes, L. B. Osorio, and A. T. de Almeida, "Robust hand gesture recognition with a double channel surface EMG wearable armband and SVM classifier," *Biomedical Signal Processing and Control,* vol. 46, pp. 121-130, 2018/09/01/ 2018.

[243] Y. Zhang, Y. Chen, H. Yu, X. Yang, W. Lu, and H. Liu, "Wearing-independent hand gesture recognition method based on EMG armband," *Personal and Ubiquitous Computing,* vol. 22, pp. 511-524, 2018.

[244] F. Amirabdollahian and M. L. Walters, "Application of support vector machines in detecting hand grasp gestures using a commercially off the shelf wireless myoelectric armband," in *2017 International Conference on Rehabilitation Robotics (ICORR)*, 2017, pp. 111-115.

[245] A. Phinyomark, R. N Khushaba, and E. Scheme, "Feature Extraction and Selection for Myoelectric Control Based on Wearable EMG Sensors," *Sensors (Basel, Switzerland),* vol. 18, p. 1615, 2018.

[246] A. S. Kundu, O. Mazumder, P. K. Lenka, and S. Bhaumik, "Hand gesture recognition based omnidirectional wheelchair control using IMU and EMG sensors," *Journal of Intelligent & Robotic Systems,* vol. 91, pp. 529-541, 2018.